ISSN 1451 - 9372 (Print)
ISSN 2217 - 7434 (Online)
OCTOBER-DECEMBER 2024
Vol.30, Number 4, 275-371

Chemical Industry & Chemical Engineering Quarterly

The AChE Journal for Chemical Engineering,
Biochemical Engineering, Chemical Technology,
New Materials, Renewable Energy and Chemistry
www.ache.org.rs/ciceq

Journal of the
Association of Chemical Engineers of
Serbia, Belgrade, Serbia

Chemical Industry & Chemical Engineering Quarterly

Journal of the
Association of Chemical Engineers of
Serbia, Belgrade, Serbia

Chemical Industry & Chemical Engineering Quarterly

Vol. 30 Belgrade, October-December 2024 No. 4

Chemical Industry & Chemical Engineering Quarterly (ISSN 1451-9372) is published quarterly by the Association of Chemical Engineers of Serbia, Kneza Miloša 9/I, 11000 Belgrade, Serbia

Editor:
Vlada B. Veljković
veljkovic@yahoo.com

Editorial Office:
Kneza Miloša 9/I, 11000 Belgrade, Serbia
Phone/Fax: +381 (0)11 3240 018
E-mail: shi@ache.org.rs
www.ache.org.rs

For publisher:
Ivana T. Drvenica

Secretary of the Editorial Office:
Slavica Desnica

Marketing and advertising:
AChE Marketing Office
Kneza Miloša 9/I, 11000 Belgrade, Serbia
Phone/Fax: +381 (0)11 3240 018

Publication of this Journal is supported by the Ministry of Education, Science and Technological Development of the Republic of Serbia

Subscription and advertisements make payable to the account of the Association of Chemical Engineers of Serbia, Belgrade, No. 205-2172-71, Komercijalna banka a.d., Beograd

Technical Editor:
Marija B. Tasić

Journal manager:
Aleksandar B. Dekanski

Printed by:
Faculty of Technology and Metallurgy, Research and Development Centre of Printing Technology, Karnegijeva 4, P.O. Box 3503, 11120 Belgrade, Serbia

Abstracting/Indexing:
Articles published in this Journal are indexed in *Thompson Reuters* products: *Science Citation Index - Expanded*™ - access *via Web of Science*®, part of *ISI Web of Knowledge*℠

CONTENTS

Anita Smailagić, Sonja Veljović, Steva Lević, Tatjana Šolević Knudsen, Viktor Nedović, Vladimir Pavlović, Maja Natić, **Chemical characterization of different wood fragments and their volatile composition in model spirit solutions**.....275

Stefan Vukmanović, Jasmina Vitas, Snežana Kravić, Zorica Stojanović, Ana Đurović, Biljana Cvetković, Radomir Malbaša, **Influence of main production variables on nutritional characteristics of winery effluent kombucha**.....285

Kumutha Ramalingam, Ilaiyavel Sivakumaran, Mathanbabu Mariappan, Barathiraja Rajendran, **Effect of salt bath nitriding on tribological properties of AISI52100 steel coatings using response surface methodology**.....295

Saman Khawaja, Muhammad Rashid Usman, Rabya Aslam, **Conceptualization and process simulation of a CO_2 based methanol production plant**.....309

Golden Stepha Nallathambi, Bharathi Gowri Sasi Kumar, Guvva Swathy, **The magnetohydrodynamic Williamson fluid flow on an extending sheet with thermophoresis and chemical reaction**.....325

Chitra Devi Venkatachalam, Premkumar Bhuvaneshwaran, Mothil Sengottian, Sathish Raam Ravichandran, **Reliability-based design optimization of screw shaft for continuous high-pressure hydrothermal co-liquefaction process**.....335

Itumeleng Kohitlhetse, Suter Kiplagat Evans, Musamba Banza, Robert Makomere, **Blast furnace slag for SO_2 capture: Optimization and prediction using response surface methodology and artificial neural network**.....349

Muhammad Thoriq Al Fath, Ghendis Ekawati Ayu, Gina Cynthia Raphita Hasibuan, Nisaul Fadilah Dalimunthe, Vikram Alexander, **The effect of glycerol and sago starch addition on the characteristics of bioplastics based on orange peel pectin**.....359

Contents: Vol. 30, Issues 1–4, 2024.....367

Author Index, Vol. 30, 2024.....369

The activities of the Association of Chemical Engineers of Serbia are supported by:

MINISTRY OF SCIENCE, TECHNOLOGICAL DEVELOPMENT AND INNOVATION OF REPUBLIC OF SERBIA

Faculty of Technology and Metallurgy, University of Belgrade

Faculty of Science, University of Novi Sad

Institute for Technology of Nuclear and Other Mineral Raw Materials, Bekgrade

Faculty of Technology, University of Novi Sad

Institute of Chemistry, Technology and Metallurgy, University of Belgrade

Faculty of Technical Sciences University of Novi Sad

Faculty of Technology, University of Niš, Leskovac

Faculty of Technical Sciences, University of Priština, Kosovska Mitrovica

IMS Institute, Belgrade

DCP HEMIGAL
Leskovac

Elixir Prahovo

CI&CEQ
Chemical Industry & Chemical Engineering Quarterly

Available online at
Association of the Chemical Engineers of Serbia AChE
www.ache.org.rs/CICEQ

Chem. Ind. Chem. Eng. Q. 30 (4) 275–284 (2024) CI&CEQ

ANITA SMAILAGIĆ[1]
SONJA VELJOVIĆ[2]
STEVA LEVIĆ[3]
TATJANA ŠOLEVIĆ KNUDSEN[4]
VIKTOR NEDOVIĆ[3]
VLADIMIR PAVLOVIĆ[3]
MAJA NATIĆ[5]

CHEMICAL CHARACTERIZATION OF DIFFERENT WOOD FRAGMENTS AND THEIR VOLATILE COMPOSITION IN MODEL SPIRIT SOLUTIONS

Article Highlights

- Volatile profiles of wood staves used to hasten brandies' aging were obtained
- Among wood samples, the lowest lignin content is detected in the wild cherry wood (23.58%)
- Volatile profiles of alternative woods and oaks significantly differ
- Sakuranin is a potential marker for wild cherry wood identification
- GC-MS is a suitable tool for distinguishing brandies aged with the alternatives

Abstract

This study characterizes oak (sessile and pedunculate oak) and alternative wood (black locust, Myrobalan plum, wild cherry, and mulberry) species as important sources of volatile compounds of aged spirits. Nowadays, their fragments are used to hasten the brandies' aging process. The ATR-FTIR spectra of analyzed wood samples are similar, only the mulberry FTIR spectrum contains unique peaks primarily due to its highest lignin content (40.93%). Using the untargeted GC-MS approach, a total of forty-one volatile compounds were identified in the wood extracts in a model spirit solution. The volatile profiles of alternative wood extracts in a model spirit solution were significantly different, both quantitatively and qualitatively, compared to those of oak. Coniferyl (23.14 μg/g–26.6 μg/g) and sinapyl (23.56 μg/g–25.82 μg/g) alcohols were the most abundant volatile compounds in investigated oak extracts. Resorcinol and coniferyl alcohol were the most abundant volatile compounds in black locust, sakuranin in wild cherry, while resorcinol and β-resorcinaldehyde in mulberry wood. To the best of our knowledge, sakuranin has not been detected in wild cherry wood until now. Besides wood chemical characteristics, the technology used during the aging process strongly influences on volatile profiles of aged brandies, thus, these compounds are potential chemical markers for discrimination between wood species as well as aging technologies.

Keywords: oak, alternative wood, volatile compounds, model spirit solutions.

[1]University of Belgrade, Innovation Center, Faculty of Chemistry Ltd, Belgrade, Serbia

[2]University of Kragujevac, Faculty of Hotel Management and Tourism, Vrnjačka Banja, Serbia

[3]University of Belgrade, Faculty of Agriculture, Belgrade, Serbia

[4]University of Belgrade, Institute of Chemistry, Technology and Metallurgy – Department of Chemistry, Belgrade, Serbia

[5]University of Belgrade, Faculty of Chemistry, Belgrade, Serbia

SCIENTIFIC PAPER

UDC 582.632.2:66:663.5

Wood barrels have been used for centuries in the process of aging brandies, which contribute to significantly better sensorial features (such as appearance and aroma), as well as the quality of brandy [1–4]. Among wood species, oak wood is distinguished as the most convenient and reputable material due to its unique mechanical, physical, and chemical properties [5]. Despite disadvantages, such as expense and length, aging has been established as a notable and irreplaceable process in the production of high-quality brandies [6].

During the process of aging, the contact between brandy and wood surface provokes a wide variety of

Correspondence: S. Veljović, University of Kragujevac, Faculty of Hotel Management and Tourism, Vojvodjanska bb, 36210 Vrnjačka Banja, Serbia.
E-mail: pecic84@hotmail.com; sonja.vejovic@kg.ac.rs
Paper received: 9 March, 2023
Paper revised: 23 November, 2023
Paper accepted: 24 December, 2023

https://doi.org/10.2298/CICEQ230309015S

physical and chemical interactions, resulting in a release of extractable compounds as well as hydrolysis of the wood's constituents (e.g. hemicelluloses and lignin) [3,4,7]. Namely, the hardwoods, exclusively utilized for barrel production, have a highly heterogeneous chemical composition, including three main components: cellulose (40–44%), hemicelluloses (15–35%), and lignin (18–25%), as well as extractives (up to 2%) [8]. In addition, the porosity and density of different wood species affect the composition of the final extract [9]. While wild cherry is highly porous, black locust and mulberry wood possess low and medium porosities, respectively [2]. During the process of aging, the linkages between the main lignin constituents (guaiacyl (G), syringyl (S), and *p*-hydroxyphenyl (H) units [10] are broken and the compounds are released from the wooden cask by alcoholysis in the initial alcohol-water mixture [11].

Since the importance of aging is unquestioned and even more fundamental for the quality of a large number of wines and spirits, the investigation of this process has been subjected to current studies to accelerate the traditional process without any quality impairment [5,8]. The International Organization of Vine and Wine (OIV) approved the use of wood fragments (wood staves or sticks) to accelerate the aging process of wines and spirits, which usage is regulated by the Oenological Codex (resolution OENO 3/2005, Oeno 430/2010) [12]. In addition, oak chips are approved for the aging of spirits according to ECFR regulation [13]. According to EEC regulation No. 1507/2006, 11 October 2006, it is possible to use oak and chestnut pieces for hastening the process of aging wine [12].

Additionally, the utilization of alternative wood fragments species from local regions to hasten aging, such as Eastern Europe or Mediterranean countries, has the potential to be another novel trend introduced into global cooperage [2,14]. Furthermore, the wood fragment made of local oaks and wood alternatives is commonly used for aging brandies in Balkan countries, mostly in homemade production, with expansion in the local industry. To our knowledge, the influence of utilized local wood fragments on the volatile profile of aged brandies has not been investigated, although a report on Slavonija oak chips can be found in the literature [15].

The present study aimed to study the volatile composition of heartwood of different wood species using model spirit solutions as well as to determine the wood samples' surface and the total lignin content. Volatile profiles of experimentally aged brandy samples were examined to collect data for differencing brandies aged by wood fragment addition used to hasten the brandies' aging process.

MATERIALS AND METHODS

Wood samples

In this study, eight different wood stave samples utilized in Balkan cooperage were investigated. They were produced by local wood cask producer VBX-SRL. D.O.O. from Kraljevo, Central Serbia. Considered staves were made of the heartwood from several botanical species, including mulberry (M) (*Morus alba* L.), Myrobalan plum (MP) (*Prunus cerasifera* Ehrh.), black locust (BL) (*Robinia pseudoacacia* L.), wild cherry (C) (*Prunus avium* (L.) L.), and oak (*Quercus petraea* (Matt.) Liebl. (SRO), and *Q. robur* L. (PSO, PGO, POO)). Besides wood samples originating from the territory of the Republic of Serbia, two samples: Slavonija oak (PSO) and Olovo (POO) oak were obtained from Croatia and Bosnia and Herzegovina, respectively. Before analysis, the wood staves were grounded in a wood mill, to enhance the extraction of volatiles from wood samples. The granulation of the obtained sawdust was in the range of 0.5–1.5 mm [16].

Wood analysis

ATR-FTIR spectroscopy

The wood samples' surface chemistry was characterized using an ATR-FTIR spectrometer IR-Affinity (Shimadzu, Japan). The spectra were obtained in the wavenumber range of 4000–600 cm^{-1} at a resolution of 4 cm^{-1}.

Determination of the lignin in wood samples

The lignin content in wood samples was determined according to the procedure reported by Soutar and Bryden [17]. In brief, sample (2 g) was added to 25 ml 72% H_2SO_4, steeped for 75 min at room temperature, diluted with 600 ml water, reflux for 2 h, filtered through a weighted Gooch crucible, washed acid-free with water, dried at 105 °C, cooled and weighed. The lignin content was calculated from the ratio between the mass of lignin and the mass of the wood sample (determined before the treatment with H_2SO_4).

Determination of moisture sorption in wood samples

The moisture sorption (M, %) was determined by the thermogravimetric method using the Infrared Moisture Analyzer (Sartorius MA35). Before moisture sorption measurement, milled wood samples were exposed to 65% relative air humidity for 24 h. The average of three measurements for each sample was considered.

Preparation of wood extracts in a model spirit solution

The extraction was carried out by a widely extended procedure using wood pieces after double distillation to simulate the aging of spirits in the cask. Hydroalcoholic wood extracts were obtained according to the methodology reported by Smailagić *et al.* [16]. In short, wood sawdust (100 g), with a granulation between 0.5 and 1.5 mm, was extracted with 1000 mL of ethanol (60%, v/v), with constant stirring in a laboratory shaker at a speed of 100 rpm for 7 days in dark at room temperature (20 ± 2 °C). Extracts were filtered through filter paper (80 g/m^2) and kept in the refrigerator (4 °C) for further analysis. All extracts were prepared in triplicate.

GC-FID and GC-MS analysis of the wood extracts

Qualitative and quantitative analyses of the wood extracts in a model spirit solution were conducted using GC-MS and GC-FID, respectively. All wood extracts were prepared using liquid-liquid extraction, according to the procedure described by Veljović *et al.* [18]. Briefly, a 50 mL aliquot of each extract was diluted with 100 mL of distilled water and then mixed with 20 mL of internal standard solution (methyl-10-undecanoate diluted in dichloromethane (0.01 mg/mL)) and 10 g of NaCl. Each resultant mixture was stirred on a magnet stirrer in iodometric closed flasks (Erlenmeyer Polishing) for one hour. After mixing, the organic layer was separated from the water layer. The upper organic layer was dried with Na_2SO_4 and then filtered and evaporated on a vacuum-evaporator (45 °C, 10 kPa) (Heidolph Hei-VAP Value rotary evaporator, Schwabach, Germany) to a volume of 2 mL. After preparation, the samples were stored in a refrigerator (4 °C) until analysis.

GC-MS was used for the identification of wood compounds. The injections of prepared extracts (1 µl) were carried out in splitless mode. For GC-MS analyses, an Agilent 7890N gas chromatograph with an HP5-MS capillary column (30 m × 0.25 mm × 0.25 µm) was used. The following temperature program was employed: 60 °C for 0 min; then 3 °C/min to 280 °C and then held for 20 min. Helium was used as a carrier gas with a flow rate of 1 mL/min. The GC was coupled to a Hewlett-Packard 5972 MSD operated at 70 eV and scanning masses in the 40-550 range. The obtained peaks were identified by comparison of their retention times (calculated relative to n-alkanes) with the literature data as well as by comparison of the mass spectra fragmentation pattern with the mass spectra in the databases (NIST/EPA/NIH mass spectral library NIST2000, Wiley/NBS registry of mass spectral data, 7th ed., electronic versions) [19,20].

GC-FID was used for semi-quantitative analyses of wood compounds. For GC-FID analyses, an Agilent 4890A gas chromatograph with an HP5-MS capillary column (30 m × 0.25 mm × 0.25 µm) was used. The employed temperature program was the same as that used for GC-MS analyses. Hydrogen was used as carrier gas (1 mL/min). The GC was coupled to a FID detector operating at 300 °C. The results of GC-MS analyses were expressed as milligrams of methyl-10-undecanoate equivalents per liter of analyzed wood extracts [18]. The limit of detection was established using the US EPA 3σ approach.

Statistical analyses

Tukey's test was used to compare the mean values of lignin content, done in triplicate, with the level of statistical significance set at 0.05 (Statistica v. 12). Principal Component Analysis (PCA) of ATR-FTIR spectra was realized using PAST software [21]. For all PCA analyses, the spectra (1800–800 cm^{-1}) were preprocessed Spectragryph software [22] as follows: the spectra were smoothed using Savitzky-Golay filters with 5 points and a second-order polynomial function, baseline corrected, while the intensities were normalized (Standard Normal Variate-SNV).

RESULTS AND DISCUSSION

Characterization of the wood samples

The wood samples were characterized in terms of their surface chemistry (ATR-FTIR) and lignin content. The FTIR analysis, a rapid and non-destructive method, was performed to distinguish differences in the chemical composition of the wood samples. Fig. 1 shows the spectra of analyzed samples separated into two groups: the FTIR spectra of samples that originated from various tree species (Fig. 1a) and the FTIR spectra of wood samples from various oak varieties (Fig. 1b).

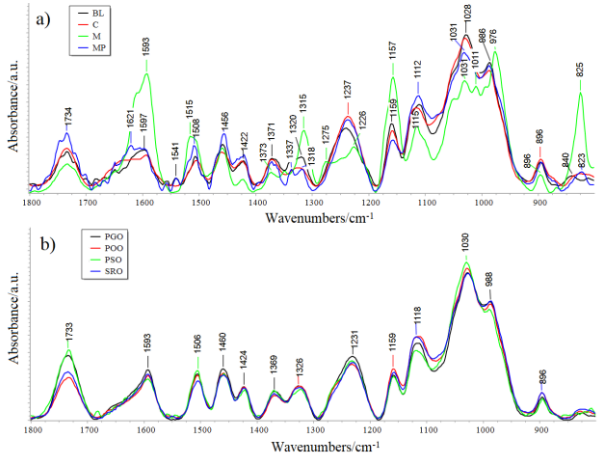

Figure 1. FTIR spectra of tested wood samples: a) Different wood samples from various tree species; b) Oak wood samples.

The FTIR spectra of all samples have major bands that are related to their primarily chemical compounds such as cellulose, hemicellulose, and lignin as well as other less abundant compounds in the wood (e.g. aromatic compounds). The main wood compound is cellulose and its bands are identified in all analyzed spectra: ~1157 cm^{-1} (symmetric C-O-C stretching vibrations) [23]; ~1030 cm^{-1} (C-C and C-O vibrations), ~1115 cm^{-1} (C-O), (C-C) [24]; 896 cm^{-1} (C-H vibrations, cellulose and hemicellulose) indicates presence of the *β*-glycosidic linkages between the cellulose glycosidic units [23, 25–26]. Also, spectra exhibit several common bands that could be related to various wood compounds: ~1733 cm^{-1} (C=O groups); ~1460 cm^{-1} (CH_2 scissoring vibrations, most probably from cellulose); ~1423 cm^{-1} (asymmetric C-H deformation) [23]. Also, the bands near 1423–1460 cm^{-1} can be associated with the C-H bend (aromatic skeletal vibration and asymmetric C-H deformations) [27] and C=C-C aromatic ring stretch modes of lignin [28].

Lignin as well as other aromatic compounds can be identified by bands at around 1596–1593 cm^{-1} and ~1505 cm^{-1} due to skeletal vibrations of the aromatic ring (C=C vibrations), while some of these bands could not be clearly visible in the case of the mulberry; this sample exhibits more intense band at 1515 cm^{-1} (most probably from lignin and other aromatic compounds) [23]. Also, the presence of lignin in the samples was detected by the bands at around 1370 cm^{-1} (symmetric C-H deformation). However, this band in the case of mulberry is broader and shows low intensity compared to other samples. The bands with a maximum of around 1237 cm^{-1} are visible in all samples (sample mulberry shows a low-intensity band around this position) that, according to Gupta *et al.* [23], originates from ring breathing of guaiacyl 'G'. According to the same authors, the band at 1315 cm^{-1} is due to ring breathing of syringyl 'S' and could be clearly visible in the case of sample mulberry, while the oak samples cluster doesn't show any strong vibrations at this position. Also, the FTIR spectrum of mulberry shows a strong band at 825 cm^{-1} most probably due to C-H vibration of aromatic compounds [23] (C-H out-of-plane bends [29]).

The results of lignin content are presented in Fig. 2. Tukey's test showed a significant difference in lignin content among wood staves. Furthermore, the investigated samples possess large variability between their lignin content; it ranges from 23.58% to 40.93%, which can be explained by the parallel influence of multiple factors including botanical species, age, the sampling position, etc. [3,11]. Among all wood samples, the lowest lignin content is detected in the wild cherry wood (23.58%). Furthermore, the oaks have lignin content in the range between 29.91% (Bosna Olovo) and 34.37% (Slavonija). According to Peterson and Perumalla [30], the lignin content of a very diverse group of oaks, which differed in species, geographical location, and application, varied from 20.1 to 30.1%. Additionally, Puech [31] analyzed the lignin content of French and foreign oak, particularly intended for barrel production, and reported its content in the range from 25.3 to 28.5%. The lignin content in black locust (35.09%, Figure 2) is significantly higher than in hardwood of mature wood (20.9–25.8%) since the wood sample investigated in this research paper is much older than in Latorraca *et al.* [32].

The results of moisture content are presented in Fig. 3. Tukey's test showed no significant difference in moisture content among wood staves. Myrobalan plum (MP) is characterized by the highest porosity as well as the highest moisture content (8.45%) compared to the pedunculate oak (Gornji Radan) (PGO) and sessile oak (SRO) (7.10 and 6.38%, respectively). Although samples PGO and SRO belong to the same group of woods (i.e. oaks), the sample PGO (pedunculate oak) has smaller vessels and higher moisture content compared to the sample SRO (sessile oak).

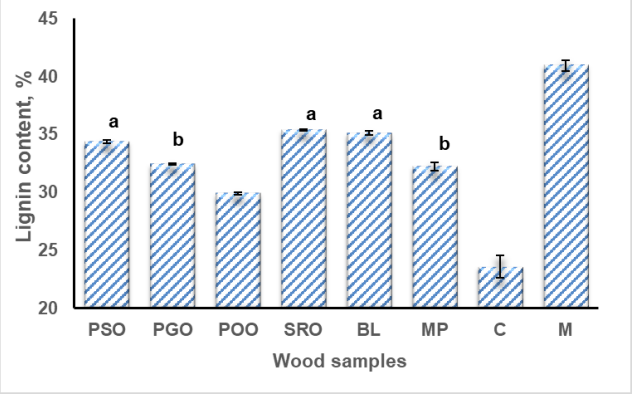

Figure 2. Lignin content of the analyzed wood fragment. The samples with the same letter are not statistically different (α = 0.05).

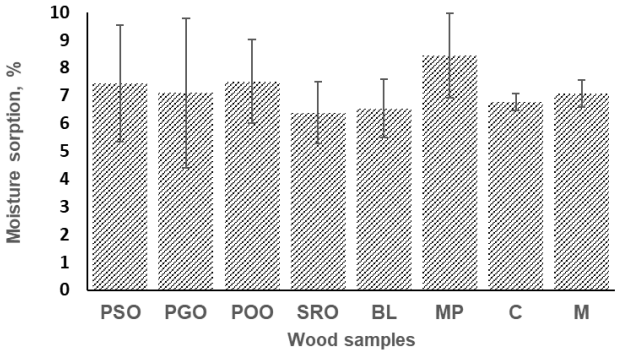

Figure 3. Moisture content of the analyzed wood fragment.

The PCA analysis (Figure 4a) confirmed that mulberry (M) showed the most distinctive spectrum among tested wood samples. As we pointed out, these differences in the mulberry spectrum primarily originated from the difference related to the lignin chemical compositions, i.e. its aromatic compounds. This is supported by loadings of PC 1, where the peaks that can be associated with the chemical composition of mulberry, such as those at 825, 972, 1157, 1311, 1519, and 1591 cm^{-1} are identified. The second group of samples separated by PC 2 is black locust (BL), Myrobalan plum (MP), and wild cherry (C), while the third group represents all studied oaks (PSO, PGO, POO, and SRO). The differences in the chemical structure between these two groups can be associated with the presence of less prominent chemical compounds, such as extractives, that in small concentrations may be crucial for the formation of specific brandy aromatic profiles.

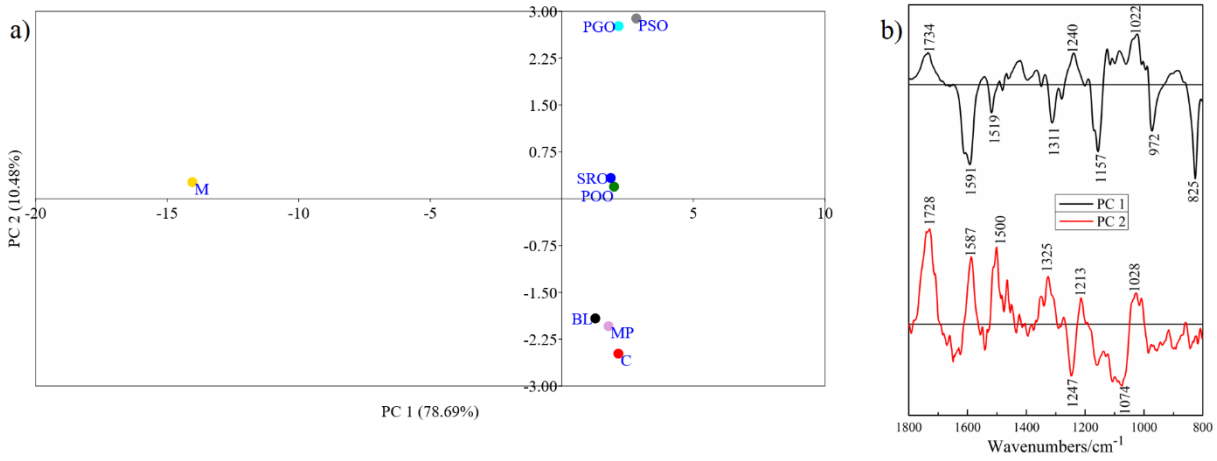

Figure 4. (a) Score plot of PCA for tested wood samples; (b) Loading plots of PC 1 and PC 2.

GC-MS analysis

A total of forty-one compounds were quantified using gas chromatography (GC-MS), Table 1. According to volatile profiles, oaks' aged spirits significantly differ from aged spirits with alternative wood species (i.e. black locust, Myrobalan plum, wild cherry, and mulberry). Although the volatile profiles of analyzed oak-aged spirits are similar, they are opposite from existing published data. Namely, the coniferyl (23.14–26.60 μg/g) and sinapyl (23.56–25.82 μg/g) alcohols are the most abundant volatile compounds in oaks' aged spirits (Table 1). Opposite to this study, De Rosso *et al.* [33] and Flamini *et al.* [34] reported that coniferyl alcohol was found in a low amount within 50% hydroalcoholic oaks' extracts (model spirit), while there was no data about the content of sinapyl alcohol.

All identified compounds in oaks' aged spirits appear due to the lignin degradation and then their oxidation during aging. As it is well known, coniferyl and sinapyl alcohols are the main lignin compounds, whose presence in the wood fragments was confirmed by the ATR-FTIR (Figure 1). During aging, these alcohols are released and converted to aromatic aldehydes (coniferyl aldehyde, and sinapyl aldehyde) relatively quickly by oxidation and to respective acids by further oxidation [7]. In general, the differences between the present and previously published results occur because the decreasing of the coniferyl and sinapyl alcohols' content, and simultaneously increasing the amount of aromatic aldehydes and acids, is necessary to prolong the aging period. Thereby, the amount of vanillin (0.30–0.78 μg/g) and syringaldehyde (1.71–2.17 μg/g), as aromatic aldehydes whose formation depends on the oaks aging time, is lower. Moreover, the amount of syringaldehyde is lower (1.71 μg/g) in sessile oak (SRO) than in pedunculate oaks (PSO, PGO, and POO) (1.85–2.17 μg/g). On the other hand, the highest amount of vanillin has PGO (0.78 μg/g), while the lowest Slavonija pedunculate oak (PSO, 0.3 μg/g). The amount of coniferyl aldehyde (3.51 μg/g) and sinapyl aldehyde (7.95 μg/g) is higher in sessile oak (SRO) than in pedunculate oaks (2.19–2.47 μg/g and 4.49–5.40 μg/g, respectively). Besides vanillin and syringaldehyde, De Rosso *et al.* [33] found that oaks contain eugenol (aromatic terpene characteristic for oak-aged beverages) [3], methoxyeugenol, and *α*-terpineol. In our case, *α*-terpineol was not detected. Furthermore, Chira and Teissedre [15] reported the presence of *cis*- and *trans*-*β*-methyl-*γ*-octalactone (known as oak lactones) in oaks. The odor intensity of *β*-methyl-*γ*-octalactone *cis* isomer (woody, coconut odor) is about 2–12 times stronger in comparison with its *trans* isomer [37,38]. Herein, *β*-methyl-*γ*-octalactone *cis* isomer is more

Table 1. Quantitative data on wood extracts volatile compounds.

Compound (μg/g of wood)	Odor quality	Odor detection threshold (ppm, mg dm^{-3})	PSO	PGO	POO	SRO	BL	MP	C	M
Limonene	Orange peel-like ((R)-Limonene)[35,]	0.20[39]	n.d.	n.d.	n.d.	n.d.	n.d.	0.49	0.72	n.d.
Acetophenone	Citrusy, orange peel-like[36] Floral[40]	0.256[41]	n.d.	n.d.	n.d.	n.d.	n.d.	n.d.	0.01	n.d.
Benzoic acid	Balsamic[35]		n.d.	n.d.	n.d.	n.d.	n.d.	0.30	n.d.	n.d.
Coumaran			n.d.	n.d.	n.d.	n.d.	n.d.	n.d.	n.d.	0.48
Vinylguaiacol	Smoky[40]	0.209[41]	0.08	0.19	0.17	0.26	n.d.	n.d.	n.d.	n.d.
o-Acetyl-*p*-cresol			n.d.	n.d.	n.d.	n.d.	0.26	n.d.	n.d.	n.d.
Eugenol	Clove[35,37] spicy, sweet[37] Flowery, clove[35]	0.0070[38]	0.08	0.54	0.48	0.03	n.d.	n.d.	n.d.	n.d.
Syringol	Spicy, phenolic[37] Burnt, smoke, burned wood[38]	0.58[38]	0.16	0.34	0.34	0.27	1.48	n.d.	n.d.	1.59
Methylresorcinol			n.d.	n.d.	n.d.	n.d.	n.d.	n.d.	n.d.	1.33
Resorcinol			n.d.	n.d.	n.d.	n.d.	10.07	n.d.	n.d.	62.00
β-Resorcinaldehyde			n.d.	n.d.	n.d.	n.d.	3.46	n.d.	n.d.	13.76
Resacetophenone			n.d.	n.d.	n.d.	n.d.	2.08	n.d.	n.d.	n.d.
trans-*β*-methyl-*γ*-octalactone	Coconut[c37] Sweet, flowery[38]	0.79[38]	0.17	0.25	0.24	0.72	n.d.	n.d.	n.d.	n.d.
cis-*β*-methyl-*γ*-octalactone	Coconut[37] Coconut, sweet[38]	0.067[38]	0.34	1.65	1.59	0.05	n.d.	n.d.	n.d.	n.d.
Vanillin	Vanilla[35-39]	0.022[38]	0.30	0.78	0.76	0.64	n.d.	n.d.	n.d.	n.d.
Isoeugenol (*cis*- or *trans*-)			n.d.	0.16	n.d.	n.d.	n.d.	n.d.	n.d.	n.d.
Homovanillyl alcohol			0.28	0.38	0.35	0.43	0.20	n.d.	n.d.	n.d.
Vanillyl propan-2-one			0.69	1.00	0.72	0.12	0.95	n.d.	n.d.	n.d.
Vanillic acid			n.d.	0.05	0.19	0.88	n.d.	n.d.	0.09	n.d.
Propiovanillone			0.32	0.36	0.32	0.09	n.d.	n.d.	n.d.	n.d.
3,4,5-Trimethoxy-phenol			n.d.	n.d.	n.d.	n.d.	n.d.	0.09	7.64	n.d.
Methoxyeugenol			0.32	0.56	0.26	0.79	0.67	n.d.	n.d.	n.d.
Homovanillic acid			0.50	0.50	0.38	0.44	n.d.	n.d.	n.d.	n.d.
Methyl homovanillate			0.33	0.32	0.27	0.44	n.d.	n.d.	n.d.	n.d.
Syringaldehyde	green, woody[32] green, woody, sweet[33]		1.85	2.17	2.04	1.71	0.94	0.20	n.d.	n.d.
Syringic acid			0.25	0.92	0.32	1.02	n.d.	n.d.	0.12	n.d.
Syringyl propan-2-one			0.73	0.73	0.50	0.86	n.d.	n.d.	n.d.	n.d.
Butyrosyringone			0.52	0.57	0.47	0.54	n.d.	n.d.	n.d.	n.d.
Coniferyl alcohol			26.6	25.73	24.47	23.14	9.75	n.d.	n.d.	0.36
Coniferyl aldehyde			2.47	2.21	2.19	3.51	2.14	n.d.	n.d.	1.55
4-hydroxy-3,5-dimethoxybenzoic acid			n.d.	n.d.	n.d.	n.d.	n.d.	0.18	n.d.	n.d.
Scopoletin			n.d.	n.d.	n.d.	n.d.	n.d.	0.03	n.d.	n.d.
Sinapyl aldehyde			5.40	4.89	4.49	7.95	4.88	n.d.	0.1	n.d.
Sinapyl alcohol			23.56	24.84	24.71	25.82	1.53	0.03	n.d.	n.d.
Dihydrosinapyl alcohol			0.09	0.53	0.58	0.51	n.d.	n.d.	n.d.	n.d.
Pinocembrin			n.d.	n.d.	n.d.	n.d.	n.d.	n.d.	0.80	n.d.
Tectochrysin			n.d.	n.d.	n.d.	n.d.	n.d.	n.d.	220.15	n.d.
2,6-Dimethoxybenzoquinone			n.d.	n.d.	n.d.	n.d.	n.d.	n.d.	0.30	n.d.
Chrysin			n.d.	n.d.	n.d.	n.d.	n.d.	n.d.	467.22	n.d.
Sakuranin			n.d.	n.d.	n.d.	n.d.	n.d.	n.d.	896.65	n.d.
Naringenin			n.d.	n.d.	n.d.	n.d.	n.d.	n.d.	75.91	n.d.
Total volatile compounds			65.04	69.67	65.84	70.22	38.41	1.32	1669.71	81.07

n.d. - not detected. Results are expressed as milligrams of methyl -10-undecanoate equivalents per liter of analyzed wood extracts

abundant in pedunculate oak samples (0.34-1.65 μg/g), while *trans* isomer is more abundant in sessile oak (0.72 μg/g). These two isomers, along with vanillin are major oak wood aroma compounds that have a great influence on wine aroma [30].

The main characteristic of wild cherry volatile profile, in comparison with other analyzed wood samples, was the high content of flavonoids, whose presence was also previously confirmed by HPLC-MS [16]. Five flavonoids including three flavanones (pinocembrin, naringenin, and sakuranin) and two flavones (467.22 μg/g chrysin and 220.15 μg/g tectochrysin) are exclusively detected in wild cherry (C). It is good to mention that the amount of sakuranin (896.65 μg/g) found in wild cherry is significantly higher than the two other flavanones. In another study, besides the aforementioned flavonoids, Vinciguerra *et al.* [42] identified three more flavanones (sakuranetin, pinostrobin, dihydrowogonin) and one dihydroflavonol (aromadendrin-7-methylether) in the heartwood of *Prunus avium*. Moreover, several flavonoids such as eriodictyol, sakuranetin, pinocembrin, and chrysin are suggested as markers of cherry hardwood and wine aged in cherry wood [16,43]. To our knowledge, sakuranin has not previously been detected in wild cherry wood, consequently. Additionally, it can be concluded that the hardwood of *Prunus avium* L. (wild cherry) species contains a significant amount of flavonoids compared with oak wood species, which is in agreement with the literature [2]. Wild cherry wood aged spirit (C) contains a high amount (7.64 μg/g) of 3,4,5-trimethoxy-phenol and a low amount of volatile compounds, which is in agreement with the previously published research [33,34].

Myrobalan plum has a significantly lower amount of volatiles (1.32 μg/g, Table 1) compared to the oaks (65.04–70.22 μg/g). Quantitatively, the most abundant volatile compounds in Myrobalan plum are terpene limonene (0.49 μg/g) and benzoic acid (0.30 μg/g). According to Bandeira Reidel *et al.* [44], limonene was detected as the most abundant compound in a stem of *P. cerasifera* 'Pissardii', while this compound was not detected in a stem of *P. cerasifera*. The presence of limonene was also confirmed in apple brandies aged with mulberry and sessile oak [5], which is opposite from our research, whereas limonene is detected in Myrobalan plum and wild cherry. The limonene, with citrus and herbal aroma notes, is the only detected terpene in all analyzed samples. Moreover, scopoletin was detected exclusively in Myrobalan plum-aged spirit. This is the opposite of literature data, where scopoletin was first considered as a marker for oak wood, but later it was detected also in chestnut and wild cherry wood [6].

Besides in black locust, the resorcinol is dominant compound in mulberry (M) with an amount of 62.00 μg/g, followed by a significant amount of *β*-resorcinaldehyde (13.76 μg/g), syringol (1.59 μg/g). De Rosso *et al.* [33] found a large amount of *β*-resorcinaldehyde in mulberry wood extract in a model spirit solution. Interestingly, the volatile profile of black locust (BL) differs from the results reported in the literature. In our case, the most abundant compound in black locust is resorcinol (10.07 μg/g), followed by coniferyl alcohol (9.75 μg/g), while the contents of coniferyl aldehyde and syringaldehyde were slightly lower (2.14 μg/g and 0.94 μg/g, respectively). Fernández de Simón *et al.* [46] also detected resorcinol, but not as the most abundant compound in black locust. De Rosso *et al.* [33] and Flamini *et al.* [34] found syringaldehyde as the dominant black locust compound as well as a large amount of vanillin, which is not found in the investigated black locust. On the other hand, Fernández de Simón *et al.* [45] observed coniferyl alcohol and sinapyl aldehyde as dominant compounds in seasoned black locust wood aged spirit. A high amount of *β*-resorcinaldehyde (3.46 μg/g) and no eugenol were found in the investigated black locust wood-aged spirit, which was in accordance with the findings of De Rosso *et al.* [33], and Flamini *et al.* [34]. In addition, the presence of methoxyeugenol, as in our case, was also confirmed by De Rosso *et al.* [33]. Generally, the composition of black locust wood extract in the model spirit solution is in accordance with the previous studies.

Herein, some volatile compounds were unique components of the volatile profile of certain alternative and oak species, which can contribute to the identification of specific wood species. Therefore, 2,6-dimethoxybenzoquinone and volatile flavonoids (pinocembrin, naringenin, sakuranin, chrysin, and tectochrysin) were quantified only in wild cherry wood. The coumaran and methylresorcinol are present only in mulberry (M), while *o*-acetyl-*p*-cresol and resacetophenone are present only in the black locust (BL). Benzoic acid, scopoletin, and 4-hydroxy-3,5-dimethoxybenzoic acid were found only in Myrobalan plum. Many compounds, such as oak lactones, vinylguaiacol, eugenol, vanillin, propiovanillone, homovanillic acid, methyl homovanillate, syringyl propan-2-one, butyrosyringone, and dihydrosynapic alcohol were found only in oak samples. Interestingly, isoeugenol was found only in oak from Gornji Radan (PGO).

CONCLUSION

The main idea of the current research was about the chemical degradation of lignin-based matrices in

the presence of hydroalcoholic solution, as well as surface chemistry and lignin content of local wood fragments traditionally used in Balkan countries for hastening brandies' aging. The ATR-FTIR spectra of the samples are similar, only the mulberry FTIR spectrum contains unique peaks due to its highest lignin content (40.93%). Wild cherry stood up from other wood species by the lowest lignin content, as well as the richness in flavonoids in its volatile profile. The profiling of volatile compounds released from local wood fragments can provide valuable data on local wood and aged spirits to improve the products' quality. In addition to GC-MS analyses, FTIR spectral analysis in combination with PCA can be promising as a potentially effective tool used to distinguish oak and alternative wood samples.

To conclude, with the presented results we are closing the loop. The outcomes from the current research, together with our previously published results on characteristic phenolic profiles of the same wood pieces, may be considered as a good starting point to consider the utilization of wood pieces of alternative wood species from local regions for hastening brandy aging to decrease the cost of aging technology. To the best of our knowledge, the wood particles (smaller than 2mm) used in this research could be used for aging, but the aging time must be optimized. Concerning the type of wood used in the aging process, mulberry wood stood out with the highest lignin content, and its aging potential can be further investigated. Collected data can pave the way to establish geographical indicators of famous aged fruit brandies to protect authenticity and locally sourced products, as well as reduce fraudulent production. Furthermore, this study could be the initial step for establishing regulation in the aging process of alcoholic brandy at the local and regional levels.

ACKNOWLEDGMENT

This work was supported by the Ministry of Education, Science and Technological Development, Republic of Serbia (Contact No. 451-03-68/2022-14/200116, 451-03-68/2022-14/200135 and 451-03-65/2024-03).

REFERENCES

[1] M. Carpena, A.G. Pereira, M.A. Prieto, J. Simal-Gandara. Foods 9 (2020) 1160. https://doi.org/10.3390/foods9091160.

[2] A. Martínez-Gil, M. Del Alamo-Sanza, R. Sánchez-Gómez, I. Nevares, Beverages 4 (2018) 94–118. https://doi.org/10.3390/beverages4040094.

[3] J.R. Mosedale, J.L. Puech, Trends Food Sci. Technol. 9 (1998) 95–101. https://doi.org/10.1016/S0924-2244(98)00024-7.

[4] B. Zhang, J. Cai, C.-Q. Duan, M.J. Reeves, F.A. He, Int. J. Mol. Sci. 16 (2015) 6978–7014. https://doi.org/10.3390/ijms16046978.

[5] P. Híc, M. Horák, J. Balík, K. Martinák, Wood Sci. Technol. 55 (2021) 257–270. https://doi.org/10.1007/s00226-020-01225-x.

[6] T.E. Coldea, C. Socaciu, E. Mudura, S.A. Socaci, F. Ranga, C.R. Pop, F. Vriesekoop, A. Pasqualone, Food Chem. 320 (2020) 126643. https://doi.org/10.1016/j.foodchem.2020.126643.

[7] S. Cernîsev, Food Control. 73 (2017) 281–290. https://doi.org/10.1016/j.foodcont.2016.08.015.

[8] M. Guerrero-Chanivet, M.V, García-Moreno, M.J., Valcárcel-Muñoz, D.A., Guillén-Sánchez, Wood Sci Technol (2023) 861–878. https://doi.org/10.1007/s00226-023-01478-2.

[9] E. Sjöström, R. Alén, Analytical methods in wood chemistry, pulping, and papermaking, Verlag Berlin Heidelberg: Springer, Berlin (1999), p. 1–19. https://doi.org/10.1007/978-3-662-03898-7_1.

[10] L. Wang, H. Ni, J. Zhang, Y. Zhao, G. Tian, Z. Wang, Sci. Total Environ. 717 (2020) 137241. https://doi.org/10.1016/j.scitotenv.2020.137241.

[11] A. Le Floch, M. Jourdes, P.L. Teissedre, Carbohydr. Res. 417 (2015) 94–102. https://doi.org/10.1016/j.carres.2015.07.003.

[12] Organisation Internationale de la Vigne et du Vin (OIV). International Code of Oenological Practices; OIV: Paris, France, (2015), pp. 1–17. ISBN 979-10-91799-10-2.

[13] European Union. Commission Regulation (EC) No 1507/2006. Off. J. Eur. Union 2006, 280, 1–9.

[14] C. Bargalló-Guinjoan, P. Matias-Guiu, J.J. Rodríguez-Bencomo, F. López, Wood Sci. Technol. 57 (2023) 307–323. https://doi.org/10.1007/s00226-022-01435-5.

[15] K. Chira, P.L. Teissedre, Eur. Food Res. Technol. 240 (2015) 533–547. https://doi.org/10.1007/s00217-014-2352-3.

[16] A. Smailagić, S. Veljović, U. Gašić, D. Dabić Zagorac, M. Stanković, K. Radotić, M. Natić, Ind. Crops Prod. 132 (2019) 156–167. https://doi.org/10.1016/j.indcrop.2019.02.017.

[17] T. H. Soutar, M. Bryden (1955) J. Textile Inst. Transactions, 46 (1955) 8, T521–T528, https://doi.org/10.1080/19447027.1955.1075033.

[18] S. Veljović, N. Tomić, M. Belović, N. Nikićević, P. Vukosavljević, M. Nikšić, V. Tešević, Food Technol. Biotech. 57 (2019) 408–417. https://doi.org/10.17113/ftb.57.03.19.6106.

[19] R.P. Adams, Identification of essential oil components by gas chromatography/mass spectrometry, Allured Publishing Corporation, Carol Stream, IL (2007), p. 1902–1903. https://doi.org/10.1016/j.jasms.2005.07.008.

[20] R. Flamini, P. Traldi, Mass spectrometry in grape and wine chemistry. USA: John Wiley & Sons, Inc, New Jersy (2010) p. 95–116. https://doi.org/10.1002/9780470552926.ch5.

[21] Ø. Hammer, D.A.T. Harper, P.D. Ryan. Palaeontol.

Electron. 4(1) (2001) 9. http://palaeo-electronica.org/2001_1/past/issue1_01.htm.

[22] F. Menges, "Spectragryph - optical spectroscopy software", Version 1.2.8, 2018, http://www.effemm2.de/spectragryph/.

[23] B.S. Gupta, B.P. Jelle, T. Gao, (2015) Int. J. Spectrosc., 521938, https://doi.org/10.1155/2015/521938.

[24] I. Kubovský, D. Kačíková, F. Kačík, Polymers 12 (2020) 485. https://doi.org/10.3390/polym12020485.

[25] Z. Shi, G. Xua, J. Denga, M. Dong, V. Murugadoss, C. Liuc, Q. Shaoe, S. Wufand, Z. Guo, Green Chem. Lett. Rev. 12 (3) (2019) 235–243. https://doi.org/10.1080/17518253.2019.1627428.

[26] P. Bock, N. Gierlinger, J. Raman Spectrosc.50 (2019) 778–792 https://doi.org/10.1002/jrs.5588.

[27] H. Schulz, M. Baranska, Vib. Spectrosc. 43 (2007) 13–25. https://doi.org/ 10.1016/j.vibspec.2006.06.001.

[28] C. Ganne-Chedeville, A.-S. Jääskelaäinen, J. Froidevaux, M. Hughes, P. Navi, Holzforschung 66 (2012) 163–170. https://doi.org/10.1515/HF.2011.148.

[29] Ö. Özgenç, S. Durmaz, I.H. Boyaci, H. Eksi-Kocak, Spectrochim. Acta A Mol. Biomol. Spectrosc. 171 (2017) 395–400. https://doi.org/10.1016/j.saa.2016.08.026.

[30] C.A. Peterson, C.J Perumalla, J. Exp. Bot. 35 (1984) 51–57. http://www.jstor.org/stable/23688558.

[31] J.L. Puech, Am. J. Enol. Vitic. 35 (1984) 77–81. https://doi.org/10.5344/ajev.1984.35.2.77.

[32] J.F.V. Latorraca, O. Dünisch, G. Koch, An. Acad. Bras. Cienc. 83 (2011) 1059–68. https://doi.org/10.1590/s0001-37652011005000016.

[33] M. De Rosso, D. Cancian, A. Panighel, A. Dalla Vedova, R. Flamini, Wood Sci. Technol. 43 (2009) 375–385. https://doi.org/10.1007/s00226-008-0211-8.

[34] R. Flamini, A. Dalla Vedova, D. Cancian, A. Panighel, M. De Rosso, J. Mass Spec. 42 (2007) 641–646. https://doi.org/10.1002/jms.1193.

[35] R. Ghadiriasli, M.A.A. Mahmoud, M. Wagenstaller M, J.W. van de Kuilen, A. Buettner, Food. Res. Int. 150 (2021) 110776. https://doi.org/10.1016/j.foodres.2021.110776.

[36] R. Ghadiriasli, M. Wagenstaller, A. Buettner, Anal. Bioanal. Chem. 410 (25) (2018) 6595–6607. https://doi.org/10.1007/s00216-018-1264-7.

[37] L. Culleré, B. Fernández de Simón, E. Cadahía, V. Ferreira, P. Hernández-Orte, J. Cacho, LWT - Food Sci. Technol. 53 (1) (2013) 240–248. https://doi.org/10.1016/j.lwt.2013.02.010.

[38] Caldeira, R. Santos, J. M. Ricardo-da-Silva, O. Anjos, H. Mira, A.P. Belchior, S. Canas, Food Chem. 211 (2016) 937–946. https://doi.org/10.1016/j.foodchem.2016.05.129.

[39] H. Tamura, S. Boonbumrung, T. Yoshizawa, W. Varanyanond. Food Sci. Technol. Res., 7 (1) (2001) 72–77. https://doi.org/10.3136/fstr.7.72.

[40] S. Chen, J. Tang, S. Fan, J. Zhang, S. Chen, Y. Liu, Q. Yang, Y. Xu. Foods10(10) (2021) 2392. https://doi.org/10.3390/foods10102392.

[41] J.S. Câmara, M.A. Alves, J.C. Marques, Anal. Chim. Acta 563 (2006) 188–197. https://doi.org/10.1016/j.aca.2005.10.031.

[42] V. Vinciguerra, M. Luna, A. Bistoni, F. Zollo, Phytochem. Anal. 14 (2003) 371–377. https://doi.org/10.1002/pca.730.

[43] F. Chinnici, N. Natali, A. Bellachioma, A. Versari, C. Riponi, LWT - Food Sci. Technol. 60 (2015) 977–984. https://doi.org/10.1016/j.lwt.2014.10.029.

[44] R. V. Bandeira Reidel, P. L. Cioni, L. Pistelli, Biochem. Syst. Ecol. 75 (2017) 10–17. https://doi.org/10.1016/j.bse.2017.10.001.

[45] B. Fernández de Simón, M. Sanz, E. Cadahía, N. Sanz, E. Esteruelas, A.M. Muñoz, J. Mass Spec. 49 (2014) 353–70. https://doi.org/10.1002/jms.3347.

[46] B. Fernández de Simón, E. Esteruelas, A.M. Muñoz, E. Cadahía, M. Sanz, J. Agri. Food Chem. 57 (2009) 3217–3227. https://doi.org/10.1021/jf803463h.

ANITA SMAILAGIĆ[1]
SONJA VELJOVIĆ[2]
STEVA LEVIĆ[3]
TATJANA ŠOLEVIĆ KNUDSEN[4]
VIKTOR NEDOVIĆ[3]
VLADIMIR PAVLOVIĆ[3]
MAJA NATIĆ[5]

[1]Univerzitet u Beogradu, Inovacioni centar Hemijskog fakulteta, Beograd, Srbija

[2]Univerzitet u Kragujevcu, Fakultet za hotelijerstvo i turizam, Vrnjačka Banja, Srbija

[3]Univerzitet u Beogradu, Poljoprivredni fakultet, Beograd, Srbija

[4]Univerzitet u Beogradu, Institut za hemiju, tehnologiju i metalurgiju – Departman za hemiju, Beograd, Srbija

[5]Univerzitet u Beogradu, Hemijski fakultet, Beograd, Srbija

NAUČNI RAD

HEMIJSKA KARAKTERIZACIJA RAZLIČITIH FRAGMENATA DRVETA I SASTAV ISPARLJIVIH JEDINJENJA U MODEL RASTVORU ALKOHOLNIH PIĆA

U ovoj studiji okarakterisane su različite vrste hrasta (hrast kitnjak i lužnjak) i alternativne vrste drveta (bagrem, džanarika, trešnja i dud) kao važan izvor isparljivih jedinjenja u alkoholnim pićima koja su odležavala u kontaktu sa drvetom. Danas se fragmenti navedenih vrsta drveta koriste za ubrzavanje procesa odležavanja rakija. ATR-FTIR spektri analiziranih uzoraka drveta su slični, jedino FTIR spektar duda sadrži jedinstvene pikove uglavnom zbog najvećeg sadržaja lignina u ovom uzorku (40,93%). Koristeći neselektivnu metodu gasne hromatografije (GC-MS), identifikovano je ukupno četrdeset i jedno isparljivo jedinjenje u model rastvoru alkoholnih pića. Profil isparljivih jedinjenja u ekstraktima alternativnih vrsta drveta u model rastvoru su se kvalitativno i kvantitativno značajno razlikovali u poređenju sa profilom hrasta. Najzastupljenija isparljiva jedinjenja u analiziranim ekstraktima hrasta bili su koniferil (23,14 μg/g–26,6 μg/g) i sinapil (23,56 μg/g–25,82 μg/g) alkohol. Rezorcinol i koniferil alkohol su bili najzastupljenija isparljiva jedinjenja u bagremu, sakuranin u divljoj trešnji, dok su rezorcinol i β-rezorcinaldehid bili najzastupljeniji u drvetu duda. Koliko nam je poznato, sakuranin do sada nije otkriven u drvetu divlje trešnje. Pored hemijskih karakteristika drveta, tehnologija korišćena tokom procesa odležavanja značajno utiče na profil isparljivih jedinjenja u rakijama koje su odležavale u kontaktu sa drvetom, tako da su navedena jedinjenja potencijalni hemijski markeri za razdvajanje između korišćenih vrsta drveta kao i tehnologija odležavanja.

Ključne reči: hrast, alternativne vrste drveta, isparljiva jedinjenja, model rastvor alkoholnih pića.

CI&CEQ
Chemical Industry & Chemical Engineering Quarterly

Available online at
Association of the Chemical Engineers of Serbia AChE
www.ache.org.rs/CICEQ

Chem. Ind. Chem. Eng. Q. 30 (4) 285–294 (2024) CI&CEQ

STEFAN VUKMANOVIĆ[1]
JASMINA VITAS[1]
SNEŽANA KRAVIĆ[1]
ZORICA STOJANOVIĆ[1]
ANA ĐUROVIĆ[1]
BILJANA CVETKOVIĆ[2]
RADOMIR MALBAŠA[1]

[1]University of Novi Sad, Faculty of Technology Novi Sad, Bulevar cara Lazara 1, Novi Sad, Serbia

[2]University of Novi Sad, Institute of Food Technology, Bulevar cara Lazara 1, Novi Sad, Serbia

INFLUENCE OF MAIN PRODUCTION VARIABLES ON NUTRITIONAL CHARACTERISTICS OF WINERY EFFLUENT KOMBUCHA

Article Highlights

- Total sugars, nitrogen, and phosphorus consumption rates were determined
- The influence of temperature on sugar, nitrogen, and phosphorus content was observed
- Sugar was the most influential nutrient for kombucha winery effluent fermentation

Abstract

Determination of sugar, nitrogen, and phosphorus consumption by kombucha culture is necessary to gain additional insight into the kombucha metabolic pathways and nutritional value of the produced beverages and to set a basis for optimizing the conditions for large-scale production. Kombucha beverage was made using effluent obtained from grape must clarification phase of white wine production. The fermentation medium was prepared by diluting the sterilized initial medium with approximately 16% of total reducing sugars to 3, 5, and 7% of total reducing sugars. The duration of the fermentation was nine days at 20, 25, and 30 °C. Sugars, nitrogen, and phosphorus content were measured using DNS, Kjeldahl, and molybdenum blue methods, respectively. The highest sugar content was in the initial medium (16.34%) and the lowest was after nine days of fermentation at 30 °C with 3% initial sugar content (0.17%). Residual levels of sugars, nitrogen, and phosphorus after three days were modeled using response surface methodology. The proposed mathematical models for sugars and nitrogen content showed an exceptional correlation with the experimentally obtained values. With this study insight into kombucha's consumption of basic nutrients, nutritional value of the obtained products, and optimization of product composition was provided.

Keywords: kombucha, nutrient utilisation, sugars, nitrogen, phosphorus.

SCIENTIFIC PAPER

UDC 582.282.23:663.2

Kombucha is a fermented beverage produced by a symbiotic culture of yeasts and bacteria (SCOBY) using a medium rich in nutrients [1]. Traditional kombucha is made using black or green tea (1.5 g/L) decocts sweetened by sucrose (7% w/v) with a typical fermentation period of 7 days at 25 °C [2,3]. Tea is used as a nitrogen source [4], while sucrose is a source of carbon, being hydrolyzed to glucose and fructose [5]. Symbiotic metabolic interactions between species in SCOBY influence kombucha's physical, chemical, biological, and sensory properties [6]. Two phases can be observed during kombucha fermentation, sour liquid beverage and floating cellulose pellicle [7].

Health benefits associated with kombucha consumption have been attributed to the polyphenolic compounds, organic acids, vitamins, amino acids, antibiotics, and micronutrients synthesized during kombucha fermentation [8]. Kombucha beverage is nowadays available in many forms and flavors, which

Correspondence: J. Vitas, University of Novi Sad, Faculty of Technology Novi Sad, Bulevar cara Lazara 1, 21000 Novi Sad, Serbia.
E-mail: vitasj@uns.ac.rs
Paper received: 2 October, 2023
Paper revised: 25 December, 2023
Paper accepted: 16 January, 2024

https://doi.org/10.2298/CICEQ231002001V

together with confirmation of its beneficial properties by many researchers contributed to its popularity and increased widespread availability [9]. Particularly in the United States, kombucha has been popularized by social media, highlighting its health benefits [10]. The recommended daily consumption of kombucha beverages is around 120 mL for healthy adults, according to the USA Centers for Disease Control and Prevention.

It is very well known that nutrients represent the substances present in food that determine biological activity and are vital for the human body. They are categorized as carbohydrates, proteins, minerals, fats, and vitamins. They are involved in building all parts (proteins), producing energy (carbohydrates), and keeping the good working order (minerals) of the human organism.

The carbon availability is an essential growth factor for any microbial culture. Previous studies demonstrated that kombucha products can be successfully obtained by using winery effluent as an alternative substrate for the fermentation process [32]. For kombucha cultivated on winery effluent, the main carbon sources are simple sugars, i.e. glucose and fructose.

Although at the very early stadium of the grape berry development, there is a certain amount of sucrose, at later stadiums sucrose is almost completely hydrolyzed to glucose and fructose, but that ratio is never 1:1. At the beginning, the glucose content is higher, and it drops during the harvest, whilst the fructose content is constant, so at the end, the grape contains negligible more fructose than glucose [11]. Scientific research established that the carbon source influences different metabolic pathways activation in kombucha culture microorganisms. For example, fructose and sucrose stimulate ethanol synthesis, while glucose has the opposite effect. Sucrose also enables the biosynthesis of lactic acid [12].

Nitrogen is an essential element for all forms of life and is the structural component of amino acids [13]. Only six members of *Acetobacteriacaeae* can fix nitrogen, among which *Gluconobacter kombuchae* sp. nov. was isolated from kombucha tea [14]. Several strains of *Komagataeibacter* spp. express nitrogen fixation with *K. hanseii* RG3 displaying the ability to synthesize cellulose besides the fixation of nitrogen [15]. The Recommended Dietary Allowance of nitrogen for adults both men and women is 800 mg/day of body weight [16].

Phosphorus is an essential mineral element found in rocks, soil, plants, and animal tissues, while in aquatic systems phosphorus plays a critical role in the process of eutrophication, as the nutrient that limits the growth of phytoplankton. Phosphorus homeostasis in the body is controlled by hormonal and renal control systems [17,18]. It makes up from 0.65 to 1.1% of an adult body, 85% of which is in bones and the Recommended Dietary Allowance for both men and women older than 19 years is 700 mg/day [19]. The presence of carbon, phosphorus, and nitrogen in kombucha beverages on winery effluent was also related to its very well-known presence in wastewater used for fermentation.

This article aimed to determine the basic nutrients consumed by kombucha winery effluent-based culture to gain an additional understanding of the kombucha metabolic pathways and nutritional composition of the beverage and to set the basis for the optimal conditions for the kombucha on winery effluent production on a larger scale.

MATERIALS AND METHODS

Kombucha starter culture

Traditional kombucha culture, which represented the basis for this investigation, consisted of two bacterial strains of the *Acetobacter* genera and five yeast strains (*Saccharomycodes ludwigii*, *Saccharomyces cerevisiae*, *Saccharomyces bisporus*, *Torulopsis* sp., and *Zygosaccharomyces* sp.) [20,21].

The kombucha starter culture used in this investigation for obtaining novel kombucha products was produced by three passages of the traditional kombucha culture, on the winery effluent with 7% of total reducing sugars at 25 °C, during 6 days. Only the liquid part of the obtained kombucha starter culture was added in the amount of 10% (v/v) to the appropriate fermentation medium. Winery effluent was cultivated in the incubator in sterilized glass beakers covered with sterile cheesecloth.

Initial medium, fermentation medium, and process parameters

The initial medium (IM) was filtrated and sterilized winery effluent generated after must flotation using gelatine, in the white wine production. The plate filter press and the filter paper were used for filtration. Sterilization was performed in an autoclave (121 °C, 20 min).

The initial medium contained 16.34% of total reducing sugars. The fermentation medium was prepared by the dilution of the initial medium with boiled tap water to three different sugar levels (3, 5, and 7% of total reducing sugars). These sugar levels referred to the initial total reducing sugar content.

The fermentation process was performed at three different temperatures (20, 25, and 30 °C) and the samples were collected at the start of the fermentation (day 0), after 3, 6, and 9 days.

The initial medium and fermentation mediums were analyzed as well.

Determination of total reducing sugar content

Total reducing sugar content was determined by the Miller method [22]. The reaction mixture consisted of 0.5 mL of the sample and 0.75 mL of the DNS reagent. After heating to the boiling point for 5 min, the mixture was cooled to room temperature, and 3.75 mL of the distilled water was added. The sample reaction mixture was homogenized and the absorbance was measured at 540 nm (*LLG-uniSPEC2 Spectrophotometer,* Meckenheim, Germany). The blank sample used distilled water instead of the sample. The ripe grape contains almost equal amounts of glucose and fructose. Since both of these sugars react in the same way with the DNS reagent, glucose was selected for the preparation of the calibration curve [23,24]. Results were expressed as grams of glucose per liter of the sample.

Determination of total nitrogen content

Total nitrogen content was determined by the Kjeldahl method [25,26]. The appropriate volume of the sample (1 or 2 mL, depending on the sample) was transferred to the Kjeldahl flask, and 2 mL of concentrated sulphuric acid and 1 g of catalyst mixture were added. The obtained reaction mixture was heated until the solution changed color to slightly green. The prepared sample was transferred to the distillation flask by using a small amount of distilled water. To the Erlenmeyer flask, 10 mL of 0.01 mol/L HCl and 3 drops of the mixed indicator were added. To the distillation flask, gradually, 33% sodium hydroxide was added until the alkaline reaction (the flask content is dark blue and all of the nitrogen is extruded in the form of ammonia). The distillation process was conducted for 6 minutes, in total. After that, the unreacted excess of HCl is retitrated with 0.01 mol/L of sodium hydroxide, in the presence of the mixed indicator, until the color changes to green. Results were expressed as milligrams of nitrogen per liter of the sample.

Determination of total phosphorus content

Phosphorus was analyzed by spectrophotometry using the molybdenum blue method [25]. Five mL of the samples were dried until dryness at 115 °C and allowed to cool to room temperature. The dry residue of each sample was digested using 5 mL of concentrated sulphuric acid and 15 drops of nitric acid. The obtained mixture was set on a hot plate until a clear or slightly green color was obtained (after around 1 h). After cooling, digested samples were transferred to the volumetric flask and neutralized by adding several drops of 30% NaOH (1% solution of phenolphthalein was used for the indication), and finally diluted with doubly distilled water to 100 mL. Furthermore, a certain volume of diluted sample (5, 10, 15, or 20 mL depending on the sample) was transferred to the 100 mL volumetric flask, and 5 mL 5% ammonium heptamolybdate, 1 mL 11% sodium sulfite and 1 mL 0.5% hydroquinone were added. After 45 min the absorbance was measured at 750 nm (UV-2100 Spectrophotometer, Cole Parmer, Vernor Hills, IL, USA) and the results were expressed as mg/L. The calibration curve was defined with KH_2PO_4 from 0.05 to 0.4 mg P.

Statistical analysis

Statistical analysis and graphical representation of the data were performed using Statistica 13.5 software (StatSoft, USA). The coefficient of determination (R^2), model p-value (p = 0.05), and F-value were used to evaluate the adequacy of the model. Response Y was fitted by RSM using second-degree polyoma:

$$Y = b_0 + \sum b_i X_i + \sum b_{ii}^2 X_{ii}^2 + \sum b_{ij} X_i X_j \quad (1)$$

where b_0 is the intercept, b_i, b_{ii}, and b_{ij} are the linear, quadratic, and interaction effects of the factors, respectively. The factor variables were the fermentation temperature, X_1: 20, 25, and 30 °C, and the initial total reducing sugar content, X_2: 3, 5, and 7%). As determined previously by sensory analysis, the kombucha beverage after three days was suitable for consumption, therefore RSM modeling was performed only on those samples.

All analyses were performed in triplicate, and the data reported represent the average values of three determinations ± standard deviation (mean±StDev).

RESULTS AND DISCUSSION

Total reducing sugar content in kombucha products on winery effluent

The total reducing sugar content of kombucha products on winery effluent and the fermentation mediums are given in Table 1. It is very well known that the bacterial strains of *Acetobacter* genera, yeasts *Saccharomycodes ludwigii, Saccharomyces cerevisiae,* and *Zygosaccharomyces* use sugars as the main nutrients [37,38]. Fermentation medium, only for fermentations with 7% of initial total reducing sugar

content, showed a slightly higher value than expected (7.57%), potentially because the homogenization was not good enough after the dilution of the sterilized effluent with the boiling tap water. Second homogenization was performed after the inoculation, when the value dropped by around 10%, in regards to the 7% of the initial content, which agreed with the expectation. During the entire course of the fermentation, sugar content decreased continually, but in different dynamics, depending on the initial content.

The most pronounced decrease was established after three days of fermentation, at 30 °C, when the initial sugar content was the lowest; from 2.9% on day 0 to just 0.4%. For the samples with 5% of initial total reducing sugar content, the decrease was over 40% during the first three days of the process. On the contrary, when the initial total reducing sugar content was the highest, the decrease was merely from 6.3 to 6.1%. This fact indicated the possibility of substrate inhibition. Therefore, it is more reasonable to use fermentation mediums with a slightly lower reducing sugar content, because it stimulates the bioprocess dynamics, lowers the initial costs, and provides the beverage with lower sugar content, although some authors successfully produced kombucha beverage with 10% of the initial sugar [27]. The differences in sugar metabolism can be also explained by the fact that winery effluent contains glucose and fructose as carbon sources. Therefore, there is no need for the invertase activity by the kombucha culture to break sucrose into glucose and fructose, which are further metabolized by kombucha.

At the fermentation temperature of 25 °C, when the reducing sugar content was taken into account, the bioprocess dynamics were the most pronounced. After just three days of fermentation, the initial total sugar content of 6.3% was reduced to almost one-third. The same pattern was established when the initial content was 2.9%. For the products with 4.7% of the initial content, the total residual reducing sugar content was decreased by over 50%. At the fermentation temperature of 20 °C, the kombucha culture showed similar activity: in the products with 3% of the initial sugar content, the residual sugar content decreased by almost 50%, for products with 5% of the initial sugar content, the residual sugar content was lowered for 40%. Products with 7% of the initial sugar content had the least pronounced decrease, which amounted to around one-quarter.

Table 1. Total reducing sugar content of kombucha products on winery effluent and the fermentation mediums.

		Total reducing sugar content (g/L)[a]		
		Initial total reducing sugar content (%)		
t (°C)	τ (day)	7	5	3
fermentation medium		75.73±0.31	50.23±0.56	29.89±0.41
day 0		63.08±0.62	46.93±0.56	29.17±0.06
30	3	61.09±0.37	28.43±0.50	4.19±0.08
	6	33.47±0.12	11.73±0.04	2.07±0.05
	9	12.39±0.05	9.37±0.02	1.68±0.01
25	3	22.29±0.34	21.17±0.41	10.82±0.34
	6	14.28±0.06	8.10±0.01	3.82±0.02
	9	10.35±0.10	4.05±0.07	3.24±0.03
20	3	54.07±0.65	30.11±0.62	16.80±0.16
	6	45.12±0.12	28.71±0.34	13.14±0.23
	9	36.31±0.78	15.29±0.55	5.99±0.14

[a]mean±StDev, n=3.

After nine days of fermentation, at 25 and 30 °C, for products with 5 and 3% of the initial total reducing sugar content, the residual total reducing sugar content was below 1%.

The consume day kombucha products contained 0.84 to 12.22 g/200 mL (i.e. a glass of the beverage), which was significantly lower than commercially available non-alcoholic beverages, which commonly contain over 20 g/200 mL of sugar [39].

Experiments by other authors, that obtained kombucha products with different herbal teas, indicated a significantly less pronounced lowering in total sugar content. From 10% at the start of the fermentation process, only the kombucha product with yerba mate, after 30 days, showed 50% lower content. The rest of the kombucha samples had sugar content that amounted to almost 75% of the initial value [28]. Kombucha beverage with seaweed (*Porphyra dentata*) produced at 25 °C, had a mild increase in sugar content in comparison with the beginning of the process, until the 16th day, when the sugars started to decrease, but

after 22 days it was still higher than at the fermentation start. At the fermentation temperature of 30 °C, with minor oscillations, the decrease was constant and after 20 days it amounted, to approximately, a fifth of the initial content [29]. Leonarski *et al.* [30] demonstrated that kombucha microorganisms showed a preference for glucose as a carbon source, when acerola by-product, which contains the same amounts of glucose and fructose, was used as the fermentation medium. The sugar consumption was directly proportional to acerola by-product content and different studies confirmed that yeasts species metabolize glucose over fructose. Products with high sugar content can be applied in bacterial cellulose production [31], which is also generated as a result of kombucha metabolic activity [2].

Modelling of residual total reducing sugar content in kombucha beverages on winery effluent after three days of fermentation

Results measured for the residual total reducing sugar content after three days of kombucha fermentation were modeled by response surface methodology (Figure 1a). Results of the ANOVA analysis of variance, regression equation coefficients, and their p-values were presented in Table 2.

The model was significant, at the confidence interval of 95%, with a *F*-value of 5890.123. The coefficient of determination was 0.999, which indicated the excellent reliability of the model (Table 2). Statistically significant influence on the model showed

Table 2. Analysis of variance (ANOVA), regression equation coefficients, and their p-values of the modeled response of the residual total reducing sugars, residual total nitrogen, and residual total phosphorus content in kombucha beverages on winery effluent after three days of fermentation.

Response	Residual			Model					
							F- value	*p*-value	R^2
	DF	SS	MS	DF	SS	MS			
Residual total sugar content	18	3.230	0.181	8	8534	1067	5890.123	0.000	0.999
Residual total nitrogen content	8	162.424	9.024	8	107111	13388	1483.773	0.000	0.998
Residual total phosphorus content	24	26405.910	1100.246	5	48891	9778	8.890	0.000	0.649

Effects		Intercept	Linear		Quadratic	Interaction	
		b_0	b_1	b_2	b_{11}	b_{22}	b_{12}
Residual total sugar content	estimate	409.510	-31.405	0.574	-0.757	0.004	0.049
	p-value	0.000[a]	0.000[a]	0.000[a]	0.467	0.626	0.049[a]
Residual total nitrogen content	estimate	-381.140	5.987	0.063	17.243	-0.135	-0.086
	p-value	0.523	0.894	0.943	0.018[a]	0.022[a]	0.584
Residual total phosphorus content	estimate	56.372	-7.531	0.121	3.488	-0.083[a]	0.207[a]
	p-value	0.875	0.778	0.817	0.397	0.017[a]	0.035[a]

DF – degree of freedom, SS – sum of squares, MS – mean squares. [a]Effects are statistically significant, $p < 0.05$; 1 – temperature; 2 – initial sugar content.

linear effects of the initial total reducing sugar content and fermentation temperature, as well as their interaction. Both were expected, since the residual total reducing sugar content had to be correlated with the initial, and the bioprocess temperature significantly influences the velocity of all metabolic functions. Higherinitial total reducing sugar content, as expected, provided higher residual total reducing sugar content. The influence of temperature was not that clear (Table 2).

The lowest value of the residual total reducing sugar content had samples produced at 25 °C and the measured content was as follows: 1.1% for products with 3% of the initial sugars and almost equal values were established for samples with 7 and 5% of the initial total reducing sugars – 2.2 and 2.1%. The highest content showed products obtained at 30 °C (the highest value was 6.1% for samples with 7% of the initial sugars). This fact suggested that 7% of initial sugars and fermentation temperature of 30 °C were above the optimal conditions for the kombucha culture metabolic activity. Since the sugar amount in the beverage is highly important for the consumer, it can be concluded that a fermentation temperature of 25 °C is the most suitable. It is reasonable that the majority of the population wants to lower indiscriminate calorie consumption, as well as the simple sugar calories that possess a high glycaemic index.

Total nitrogen content in kombucha products on winery effluent

After the carbon, nitrogen is the most important macroelement, necessary for protein synthesis in all cells. The source of nitrogen greatly affects the production of bacterial cellulose by kombucha. Research has demonstrated that yeast extract powder (freeze-dried) was the most suitable, both in shaking and static conditions while yeast extract, beef extract, tryptone, or peptone caused low levels of bacterial

cellulose production [15]. It is very well known that yeasts, such as *Saccharomyces cerevisiae*, need nitrogen and phosphorus for their metabolic activity, besides carbon [38]. The total nitrogen content is given in Table 3. The initial medium contained 370.2 mg/L of total nitrogen.

Contrary to expectations, the total nitrogen content in fermentation mediums was inversely proportional to the total reducing sugar content, meaning that the dilution process caused the increase in the values. The addition of kombucha inoculum to fermentation mediums (day 0) showed no clear influence on nitrogen content, which remained the same for samples with 7% of initial sugars. For products with 5 and 3% initial sugar, the nitrogen values were lower than the ones measured in fermentation mediums and higher for samples with 5% initial sugar. Values for day 0 products were in the range 106.68–144.33 mg/L. In consume day samples, the highest total nitrogen content showed samples with 7% of the initial total reducing sugar content, when the fermentation was performed at 30 and 20 °C, and it amounted to 269.8 mg/L and 225.9 mg/L, respectively. At 25 °C, the highest nitrogen content was measured for samples with 5% of initial total reducing sugars (288.7 mg/L).

Table 3. Total nitrogen content of kombucha products on winery effluent and the fermentation mediums.

		Total nitrogen content (mg/L)[a]		
		initial total reducing sugar content (%)		
t (°C)	τ (day)	7	5	3
fermentation medium		106.68±3.14	166.29±1.57	261.98±1.57
day 0		106.68±0.00	144.33±3.14	109.81±3.14
30	3	269.83±3.14	203.94±3.14	166.29±0.00
	6	294.93±3.14	156.88±0.00	40.79±1.57
	9	288.65±0.00	200.80±0.00	47.06±1.57
25	3	109.81±3.14	288.65±0.00	164.72±4.71
	6	149.03±1.57	181.98±1.57	100.40±6.28
	9	194.53±1.57	480.04±3.14	323.16±1.57
20	3	225.90±3.14	181.98±3.14	87.85±3.14
	6	247.86±3.14	214.92±3.14	47.06±3.14
	9	228.25±0.78	181.98±1.57	144.33±3.14

[a]mean±StDev, n=3.

During the fermentation, the total nitrogen content changed improperly, without a clear pattern concerning the fermentation temperature or the initial total sugar content. Despite that, samples with 7% of initial total reducing sugars produced at 25 °C showed a linear increase in content during the fermentation. This trend and decrease in values, respectively, were established for products with 5% and 3% of initial total reducing sugars after six and three days of the process, with the decrease in fermentation temperature. The highest value was established for the kombucha product obtained at 25 °C that contained 5% of the initial total sugar content, after nine days of the process (480 mg/L), which was the only sample with higher nitrogen content than the initial medium. The lowest value was measured after six days of fermentation at 30 °C with 3% of the initial total reducing sugar content (40.8 mg/L). Mendes-Ferreira *et al.* [40] suggested that nitrogen content control was crucial for the metabolism of nitrogen by yeasts.

The increase in nitrogen content during fermentation compared to the initial fermentation medium is a consequence of the growth of microorganisms, bacteria, and yeasts during cultivation, which is very intensive. This is confirmed by the previously published results, which indicate a much higher biomass growth of winery effluent kombucha compared to the traditional, black tea kombucha [32]. The above facts indicate that kombucha cultivated on winery effluent uses relatively small amounts of nitrogen for its growth and metabolism. Food waste can be a source of significant amounts of nitrogen (2–15 g/L) and phosphorus (0.5–1 g/L) and therefore be used in value-added products production [33], such as kombucha. Also, microorganisms use nitrogen to produce different types of biofuels [33].

Modelling of residual total nitrogen content in kombucha beverages on winery effluent after three days of fermentation

Results of the ANOVA analysis of variance, regression equation coefficients, and their *p*-values were presented in Table 2. Results measured for the residual total nitrogen content after three days of kombucha fermentation were modeled by response

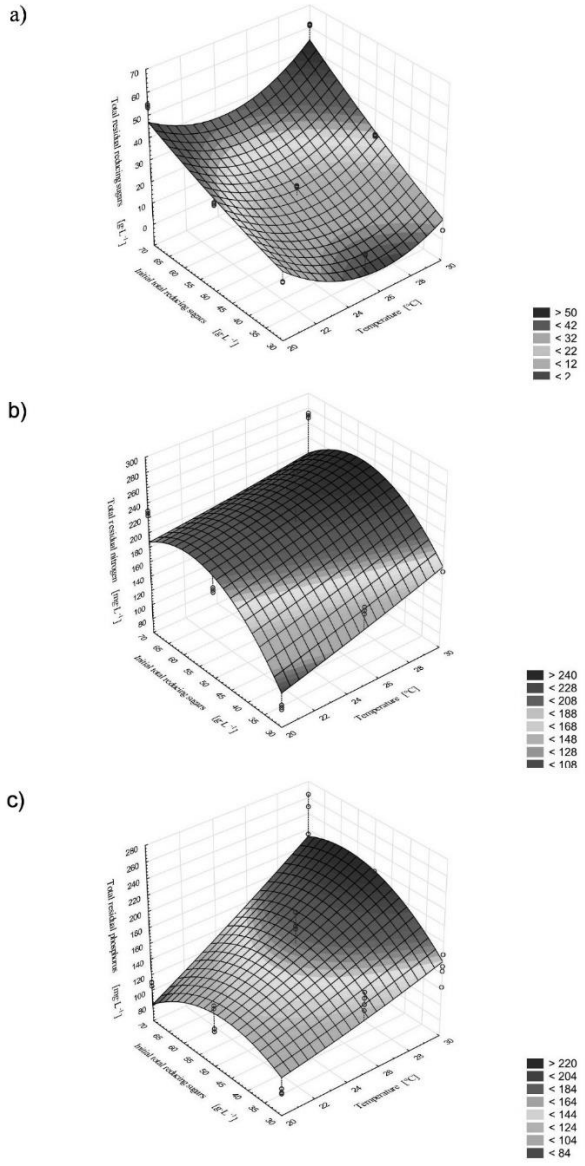

Figure 1. Response surface that describes the influence of fermentation temperature and initial total reducing sugar content on the (a) residual total reducing sugar content in kombucha beverages on winery effluent after three days of fermentation, (b) residual total nitrogen content in kombucha beverages on winery effluent after three days of fermentation, (c) residual total phosphorus content in kombucha beverages on winery effluent after three days of fermentation.

surface methodology (Figure 1b). The model showed excellent reliability and it can be regarded that it had completely described the system, at a confidence interval of 95% and a very high *F*-value (1483.773) (Table 2). Statistically significant parameters of the model were just the quadratic effects of both process parameters. The fermentation temperature had more influence (Table 2). From the graphical representation of the model, it can be observed that the highest total nitrogen content was predicted at the fermentation temperature of 25 °C. This can be explained by the fact that the biomass production, determined in a previous study, was lower at that temperature and the amount of nitrogen that is in cellulosic pellicle was lower [32]. Therefore, the higher nitrogen content is in the kombucha beverage.

Total phosphorus content in kombucha products on winery effluent

Phosphorus is naturally occurring in many different foods; mostly in the form of phosphates and phosphate esters [34]. The total phosphorus content (Table 4) of 250.0 mg/L was determined in the initial medium. The dilution of the initial medium correlated with the phosphorus values measured for the fermentation mediums. The addition of kombucha inoculum to fermentation mediums caused an increase in phosphorus values, and with the lowering of the initial sugars, the phosphorus values were higher. This fact is an indication of phosphorus presence in the added kombucha inoculum, which could be related to the degradation of ATP and/or the increase in the number of microorganisms. The range of all other samples was between 80.33 mg/L after 9 days at 30 °C with 3% initial total reducing sugar content to 262.41 mg/L also after 9 days at 30 °C, but with 7% initial total reducing sugar content. Samples with 5 and 7% total initial sugar content had higher phosphorus content than in the fermentation medium, after nine days, when fermentation temperature was 25 and 30 °C, while for 3% of initial total reducing sugars phosphorus content was higher only at 25 °C. All kombucha products with 7% of initial sugars obtained at 30 °C had higher phosphorus content than samples from the fermentation start (day 0). This fact was established for samples produced at 25 °C after 6 and 9 days, as well. The products obtained at 20 °C had lower content than fermentation start products. Samples with 5 and 3% of initial sugars after 6 days of the process at 20 °C, as well as the product with 3% of the initial sugars after 9 days at 25 °C showed also higher phosphorus content than the products from the beginning of the process.

Other authors measured 6.637 mg/L of phosphorus at the beginning of the fermentation (day 0) of kombucha using black tea and cane sugar, which reduced slightly, to 6.448 mg/L after 14 days. Green tea kombucha contained less phosphorus, 4.201 mg/L at the beginning and 5.332 mg/L after 14 days of fermentation. The highest content was determined in the white tea kombucha, 8.865 mg/L at the beginning (day 0) and 10.31 mg/L after 14 days of fermentation [35].

During the fermentation, the total phosphorus content, as nitrogen, changed improperly, without a clear pattern in relation to the fermentation temperature or the initial total sugar content. Samples produced at 25 °C with 5% of initial sugars showed linear decrease

Table 4. Total phosphorus content of kombucha products on winery effluent and the fermentation mediums.

		Total phosphorus content (mg/L)[a]		
		Initial total reducing sugar content (%)		
t (°C)	τ (day)	7	5	3
Fermentation medium		159.28±13.61	148.50±12.32	145.39±0.35
Day 0		176.56±14.17	202.48±18.07	218.84±16.88
30	3	242.29±25.56	199.70±21.54	144.80±17.12
	6	230.87±13.47	202.17±13.84	149.89±8.18
	9	262.41±7.12	158.23±9.13	80.33±1.44
25	3	85.58±1.99	195.24±11.12	152.67±9.85
	6	222.57±12.75	183.22±13.84	205.91±9.89
	9	213.86±9.93	172.11±4.98	232.76±23.43
20	3	108.52±2.81	121.19±16.92	90.31±3.45
	6	166.10±11.54	247.57±12.10	253.12±6.60
	9	156.84±17.92	118.88±12.45	128.14±12.52

[a]mean±StDev, n=3.

in values during the fermentation time, whilst products with 3% of initial sugars had an increase in values during the process. After three days of fermentation, the increase in fermentation temperature caused an increase in phosphorus content for beverages with 5% of initial sugars. This trend was also established for products with 7% of initial sugars after six and nine days of fermentation. For products with 3% of initial sugars, after six days of the process, the increase in temperature caused the lowering of phosphorus content. Relatively high phosphorus contents during fermentation indicate similarity with nitrogen as a nutrient, where it can also generally be considered that the phosphorus content required for kombucha activity is relatively low. Phosphorus was determined in green crop fractions and it was established that juice, deproteinized juice, and leaf protein concentrate contain phosphorus in low amounts. The pressed crop showed the highest values. The distribution of phosphorus was not uniform [36].

Modelling of residual total phosphorus content in kombucha beverages on winery effluent after three days of fermentation

Results of ANOVA analysis of variance, regression equation coefficients, and their p-values were presented in Table 2. Results measured for the residual total phosphorus content after three days of kombucha fermentation were modeled by response surface methodology (Figure 1c). The model did not show reliability, explaining only around two-thirds of modeled values with an *F*-value of 8.89 (Table 2).

Statistically significant parameters were the quadratic effect of the initial total reducing sugar content and the interaction between it and fermentation temperature (Table 2). From the graphical display of the model (Figure 1c), it can be concluded that samples with 7 and 3% initial total sugars had lower phosphorus content which indicates that at those conditions phosphorus consumption rate was higher. Contrary to that, higher temperature meant lower phosphorus intake with higher values measured at higher temperatures, for all three sugar contents.

CONCLUSION

Sugar content changed through the fermentation according to the expectation, i.e. to the pattern established for the traditional kombucha fermentation. After three days of the process, the temperature did not show a significant effect, although samples fermented at 25 °C had the lowest residual total reducing sugar content regardless of initial total reducing sugar content, compared to those fermented at 20 and 30 °C.

To our knowledge, this is the first extensive measurement of nitrogen and phosphorus contents in kombucha products on an alternative medium, through fermentation. Changes were inconsistent. Based on the obtained results, this study suggested that the most significant nutrient for kombucha culture activity on winery effluent was carbon, i.e. sugar consumption. The comprehensive nitrogen and phosphorus analysis indicated that these elements play a minor role in the kombucha metabolism of winery effluent. Further studies are necessary to elucidate which microorganisms utilize examined nutrients and in what amount. By the determined contents of carbon, nitrogen, and phosphorus in winery effluent-based kombucha beverages, it can be concluded that these products could represent a part of the daily well-balanced nutrition of healthy adults.

ACKNOWLEDGMENT

This work was supported by the Ministry of

Science, Technological Development and Innovations, Republic of Serbia (Grant number 451-03-65/2024-03/200134.).

REFERENCES

[1] D. Laureys, S.J. Britton, J. De Clippeleer, J. Am. Soc. Brew. Chem. (2020) 165–174. https://doi.org/10.1080/03610470.2020.1734150.

[2] R. Jayabalan, R.V. Malbaša, E.S. Lončar, J.S. Vitas, M. Sathishkumar, Compr. Rev. Food Sci. Food Saf. 13 (2014) 538–550. https://doi.org/10.1111/1541-4337.12073.

[3] J.S. Vitas, S. Vukmanović, J. Čakarević, L. Popović, R. Malbaša, Chem. Ind. Chem. Eng. Q. 26 (2020) 157–170. https://doi.org/10.2298/ciceq190708034v.

[4] N.H. Avcioglu, M. Birben, I. Seyis Bilkay, Process. Biochem. 108 (2021) 60–68. https://doi.org/10.1016/j.procbio.2021.06.005.

[5] A. Sknepnek, S. Tomić, D. Miletić, S. Lević, M. Čolić, V. Nedović, M. Nikšić, Food Chem. 342 (2021) 128344. https://doi.org/10.1016/j.foodchem.2020.128344.

[6] B.M. Bortolomedi, C.S. Paglarini, F.C.A. Brod, Food Chem. 385 (2022) 132719. https://doi.org/10.1016/j.foodchem.2022.132719.

[7] C. Chen, B.Y. Liu, J. Appl. Microbiol. 89 (2000) 834–839. https://doi.org/10.1046/j.1365-2672.2000.01188.x.

[8] R. Vijayaraghavan, M. Singh, P.V. Rao, R. Bhattacharya, P. Kumar, K. Sugendran, O. Kumar, S.C. Pant, R. Singh, Biomed. Environ. Sci. 13 (2000) 293–299. https://pubmed.ncbi.nlm.nih.gov/11351863/.

[9] G.Ö. Sinir, C.E. Tamer, S. Suna, in Fermented Beverages, A.M. Grumezescu, A.M.Holban Eds., Woodhead Publishing, Sawston (2019) pp. 401–432. https://doi.org/10.1016/B978-0-12-815271-3.00010-5.

[10] P. Bishop, E.R. Pitts, D. Budner, K.A. Thompson-Witrick, Food Chem. Adv. 1 (2022) 100025. https://doi.org/10.1016/j.focha.2022.100025.

[11] W.M. Kliewer, Am. J. Enol. Vitic. 18 (1967) 33–41. https://doi.org/10.5344/ajev.1967.18.1.33.

[12] J. Reiss, Z. Lebensm.-Unters. Forsch. 198 (1994) 258–261. https://doi.org/10.1007/BF01192606.

[13] G. Hanrahan, G. Chan, in Encyclopedia of Analytical Science, 2nd Edition, P. Worsfold, A. Townshend, C. Poole Eds., Elsevier, Amsterdam (2004), pp. 191–196. ISBN-10: 0127641009.

[14] D. Dutta, R. Gachhui, Int. J. Syst. Evol. Microbiol. 57 (2007) 353–357. https://doi.org/10.1099/ijs.0.64638-0.

[15] J. Li, G. Chen, R. Zhang, H. Wu, W. Zeng, Z. Liang, Biotechnol. Appl. Biochem. 66 (2019) 108–118. https://doi.org/10.1002/bab.1703.

[16] Recommended Dietary Allowances, 10th Edition, National Academies of Sciences, Engineering, and Medicine, The National Academies Press, Washington (1989). https://doi.org/10.17226/1349.

[17] I.D. McKelvie, A. Lyddy-Meaney, in Encyclopedia of Analytical Science, 2nd Edition, P. Worsfold, A.Townshend, C. Poole Eds., Elsevier, Amsterdam (2004), pp. 167–173. ISBN-10: 0127641009.

[18] H. Robles, in Encyclopedia of Toxicology, 3rd Edition, P. Wexler Ed., Academic Press, Amsterdam (2014), pp. 920–921. ISBN: 9780123864550.

[19] Dietary Reference Intakes for Calcium, Phosphorus, Magnesium, Vitamin D, and Fluoride Institute of Medicine (US) Standing Committee on the Scientific Evaluation of Dietary Reference Intakes National Academies Press (US), Washington (DC) (1997) https://doi.org/10.17226/5776.

[20] S. Markov, R. Malbaša, M. Hauk, D. Cvetković, Acta Period. Technol. 32 (2001) 133–138. http://scindeks-clanci.ceon.rs/data/pdf/1450-7188/2001/1450-71880132133m.pdf.

[21] S. Markov, D. Cvetković, A. Velićanski, Arch. Biol. Sci. 64 (2012) 1439-1447. https://doi.org/10.2298/ABS1204439M.

[22] G.L. Miller, Anal. Chem. 31 (1959) 426–428. https://doi.org/10.1021/ac60147a030.

[23] R.S. Jackson, in Wine Science: Principles and Applications, 4th Edition, R.S. Jackson, Ed., Academic Press, San Diego (2014), pp. 69–141, ISBN: 978-0-12-381468-5.

[24] R.S. Jackson, in Wine Science: Principles and Applications, 4th Edition, R.S. Jackson, Ed., Academic Press, San Diego (2014), pp. 347–426. ISBN: 978-0-12-381468-5.

[25] S. Kravić, Z. Stojanović, Analiza hrane, vode, zemljišta, vazduha u predmeta opšte upotrebe - praktikum, Univerzitet u Novom Sadu, Tehnološki fakultet Novi Sad, Novi Sad, Serbia (in Serbian) (2016), pp. 18–24, pp. 54–60. ISBN: 978-86-6253-062-2.

[26] J. Trajković, J. Baras, M. Mirić, S. Šiler, Analize životnih namirnica, Univerzitet u Beogradu, Tehnološko-metalurški fakultet, Beograd, Jugoslavija (in Serbian) (1983), pp. 75–80.

[27] P. Blanc, Biotechnol. Lett. 18 (1996) 139–142. https://doi.org/10.1007/BF00128667.

[28] Y.A. Ramírez Tapias, M.V. Di Monte, M.A. Peltzer, A.G. Salvay, Food Chem. 372 (2022) 131346. https://doi.org/10.1016/j.foodchem.2021.131346.

[29] T. Aung, J.B. Eun, LWT - Food Sci. Technol. 154 (2022) 112643. https://doi.org/10.1016/j.lwt.2021.112643.

[30] E. Leonarski, K. Cesca, E. Zanella, B.U. Stambuk, D. de Oliveira, P. Poletto, LWT - Food Sci. Technol. 135 (2021) 110075. https://doi.org/10.1016/j.lwt.2020.110075.

[31] S. Varjani, W. Yan, A. Priya, F. Xin, C.S.K. Lin, Curr. Opin. Green Sustain. Chem. 41 (2023) 100806. https://doi.org/10.1016/j.cogsc.2023.100806.

[32] S. Vukmanović, J. Vitas, A. Ranitović, D. Cvetković, A. Tomić, R. Malbaša, LWT - Food Sci. Technol. 154 (2022) 112726. https://doi.org/10.1016/j.lwt.2021.112726.

[33] P. Sharma, V.K. Gaur, R. Sirohi, S. Varjani, S.H. Kim, J.W.C. Wong, Bioresour. Technol. 325 (2021) 124684. https://doi.org/10.1016/j.biortech.2021.124684.

[34] https://ods.od.nih.gov/factsheets/Phosphorus-HealthProfessional/ [accessed 28 May 2023].

[35] M.I. Kluz, K. Pietrzyk, M. Pastuszczak, M. Kacaniova, A. Kita, I. Kapusta, G. Zaguła, E. Zagrobelna, K. Struś, K. Marciniak-Lukasiak, J. Stanek-Tarkowska, A.V. Timar, C.

Puchalski, Foods 11 (2022) 1523. https://doi.org/10.3390/FOODS11101523.

[36] R.K. Jadhav, Int. J. Bioassays 4.9 (2015) 4329–4332. https://www.ijbio.com/articles/distribution-of-ash-calcium-and-phosphorus-in-the-byproducts-of-green-crop-fractionation.pdf.

[37] A.N. Hall, I. Husain, K.S. Tiwari, T. K. Walker, J. Appl. Bacteriol. 19 (1956) 31–35. https://doi.org/10.1111/j.1365-

[40] A. Mendes-Ferreira, A. Mendes-Faia, C. Leao, J. Appl. Microbiol. 97 (2004) 540–545. https://doi.org/10.1111/j.1365-2672.2004.02331.x.

2672.1956.tb00040.x.

[38] J.R. Broach, Genet. 192 (2012) 73–105. https://doi.org/10.1534/genetics.111.135731.

[39] V.E. Agbazue, A. Ibezim, N.R. Ekere, Int. J. Chem. Sci. 12 (2014) 327–334. https://www.tsijournals.com/articles/assessment-of-sugar-levels-in-different-soft-drinks.pdf.

STEFAN VUKMANOVIĆ[1]
JASMINA VITAS[1]
SNEŽANA KRAVIĆ[1]
ZORICA STOJANOVIĆ[1]
ANA ĐUROVIĆ[1]
BILJANA CVETKOVIĆ[2]
RADOMIR MALBAŠA[1]

[1]Univerzitet u Novom Sadu, Tehnološki fakultet Novi Sad, Bulevar cara Lazara 1, 21000 Novi Sad, Republika Srbija

[2]Univerzitet u Novom Sadu, Naučni institut za prehrambene tehnologije, Bulevar cara Lazara 1, 21000 Novi Sad, Republika Srbija

NAUČNI RAD

UTICAJ GLAVNIH PROIZVODNIH PROMENLJIVIH NA NUTRITIVNE KARAKTERISTIKE KOMBUHE NA OTPADNOM TOKU IZ PROIZVODNJE VINA

Određivanje potrošnje šećera, azota i fosfora od strane kulture kombuhe je potrebno da bi se dobio dodatni uvid u metaboličke puteve kombuhe i nutritivnu vrednost proizvedenih napitaka kao i da bi se postavila osnova za optimizaciju uslova proizvodnje na industrijskom nivou. Kombuha napitak je dobijen korišćenjem otpadnog toka koji nastaje u fazi bistrenja šire grožđa u proizvodnji belog vina. Fermentacioni medijum je pripremljen razblaživanjem sterilizovanog početnog medijuma, koji je imao oko 16% ukupnih redukujućih šećera, na sadržaj ukupnih redukujućih šećera koji je iznosio 3, 5 i 7%. Vreme trajanja fermentacije je bilo devet dana na temperaturi od 20, 25 i 30 °C. Sadržaj šećera, azota i fosfora je određen primenom DNS, Kjeldal i molibden plavo metode, redom. Najveći sadržaj šećera je izmeren u početnom medijumu (16.34%), a najmanji je određen u uzorku nakon devet dana fermentacije na 30 °C sa 3% početnog sadržaja šećera (0.17%). Preostali nivoi šećera, azota i fosfora u uzorcima nakon tri dana fermentacije su modelovani primenom metode odzivne površine. Predloženi modeli za sadržaj šećera i azota su pokazali izuzetnu korelaciju sa eksperimentalno dobijenim vrednostima. Ovim radom je obezbeđeno dobijanje uvida u potrošnju osnovnih nutrijenata od strane kulture kombuhe, nutritivnu vrednost i optimizaciju sastava kombuha proizvoda.

Ključne reči: kombuha, iskorišćenje hranljivih materija, šećeri, azot, fosfor.

CI&CEQ
Chemical Industry & Chemical Engineering Quarterly

Available online at
Association of the Chemical Engineers of Serbia AChE
www.ache.org.rs/CICEQ

Chem. Ind. Chem. Eng. Q. 30 (4) 295–307 (2024) CI&CEQ

KUMUTHA RAMALINGAM[1]
ILAIYAVEL SIVAKUMARAN[2]
MATHANBABU MARIAPPAN[3]
BARATHIRAJA RAJENDRAN[4]

[1]Department of Mechanical Engineering, Loyola Institute of Technology, Palanchur, Chennai, India

[2]Department of Mechanical Engineering, Sri Venkateswara College of Engineering, Pennalur, Sriperumbudur, Chennai, India

[3]Department of Mechanical Engineering, Government College of Engineering, Bargur, Krishnagiri, Tamilnadu, India

[4]Department of Mechanical Engineering, Einstein College of Engineering, Tirunelveli, Tamilnadu, India

EFFECT OF SALT BATH NITRIDING ON TRIBOLOGICAL PROPERTIES OF AISI52100 STEEL COATINGS USING RESPONSE SURFACE METHODOLOGY

Article Highlights

- This investigation employs the salt bath nitriding to extend the service life
- Improve the surface characteristics of AISI 52100
- Surface hardness, friction coefficient, wear coefficient, loss in wear is measured
- The response surface methodology (RSM) design approach was performed to find the best outcomes
- Processing maps to be developed can be effectively used to identify the feasible working range

Abstract

This investigation employs the salt bath nitriding to extend the service life and improve the surface characteristics of AISI 52100, commonly employed in bearing applications. A wear test was conducted using a pin-on-disc device according to the ASTM G-99 standard, and the findings show a 30% reduction in wear loss. Sliding wear experiments were conducted at 1.5 m/s with a 5 N force at room temperature on uncoated and nitrided pins which was obtained as optimum value from RSM. The three variables and five levels of central composite design (CCD) were utilized to reduce the number of trials and the model relations were examined through ANOVA. Surface hardness, friction coefficient, wear coefficient, and loss in wear are measured over pins without coating and nitride pins. Investigations were done into how 5W30 oil affected passive and drip lubrication. Nitride substrates had a hardness of 590 HV. Also, nitriding has a favorable effect on the friction coefficient, lowering it by up to 23%. The 5W30 lubricant will further decrease the friction coefficient. The lowest friction coefficient was seen with the addition of 14% drip oil lubrication. Significantly less wear loss in the pin was caused by a combination of high hardness and low friction coefficient.

Keywords: salt bath nitriding, wear, hardness, friction coefficient, lubrication.

SCIENTIFIC PAPER

UDC 669.14-155.3:621:620:061.23

AISI 52100 steel is used as a bearing element predominantly in a number of applications like bearings for antifriction, cams, crankshafts, etc. [1]. The major element present in AISI 52100 steel is chromium, along with carbon, manganese, and silicon. Although the presence of chromium makes this steel more corrosive-resistant and wear-resistant, since these bearings are working relentlessly, they may undergo wear and corrode. One of the most versatile methods to protect against wear and corrosion is surface treatment [2]. Several coating methods are available to maintain the performance of the bearing during operation [3]. The most commonly used coating process for improving the wear resistance of steel is salt bath nitriding [4]. In comparison to other surface treatment processes like carburizing and carbo nitriding, this salt nitriding

Correspondence: K. Ramalingam, Department of Mechanical Engineering, Loyola Institute of Technology, Palanchur, Chennai-600123, India.
E-mail: kamaleshmp@gmail.com
Paper received: 24 August, 2023
Paper revised: 6 January, 2024
Paper accepted: 11 February, 2024

https://doi.org/10.2298/CICEQ230824002R

process is found to be best at improving surface hardness and corrosion resistance [5].

In the salt bath nitriding process, the nitrides are deposited in the layer of steel. This nitride then reacts with chromium to form a passive layer of CrN, which is white or pale yellow. This layer is extremely hard and will not corrode or wear easily. The over-hardness of the surface may lead to brittleness, so it is machined in some cases [6,7]. The passive layer formed is in. It is thin and extremely hard. The use of lubricants is an avoidable factor in the case of bearings, so it is important to analyze the performance of surface-treated bearings with the application of lubricants [8]. One of the simplest and most reliable methods of lubrication that is commonly used is drip oil lubrication, which involves dripping oil periodically onto the bearing surfaces, creating a thin film that reduces friction and wear [9]. Passive oil lubrication is another promising method of lubrication in which the flow of lubrication is achieved without the aid of external forces [10]. Since many parameters are involved, optimization of the process is important, which can be done by the RSM method due to its efficacy in producing results [11].

Nitriding is an old-age technique that is followed still to improve the performance of various types of steel, so a lot of work has been done in nitriding on various types of steel. Low-temperature salt nitriding was done on austenitic stainless steel by Charan *et. al*. [12]. The results of the wear test conducted using a pin-on-disc apparatus revealed that the wear rate was decreased for nitrided specimens in comparison to uncoated specimens. AISI 421 martensite steel was salt bath nitrided by Deshini *et.al*. [13]. Initially, tempering treatments were carried out followed by salt bath nitriding. SEM image results showed uniform coating and a reduced wear rate was observed in the pin and disc experiment. Srikanth *et.al.* [14], subjected three specimens of austenitic stainless steel to salt nitriding at 570 °C for different timings of 60 minutes, 120 minutes, and 180 minutes. It was found that wear volume was reduced to a great extent after nitriding. Jun Wang *et al*. [15] performed salt bath nitriding on 304 austenitic stainless steel. The outcomes of the experimentation revealed that the thickness of the coating improved with an increase in nitriding time. The specimens that were subjected to nitriding for 16 hours were found to have the best corrosive resistance.

Colombini *et al*. [16] used response surface methodology to optimize the parameters involved in the nitriding process. Using RSM it was able to obtain the number of surface hardness values and different wear rates for various parameters. The minimum wear rate was observed for the sample which was laser quenched at 1150 °C. Hamad *et al*. [17] incorporated the design of an experimental statistical method to optimize the laser nitriding process. The optimized parameters were 2.84 kW of laser power, 5 mm/s scanning speed, and a 2076 L/h nitrogen flow rate. Based on the prediction, the maximum microhardness was 1920 HV0.15, but the maximum microhardness was 1382 HV0.15. In this investigation, three variable-five levels central composite design (CCD) were utilized to reduce the number of trials, and the model relations were examined through ANOVA.

Although a lot of work has been carried out in the field of salt bath nitriding for various types of steel, no literature records were found for nitriding on AISI 52100 steel along with drip and passive lubrication. This makes this research a novel contribution to the field of nitriding. The foremost aim of salt bath nitriding is to increase the AISI 52100 steel's service life and further reduce wear loss and friction *coefficient* (COF) through passive and drip lubrication. This study attempts to scientifically observe the surface characteristics, such as wear and hardness, of salt-nitrided AISI steel for coated and uncoated specimens. Response surface methodology is used for optimizing the number of parameters involved to find the best outcome.

MATERIALS AND METHODS

Sample preparation

The material used is AISI 52100 steel purchased in the form of substrates and rods. The specimens used are shown in Figure 1. The chemical composition of the steel is listed in Table 1a.

Using the CNC machine, from the steel rod purchased, the pins for the wear test were prepared for 8 mm diameter and 32 mm length. The specimens were initially ground, and to achieve a good surface finish, polishing was done using emery paper of different granule sizes, from 240 to 2000 mesh. The ASME Y 14.5 standard was used to verify the flatness, roughness, and perpendicularity of the material.

Nitriding

Three processes make up the nitriding process: pre-oxidation, salt bath nitriding, and cooling. Before being nitrided, the samples were pre-oxidized at 350 °C in a salt bath pre-oxidation medium or an air furnace.

The nitriding process done is salt bath nitriding. It consists of three steps: pre-oxidation, salt bath nitriding, and cooling. In the pre-oxidation process, the steel is heated in air at a temperature of 350 °C in an air furnace. A thin oxide layer is formed during preoxidation, which improves adhesion, enhances the

Table 1a. Material composition in weight percentage.

C	Cr	Si	Mn	S	P	Fe
1.1	1.4	0.26	0.39	0.019	0.011	Bal

Table 1b. Salt proportion in weight percentage

Salt	Proportion in weight %	Purpose
Potassium nitrate (KNO_3)	70	Diffusion of nitrogen
Sodium carbonate (Na_2CO_3)	20	Fluxing agent
Carbamide ($CO(NH_2)_2$	5	Adjust melting point
Borides ($Na_2B_4O_7$)	4	Enhance wear resistance
Aluminium oxide (Al_2O_3)	1	Nitride layer adhesion

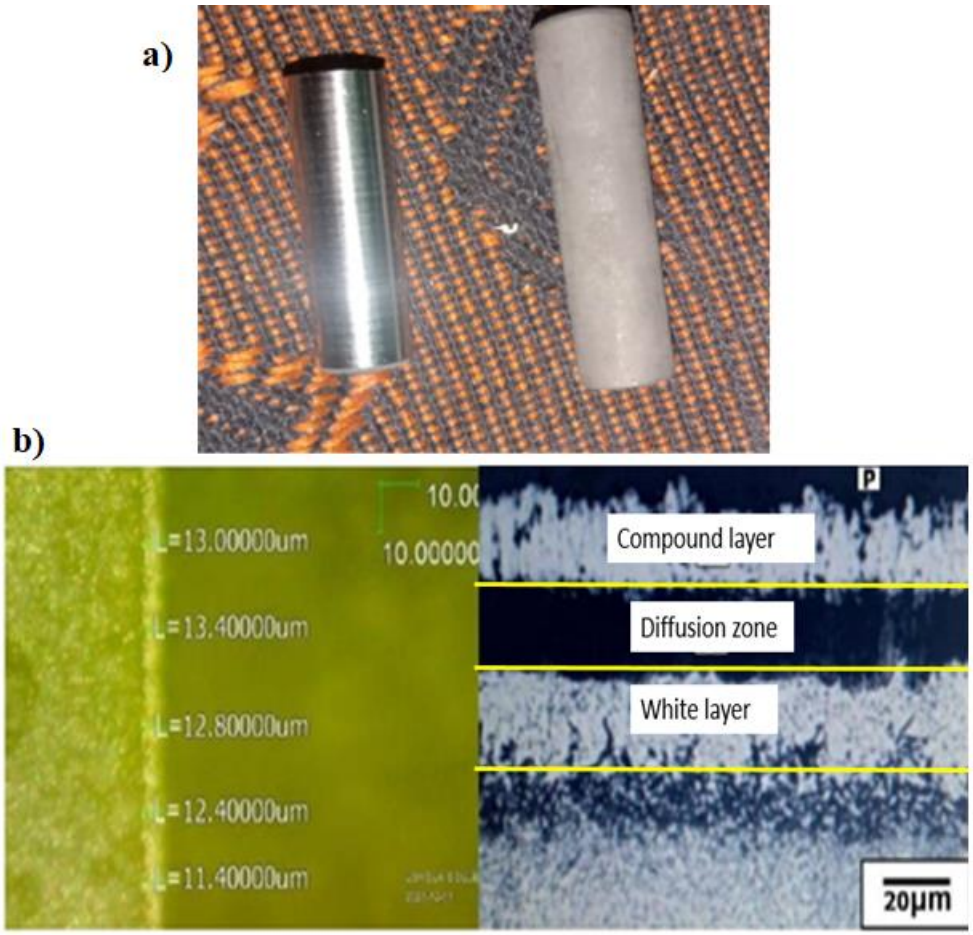

Figure 1. (a) Specimens used for experimentation and (b) different layers observed in SEM-EDS (compound layer, diffusion zone, and white layer).

diffusivity of nitrogen atoms and reduces white layer formation. Then the substrate is dipped in a molten salt bath. The proportion of each salt in the salt bath is tabulated in Table 1b.

The samples are immersed in a salt bath for three hours at 565 ± 8 °C. The range of temperature for nitriding is from 500 °C to 700 °C for low-temperature nitriding [18], which represents the ferritic that occur at 570 °C and 700 °C, respectively. The austenitic phase occurs above 900 °C. This is high-temperature nitriding. Two types of nitridings are commonly carried out: ferritic nitrocarburizing (FNC) and higher temperature nitriding known as austenitic nitrocarburizing (ANC). In this work, FNC is carried out. Finally, the specimens were cooled in water at room temperature [19].

Lubricant

5W30 oil was employed as the lubricant in this experiment. The oil has a kinematic viscosity of 63.2 m^2/s at 40 °C and 10.5 at 100 °C. It has a density of 0.859 x 10^3 kg/m^3. Before conducting wear testing, nitriding was applied over passive, and drip oil lubrication was done for about 10 minutes at room

temperature. Oil lubrication reduces the heat produced by friction.

Surface characterization

Surface roughness (Ra) and Hardness

According to the ASTM E950 standard, the surface roughness was assessed using a profilometer. The roughness value was first determined after the pin's perpendicularity and flatness were verified. The micro-Vickers hardness tester was used to measure surface hardness. The hardness with respect to the depth is shown in Figure 2a.

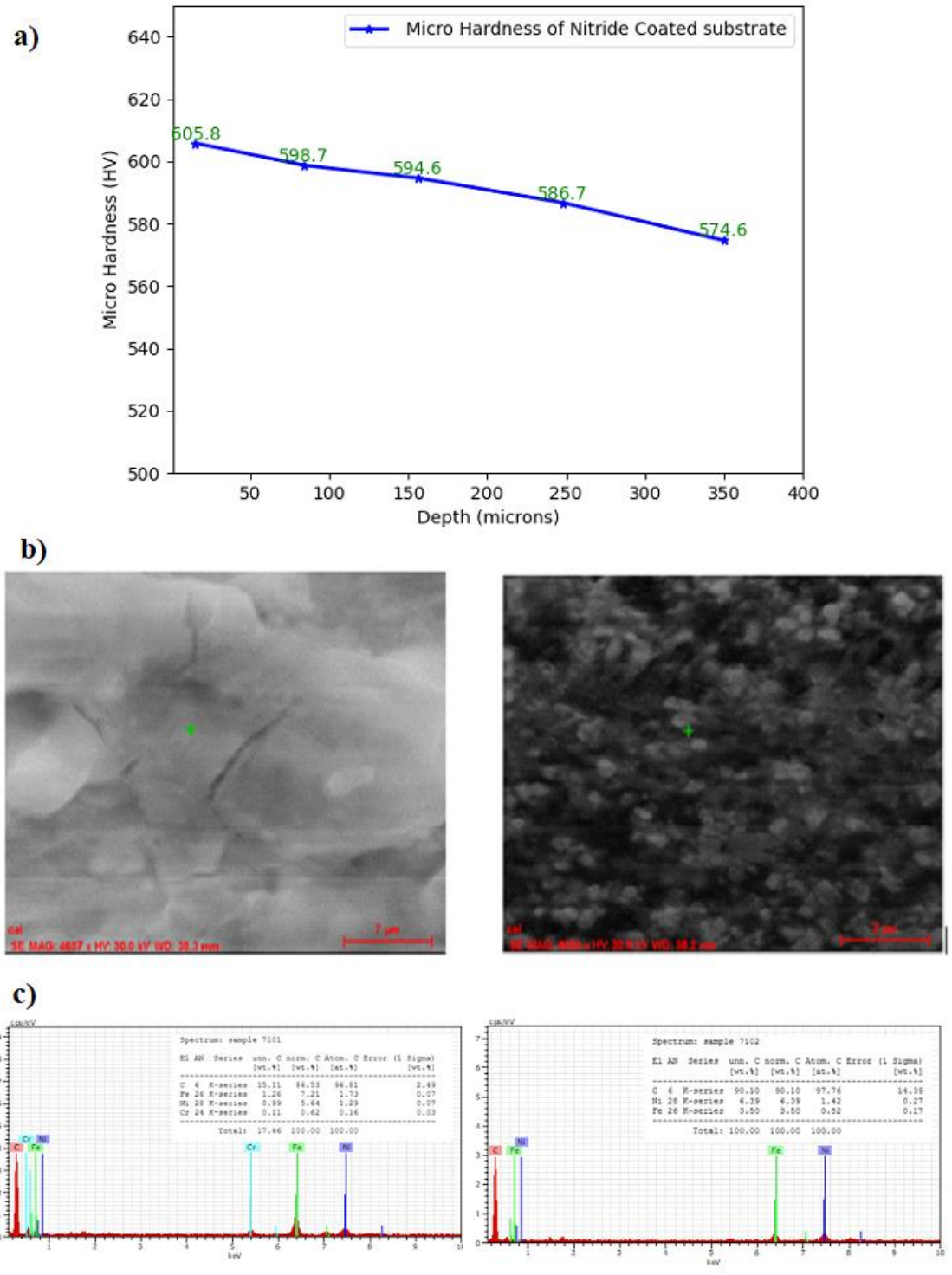

Figure 2. (a) Microhardness with respect to depth (b) EDS image for uncoated; and (c) EDS pattern for coated AISI 52100 Pins.

Wear

The wear performance of materials is frequently determined through testing on pin-on-disc machinery using the ASTM G99 standard approach. It provides a standard procedure for conducting sliding wear testing in laboratories. The experiments were carried out using a force of 5 N as well as a uniform sliding radius of 10 mm at a speed of 1.5 m/s which is selected as the optimum combination from the RSM optimization. The disc is rotated at 300 rpm, and the sliding distance is 3000 m. Load cell series were used to measure the tangential force during testing, and a computerized data-collecting system kept track of it. In each case, the average value of the pins was utilized to estimate the friction coefficient, wear loss, and wear coefficient of the pin.

Morphology and structural composition

By observing the coated specimen at various magnifications (10 μm, 20 μm, 50 μm, 100 μm, and 200 μm) in the VEGA3 TESCAN SEM equipment it was able to make the microstructural examination visible. Double-sided conductive carbon adhesive tapes were used to position and secure the specimen to the SEM holder and prevent charge buildup while it was exposed to the electron beam.

This test is also useful in determining the component's chemical composition along with the corresponding weight proportion, which is known as EDX analysis. This research will assist in improving the structural composition of the material concerning the appropriate chemical elements that are present.

The fundamental requirement in any process is the selection of appropriate input parameters for generating the best outcome. For the present study, three important parameters were considered: type of coating, sliding velocity, and applied load. The output performances considered were wear and COF. The RSM approach was utilized to achieve the salt bath nitriding process on AISI52100 Steel. The levels, the machining variables, and the DoE are listed in Table 2. Optimal DOE was implemented to reduce the required experimental trials [20,21].

RESULTS AND DISCUSSION

The variation in microhardness of nitriding-coated substrates for different layers can be seen in Figure 2. Surface hardness values show evidence of nitriding, which is represented graphically in Figure 3. The values obtained are in line with those obtained by researchers in the literature for other steels that were nitride. The microstructure of the salt bath layer is depicted in Figure 1b.

Optical microscope observations revealed that 321.9 HV0.1 is the core hardness, and the yellow highlighted area (Figure 2) represents the cutoff hardness at a depth of 315 micrometers. There was a compound layer between 11 and 13 microns. The diffuse zone is also seen in Figure 2, beneath the white layer. [22]. The diffusion layer and two compound layers make up the nitriding layer [23].

The EDX analysis of the substrate shows the phases of the steel matrix as well as a group of phases that are linked to chromium and are spread out in the structures of the material. The peaks in the matrix belong to Fe, whereas the remaining phases are carbides produced by alloying elements. The EDS image and spectrum are displayed in Figure 2b.

According to the outcome of the energy-dispersive X-ray investigation, as shown in Figure 2b, the uncoated sample contained the key components (C, Fe, Ni, and Cr). The greatest amounts of the unnormalized percentage of weight concentration, the normalized percentage of weight concentration, the proportion of atomic weight, and the weight percentage concentration inaccuracy at the sigma level one are all present in the carbon element. The results also showed that the phosphorus components have the lowest atomic weight percentage, unnormalized weight concentration percentage, normalized weight concentration proportion, and concentration of weight percentage error at the one sigma level.

Influence of process parameters on wear

As seen in Figure 3, the material was noticeably peeled off, along with the fissures that had developed on the uncoated specimen surface. The properties of the diffusion zone were examined in this work. A clear and distinct compound layer is visible in every SEM image, and the compound layer will have incredibly small micro-etches pits.

Figures 3b and Figures 3c depict the thick free compound layers found in the etch pits 3 (b). When small amounts of nitrogen dissolve just below the compound region, the substrate's wear resistance is affected by the forms of nitrides that are rarely made. On the other hand, when there are higher nitrogen diffusion zones, more nitrides are made, which strengthens the wear resistance.

The nitride pin's wear track is shown in Figure 3d. The interior of the wear track is visible with wear debris and delamination. For steady-state wear, Archard [24] proposed Eq. (1) for volumetric material loss as:

$$V = \frac{K_S \cdot P \cdot L}{3H} \quad (1)$$

Table 2. Variables, levels, and RSM optimal design with experimental results.

Factors/Level	Type of coating	Sliding velocity (B) in m/s	Applied load (A) in N
-1	Coating 1 (Nitriding)	1(0.3 m/s)	5
0	Coating 2 (Nitriding+ Dripoil Lubrication)	2(1 m/s)	25
1	Coating 3 (Nitriding+ passive oil Lubrication)	3(1.5 m/s)	50

	Process Parameters			Responses	
Exp. No.	Type of coating	Sliding velocity (B) in m/s	Applied load (A) in N	Wear (μm)	Coefficient of Friction
1	1	1 (0.3 m/s)	5	0.0647563	0.54945
2	1	1	25	0.0475563	0.446506
3	1	1	50	0.0462875	0.282919
4	1	2 (1 m/s)	5	0.0709812	0.3627
5	1	2	25	0.0545875	0.370225
6	1	2	50	0.0548187	0.341662
7	1	3 (1.5 m/s)	5	0.02895	0.155006
8	1	3	25	0.0124937	0.242981
9	1	3	50	0.013475	0.31705
10	2	1	5	0.0433562	0.315606
11	2	1	25	0.0293625	0.357637
12	2	1	50	0.0328	0.372287
13	2	2	5	0.0531063	0.0856937
14	2	2	25	0.0397187	0.239725
15	2	2	50	0.0434875	0.3857
16	2	3	5	0.0134562	-0.213031
17	2	3	25	0.00074375	0.0742437
18	2	3	50	0.0049625	0.33905
19	3	1	5	0.00909375	0.302638
20	3	1	25	0.0245625	0.242119
21	3	1	50	0.0650312	0.131944
22	3	2	5	0.0324813	0.191238
23	3	2	25	0.0492125	0.241363
24	3	2	50	0.1029	0.2703
25	3	3	5	0.003725	0.0530938
26	3	3	25	0.0214625	0.174613
27	3	3	50	0.059175	0.325694

where V is the volumetric material loss, L is the slide over a length L P is the perpendicular force toward the worn layer, H is the pin's Brinell hardness value, and Ks is the standard wear coefficient.

Considering specific parameters of V, P, L, and H, the normal coefficient of wear can be determined using Eq. (2):

$$K_s = \frac{3HV}{PL} \quad (2)$$

Volumetric wear loss can be calculated using the weight loss W and density.

The larger preliminary running-in rate of wear, according to Yang [24], will initially have a greater value inside the transitional wear phase and may gradually acquire a constant level whenever the wear loss approaches a uniform level. The wear coefficient varies as there is a change in the distance of sliding, as seen in Figure 4a**.** It has been found that greater sliding distance causes a decrease in the wear coefficient. Nitriding with drip oil lubrication pins, however, exhibits the lowest wear coefficient under identical circumstances. The lowest volumetric loss ever observed is the main factor. According to the literature [25], the dehydrated, as well as the changed fresh surface coating, is more reactive to lubrication than the original Huralite.

Figure 4a depicts the sliding distance and wear. It reveals the wear COF of uncoated, coated, nitriding with passive oil lubrication, and nitriding with drip oil

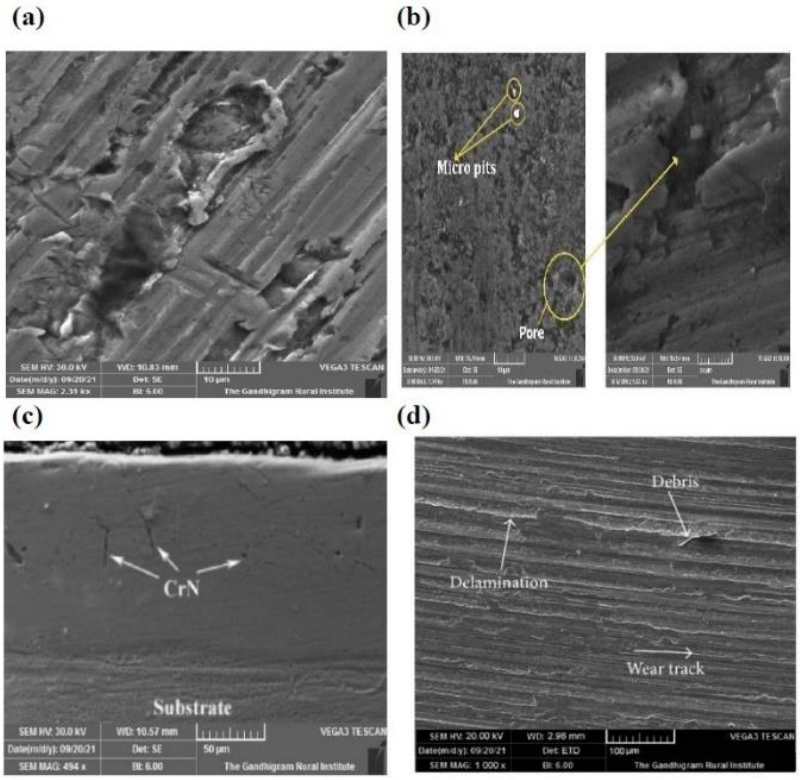

Figure 3. SEM image for nitride specimen.

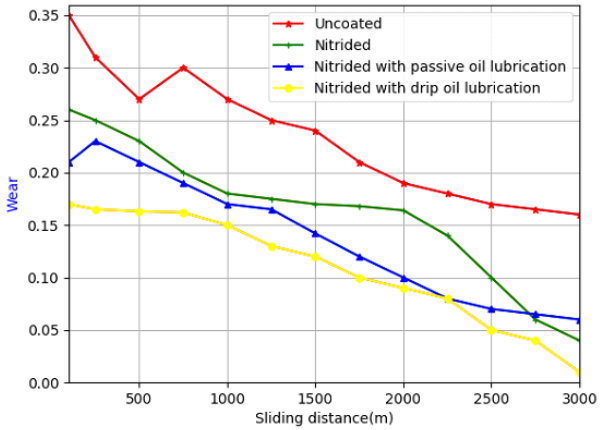

(a)

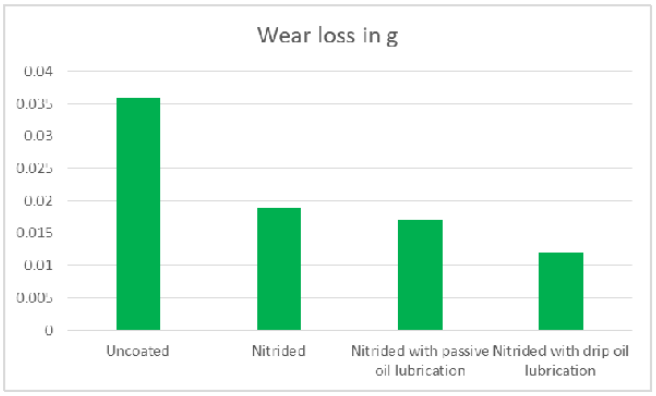

(b)

Figure 4. (a) Sliding distance vs wear and (b) wear loss with respect to coating.

lubrication. The starting and ultimate weights of the pin are used to compute the wear loss. When nitriding, drip oil-lubricated pins show lower wear loss than uncoated pins. Table 3 shows the ANOVA for wear. From that, it is observed that the sliding velocity is the most predominant parameter that affects the surface quality. The R^2 value for wear is 0.9920. The model is significant.

From Figure 4b, it is evident that the uncoated sample will have a more significant wear loss compared to the coated specimen. Nitriding with drip oil lubrication, Nitriding with passive oil lubrication, and Nitriding coating methods were used in this experimentation. Among all the three coating methodologies, the Nitriding with drip oil lubrication methodology was observed to produce less wear loss. When compared to the surface of the AISI steel substrate, there was a significant drop. The wear markings on AISI steel are much wider than the wear marks on the other samples, which are at different widths. This is so that the AISI 52100 steel's wear resistance may be greatly increased by the nitriding surface. The correlation graphs between the predicted and actual values for wear and COF are displayed in Figure 5 (a,b).

Figure 5 (c–e) presents the 3D surface images for the wear of nitriding, nitriding with drip oil lubrication, and nitriding with passive oil lubrication. It is clearly observed that the applied load is directly proportional to the wear. Figure 5c illustrates the increased wear that the nitriding pin produces. During the nitriding process, the amount of nitrogen diffused into the sample surface determines the wear resistance of the specimen. From the detailed experimental procedure, it can be inferred that when the nitriding process is aided by proper lubrication, a higher concentration of nitrogen will diffuse into the steel periphery. In relevance to the characteristics, the Nitriding process

Table 3. ANOVA of Wear and COF.

ANOVA of Wear

Source	Σ^2	Dof	Mean Squares	F-statistics	p-value	Remarks
Model	0.0152	11	0.0014	168.52	< 0.0001	significant
A-Sliding Velocity	0.0017	1	0.0017	211.55	< 0.0001	
B-Applied Load	0.0007	1	0.0007	81.29	< 0.0001	
C-Type of coating	0.0011	2	0.0006	67.07	< 0.0001	
AB	3.156E-06	1	3.156E-06	0.3844	0.5446	
AC	0.0008	2	0.0004	47.53	< 0.0001	
BC	0.0055	2	0.0028	335.54	< 0.0001	
A^2	0.0049	1	0.0049	593.73	< 0.0001	
B^2	0.0005	1	0.0005	66.46	< 0.0001	
Residual	0.0001	15	8.209E-06	R^2		0.9920
Cor Total	0.0153	26		Adjusted R^2		0.9861
				Predicted R^2		0.9728
				Adeq Precision		49.5553

ANOVA of COF

Source	Σ^2	Dof	Mean Squares	F-statistics	p-value	Remarks
Model	0.5751	11	0.0523	353.05	< 0.0001	significant
A-Sliding Velocity	0.1246	1	0.1246	841.00	< 0.0001	
B-Applied Load	0.0506	1	0.0506	341.75	< 0.0001	
C-Type of coating	0.0935	2	0.0468	315.80	< 0.0001	
AB	0.1562	1	0.1562	1054.73	< 0.0001	
AC	0.0438	2	0.0219	147.71	< 0.0001	
BC	0.0940	2	0.0470	317.20	< 0.0001	
A^2	0.0107	1	0.0107	72.09	< 0.0001	
B^2	0.0019	1	0.0019	12.51	0.0030	
Residual	0.0022	15	0.0001	R^2		0.9962
Cor Total	0.5774	26		Adjusted R^2		0.9933
				Predicted R^2		0.9853
				Adeq Precision		91.1079

without lubrication will eventually diffuse less nitrogen than the Nitriding aided by drip and passive lubrication systems.

It can in turn result in insignificant wear resistance improvement compared to the nitriding methods with lubrication. The sliding velocity and applied load can influence the wear values of the nitrided steel. However, the range of wear will be high in the plain nitride process when compared with the other methods. Out of all the three methods of nitriding investigated in this research, the drip lubrication nitriding procedure proved to be capable of depositing a greater quantity of nitrogen on the surface. This makes the specimen treated with drip lubrication nitriding have good wear properties when compared with the other two methods. The outcome can be clearly understood from Figure 5d.

From Figure 5 (c–e), the amount of nitrogen deposition determines the wear properties of any metal. It is understood from the inference that nitriding methodologies with lubrication can ultimately deposit a significant quantity of nitrogen on the steel surface. The amount of nitrogen sediment on the sample surface in the case of nitriding with passive lubrication will be higher than in the plain nitrogen-adding process. It can make the specimen that undergoes passive lubrication nitriding have better wear characteristics than those of the normal nitriding procedure.

Influence of process parameters on COF

The necessary test protocols were used to conduct pin-on-disc testing at around 1.5 meters per

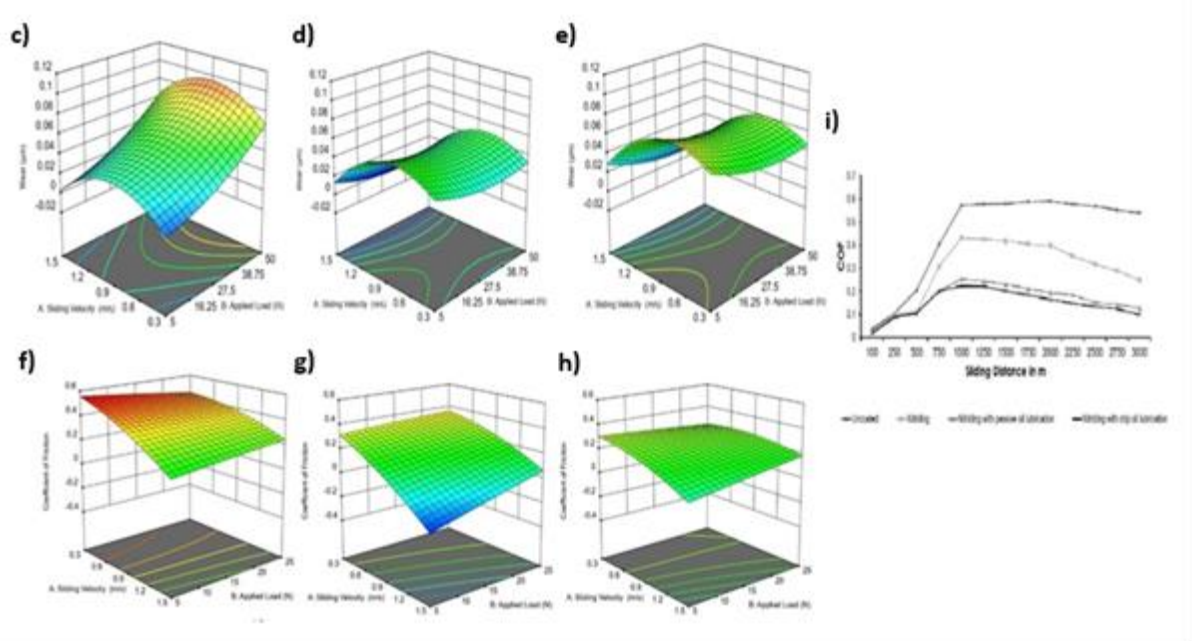

Figure 5. (a–b) Correlation graphs for wear and COF; (c-e) 3D surface graphs of nitriding nitriding with drip oil lubrication nitriding with passive oil lubrication wear; (f-h) COF (i) friction coefficient vs sliding distance.

second as obtained from RSM as an optimized value [26]. The wear, frictional force, and time were measured under a load of 10 N at every 15 minutes of sliding. Figure 5i depicts the relationship between friction coefficient and sliding distance for uncoated, nitrided, nitrided with passive oil, and nitrided with drip oil lubrication.

The difference in the COF with respect to the sliding velocity of the specimens' nitrides with different methods is detailed in Figure 5 (f–h). From the investigation, it is evident that the drip lubrication nitriding method can produce significantly less COF friction than the other two methods. The specimens that are being nitrided with drip lubrication exhibit less wear loss due to their low COF.

It demonstrates the pattern with which the COF reduces with sliding distance, which is a distinctive aspect of the diagrams. The load does not affect the friction coefficient of pure metals; nevertheless, on the surface of a nitrided metal, the breakdown in the nitride layer can change the COF. By nitriding with drip oil lubrication, the friction coefficient can be reduced by 0.1. Table 3 represents the ANOVA for COF. From the table, it can be inferred that the sliding velocity is the most influential parameter that affects the quality. R^2 for COF is 0.9962, and the adequate precision is 91.1079.

Comparing the nitriding, drip lubrication nitriding, and passive lubrication methodologies, the nitriding treatment sample exhibits more COF. The nitriding

process without lubrication can result in a more significant variation of COF concerning the sliding velocity and applied load. The plain nitrided samples will have a COF value of 0.5, and the value drastically changes with sliding velocity and load, as shown in Figure 5f. The drip lubrication process, including the nitriding process, can stabilize the variation of COF with respect to sliding velocity and applied load, as shown in Figure 5i. By treating the AISI 52100 steel with a drip lubrication nitriding process, the COF can eventually be reduced, which in turn enhances the wear characteristics of the material. Comparing all three nitriding techniques, the drip lubrication nitriding procedure can restrict wear significantly with its lower COF values. During the passive lubrication nitriding process, a moderate quantity of nitrogen will be deposited over the surface of the specimen. This can restrict the wear to a maximum value of 0.3. While contrasting all three nitriding processes, nitriding with passive lubrication can eventually result in drastic variation in COF with respect to the variation of sliding velocity and applied load. The variation pattern of COF is detailed in Figure 5i.

Validation of optimizing procedures

The quadratic models are developed for all of the responses (wear and COF) to find the optimal combinations of input variables. The goal of optimization is to decrease the wear rate. Table 4a displays the outcome of the optimization parameters. The highest limits of wear and COF are 0.1029 and 0.54945, respectively. The final set of process variables is sliding velocity (1.5 m/s) and applied load (5 N).

Figure 6 shows the various solution models created for validating the models. Five models are constructed for predicting the response, and the outcome reveals that the desirability of the produced model is greater than 0.895, which can be inferred from Table 4b. A validation test was also carried out to validate the optimized findings, as shown in Table 4c, which shows the error percentages attained after running confirmation tests. The obtained error percentage is negligible and is 2.41% for sliding velocity and 3.33% for applied load. Since the validation test is carried out using the variables specified from the previous findings and various combination sets are allocated, the results demonstrate that the features seem closely related [27–40].

CONCLUSION

Salt bath nitrided pins of surface roughness 0.3 were successfully tested for their friction, wear, and

Table 4a. Conditions of output responses.

Parameter	Goal	Lower Limit	Upper Limit	Lower Weight	Upper Weight	Importance
Sliding Velocity	Is in range	6	10	1	1	3
Applied Load	Is in range	10	30	1	1	3
Types of Coating	Is in range	Coating 1	Coating 3	1	1	3
Wear	Minimize	0.000743	0.1029	1	1	3
COF	Minimize	0.1620	0.54945	1	1	3

Table 4b. Optimum combination solutions of multi-responses for higher desirability.

No	Sliding Velocity	Applied Load	Types of Coatings	Wear	COF	Desirability	
1	1.5	5	3	0.01311	0.183	0.9192	Selected
2	1.48	5	3	0.01315	0.187	0.9160	
3	1.5	4.8	3	0.01320	0.192	0.9140	
4	1.5	4.5	3	0.01364	0.195	0.905	
5	1.4	4.5	3	0.01370	0.198	0.895	

Table 4c. Confirmation experiments for optimization.

Variable	Settings	Responses	Prediction Value	Experimental Value	% Error
Sliding Velocity	1.5	Wear	0.01311	0.0145	2.41
Applied Load	5	COF	0.1836	0.192	3.33

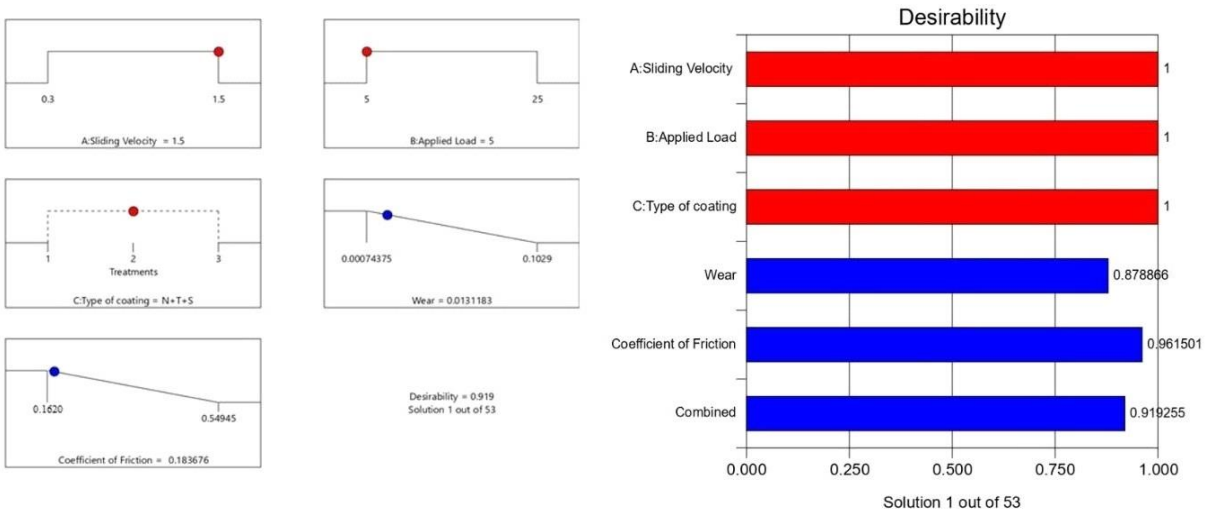

Figure 6. Desirability graph of variables for RSM.

wear loss under a 5 N load and a sliding velocity of 1.5 meters per second. The pins were tested for four conditions: uncoated, nitrided, nitrided with passive oil lubrication, and nitrided with drip oil lubrication. The important results of these tests are as follows.

When nitriding using drip oil-lubricated pins, the friction coefficient is significantly less when the pins are uncoated. In comparison to uncoated pins, nitride pins with drip oil lubrication experienced a significant reduction in friction coefficient. Response surface methodology optimization was useful in optimizing the parameters involved in the experimentation with a low-level error between actual and predicted values. The optimum combination solution obtained of multi-response for higher desirability is 1.5 m/s sliding velocity, 5 N applied load, and the coating of nitride with drip oil lubrication which has a low wear rate of 0.0131. The combined effect of nitriding and drip oil lubrication leads to a low friction coefficient of 0.101 is observed under 1.5 m/s and 5 N, which is attributed to the enhanced tribological properties. Drip oil lubrication of nitrided substrates reduced the wear coefficient to 0.00218 under a 5 N load and sliding speed of 1.5 m/s which signifies exceptional wear resistance. Nitriding with drip oil lubrication reduces wear loss due to minimized material degradation. Scanning electron microscopy (SEM) provides visual evidence of the superior bonding achieved through nitriding with drip oil lubrication. This enhanced bonding plays a key role in the observed reduction in COF and wear exhibited by these pins.

ACKNOWLEDGMENT

The authors are grateful to the Government College of Engineering, Bargur, India, and Gandhigram Rural Institute, Dindugal, India for the characterization facility to carry out this investigation and also thankful to Dr. S. Ramesh Babu, Professor & Head, Department of Mechanical Engineering, Sri Venkateswara College of Engineering, Sriperumbudur, India for continuous encouragement and valuable suggestions for the completion of the experimental work.

REFERENCES

[1] D. Umbrello, J. Hua, R. Shivpuri, Mater. Sci. Eng. A. 374(1-2) (2004) 90–100. http://dx.doi.org/10.1016/j.msea.2004.01.012.

[2] A. Bendavid, P.J. Martin, T.J. Kinder, E.W. Preston, Surf. Coat. Tech. 163-164 (2003) 347–352. https://doi.org/10.1016/S0257-8972(02)00623-0.

[3] E.M. Berton, B.C.E.S. Kurelo, A.C. Rovani, T. Cousseau, J.C.K. das Neves, G. Pintaude, P.C. Borges, Surf. Topogr.: Metrol. Prop. 10 (2022) 24006. https://doi.org/10.1088/2051-672X/ac7b3a.

[4] Y. Lin, J. Wang, D,J. .Zeng, Materi. Eng. Perform. 22 (2013) 2567–2573. https://doi.org/10.1007/s11665-013-0545-8.

[5] J. Wang, Y. Lin, Metall. Mater. Trans. B. 44 (2013) 1010–1016. https://doi.org/10.1007/s11663-013-9841-9.

[6] H. Aydin, A. Bayram, Ş. Topçu, Mater. Sci. 19(1) (2013) 19–24. https://doi.org/10.5755/j01.ms.19.1.3819.

[7] A. Mahmoudi, M. Esmailian, Adv. Mater. Res. 83-86 (2009) 41–48. http://dx.doi.org/10.4028/www.scientific.net/AMR.83-86.41.

[8] S.C. Sharma, V. Singh, V.K. Chawla, Wear 257(1-2), (2005) 86–95. https://doi.org/10.1016/j.surfcoat.2019.125216.

[9] K.D. Bakoglidis, I. Nedelcu, I.G. Ivanov, R. Meeuwenoord, S. Schmidt, E. Janzan, P. Ehret, G. Greczynski, L. Hultman, Tribol. Int. 114 (2017) 141–151. https://doi.org/10.1016/j.triboint.2017.04.006.

[10] L. Hua, T. Jurkschat, T. Lohne, K. Stahl, Lubricants 6(2)

(2018) 47. https://doi.org/10.3390/lubricants6020047.

[11] I. Saravanan, A.E. Perumal, S.C. Vettivel, N. Selvakumar, A. Baradeswaran, Mater. Des. 67 (2015) 469–482. https://doi.org/10.1016/j.matdes.2014.10.051.

[12] P.S. Charan, K. Jayakumar, D. Alankrutha, G. Sindhu, R. Subbiah, Mater. Today Proc. 27 (2020) 1541–1544, https://doi.org/10.1016/J.MATPR.2020.03.195.

[13] A. Deshini, S. Sathish, S. Krishnaraj, A. Kumar, J. Saranya, V.S. Viswanth, R. Subbiah, Mater. Today Proc. 82 (2023) 217–221. https://doi.org/10.1016/j.matpr.2023.01.119.

[14] S. Srikanth, A.A. Johnson, N. Sateesh, A. Kumar, J. Saranya, V.S. Viswanth, R. Subbiah, Mater. Today Proc. 82 (2023.) 47–52. https://doi.org/10.1016/j.matpr.2022.11.262.

[15] J. Wang, Y. Lin, H. Fan, D. Zeng, Q. Peng, B. Shen, JMEP, 21 (2012) 1708–1713. https://doi.org/10.1007/s11665-011-0077-z.

[16] E. Colombini, R. Sola, G.I.A.N. Parigi, P. Veronesi, G. Poli, Metall. Mater. Trans. A. 45 (2014) 5562–5573, https://doi.org/10.1007/s11661-014-2490-z.

[17] A.R. Hamad, J.H. Abboud, F.M. Shuaeib, K.Y. Benyounis, Adv. Eng. Softw. 41(4) (2010) 674–679, https://doi.org/10.1016/j.advengsoft.2009.10.010.

[18] T. Peng, M. Dai, W. Cai, W. Wei, K. Wei, J. Hu, Appl. Surf. Sci. 484 (2019) 610–615. https://doi.org/10.1016/j.apsusc.2019.04.134.

[19] V.T. Bonow, D.S. Maciel, N.L. Fenner, A.R.A. Zimmer, C.G. Zimmer, Clean. Eng. Technol. 4, (2021) 100169, https://doi.org/10.1016/j.clet.2021.100169.

[20] A. Pattanaik, V. Rayasam, Adv. Powder Technol. 29 (2018) 3404–3414. https://doi.org/10.1016/j.apt.2018.09.021.

[21] C. Gopinath, P. Lakshmanan, S. Palani, Mater. Manuf. Process. 37 (2022) 985–994. https://doi.org/10.1080/10426914.2021.1981939.

[22] J. Spille, J. Wranik, S. Barteldes, J. Mayer, A. Schwedt, M. Zurcher, T. Lutz, L. Wang, W. Holweger, Wear. 477 (2021) 203864. https://doi.org/10.1016/j.wear.2021.203864.

[23] A.P. de Andrade Manfridini, G.C.D. de Godoy, L.de Arruda Santos, J. Mater. Res. Technol. 6 (2017) 65–70. https://doi.org/10.1016/j.jmrt.2016.07.001.

[24] B. Liu, S. Bruni, R. Lewis. Wear 490-491 (2022) 204188. https://doi.org/10.1016/j.wear.2021.204188.

[25] L.J. Yang, Wear. 225 (1999) 557–562. https://doi.org/10.1016/S0043-1648(98)00380-9.

[26] G. Yan, S. Lu, M. Zhang, J. Wang, X. Yang, Z. Zhang, J. Gu, C. Li, Appl. Surf. Sci. 530 (2020) 147306. https://doi.org/10.1016/j.apsusc.2020.147306.

[27] W. Grzesik, Z. Zalisz, S. Krol, P. Nieslony, Wear 261(11-12) (2006) 1191–1200. https://doi.org/10.1016/j.wear.2006.03.004.

[28] E.L. Dalibon, G. Prieto, W.R. Tuckart, S.P. Brühl, Surf. Topogr.: Metrol. Prop. 10 (2022) 34003. https://doi.org/10.1088/2051-672X/ac8946.

[29] L.D. Tadepalli, A.M. Gosala, L. Kondamuru, S.C. Bairi, A.A. Lakshmi, R. Subbiah, E3S Web Conf. 184 (2020) 01020. https://doi.org/10.1051/e3sconf/202018401020.

[30] J. Ping, X. Cui, J. Pu, X. Jiang, X. Zhang, Y. Zhong, Surf. Topogr.: Metrol. Prop. 8 (2020) 15005. https://doi.org/10.1088/2051-672X/ab6438.

[31] A. Peric, B. Nedic, D. Trifkovic, M. Vuruna, J. Mech. Eng. 59 (2013) 443–450. http://doi.org/10.5545/sv-jme.2012.870.

[32] L. Govind Sanjeev Kumar, D. Thirumalaikumarasamy, K. Karthikeyan, M. Mathanbabu, T. Sonar, Int. J. Interact. Des. Manuf. (2023). https://doi.org/10.1007/s12008-023-01501-7.

[33] M. Mathanbabu, D. Thirumalaikumarasamy, M. Tamilselvi, S. Kumar, Mater. Res. Express. 9 (2022) 096505. https://doi.org/10.1088/2053-1591/ac8857.

[34] S. Seshaiah, D. Sampathkumar, M. Mariappan, A. Mohankumar, G. Balachandran, M. Kaliyamoorthy, R. Gopal, Adv. Mater. Sci. Eng. (2022) 2022. https://doi.org/10.1155/2022/6022550.

[35] S. Taktak, S. Ulker, I. Gunes, Surf. Coat. Tech. 202(14) (2008) 3367–3377. https://doi.org/10.1016/j.surfcoat.2007.12.015.

[36] A. Mohankumar, T. Duraisamy, D. Sampathkumar, S. Ranganathan, G. Balachandran, M. Kaliyamoorthy, M. Mariappan, L. Mulugeta, J. Nanomater. (2022) 7900150. https://doi.org/10.1155/2022/7900150.

[37] H. Nazari, H. Aghajani, F.H.S. Al-Azawi, Surf. Topogr.: Metrol. Prop. 10 (2022) 15049. https://doi.org/10.1088/2051-672X/ac5a73.

[38] A. Alok, M. Das, J. Manuf. Process. 46 (2019) 16–25. https://doi.org/10.1016/j.jmapro.2019.08.016.

[39] M.S. Liborio, G.B. Praxedes, L.L.F. Lima, I.G. Nascimento, R.R.M. Sousa, M. Naeem, T.H. Costa, S.M. Alves, J. Iqbal, J. Surf. Coat. Technol. 384 (2020) 125327. https://doi.org/10.1016/j.surfcoat.2019.125327.

[40] L.R. Bhandarkar, M. Behera, P.P. Mohanty, S.K. Sarangi, Measurement. 172 (2021) 108842. https://doi.org/10.1016/j.measurement.2020.108842.

KUMUTHA RAMALINGAM[1]
ILAIYAVEL SIVAKUMARAN[2]
MATHANBABU MARIAPPAN[3]
BARATHIRAJA RAJENDRAN[4]

[1]Department of Mechanical Engineering, Loyola Institute of Technology, Palanchur, Chennai, India

[2]Department of Mechanical Engineering, Sri Venkateswara College of Engineering, Pennalur, Sriperumbudur, Chennai, India

[3]Department of Mechanical Engineering, Government College of Engineering, Bargur, Krishnagiri, Tamilnadu, India

[4]Department of Mechanical Engineering, Einstein College of Engineering, Tirunelveli, Tamilnadu, India

NAUČNI RAD

ISTRAŽIVANJE UTICAJA NITRIRANJA SLANOM KUPATILU NA TRIBOLOŠKA SVOJSTVA PREMAZA ČELIKA AISI52100 KORIŠĆENJEM METODOLOGIJE POVRŠINE ODZIVA

Ovo istraživanje koristi nitriranje u slanom kupatilu da bi se produžio vek trajanja i poboljšale karakteristike površine čelika AISI 52100, koji se obično koristi za izradu ležajeva. Test habanja je sproveden korišćenjem pin-on-disc uređaja prema ASTM G-99 standardu, a nalazi pokazuju smanjenje gubitka od habanja za 30%. Eksperimenti kliznog habanja su sprovedeni pri brzini od 1,5 m/s sa silom od 5 N na sobnoj temperaturi na neobloženim i nitriranim čivijama. Ovi uslovu su određeni kao optimalni korišćenjem metodologije površine odziva i centralnog kompozitnog dizajna sa tri faktora na pet nivoa. Razvijeni model je evalurina analizom varijanse (ANOVA). Površinska tvrdoća, koeficijent trenja, koeficijent habanja i gubitak habanjem mereni su za nepremazane i nitrirane čivije. Istraživanja su sprovedena o tome kako ulje 5V30 utiče na pasivno podmazivanje i podmazivanje kap po kap. Nitriranne podloge su imale tvrdoću od 590 HV. Takođe, nitriranje povoljno utiče na koeficijent trenja, snižavajući ga i do 23%. Mazivo 5V30 dodatno smanjuje koeficijent trenja. Najmanji koeficijent trenja je postignut sa dodatkom 14% ulja kap po kap. Kombinacija visoke tvrdoće i niskog koeficijenta trenja značajno smanjuje gubitke habanjem čivija.

Ključne reči: slano kupatilo, nitriranje, habanje, tvrdoća, koeficijent trenja, podmazivanje.

CI&CEQ
Chemical Industry & Chemical Engineering Quarterly

Available online at
Association of the Chemical Engineers of Serbia AChE
www.ache.org.rs/CICEQ

Chem. Ind. Chem. Eng. Q. 30 (4) 309–323 (2024) CI&CEQ

SAMAN KHAWAJA[1,2]
MUHAMMAD RASHID USMAN[1,3]
RABYA ASLAM[1]

[1]Institute of Chemical Engineering and Technology, University of Punjab, New Campus, Lahore, Pakistan

[2]School of Chemical Engineering, Minhaj University Lahore,Civic Center, Twp, Lahore, Pakistan

[3]Engineering Research Centre, University of Punjab, New Campus, Lahore, Pakistan

SCIENTIFIC PAPER

UDC 66:662:546.264-31

CONCEPTUALIZATION AND PROCESS SIMULATION OF A CO_2-BASED METHANOL PRODUCTION PLANT

Article Highlights

- A process plant based on CO_2 hydrogenation to methanol is conceptualized and simulated
- A step-by-step hierarchical procedure is adopted to develop the most profitable flowsheet
- Reactor cooling by boiler-feed water with steam generation is found a more favorable solution
- The price of hydrogen has emerged as a major factor in determining the feasibility of the process

Abstract

The present study conceptualizes and simulates a methanol production process through the direct hydrogenation of captured CO_2. CuO/ZnO/ZrO_2 was employed as the catalyst and Aspen HYSYS was used for the process simulation. Configurational optimization of the process flowsheet was carried out using a step-by-step hierarchical approach. Many alternate flowsheets have resulted, and their capital investment, product cost, and profitability measures were calculated. The discrimination among the competing flowsheets was carried out based on net profit and percent return on investment. The retained flowsheet was further analyzed for optimizing the recycle ratio and evaluating the effect of the price of captured CO_2, green H_2, natural gas (fuel), and catalyst on the economic performance of the plant. The optimum value of the recycle ratio was computed to be 4.23. Additionally, it was found that the price of H_2 is the most important parameter in defining the feasibility and profitability of the process. Mathematical correlations were also developed that relate the profitability and price of the above-mentioned feed materials.

Keywords: CO_2 capture, CO_2 utilization, methanol economy, CO_2 hydrogenation, CuO/ZnO/ZrO_2 catalyst.

Crude oil, natural gas, and coal supply nearly 82% of the world's energy demand [1]. These fossil fuels are a source of a large quantity of human-derived CO_2 that amounted to 34.9 giga tonne, alone in the year 2021 [2]. CO_2 is a greenhouse gas, the second most important after water vapors, that is responsible for increasing the Earth's temperature. Scientists believe that the average temperature rise of the Earth's atmosphere from the preindustrial era must be limited to 2°C [3] to avoid the unparalleled catastrophic effects of global warming. To decrease the CO_2 emissions linked with the burning of fossil fuels, the produced CO_2 must be captured and sequestrated or utilized in the production of useful chemicals. Utilizing CO_2 in the production of useful chemicals, not only helps in the management of CO_2 emissions but also exploits the potential chemical resource of CO_2. One way to utilize CO_2 is to convert it into methanol in the contest of the so-called "Methanol Economy", an idea initiated by Olah [4]. Methanol is a valuable product that is not only

Correspondence: M.R. Usman, Institute of Chemical Engineering and Technology, University of Punjab, New Campus, Lahore 54590, Pakistan.
E-mail: mrusman.icet@pu.edu.pk
Paper received: 17 August, 2023
Paper revised: 5 February, 2024
Paper accepted: 14 February, 2024

https://doi.org/10.2298/CICEQ230817003K

an alternative fuel, but it is also a precursor to many important chemicals. Methanol is a feedstock for gasoline (MTG), olefins (MTO), formaldehyde, tert-amyl methyl ether (TAME), dimethyl ether, acetic acid, methyl tertiary butyl ether (MTBE), methyl esters, etc. When CO_2 for methanol is obtained from an energy source such as biomass or captured from a power plant and hydrogen is produced from the electrolysis of water, realized by a renewable source of energy, the whole process is believed to be green and sustainable.

In the 70s copper-based heterogeneous catalyst, $CuO/ZnO/Al_2O_3$, was developed [5] for the methanol synthesis realized by the hydrogenation of CO and CO_2. The said hydrogenation process occurs at a modest temperature (200–300°C) [6,7] and at a fairly high pressure (5–10 MPa) [6,7] where a high heat of reaction is involved. The direct conversion of CO_2 to methanol occurs under the same operating conditions but with a lower heat of reaction and the formation of reduced amounts of byproducts [8]. The production of water along with methanol may cause expensive downstream methanol purification and may affect the life of the catalyst [9]. CO_2 to methanol synthesis involves the following three reactions; CO_2 hydrogenation to methanol, reverse water gas shift reaction (RWGS), and CO hydrogenation to methanol:

CO_2 hydrogenation:

$$CO_2 + 3H_2 \rightleftharpoons CH_3OH + H_2O \qquad \Delta h^\circ = -49.5 \text{ kJ/mol} \qquad (1)$$

RWGS:

$$CO_2 + H_2 \rightleftharpoons CO + H_2O \qquad \Delta h^\circ = +41.2 \text{ kJ/mol} \qquad (2)$$

CO hydrogenation:

$$CO + 2H_2 \rightleftharpoons CH_3OH \qquad \Delta h^\circ = -90.8 \text{ kJ/mol} \qquad (3)$$

Numerous literature studies discuss the process simulation and economic feasibility of the direct synthesis of methanol from CO_2 and H_2. Van-Dal and Bouallou [10] proposed a flow scheme where they integrated CO_2 into a methanol plant with a CO_2 capture facility. The design and simulation of the process were carried out using Aspen Plus. They found that the cost of the capture is considerably reduced as the methanol plant supplies 36% of the thermal energy needed for CO_2 capture. Also, they showed that abatement of 1.2 tonne of CO_2 per tonne of methanol produced is possible. A different source of CO_2 was employed by Matzen *et al.* [11] as the CO_2 was supplied from an ethanol production facility. Wind-based electrolytic H_2 was used and Aspen Plus software was utilized to develop the methanol synthesis plant. The economic evaluation of the process revealed that the cost of the electrolytic hydrogen is the major factor in defining the feasibility of methanol synthesis. Pérez-Fortes *et al.* [12] adopted the synthesis scheme of Van-Dal and Bouallou [10] and modified its configuration by applying a pinch analysis. Unlike Van-Dal and Bouallou [10], they developed their flowsheet in CHEMCAD software and performed a rather detailed economic analysis. Comparing their analysis with conventional methanol plants, they estimated a decreased capital cost than the traditional plants, however, the price of raw material, i.e., those of green H_2 and captured CO_2, financially discouraged their proposed scheme. Another study that was targeted to mitigate CO_2 emissions from a bioethanol plant was carried out by Wiesberg *et al.* [13]. They compared direct CO_2 conversion to methanol (Route A) with CO_2 to methanol by the bi-reforming process (Route B) and used Aspen HYSYS for their work. In bi-reforming, natural gas, steam, and CO_2 were used as reactants to produce syn gas which was converted to methanol. In each case, the methanol synthesis followed a novel scheme where CO_2 was compressed to a restricted pressure in the first reactor and only partially converted to methanol. After separating the methanol, the remaining CO_2 was compressed to a higher pressure and converted in the second reactor. This novel scheme was adopted to save the cost of compression. The authors claimed 5 times more CO_2 consumption in Route A and reasoned that Route A is more profitable than Route B. However, they found neither of the two processes is feasible economically. The flow scheme of Route A was further studied by Borisut and Nuchitprasittichai [14] to minimize the methanol production cost. They applied response surface methodology (RSM) and non-linear programming for the optimization and successfully optimized the process. As a variety of hydrogen sources and production methods can be used for CO_2 hydrogenation, Kiss *et al.* [15] employed by-product wet H_2 from the chloralkali industry. They applied a stripper column where the wet hydrogen was contacted with the methanol-water mixture obtained in the product separator. They reasoned that this way CO and CO_2 are virtually removed from the product and wet hydrogen is dried. The process simulation was carried out in Aspen Plus and the results claimed a significant reduction in utility requirements. Roh *et al.* [16] reviewed the CO_2 conversion processes and discussed the issues and future possibilities in such processes. They suggested finding new and innovative routes that offer reduced CO_2 impacts, are economically viable, and address improved sustainability aspects. The use of biomass for methanol synthesis was studied by Martín and Grossmann [17]. They described an integrated facility for methanol production from switch grass. The concept was to produce syn gas from the biomass and capture some of the CO_2 present in the syn gas. Both the syn gas and the recovered CO_2 were then used to produce methanol in separate synthesis

trains. The authors concluded that massive energy needs and large capital investment are the principal drawbacks of their strategy. The idea of a photocatalytic hydrogen source was employed by AlSayegh *et al.* [18]. The risk of H_2 and O_2 explosion was prevented by adding captured CO_2 to the system to escape the explosive limits. A membrane separator was then employed to recover an H_2 and CO_2 mixture of a 3:1 molar ratio. The flow diagram of Van-Dal and Bouallou [10] was employed and simulated in Aspen Plus. The authors reported a high production cost of methanol in comparison to conventional methanol from natural gas. To reduce the energy requirements, Szima and Cormos [19] came up with the idea of utilizing the purge stream in a gas turbine and low-temperature off-streams in organic Rankine cycles. The plant simulation was carried out in CHEMCAD and an economic analysis was carried out. With the above modification, they presented an energy-sufficient plant with decreased operational costs. Realizing the fact that cement production is the biggest source of CO_2 emissions, Meunier *et al.* [20] routed captured CO_2 from a cement plant to produce methanol. They also performed the life cycle assessment to identify the areas of main environmental concern. Aspen Plus was employed for the simulation and the flow scheme was based on the work of Van-Dal and Bouallou [10]. The process was not found economically practicable owing to the high hydrogen production cost. Also, the environmental analysis found hydrogen supply to be the main environmental concern. In the same year, Nguyen and Zondervan [21] investigated three routes, namely bi-reforming, tri-reforming, and direct hydrogenation of CO_2 to methanol. The analysis was carried out with the help of Aspen Plus. The results demonstrated that reforming processes are more economically practicable though less environmentally friendly and can be employed for an interim period till the CO_2 hydrogenation with H_2 from a renewable source becomes economically competitive. An algorithmic approach was used by Lee *et al.* [22] to optimize the methanol synthesis flowsheet. Similar to the work of Wiesberg *et al.* [13] and Borisut and Nuchitprasittichai [14], they used adiabatic reactors in series with interstage condensation of methanol. They successfully solved the superstructure and obtained an economically optimized design. Campos *et al.* [23] also used a multibed reactor with interstage condensation of methanol. They too found a substantial increase in single-pass CO_2 conversion, which helped in reducing the overall cost of the process, especially that associated with the recycle structure. The approach of using interstage methanol separation where enhanced single pass conversion has resulted, sounds promising and is expected to significantly improve the plant performance. The simulation of CO_2 hydrogenation to methanol over a non-conventional In-Co catalyst was carried out by Cordero-Lanzac *et al.* [24]. The authors developed the kinetics of the catalyst and used Aspen Plus for their simulation. Additionally, they carried out the life cycle assessment of the CO_2 hydrogenation plant linked with a cement plant. Their findings suggest that the methanol plant can not completely overcome the emissions of a cement plant. To reduce the cost of the produced methanol, Yousaf *et al.* [25] combined the solid oxide electrolyzer (SOE) employed for hydrogen generation with a CO_2 hydrogenation plant. A slightly modified flowsheet of Van-Dal and Bouallou [10] was employed and Aspen Plus was used for the simulation. In the modified flowsheet, the waste gases were also sent back to the reactor. The authors found a substantial decrease in the cost of methanol production compared to the literature works with proton exchange membranes (PEM) and alkaline electrolyzers. In a more recent work, Haghighatjoo *et al.* [26] compared the direct and indirect conversion of CO_2 to methanol. The simulation of the two processes was carried out in Aspen Plus and the operating conditions were optimized. They found that the direct method requires lower fixed capital investment as well as poses decreased environmental threats, whereas the indirect method offers higher net profit. Chiou *et al.* [27] studied six reactor schemes constituting adiabatic and non-adiabatic reactors and compared the schemes for their economic feasibility. The authors came up with the result that a two-reactor system where a non-adiabatic reactor stage followed by an adiabatic stage is the most economical case. They also developed a suitable control system to handle the changes in flow rates and compositions in their process scheme.

In the literature studies discussed above, some researchers discussed flowsheet development, however, a systematic approach to developing a conceptual flowsheet is found to be missing. The discrimination of various rival flowsheets based on profitability analysis is also not done in the literature. For example, Lee *et al.* [22] used an algorithmic approach to reach their final flowsheet. It is not clear what schemes were compared, but the major focus was on the development of the reactor system (with interstage condensation and separation) and parametric optimization. Borisut and Nuchitprasittichai [14] optimized the parameters for a selected flowsheet that used adiabatic reactors in series with condensation in between the equilibrium reactors. Roh *et al.* [16] have only partially studied the CO_2 to methanol process and mostly discussed the issues of process systems engineering for carbon dioxide conversion processes and their integration with

other systems. Martín and Grossmann [17] integrated the methanol synthesis from syn gas produced out of switch grass and the methanol synthesis from CO_2 hydrogenation, where CO_2 was obtained during syn gas purification. Their study focused on the integration of the above two schemes and not flowsheet development for CO_2 hydrogenation to methanol. Chiou *et al.* [27] selected a single flowsheet and compared different configurations of reactor systems only. They used a single adiabatic reactor, a single non-adiabatic reactor, and a two-stage adiabatic reactor. No effort was made towards the development of a process flow scheme.

In the present study, inspired by the original work of Douglas [28], a step-by-step hierarchical procedure is developed to discriminate among the alternate flowsheets and to reach the most profitable flowsheet. Knowledge of process design including heuristics and cost estimation is employed to carry out the techno-economic analysis of the process with a main focus on the configurational optimization conducted through the methodology developed in the present study. Additionally, CuO-ZnO-ZrO_2, a non-traditional catalyst has been applied for the analysis.

MATERIALS AND METHODS

Process and simulation basis

CO_2 captured from a 100 MW natural gas power plant and hydrogen from a green source, i.e., by electrolysis of water using solar or wind energy, was used as the starting point for the simulation. The amount of CO_2 captured was computed for a 60% thermally efficient power plant [29] and a natural gas of the following composition: 90.45% methane, 3.56% ethane, 3.32% N_2, 0.05% O_2/Ar, 0.8% propane, 0.17% *n*-butane, 0.16% isobutane, 0.05% *n*-pentane, 0.07% *iso*pentane, 0.04% C_6+, and 1.34% CO_2 [30] with 112 kg/E6m^3 H_2O/MMSCF gas [31]. 10% excess air was employed, and 40% relative humidity of air was assumed. With 0.4% impurity (N_2) in CO_2 feed [32], 796.7564 kmol/h of CO_2 was calculated that entered at 1 bar and 25°C to the methanol plant. Pure hydrogen gas [33] at 25°C and a pressure of 30 bar [34] was used in the simulation. Other conditions employed for the simulation are listed below:

- Aspen HYSYS was employed for the steady-state simulation.

- The non-random two-liquid (NRTL) model was applied as the fluid package in association with the vapor phase Soave-Redlich-Kwong (SRK) property model. The NRTL was selected as polar compounds in the liquid phase were expected to be present and it has been employed by other researchers [11,15,35,36] as well. For a better estimation of liquid density, the Costald method was selected for the estimation of liquid density [37].

- For CO_2 compression, a three-stage compressor was used where the pressure ratio in each stage was kept the same.

- Cooling water inlet was at 90 °F (32.22 °C) and the outlet was at 120°F (48.89 °C). The minimum temperature difference of 10 °F (5.56 °C) was maintained [28]. The hot stream outlet temperature was therefore kept at 100 °F (37.78 °C).

- Aspen HYSYS “Conversion Reactor” unit was used to simulate the water-cooled isothermal reactor that operated at 50 bar and 250 °C. An isothermal reactor was selected as methanol synthesis from direct CO_2 hydrogenation is moderately exothermic in contrast to methanol from CO (nearly half the heat of reaction for CO_2 hydrogenation compared to that of CO hydrogenation). Therefore, only a moderate rise in temperature in an adiabatic reactor is expected which can be made virtually isothermal in a multitubular reactor. High rates of reaction can be maintained in an isothermal reactor along with an improved yield of methanol compared to an adiabatic reactor. Also, the excess heat evolved from the reaction can be more conveniently utilized for, say, generating steam compared to a multibed reactor with interstage cooling.

- All three reactions outlined above in Eqs. (1–3) were incorporated into the simulation.

- Owing to the superior performance of the CuO-ZnO-ZrO_2 catalyst over CuO-ZnO-Al_2O_3 [38], the former was used in the present study. Arena *et al.* [38] compared the performance of both these catalysts and found that under identical conditions of 50 bar pressure and 513 K temperature, CuO-ZnO-ZrO_2 gives 22.4% CO_2 conversion and 14.3% methanol yield compared to 19.5% CO_2 conversion and 11.9% methanol yield over the CuO-ZnO-Al_2O_3 catalyst.

Over a particle bed of the zirconia-based catalyst, according to the experimental data of Yang *et al.* [39] at 50 bar and 250 °C, 15% conversion was regarded for the CO_2 hydrogenation reaction (Eq. 1), 10% in the case of the RWGS reaction (Eq. 2), and 50% for the CO hydrogenation to methanol reaction (Eq. 3).

- In each simulation run, the molar ratio of H_2 to CO_2 at the reactor inlet was always kept at a constant value of 3:1. The ratio was fixed by varying the molar flow rate of the inlet (makeup) H_2 flow stream.

- Pumps and centrifugal compressors were considered 75% efficient, while adiabatic compressors

were taken as 90% efficient.

- The pressure drop in each heat exchanger was taken as 10 psi (68.95 kPa) which is commonly considered as the maximum allowable pressure drop across a heat exchanger. The pressure drop across the reactor was used as 100 kPa as expected due to the presence of a particle bed.

- Aspen HYSYS "Distillation Column" unit was used for simulating the methanol product column. The column was fitted with a partial condenser, to remove the lighter ends, and it contained 15 theoretical trays. The top pressure was maintained at 110 kPa for which the dew point remained always higher than 100 °F (37.78 °C) and cooling water was therefore used in the condenser. Methanol product purity was set at 98.5 mol% (99.3 wt%) while water purity at the bottom was fixed at 99.9 mol%. 99.0 mol% of methanol in the distillation column feed was recovered in the distillate product. The number of theoretical trays was optimized in initial trials, and in all cases, it fulfilled the above requirements.

Flowsheet development

Initially, a trivial flowsheet without recycle, heat integration, and more effective downstream separation was conceived and simulated in Aspen HYSYS. The requisite equipment design was carried out and both the capital and product costs were estimated. Based on these costs, the profitability of the process was computed. Later, a step-by-step hierarchical modification of the flowsheet was realized in light of heuristics and process design understanding. After each change in the flowsheet, the costs and profitability of the process were figured out. A suitable profitability measure was used, which is to be discussed in the next section, to discriminate among the various alternate solutions (flowsheets). By a step-by-step hierarchical approach we mean that for the trivial flowsheet mentioned above, firstly, a recycle structure was introduced and tested to determine whether recycling was important or not. This was followed by product separation where various separation schemes were compared. Knowing the best scheme, the heat integration was carried out and a couple of heat integration strategies were tried. In the last step, the parametric optimization of the final configured flowsheet was carried out. However, only the effect of recycle ratio was studied which was visualized as the most important parameter.

In total, seven flowsheet configurations or cases were constructed as outlined in Table 1. In the initial flowsheet (Case-I), as mentioned earlier, only essential processes and equipment were introduced and no recycling, heat integration, and efficient product separation were employed. While recycling is often necessary for low-conversion systems, however, in some cases adding recycling negatively affects the profitability of the plant. For example, with gas recycling, the recycling compressor and its associated compression cost have to be considered. Also, the recycling increases the size of the equipment (heat exchangers, heaters, reactor vessels, coolers, and phase separator vessels) and the amount of the utilities required together with the additional piping in the recycle loop, which escalates the associated costs. A recycle and a purge stream were introduced in Case II. Many recycling ratios were studied and a suitable value of recycle ratio was selected and applied in the subsequent cases. A second, but low-pressure vapor-liquid equilibrium (LP VLE) phase separator was used in the next case (Case III). An absorption column was tried in Case IV and a stabilizer column was introduced in Case V. After finalizing the purification step, heat integration was carried out with cooling water and boiler feed water, respectively, in Case VI and Case VII. Lastly, the recycle ratio was optimized and the effect of the price of the raw materials, energy, and catalyst on the plant's economics was studied for the optimum case (Case VII-11).

Table 1. List of cases simulated in the present study.

Case	Description	Figure
I	Only the essential equipment is employed and no recycling is used	Fig. 1a
II	A gas recycle stream with a purge is included in Case I	Fig. 1b
III	A low-pressure VLE separator is integrated with Case II	Fig. 2a
IV	A gas absorber is incorporated in Case III	Fig. 2b
V	A stabilizer column is employed in Case II	Fig. 2c
VI	Heat integration is carried out with Case III, and cooling water is used for reactor cooling	Fig. 3a
VII	Heat integration of Case III is performed, and boiler feed water is used for reactor cooling with subsequent steam generation	Fig. 3b

Economic evaluation

For the capital cost estimation, the factorial method based on delivered equipment cost [40] was applied. The purchased cost of equipment was calculated by the cost correlations of Seider *et al.* [41] as validated by Feng and Rangaiah [42]. A 10% delivery cost was added to the total purchased equipment cost to obtain the delivered equipment cost. 2% and 15% of total capital investment were set as land cost and working capital, respectively. The required information for calculating the purchased cost of equipment was obtained from the simulation results and when needed additional information was obtained through the design methods discussed below:

Heat exchanger: The surface area (A) was

calculated from the *UA* value obtained from Aspen HYSYS and dividing *UA* by the typical overall heat transfer coefficient (*U*) for the given situation [43]. An average value of the overall heat transfer coefficient is used from the range provided by Sinnot and Towler [43].

Reactor: The weight of the catalyst was calculated from the space velocity, conversion, and selectivity data of Yang *et al.* [39]. Using the calculated weight, the total number of tubes was figured out while considering 1300 kg/m^3 as the bulk density of the catalyst. Each tube was 42.42/50.8 mm ID/OD with a 7.62 m length. The surface area was calculated for the total number of tubes and the cost was calculated for a fixed-head heat exchanger.

Vapor-liquid separator: The diameter and length of the vessel were calculated by the method given by Branan [44] and Watkins [45].

Distillation and absorption columns: The diameter of the column was calculated based on the widely used Fair correlation [46]. Operating velocity was taken as 80% of the flooding velocity. Sieve trays were employed, and a 10% downcomer area was used. Overall column efficiency was taken as 60% for a distillation column and 55% for a gas absorber. 0.457 m tray spacing was used and 1.524 m additional height was added to obtain the total column height.

The details about the elements of the capital cost estimation method used in the present study are provided in Table S1 (Supplementary material).

For the product cost, again the method of Peters *et al.* [40] was employed. Labor cost was taken as 15% of total product cost while utility costs were based on process module costs and calculated from the recommendations of Ulrich and Vasudevan [47]. The non-condensables from the distillation column and the purge stream were taken as energy credits and therefore, the equivalent cost of energy of these streams was subtracted from the total cost of utilities. The land price was considered paid, so rent on land was taken as zero. 8400 hours were taken as working hours in a year. A fixed value of depreciation for each year, taken as 10% of the fixed capital investment, was used. The unit price of captured CO_2 was considered to be \$0.0471 [48], \$1.5 for green H_2 [49], \$60/kg for the catalyst (expecting a little higher price than an alumina-contained copper-based catalyst), and \$7.3/MMBtu (\$6.9188/GJ) for the natural gas [50]. The price of \$1.5 for green H_2 is the best-case wind scenario coupled with a low-cost electrolyzer. The detailed breakdown of the product cost calculation is shown in the electronic supplementary material in Table S2. Additionally, chemical (CO_2) conversion efficiency was also calculated by Eq. (4):

$$\%CCE = \frac{\text{moles of methanol produced}}{\text{moles of } CO_2 \text{ fed}} \quad (4)$$

Net profit (NP), return on investment (ROI), and payback period (PBP, based on fixed capital investment) were calculated for the methanol selling price of \$1.5/kg. Income tax was taken as 35% of the gross profit. For comparison purposes, the selling price of methanol (SPM) for 0% ROI (zero net profit) was also calculated. The formulas employed for the above quantities are given in Eqs. S1 S5.

Process description

Case I: Fig. 1a shows the flow scheme for Case I, the simplest among all the flow schemes. CO_2 received from a CO_2-captured plant is compressed from 1 bar to 50.69 bar in a three-stage compressor (K-101) with interstage cooling. H_2 obtained from an electrolyzer at a pressure of 30 bar and 25 °C is compressed in a single-stage H_2 compressor (K-102), again, to 50.69 bar. Both compressors are selected as the centrifugal type. The two gases are heated in a fixed-head shell-and-tube heat exchanger (HE-102) by high-pressure steam. The temperature of the outlet stream (Stream 6) reaches 250 °C. The reaction takes place in an isothermal multitubular fixed bed reactor (R-101) at 50 bar and 250 °C. As the methanol synthesis process is exothermic, cooling water is used to maintain the isothermal reactor conditions. The product gases are cooled in a floating head shell-and-tube heat exchanger (HE-104) again by cooling water. The cooled product is a vapor-liquid mixture and enters V-101, a vertical high-pressure vapor-liquid equilibrium (HP VLE) separator. The gases mainly H_2, CO, and CO_2 vent out at the top while liquid containing primarily methanol and water leaves at the bottom. The pressure of the liquid stream is decreased to 1.5 bar with the help of an expansion valve (VLV-101) and the liquid is directed to a distillation column (T-101) fitted with a partial condenser (fixed head, HE-105) at the top. Non-condensables leave at the top and methanol is recovered as a distillate product. The wastewater is collected at the bottom of the distillation column where low-pressure steam is employed in a kettle-type reboiler (HE-106).

Case II: The process flowsheet for Case II is shown in Fig. 1b. Unlike Case II, the top product of the HP VLE separator (V-101) is recycled back to the reactor inlet. A recycle compressor (K-103) of centrifugal type is employed for this purpose. As the separator is operated at 48.31 bar, only a small increase in pressure is required for the recycle stream (Stream 9R). Additionally, a small stream (Stream 9P) is also purged to avoid the buildup of the inert present

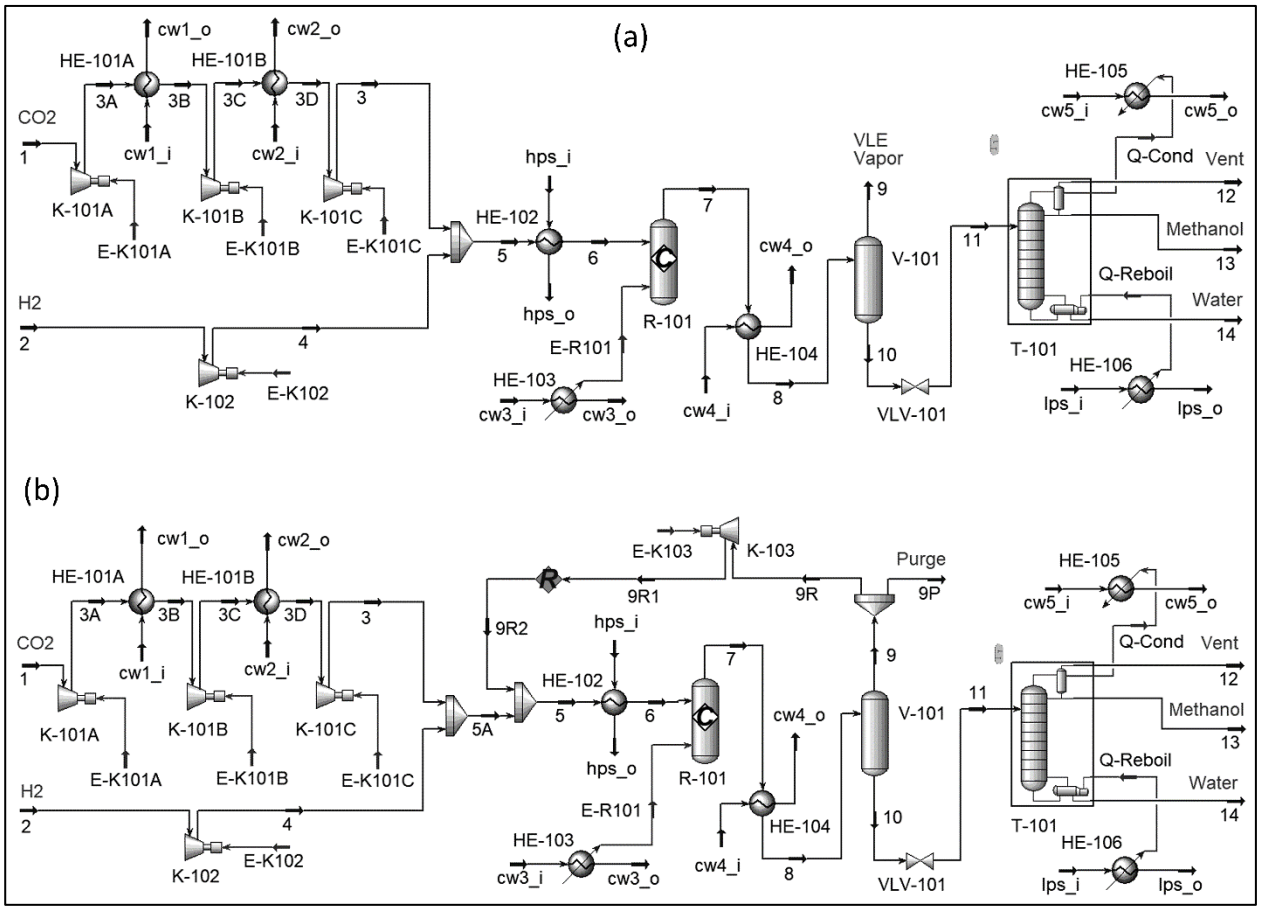

Figure 1. Simulation flowsheet for: (a) Case I–Basecase; (b) Case II–Introduction of recycle stream with purge.

in the feed CO_2.

Case III: As shown in Fig. 2a, the liquid leaving the high-pressure separator (V-101) is expanded in an expansion valve (VLV-101) to release the gases soluble in the methanol-water mixture. The pressure is decreased from 48.31 bar to 2.19 bar and a second VLE separator (V-102) is operated at this lower pressure. Owing to a large liquid-to-vapor ratio, the second separator is horizontally oriented. The gases leaving at the top of the separator are also pressurized and recycled back to the reactor. A reciprocating compressor (K-104) is called for this duty. The liquid departing at the bottom of the LP VLE is subjected to a further decrease in pressure to reach the distillation column (T-101) inlet at a pressure of 1.5 bar.

Case IV: The case is shown in Fig. 2b. The vapors leaving the high and low-pressure VLE separators and the vent vapors from the top of the methanol distillation column are pressurized to 51.88 bar, cooled, and sent to the gas absorber (19 sieve plates, T-102). The water leaving the distillation bottom is cooled and used as a solvent in the gas absorber, i.e., a part of the distillation bottom is cooled to 37.78 °C and pressurized to absorber conditions and used as a solvent for methanol recovery. The solvent leaving at the bottom of the distillation column is mixed with the LP VLE separator bottom and sent back to the distillation column. This scheme does not require a separate stripper for solvent recovery.

Case V: Fig. 2c depicts the flowsheet of Case-V. The LP VLE separator of Case-III is replaced by a stabilizer column (35 sieve plates, T-102) that operates at 5 bar. Better separation of non-condensable gases from methanol-water guarantees the absence of non-condensable gases in the methanol distillation column (T-101). The stabilizer top product (Stream 10R) is also pressurized and recycled.

Case VI: Heat integration of Case III was carried out as shown in Fig. 3a. The reactor outlet gases (Stream 7) are used to preheat the reactants (Stream 5A). An additional heat exchanger (HE-102P) was therefore installed for this purpose. Moreover, the distillation bottom product (Stream 14) was used to heat the feed stream (Stream 11) to the distillation column to reduce the heat load on the distillation column. The product stream was cooled thereafter.

Case-VII: The flow scheme for Case VII is shown in Fig. 3b. Boiler feed water (Stream bfw) at 200 kPa and 32. 2 °C was used for cooling in the reactor (R-101) and heated up to the saturated conditions (saturated

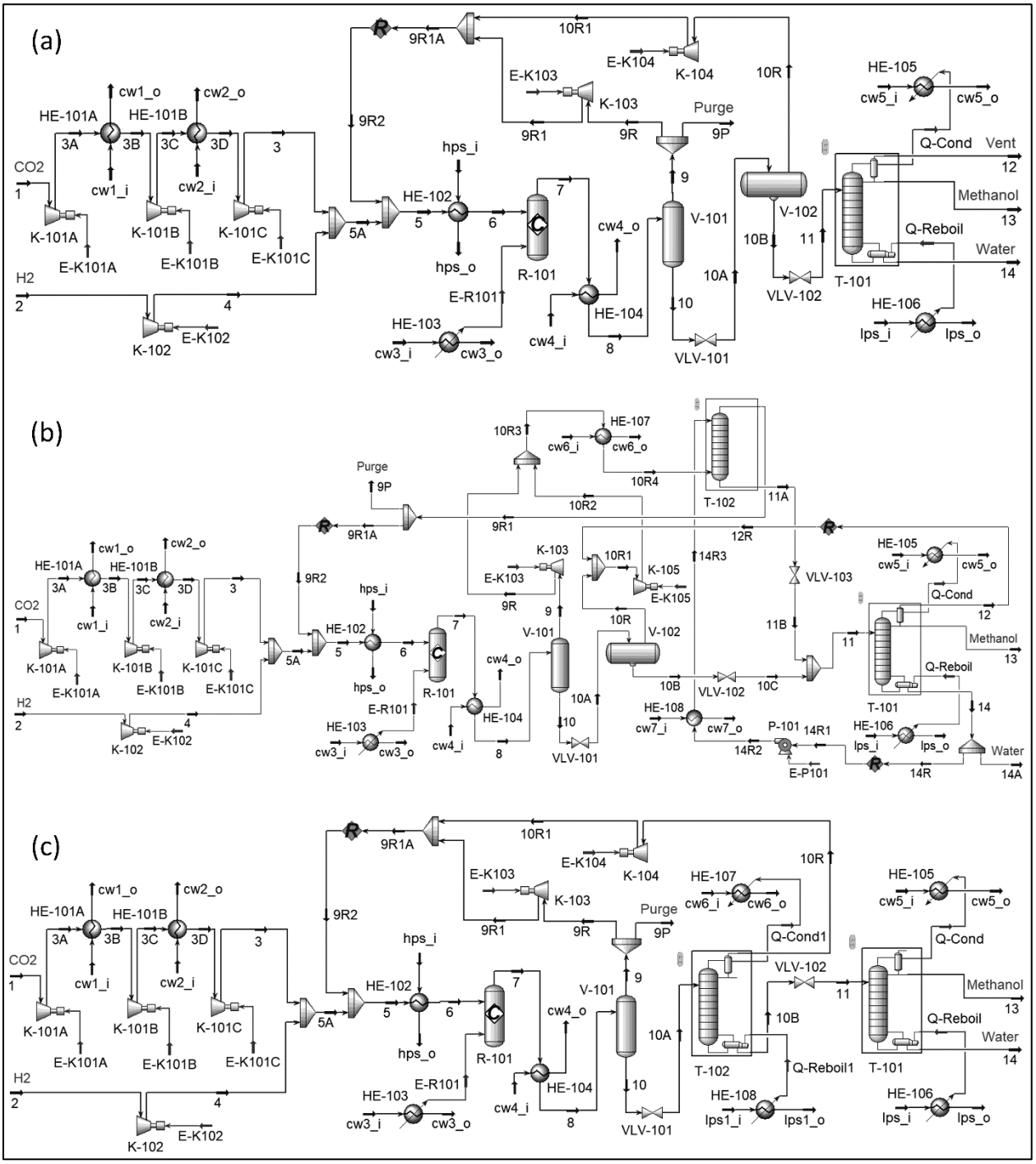

Figure 2. Simulation flowsheet for: (a) Case III–Addition of a low-pressure VLE separator; (b) Case IV–Addition of a gas absorption unit; (c) Case V–Addition of a stabilizer unit.

water at 120.2 °C). The saturated water was further heated to saturated steam (Stream s2). Part of the saturated steam was used in the reboiler of the methanol distillation column.

RESULTS AND DISCUSSION

Flowsheet configuration

The results of simulation and cost analysis for different cases of flowsheets are shown in Table 2. For Case I, the simplest formulation, the net profit is \$-6.97×10^7 (%ROI as -158.0), and the selling price of a kg of methanol for zero net profit is \$4.95. Both a negative net profit and a staggeringly high methanol price are quite undesirable. Upon the addition of a recycling structure (Case II), however, a huge economic benefit resulted. For example, for a split ratio (defined as the molar ratio of the flowrate of stream 9P

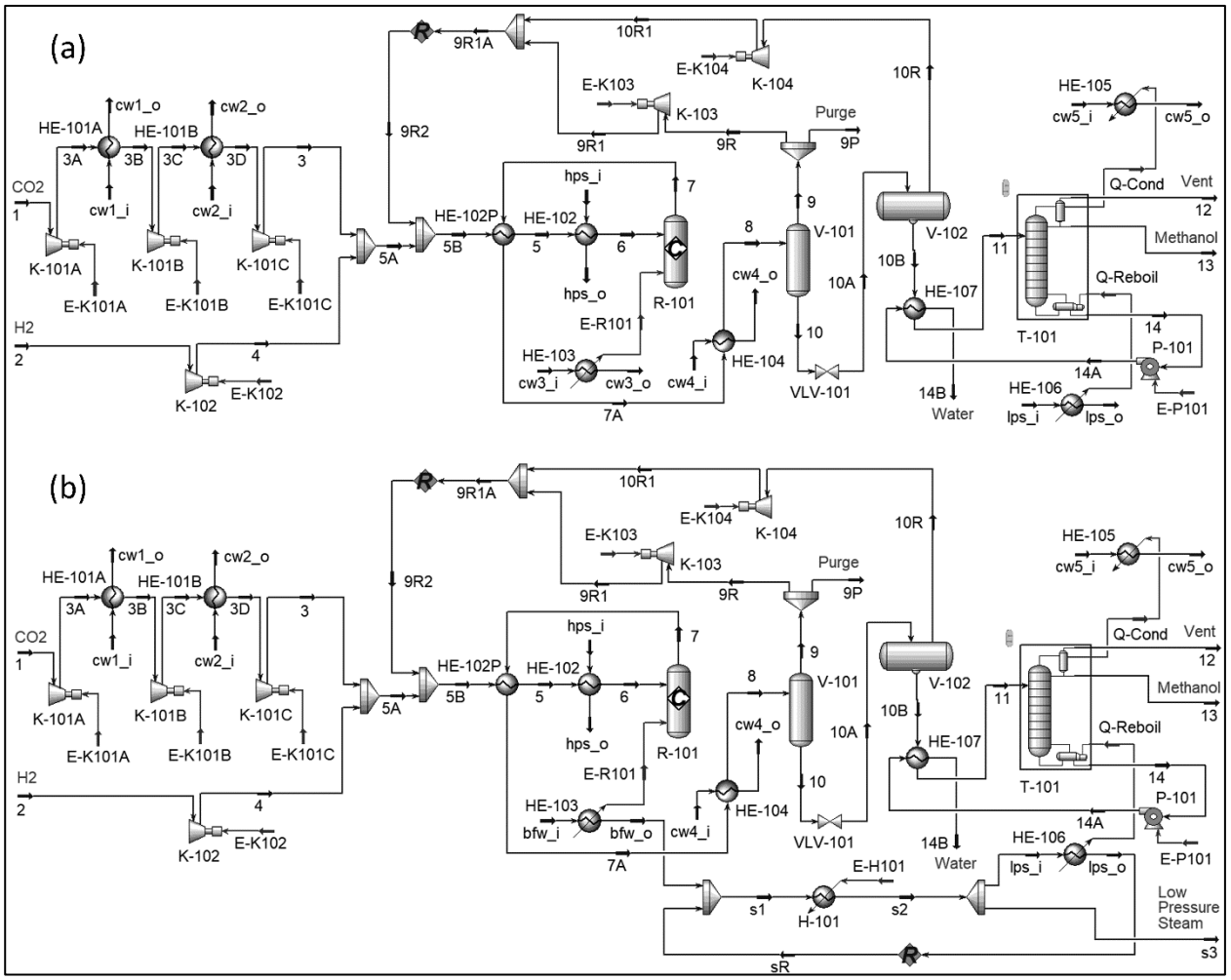

Figure 3. Simulation flowsheet for: (a) Case VI–Heat integration to Case III with reactor cooled by cooling water; (b) Case VII– Heat integration to Case III with reactor cooled by boiler feed water leading to steam generation.

to the flowrate of stream 9R) of 0.02, %ROI is increased from -158.0% to +23.96% and the price of a kg-methanol obtained for zero net profit is reduced from \$4.95 to a much lower value of \$1.37. At this stage, various split ratios (recycle ratios) were tried and a moderate split ratio of 0.02 was selected and fixed to be used in the analysis of the subsequent cases. The above value of split ratio corresponds to the recycle ratio (RCR) of 3.92 calculated by taking the ratio of the molar flowrate of the recycled stream (9R2) to the molar flowrate of the makeup hydrogen stream (2).

Table 2. Results of simulation in terms of cost and profitability measures.

Case	TCI ($)	TPC ($)	NP* ($)	ROI* (%)	PBP* (yr)	Methanol price for %ROI = 0 ($/kg methanol)	*CCE, Eq. 4* (%)
I	44120602.04	153890631.15	-69708730.43	-157.996	-	4.9486	14.65
II	70250734.29	270123796.24	16828805.84	23.9553	2.6190	1.3688	93.00
III	70333475.16	271777961.70	17460563.31	24.8254	2.5506	1.3653	93.87
IV	74903672.84	276465625.74	16646098.24	22.2233	2.7666	1.3728	94.90
V	70669945.94	276029877.3	16752064.48	23.7047	2.6394	1.3719	94.82
VI	82651188.15	265819566.18	21306871.09	25.7793	2.4796	1.3353	93.82
VII	96475299.74	260212347.28	24975190.36	25.8877	2.4718	1.3070	93.82
VII-11	100537614.7	268107909.19	29269639.83	29.1131	2.2598	1.2843	97.45

*For price equivalent to \$1.5/kg methanol.

As mentioned earlier, in the purification step, the load on the distillation column was decreased by using an LP VLE separator, a gas absorption column, or a stabilizer column, respectively as shown in Fig. 2(a–c). Comparing the three cases, the results show that the LP VLE separator is the most economical method of separation in the present situation. Table 2 shows that the %ROI is 24.83, 22.22, and 23.70, respectively, for

using the LP VLE separator alone, gas absorber, and stabilizer. Out of the three, the case with gas absorption is not only complicated, but it also provides the highest TCI and the lowest net profit. When compared with Case II over which Case III, Case IV, and Case V were developed, it is revealed that the addition of either a gas absorber (Case IV) or a stabilizer (Case V) is proved an economically poor design with adverse economic benefits. In both cases, TCI increased while the net profit decreased. The use of an LP VLE separator is not only a simplified deal, but it has also incremented about 4% net profit for virtually the same TCI. At this point, the integration of the LP VLE separator was approved, and the flowsheet developed hitherto was subjected to heat integration.

For heat integration, as mentioned earlier, two approaches were adopted. In the first scheme, cooling water was used to remove the exothermic heat of the reaction from the methanol synthesis reactor. Whereas in the second approach, boiler feed water (bfw) was used that was heated to the saturated liquid state by the excess heat of the reactor. Additionally, a boiler was installed to convert the saturated liquid water to the corresponding saturated steam. As the heat of the reaction for CO_2 hydrogenation to methanol is nearly half the heat of the reaction for CO hydrogenation, an opportunity was available to use cooling water for cooling the reactor. Boiler feed water owing to the requirements of additional treatment, is much more expensive than simple cooling water. The cost comparison between using cooling water and boiling feed water was therefore considered imperative. Fig. 2 and Fig. 3 show, respectively, the use of cooling water alone in the reactor and the use of bfw in the reactor with steam generation. For both the heat integration cases (Case VI and Case VII), a massive improvement is observed over the previous best case, Case III. Although capital investment has increased, the net profit has also increased and increased quite appreciably. The net profit increased nearly 22% for Case VI, while it increased about 43% for Case VII. Comparing Case VI and Case VII, a significantly higher net profit is obtained in Case VII though at the cost of a little more TCI which resulted in virtually the same %ROI for the two cases. Based on the highest revenue and slightly better %ROI than Case-VI, with the lowest methanol price for 0%ROI, Case VII was received as the best flowsheet configuration.

Effect of recycle ratio

The final flowsheet was additionally analyzed for various recycle ratios. As mentioned earlier, the recycle ratio was varied by varying the split ratio (moles 9P/moles 9R). This was done because it was found much more convenient to set a split ratio in Aspen HYSYS than to fix a recycle ratio. Fig. 4 shows the effect of the split ratio (recycle ratio) on the ROI of the plant. It is clearly revealed that the recycling ratio has a great effect on the economic performance of the plant. Initially, with a decrease in the recycling ratio, the ROI is linearly increased, it then reached the maximum and then decreased steadily. A mathematical equation was developed using TableCurve 2D between the split ratio (SR) and ROI as shown in Eq. (5). An excellent fit of the data with the sum of squares of the errors (SSE) of only 7.01×10^{-6} was obtained. Taking the derivative of the function with respect to SR, the maximum ROI was obtained at the split ratio of 0.00575.

$$ROI = 0.3266 - 3.1910SR + 2.3189SR^2 - \frac{0.0001046}{SR} \quad (5)$$

where SR is the split ratio defined as moles of the 9P stream divided by moles of the 9R stream.

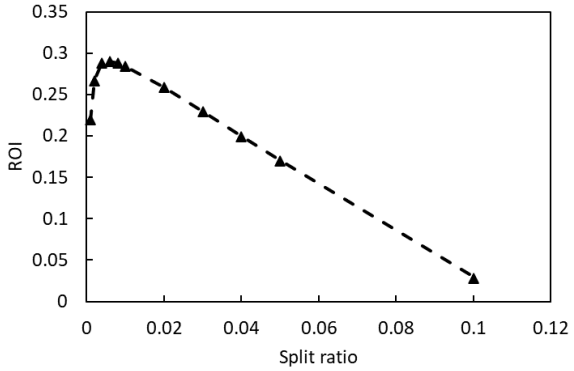

Figure 4. ROI values with a change in the split ratio (recycling ratio). The split ratio is the moles of stream 9P divided by the moles of stream 9R.

Case VII was rerun using the new split ratio and the sub-case was called Case VII-11. The material balance for Case VII-11 is shown in Table 3 whereas Tables S1 to S3 provide the detailed cost estimation and profitability analysis for Case VII-11. It can be found from the results that the final flow scheme produced 0.71 kg methanol per kg of CO_2 and that 35 tonnes of CO_2 is ready to mitigate every hour.

It is important to mention here that at the steady state, the feed flow rate of nitrogen and the purge flow rate (plus nitrogen leaving any other stream) should be the same. However, Table 3 shows a slight difference in the two flow rates caused by the tolerance selected for the simulation. It was observed that as the split ratio decreased, the convergence became more and more difficult. A smaller value of tolerance was avoided as it could create more problems in convergence thus giving no result.

Effect of the price of feed materials

Case VII-11 was further studied to observe the effect of the price of CO_2, H_2, fuel (NG), and catalyst (together called feed material) on the economic

Table 3. Material balance results for major streams of Case-VII-11, i.e., Case-VII with a split ratio of 0.00575 (RCR of 4.2972).

Stream #	Stream Name	*T* (°C)	*p* (bar)	Phase*	Molar flowrate (kmol/h)						
					CO_2	H_2	CO	Methanol	H_2O	N_2	Total
1	Feed CO_2	25.00	1.000	*g*	793.5694	-	-	-	-	3.1870	796.7564
2	Feed H_2	25.00	30.00	*g*	-	2373.0400	-	-	-	-	2373.0400
3	Compressed CO_2	169.9	51.38	*g*	793.5694	-	-	-	-	3.1870	796.7564
4	Compressed H_2	92.91	51.38	*g*	-	2373.0400	-	-	-	-	2373.0400
5B	Preheater Inlet	62.66	51.38	*g*	3115.3699	9343.7753	307.9612	56.2431	11.3332	532.4433	13367.1261
5	Heater Inlet	150.0	50.69	*g*	3115.3699	9343.7753	307.9612	56.2431	11.3332	532.4433	13367.1261
6	Reactor Inlet	250.0	50.00	*g*	3115.3699	9343.7753	307.9612	56.2431	11.3332	532.4433	13367.1261
7	Reactor Outlet	250.0	49.00	*g*	2336.5274	7010.8237	309.7491	833.2977	790.1757	532.4433	11813.0169
7A	Product Cooler Inlet	159.3	48.31	*g*	2336.5274	7010.8237	309.7491	833.2977	790.1757	532.4433	11813.0169
8	HP Separator Inlet	37.78	47.62	*g/l*	2336.5274	7010.8237	309.7491	833.2977	790.1757	532.4433	11813.0169
9	HP Separator Vapor Outlet	37.78	47.62	*g*	2328.4598	7007.7248	309.5453	55.5922	11.1873	532.4263	10244.9357
9P	Purge	37.78	47.62	*g*	13.3886	40.2944	1.7799	0.3197	0.06433	3.0615	58.9084
9R	HP Separator Recycle	37.78	47.62	*g*	2315.0711	6967.4304	307.7654	55.2725	11.1229	529.3649	10186.0273
9R2	Recycle	46.81	51.38	*g*	2321.8005	6970.7353	307.9612	56.2431	11.3332	529.2563	10197.3297
10	HP Separator Liquid Outlet	37.78	47.62	*l*	8.0676	3.0989	0.2038	777.7055	778.9884	0.01701	1568.0813
10A	LP Separator Inlet	37.37	2.189	*g/l*	8.0676	3.0989	0.2038	777.7055	778.9884	0.01701	1568.0813
10B	LP Separator Liquid Outlet	37.37	2.189	*l*	1.2592	0.006298	0.05885	776.7348	778.7781	-	1556.8372
10R	LP Separator Gas Recycle	37.37	2.189	*g*	6.8085	3.0400	0.1975	0.9707	0.2104	0.01699	11.2441
11	Distillation Column Feed	63.53	1.500	*g/l*	1.2592	0.006298	0.05885	776.7348	778.7781	-	1556.8372
12	Vent	62.59	1.100	*g*	1.1780	0.05772	0.006060	6.9995	0.04676		8.2880
13	Methanol Product	62.59	1.100	*l*	0.08120	0.001132	0.0002374	768.9674	11.6276	-	780.6776
14	Distillation Bottoms	111.2	1.500	*l*	-	-	-	0.7679	767.1038	-	767.8716
14B	Wastewater	42.71	1.810	*l*	-	-	-	0.7679	767.1038	-	767.8716

* *l*: liquid; *g*: gas.

outcome of the plant. The effect on %ROI and the selling price of methanol (SPM) for 0%ROI is shown in Fig. 5 and Fig. 6, respectively. Figs. S1 and S2 in the electronic supplement, on the other hand, show the effect on NP and PBP, respectively. In each case, as expected, with a decrease in the price of feed material, profitability is increased, and the payback period and SPM for 0%ROI are decreased. Additionally, it can be noticed that within the ranges of study, the effect is more pronounced for changes in CO_2 and H_2 prices than for changes in the prices of fuel and catalyst. Clearly, the price of H_2 is the biggest factor in defining the profitability of the process. Mathematical relationships were also developed for the graphical curves of Figs. 5, 6, S1, and S2 and reported along with the data in the figures.

Two generalized correlations that combine the effects of the price of each of CO_2, H_2, NG, and catalyst on %ROI and methanol selling price for 0%ROI were also developed as shown in Eqs. (6) and (7), respectively. For each relationship, 40 data points of Figs. 5, 6, S1, and S2 were employed, and SSE was used as the objective function to be minimized. The value of SSE for developing Eq. 6 was 8.78×10^{-5} while it was 3.61×10^{-8} for Eq. (7).

$$\%ROI|_{SPM=\$1.5} = 150.9111 - 417.9215C_{CO2} - 57.1016C_{H2} - 1.0137C_{NG} - 0.1510C_{Cat} \quad (6)$$

$$SPM|_{0\%ROI} = 0.3819 + 3.0964C_{CO2} + 0.4231C_{H2} + 0.007506C_{NG} + 0.001119C_{Cat} \quad (7)$$

where, C_i is the cost or price of the ith feed material.

Eq. 6 and Eq. 7 can be utilized for calculating %ROI and SPM for 0%ROI for any combination of costs of feed materials discussed above. For example, by halving the H_2 price ($0.75) which is expected in the near future [51], and keeping all the other costs as such, %ROI is increased from 29.11 to 71.94 and SPM for 0%ROI decreased from $1.28 to $0.97. If in addition, the energy cost is used as $3.0/MMBtu, %ROI rises to 76.30 and SPM for 0%ROI declines to $0.93/kg. Furthermore, if the price of CO_2 is reduced to zero as if part of the CO_2 meant for sequestration is routed for methanol synthesis, then %ROI and SPM for 0%ROI, respectively, are calculated as 95.98 and $0.79/kg.

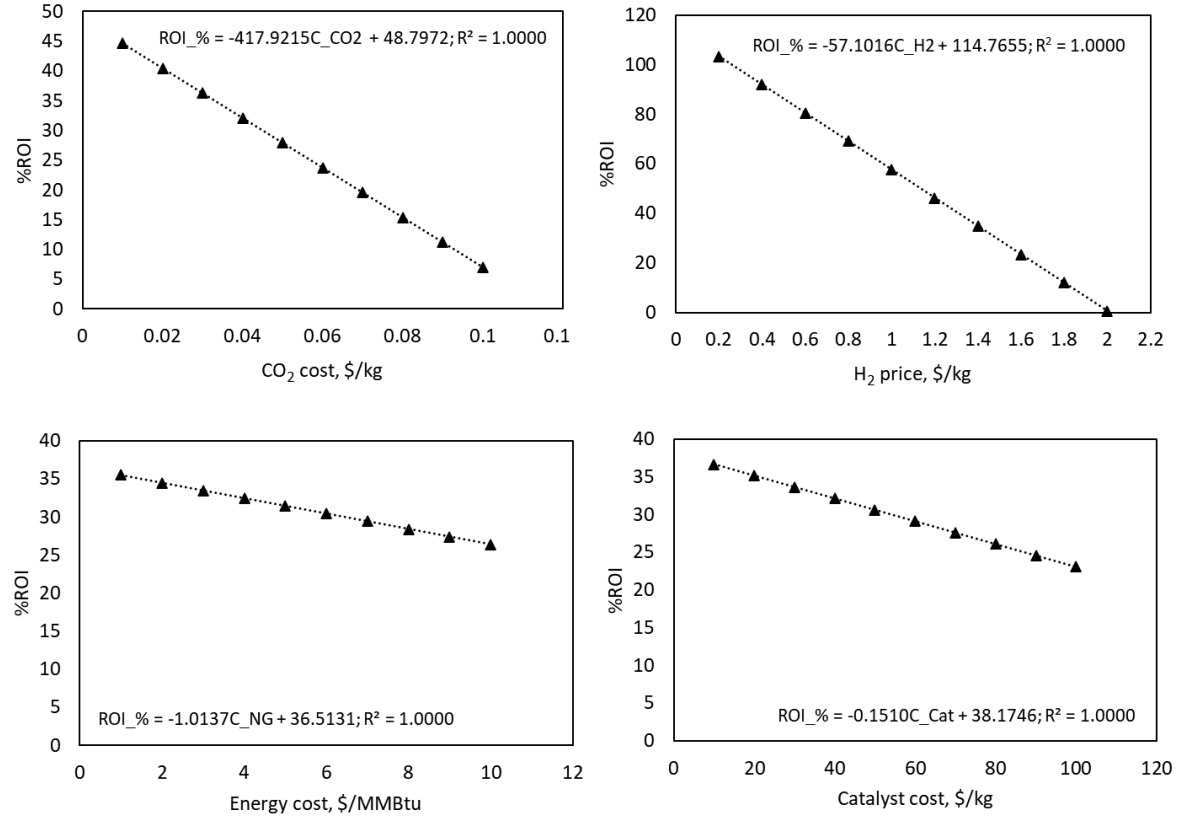

Figure 5. Effect of variation in costs of CO_2, H_2, energy (NG), and catalyst on %ROI. When not varying in the above relationships, the costs were fixed at \$0.0471/kg CO_2, \$1.5/kg H_2, \$7.3/MMBtu energy (NG), and \$60/kg catalyst.

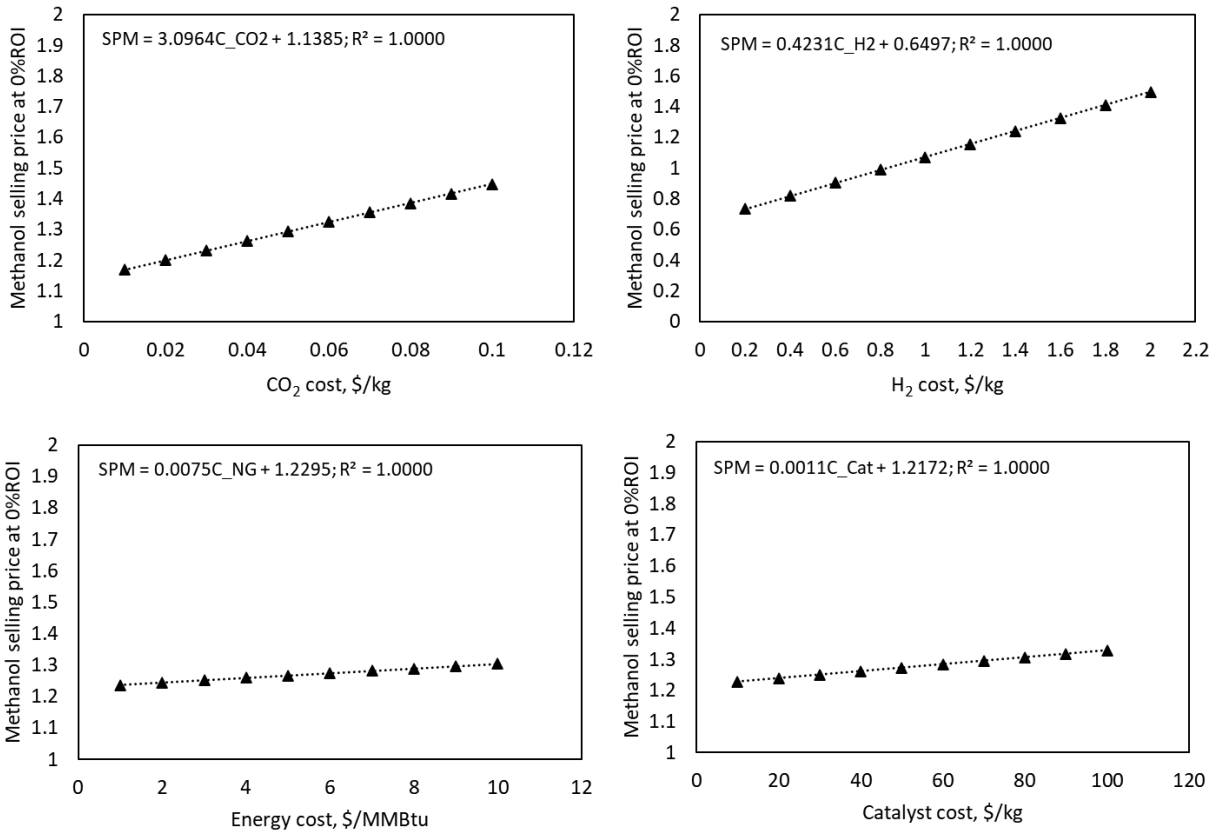

Figure 6. Effect of variation in costs of CO_2, H_2, energy (NG), and catalyst on the selling price of methanol for 0% ROI. When not varying in the above relationships, the costs were fixed at \$0.0471/kg CO_2, \$1.5/kg H_2, \$7.3/MMBtu energy (NG), and \$60/kg catalyst.

Comparing the market value of methanol taken as \$0.53/kg [52], the process studied in the present work is found economically unfavorable unless the price of both CO_2 and H_2 is decreased to a very low value. As an example, if the cost of CO_2 is kept at \$0.01/kg and the cost of H_2 at \$0.06/kg for an energy cost of \$3/MMBtu, the selling price of methanol becomes less than \$0.53/kg. However, in line with the aims of CO_2 mitigation, while exploiting the valuable chemical content of CO_2, the proposed process has the potential to be used for further research that may lead it to commercial realization.

CONCLUSION

The process flow scheme for the direct CO_2 hydrogenation to methanol was conceptualized and simulated. The incorporation of gas recycling greatly benefited the process and a 760% increase in ROI was observed when a recycle stream with a recycle ratio of 3.92 was introduced in the simplified base case. For improving the separation of light gases, a simple low-pressure VLE separator yielded a more cost-effective solution than using a gas absorption system or a stabilizer. The reactor cooling with boiler feed water leading to steam generation was proved to be an economically better approach than cooling with cooling water. The recycling ratio had a huge impact on the economic performance of the plant. The net profit first increased and then decreased with an increase in the recycling ratio. An optimum recycle ratio was worked out and calculated as 4.30. Comparing the effect of the prices of CO_2, H_2, NG, and catalyst, the price of green hydrogen has exhibited the biggest effect on the profitability of the process. The study indicates that each year 294 kilotonnes of CO_2 would be successfully abated and in addition, 209 kilotonnes of methanol would be produced that could be traded to generate a large sum of capital.

ABBREVIATIONS

bfw	Boiler feed water
cw	Cooling water
hps	High-pressure steam
lps	Low-pressure steam
HP	High pressure
ID	Internal diameter
LP	Low pressure
MTG	Methanol to gasoline
MTO	Methanol to olefins
NG	Natural gas
NP	Net profit
NRTL	Non-random two-liquid
OD	Outer diameter
PBP	Payback period
RCR	Recycle ratio
ROI	Return on investment
SPM	Selling price of methanol
SR	Split ratio
SRK	Soave-Redlich-Kwong
SSE	Sum of squares of the errors
TCI	Total capital investment
TPC	Total product cost
VLE	Vapor-liquid equilibrium

REFERENCES

[1] BP, bp Statistical Review of World Energy 2022, Seventy-first ed., 2022. https://www.bp.com/en/global/corporate/energy-economics/statistical-review-of-world-energy.html.

[2] Z. Liu, Z. Deng, S.J. Davis, C. Giron, P. Ciais, Nat. Rev. Earth Environ. 3 (2022) 217–219. https://doi.org/10.1038/s43017-022-00285-w.

[3] Y. Gao, X. Gao, X., Zhang, Engineering 3 (2017) 272–278. http://dx.doi.org/10.1016/J.ENG.2017.01.022.

[4] G.A. Olah, Angew. Chem. Int. 44 (2005) 2636–2639. https://doi.org/10.1002/anie.200462121.

[5] U.J. Etim, Y. Song, Z. Zhong, Front. Energy Res. (2020) 545431. https://doi.org/10.3389/fenrg.2020.545431.

[6] M. Behrens, F. Studt, I. Kasatkin, S. Kühl, M. Hävecker, F. Abil-Pedersen et al., Science 336 (2012) 893–897. https://doi.org/10.1126/science.1219831.

[7] K. Stangeland, H. Li, Z. Yu, Energy, Ecol. Environ 5 (2020) 272–285. https://doi.org/10.1007/s40974-020-00156-4.

[8] D.S. Marlin, E. Sarron, Ö. Sigurbjörnsson, Front. Chem. 6 (2018) 446. https://doi.org/10.3389/fchem.2018.00446.

[9] M. Bukhtiyarova, T. Lunkenbein, K. Kähler, R. Schlögl, Catal. Lett. 147 (2017) 416–427. https://doi.org/10.1007/s10562-016-1960-x.

[10] E.S. Van-Dal, C. Bouallou, J. Clean. Prod. 57 (2013) 38–45. https://doi.org/10.1016/j.jclepro.2013.06.008.

[11] M. Matzen, M. Alhajji, Y. Demirel, Energy 93 (2015) 343–353. https://doi.org/10.1016/j.energy.2015.09.043.

[12] M. Pérez-Fortes, J.C. Schöneberger, A. Boulamanti, E. Tzimas, Appl. Energy 161 (2016) 718–732. https://doi.org/10.2790/89238.

[13] I.L. Wiesberg, J.L. de Medeiros, R.M.B. Alves, P.L.A. Coutinho, O.Q.F. Araújo, Energy Convers. Manage. 125 (2016) 320–335. http://doi.org/10.1016/j.enconman.2016.04.041.

[14] P. Borisut, A. Nuchitprasittichai, Front. Energy Res. 7 (2019) 81. https://doi.org/10.3389/fenrg.2019.00081.

[15] A.A. Kiss, J.J. Pragt, H.J. Vos, G. Bargeman, M.T. de Groot, Chem. Eng. J. 284 (2016) 260–269. https://doi.org/10.1016/j.cej.2015.08.101.

[16] K. Roh, R. Frauzem, R. Gani, J.H. Lee, Chem. Eng. Res. Des. 116 (2016) 27–47. http://dx.doi.org/10.1016/j.cherd.2016.10.007.

[17] M. Martín, I.E. Grossmann, Comput. Chem. Eng. 105 (2017) 308–316. https://doi.org/10.1016/j.compchemeng.2016.11.030.

[18] S. Alsayegh, J.R. Johnson, B. Ohs, M. Wessling, J. Clean. Prod. 208 (2018) 1446–1458.

https://doi.org/10.1016/j.jclepro.2018.10.132.

[19] S. Szima, C.C. Cormos, J. CO_2 Utilization 24 (2018) 555–563. https://doi.org/10.1016/j.jcou.2018.02.007.

[20] N. Meunier, R. Chauvy, S. Mouhoubi, D. Thomas, G. De Weireld, Renewable Energy 146 (2020) 1192–1203. https://doi.org/10.1016/j.renene.2019.07.010.

[21] T.B.H. Nguyen, E. Zondervan, J. CO_2 Util. 34 (2019) 1–11. https://doi.org/10.1016/j.jcou.2019.05.033.

[22] H.W. Lee, K. Kyeongsu, J. An, J. Na, H. Kim, H. Lee, U. Lee, Energy Res. 44 (2020) 8781–8798. https://doi.org/10.1002/er.5573.

[23] B.L.de O. Campos, K. John, P. Beeskow, K.H. Herrera Delgado, S. Pitter, N. Dahmen, et al., Processes 10 (2022) 1535. https://doi.org/10.3390/pr10081535.

[24] T. Cordero-Lanzac, A. Ramirez, A. Navajas, L. Gevers, S. Brunialti, L.M. Gandía, et al. J. Energy Chem. 68 (2022) 255–266. https://doi.org/10.1016/j.jechem.2021.09.045.

[25] M. Yousaf, A. Mahmood, A. Elkamel, M. Rizwan, M. Zaman, Int. J. Greenhouse Gas Control 115 (2022) 103615. https://doi.org/10.1016/j.ijggc.2022.103615.

[26] F. Haghighatjoo, M.R. Rahimpour, M. Farsi, Chem. Eng. Process. 184 (2023) 109264. https://doi.org/10.1016/j.cep.2023.109264.

[27] H.H. Chiou, C-J. Lee, B-S. Wen, J-X. Lin, C-L Chen, B.Y Yu, Fuel 343 (2023) 127856. https://doi.org/10.1016/j.fuel.2023.127856.

[28] J.M. Douglas, Conceptual Design of Chemical Processes, McGraw-Hill, New York (1988). ISBN-13: 978-0071001953.

[29] Mitsubishi Power, Gas Turbine Combined Cycle (GTCC) Power Plants. https://power.mhi.com/products/gtcc [accessed 01 August 2023].

[30] M.A. Sheikh, Renewable Sustainable Energy Rev. 13 (2009) 2696–2702. http://doi.org/10.1016/j.rser.2009.06.029.

[31] W.A. Poe, S. Mokhatab, Modeling, Control, and Optimization of Natural Gas Processing Plants, Gulf Professional Pub., New York (2017). https://doi.org/10.1016/C2014-0-03765-3.

[32] S.O. Akpasi, Y.M. Isa, Atmosphere 13 (2022) 1958. https://doi.org/10.3390/atmos13121958.

[33] S.S. Kumar, V. Himabindu, Mater. Sci. Energy. Technol. 2 (2019) 442–454. https://doi.org/10.1016/j.mset.2019.03.002.

[34] S. Lipiäinen, K. Lipiäinen, A. Ahola A., E. Vakkilainen, Int. J. Hydrogen Energy (2023). https://doi.org/10.1016/j.ijhydene.2023.04.283.

[35] G. Leonzio, E. Zondervan, P.U. Foscolo, Int. J. Hydrogen Energy 44 (2019) 7915–7933. https://doi.org/10.1016/j.ijhydene.2019.02.056.

[36] J. Zhang, Z. Li, Z. Zhang, R. Liu, B. Chu, B. Yan, ACS Sustainable Chem. Eng. 8 (2020) 49. https://doi.org/10.1021/acssuschemeng.0c06336.

[37] M.R. Usman, Z. Shahid, M.S. Akram, R. Aslam, Int. J. Thermophys. (2020) 41:44. https://doi.org/10.1007/s10765-020-2622-1.

[38] F. Arena, G. Mezzatesta, G. Zafarana, G. Trunfio, F. Frusteri, L. Spadaro, J. Catal. 30 (2013) 141–151. https://doi.org/10.1016/j.jcat.2012.12.019.

[39] C. Yang, Z. Ma, N. Zhao, W. Wei, T. Hu, Y. Sun, Catal. Today 115 (2006) 222–227. https://doi.org/10.1016/j.cattod.2006.02.077.

[40] M.S. Peters, K.D. Timmerhaus, R.E. West, Plant Design and Economics for Chemical Engineers, fifth ed., McGraw-Hill, New York (2003). ISBN-13: 978-0071240444.

[41] W.D. Seider, D.R. Lewin, J.D. Seader, S. Widagdo, R. Gani, K.M. NG, Product and Process Design Principles: Synthesis, Analysis, and Evaluation, fourth ed., John Wiley & Sons, Inc. (2017). ISBN: 978-1119282631.

[42] Y. Feng, G.P. Rangaiah, Chem. Eng. August (2011) 22–29. https://www.chemengonline.com/evaluating-capital-cost-estimation-programs-2/?printmode=1.

[43] R. Sinnott, G. Towler, Chemical Engineering Design, sixth ed., Butterworth-Heinemann (2020). ISBN: 978-0081025994.

[44] C.R. Branan, Rules of Thumb for Chemical Engineers, fourth ed., Gulf Professional Pub., New York (2005). https://doi.org/10.1016/B978-0-7506-7856-8.X5000-2.

[45] R.N. Watkins, Hydrocarbon Process. 46 (1967) 253–256. https://dokumen.tips/documents/watkins-r-n-sizing-separators-and-accumulators-hydrocarbon-processing.html?page=1.

[46] P.C. Wankat, Separation Process Engineering: Includes Mass Transfer Analysis, third ed., Pearson Education, Inc., New York (2012). ISBN: 978-0131382275.

[47] G.D. Ulrich, P.T. Vasudevan, Chem. Eng. April (2006). https://www.chemengonline.com/articles.php?file=2006%2FEng%2FEng04012006_07.html.

[48] B. Bane, Cheaper carbon capture is on the way. PNNL, March 2021. https://www.pnnl.gov/news-media/cheaper-carbon-capture-way [accessed 11 August 2023].

[49] S.R. Bhagwat, M. Olczak, Green hydrogen bridging the energy transition in Africa and Europe. European University Institute (2020). https://africa-eu-energy-partnership.org/publications/green-hydrogen-bridging-the-energy-transition-in-africa-europe/.

[50] Markets Energy, https://www.bloomberg.com/energy [accessed 16 April 2022].

[51] C. Bettenhausen, Chem. Eng. News 101 (2023). https://cen.acs.org/materials/electronic-materials/Electrolyzers-tools-turn-hydrogen-green/101/i21 [accessed 20 January 2024].

[52] ChemAnalyst, Methanol Price Trend and Forecast. https://www.chemanalyst.com/Pricing-data/methanol-1 [accessed 11 August 2023].

SAMAN KHAWAJA[1,2]
MUHAMMAD RASHID USMAN[1,3]
RABYA ASLAM[1]

[1]Institute of Chemical Engineering and Technology, University of Punjab, New Campus, Lahore, Pakistan

[2]School of Chemical Engineering, Minhaj University Lahore,Civic Center, Twp, Lahore, Pakistan

[3]Engineering Research Centre, University of Punjab, New Campus, Lahore, Pakistan

NAUČNI RAD

KONCEPTUALIZACIJA I SIMULACIJA PROCESA POSTROJENJA ZA PROIZVODNJU METANOLA NA BAZI CO_2

Ova studija konceptualizuje i simulira proces proizvodnje metanola kroz direktnu hidrogenaciju uhvaćenog CO_2. $CuO/ZnO/ZrO_2$ je korišćen kao katalizator, a Aspen HYSYS je korišćen za simulaciju procesa. Konfiguraciona optimizacija toka procesa je sprovedena korišćenjem hijerarhijskog pristupa korak po korak. Dobijeni su mnogi alternativni tokovi i izračunate su njihove kapitalne investicije, cena proizvoda i profitabilnost. Diskriminacija među konkurentnim tokovima je izvršena na osnovu neto dobiti i procenta povraćaja investicije. Zadržana šema toka je dalje analizirana radi optimizacije odnosa reciklaže i procene uticaja cene uhvaćenog CO_2, zelenog H_2, prirodnog gasa (goriva) i katalizatora na ekonomske performanse postrojenja. Izračunata optimalna vrednost odnosa reciklaže je 4,23. Pored toga, utvrđeno je da je cena H_2 najvažniji parametar u definisanju izvodljivosti i isplativosti procesa. Razvijene su i matematičke korelacije koje povezuju isplativost i cenu gore navedenih sirovina.

Ključne reči: hvatanje CO_2, iskorišćenje CO_2, ekonomija metanola, CO_2 hidrogenacija, $CuO/ZnO/ZrO_2$ katalizator.

CI&CEQ
Chemical Industry & Chemical Engineering Quarterly

Available online at
Association of the Chemical Engineers of Serbia AChE
www.ache.org.rs/CICEQ

Chem. Ind. Chem. Eng. Q. 30 (4) 325–333 (2024) CI&CEQ

GOLDEN STEPHA NALLATHAMBI[1]
BHARATHI GOWRI SASI KUMAR[2]
GUVVA SWATHY[3]

[1]Department of Mathematics, R.M.K Engineering College, India
[2]Department of Mathematics, Ethiraj College for Women, India
[3]Mathematics Department, S. A. Engineering College, India

THE MAGNETOHYDRODYNAMIC WILLIAMSON FLUID FLOW ON AN EXTENDING SHEET WITH THERMOPHORESIS AND CHEMICAL REACTION

Article Highlights

- Non-linear system of Partial differential equations
- MATLAB bvp4c solver is used
- Examines velocity, temperature, and concentration distribution of Williamson fluid
- Chemical reaction, thermophores, and magnetic field parameters are analyzed

Abstract

This research investigates the steady, two-dimensional, incompressible flow of a pseudoplastic Williamson fluid subjected to a linearly stretched sheet. The study incorporates the effects of magnetic fields, chemical reactions, and thermophoresis on fluid behavior. By applying boundary layer techniques and similarity transformations, the governing equations are simplified for numerical analysis. The MATLAB bvp4c solver is employed to solve the reduced equations. The obtained results are visually represented and thoroughly discussed to comprehend the model's physical characteristics. The investigation highlights the magnetic field's influence, chemical reaction, and impact of thermophoresis particle deposition on the flow behavior of Williamson fluid over the extended sheet. Moreover, significant roles are found for chemical reactions and thermophoresis parameters in determining the fluid concentration near the boundary layer. It is observed that an increase in the chemical reactions and thermophoresis parameters results in a reduced thickness of the fluid concentration near the boundary layer. Notably, an increase in Schmidt value also diminished the thickness of the fluid concentration close to the boundary layer. The magnetohydrodynamic parameter significantly influences the fluid's velocity and temperature near the surface. It has been noted that an increase in the magnetohydrodynamic parameter decreases the fluid's velocity and increases the temperature near the surface. The impact of skin friction coefficient and Nusselt number and the impact of mass transfer coefficient on Williamson fluid will be discussed. The findings acquired are examined in relation to existing research and the correlation is provided as a table.

Keywords: Williamson fluid, magnetohydrodynamics, chemical reaction, thermophoresis.

SCIENTIFIC PAPER

UDC 544.33.03:66

Pseudoplastic fluids are commonly encountered in various applications and industries, making their boundary layer flow an area of significant research interest. Numerous models have been proposed to characterize the behaviour of pseudoplastic fluids; however, the Williamson fluid model has received relatively limited attention. In 1929, Williamson [1] conducted pioneering research on the flow of pseudoplastic materials. He suggested a model equation to explain pseudoplastic fluid flow and

Correspondence: G.S. Nallathambi, Department of Mathematics, R.M.K Engineering College, India.
E-mail: ngs.sh@rmkec.ac.in
Paper received: 28 September, 2023
Paper revised: 20 January, 2024
Paper accepted: 24 February, 2024

https://doi.org/10.2298/CICEQ230928005N

validated the conclusions through empirical data analysis. Despite its potential significance, the Williamson fluid model remains an underexplored aspect of pseudoplastic fluid dynamics.

In the realm of boundary layer flow, pioneering research was conducted by Sakiadis [2] on a continuously stretched surface, where he created the fundamental equations for boundary layers in two dimensions. Subsequently, Tou *et al.* [3] examined how transfer processes affect boundary layer flow on a stretching surface in depth. Erickson *et al.* [4] expanded the study to include the impacts of mass transfer, taking into account both injection and suction.

Nadeem *et al.* [5] explored the intriguing Williamson fluid behavior on a stretched sheet, revealing that as the Williamson parameter increased, velocity profiles and skin friction coefficient deteriorated. Continuing this investigation, Hayat *et al.* [6] delved into the complexities of Williamson fluid flow across a stretched surface with a magnetic field, heat radiation, and an electric field. Their findings indicated that greater values of the Williamson parameter resulted in a reduction in the wall shear stress.

Shawky *et al.* [7] brought a new perspective by analyzing the movement of a non-Newtonian fluid under the influence of a magnetic field over an extended porous sheet. They observed that when the Williamson and porosity parameters increased, the rate of heat transfer to the expanded surface significantly increased. These studies collectively shed light on the intricate dynamics of pseudoplastic fluids like Williamson fluid in various boundary layer flow scenarios, offering valuable insights for practical applications in industry and engineering. In the realm of Williamson fluid dynamics, Hussain [8] conducted a comprehensive study on the influence of nanoparticles on Williamson fluid flow over a stretching sheet. The findings revealed that various physical parameters significantly impacted heat transfer near the wall, while their effects were nearly negligible farther away from the wall.

Further exploring the characteristics of Williamson nanofluids, Nadeem and Hussain [9] investigated Williamson nanofluid magnetohydrodynamic (MHD) flow over a heated surface. Notably, they discovered that the Williamson fluid's conductivity was lower than that of Williamson nanofluid., emphasizing the importance of considering nanoparticle additives for enhanced thermal performance. Delving into the complexities of Williamson nanofluids' boundary layer stream, Kebede *et al.* [10] analyzed its stability and revealed that the velocity profile decreased as a function of various parameters, including Williamson, porosity, unsteadiness, and magnetic field parameters. These studies collectively provide valuable insights into the behavior of Williamson nanofluids, paving the way for potential applications in heat transfer and fluid dynamics research.

Numerous researchers have contributed to the understanding of the progress of boundary layers on surfaces that are linearly stretched [11–13]. Kumaran and Ramanaiah [14] investigated viscous fluid flow over a stretching surface with quadratic stretching, obtaining closed-form solutions. Ali [15] examined the thermal boundary layer's response to temperature changes and power law stretching. Elbashbeshy[16] talked about how viscous fluid flows and transfers heat under exponential stretching conditions.

By including viscous dissipation and elastic deformation, Sanjayanand and Khan [17] expanded the study to consider heat and mass transmission of viscoelastic fluid. A numerical solution for the heat and mass transfer of a viscous fluid over an exponentially extending surface was created by Magyari and Keller [18]. In their examination of the thermal radiation impacts of Jeffery fluid over an exponentially extending surface, Nadeem *et al.* [19] compared the numerical and homotopy analysis method (HAM) results. More recently, Nadeem and Lee [20] investigated the impact of nanoparticles on the exponentially stretched boundary layer flow of viscous fluid.

Numerous processes also depend on the analysis of integrated heat and mass transfer associated with chemical reactions including radioactive waste geo-repositories, packed bed chemical reactors, and heat exchangers used to cool electronic circuits. Chemical concentration is examined by numerous scholars [21–23].

The MHD flow over a stretching sheet has abundant industrial and manufacturing applications, which include polymer extrusion, continuous casting of metals, petroleum industries, and electrical power generators. Due to its large-scale applications, many researchers attempted to study and analyze the solutions of differential equations describing boundary layer and MHD fluid flow problems along a stretching sheet. Mohammed Ismail *et al.*[24] addressed the effect of thermal radiation on MHD hybrid nanofluid flow over a stretching cylinder immersed in a porous medium and discussed the various physical properties. They further extended the work in the investigation of numerically solving the heat transfer enhancement due to the radiative magnetohydrodynamics flow of a hybrid nanofluid past a porous stretching cylinder under the influence of variable viscosity as well as suction [25]. Subsequently, SM Ismail *et al.* [26] have analyzed the MHD flow of an aqueous ethylene glycol nanofluid past

a two-way exponentially extending lamina where appropriate transformation is used, thereby the temperature and velocity sketches of copper alumina in aqueous glycol nanofluid for current physical stratum are obtained.

The thermophoresis phenomenon is essential in many practical applications including the removal of small particles from gas streams, aerosol technology, deposition of silicon thin films, and radioactive particle deposition in nuclear reactor safety simulations. Several studies discussed the impact of thermophoresis particle deposition in the literature [27–28].

Williamson fluid over a continuously moving surface is often encountered in engineering such as polymer processing industries, paint and coatings manufacturing, food processing, inkjet printing, wastewater treatment, etc. Understanding the rheological properties of Williamson fluid is crucial in these engineering applications to optimize processes, ensure proper functionality, and achieve desired product characteristics.

In the current work, we focus on the mass and heat transfer analysis of Williamson fluid over a linearly stretching sheet, leveraging the Williamson fluid model, while considering the influence of a magnetic field, chemical reaction, and thermophoresis. By employing suitable similarity transformations, we simplify the governing boundary layer equations. The resulting equations are solved using numerical methods, and the outcomes are presented through graphs, offering valuable insights into the behavior of the Williamson fluid under linearly stretching conditions.

PROBLEM FORMULATION

Consider the Williamson fluid model, which is incompressible, steady, and capable of mass transfer while flowing over a linearly stretched sheet in two dimensions in the presence of the following physical properties: chemical reaction, thermophoresis, MHD, viscous dissipation.

The equations represent a comprehensive system that describes the conservation of mass, momentum, energy, and concentration for the Williamson fluid flow over the linearly stretched sheet, considering the effects of chemical reaction, thermophoresis, and magneto-hydrodynamics are [6,29].

$$\frac{\partial u}{\partial x}+\frac{\partial u}{\partial y}=0 \tag{1}$$

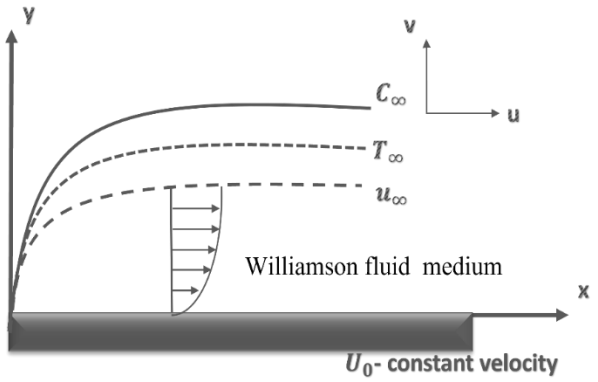

Figure 1. Schematic diagram.

$$u\frac{\partial u}{\partial x}+v\frac{\partial u}{\partial y}=v\frac{\partial^2 u}{\partial y^2}+\sqrt{2}v\Gamma\frac{\partial u}{\partial y}\frac{\partial^2 u}{\partial y^2}-\left(\frac{\sigma B^2(x)}{\rho c_p}\right)u \tag{2}$$

$$u\frac{\partial T}{\partial x}+v\frac{\partial T}{\partial y}=\frac{k}{\rho c_p}\left(\frac{\partial^2 T}{\partial y^2}\right)+\frac{v}{c_p}\left(\frac{\partial u}{\partial y}\right)^2-\left(\frac{\sigma B^2(x)}{\rho c_p}\right)u^2 \tag{3}$$

$$u\frac{\partial C}{\partial x}+v\frac{\partial C}{\partial y}=D\frac{\partial^2 C}{\partial y^2}-R_C(C-C_\infty)-\frac{\partial}{\partial y}\left(V_T(C-C_\infty)\right) \tag{4}$$

where the magnetic conduction is $B(x)=\frac{B_0}{\sqrt{2x}}$.

Because of the magnetic conduction, Eqs. (2) and (3) becomes:

$$u\frac{\partial u}{\partial x}+v\frac{\partial u}{\partial y}=v\frac{\partial^2 u}{\partial y^2}+\sqrt{2}v\Gamma\frac{\partial u}{\partial y}\frac{\partial^2 u}{\partial y^2}-\left(\frac{\sigma B_0^2}{\rho 2xc_p}\right)u \tag{5}$$

$$u\frac{\partial T}{\partial x}+v\frac{\partial T}{\partial y}=\frac{k}{\rho c_p}\left(\frac{\partial^2 T}{\partial y^2}\right)+\frac{v}{c_p}\left(\frac{\partial u}{\partial y}\right)^2-\left(\frac{\sigma B_0^2}{\rho 2xc_p}\right)u^2 \tag{6}$$

Subject to the boundary conditions:

$$\begin{aligned}&u=U_0, T=T_W, C=C_W \ \ at\ \ y=0\\&u=0, T=T_\infty, C=C_\infty \ \ at\ \ y\to\infty\end{aligned} \tag{7}$$

where the velocities along the x and y axes are denoted by u and v respectively. v is the kinematic velocity.

By using the following similarity transformations [6,27]:

$$\eta=y\sqrt{\frac{U_0}{2\gamma x}},\ \psi=\sqrt{2\gamma U_0 x}f(\eta),\ \psi-\ \text{stream function}$$

$$\begin{aligned}&u=\frac{\partial\psi}{\partial y}, v=-\frac{\partial\psi}{\partial x}\\&u=U_0 f'(\eta), v=-\frac{1}{2}\sqrt{\frac{2U_0\gamma}{x}}f+\frac{1}{2}\frac{U_0 y}{x}f'\\&T=(T_w-T_\infty)\theta(\eta)+T_\infty\\&C=(C_w-C_\infty)\varphi(\eta)+C_\infty\end{aligned} \tag{8}$$

Substituting Eq. (8) in Eq. (1), which is satisfied identically. After applying the above similarity

transformations, Equations (2–4) becomes:

$$f'''+\lambda f''f'''+ff''-Mf'=0 \quad (9)$$

$$\theta''+P_r\theta' f+P_r E_c f''+\mathrm{MP}_r E_c f'^2=0 \quad (10)$$

$$\varphi''+\mathrm{Sc}\left(f\varphi'+\mathrm{R}\varphi-\mathrm{T}_V\theta''\right)=0 \quad (11)$$

corresponding boundary conditions are:

$$\begin{aligned} &f'(0)=1,\ \theta(0)=1,\ \phi'(0)=1 \\ &f'(\infty)=0,\ \theta(\infty)=0,\ \phi'(\infty)=0 \end{aligned} \quad (12)$$

where,

Magnetic Parameter $= M=\dfrac{\sigma B_0^2}{\rho U_0}$,

Prandl Number $= P_r=\dfrac{\rho C_p \nu}{k}=\dfrac{\mu C_p}{k}$,

Eckert Number $= E_c=\dfrac{U_0^2}{C_p\left(T_w-T_\infty\right)}$,

Schmidt Number $= \mathcal{S}_c=\dfrac{\nu}{D}$,

Williamson Dimensionless Parameter $= \lambda=\dfrac{\Gamma}{\nu}\sqrt{\dfrac{U_0^3}{2x}}$

Chemical reaction parameter $R=-Rc\left(\dfrac{2x}{U_0}\right)$

Thermophoretic parameter $T_V=-\dfrac{k_T\left(T_W-T_\infty\right)}{T_\infty}$

The interesting physical parameters are the local skin-friction coefficient, the local Nusselt number, and the local Sherwood number which can be defined as follows [30]:

$$C_f=\frac{\tau_W}{\rho U_0^2},\ NU_x=\frac{xq_W}{k\left(T_W-T_\infty\right)},\ Sh_x=\frac{xq_M}{D\left(C_W-C_\infty\right)},$$

where $\tau_W=\mu\left[\dfrac{\partial u}{\partial y}+\dfrac{\Gamma}{\sqrt{2}}\left(\dfrac{\partial u}{\partial y}\right)^2\right]_{y=0}$, $q_W(x)=\left[-k\dfrac{\partial T}{\partial y}\right]_{y=0}$.

Using the similarity variable, we get:

$$\sqrt{2}C_f\,\mathrm{Re}_x^{1/2}=\left[f''(0)+\frac{\lambda}{2}\left(f''(0)\right)^2\right],\ NU_x\,\mathrm{Re}_x^{-1/2}=\frac{-\theta'(0)}{\sqrt{2}}$$

$$Sh_x\,\mathrm{Re}_x^{-1/2}=\frac{-\varphi'(0)}{\sqrt{2}}.$$

METHOD OF SOLUTION

The collection of non-linear partial differential equations Eqs. (2–4) were transformed into the ordinarily differentiable Eqs. (8–10) by using similarity transformation for the proposed parameter *Pr*, *M*, *Sc*, *Ec*, *λ*, *R*, *Tv*. Further, the equations Eqs. (8–10) are converted to first-order equations as follows:

$$f(1)=f,\ f(2)=f',\ f(3)=f'',\ f(4)=\theta,\ f(5)=\theta',$$
$$f(6)=\varphi,\ f(7)=\varphi',$$

and Eqs. (8–10), have been written as:

$$f'=\mathrm{f}(2)$$

$$f'''=\left(1/\left(1+\lambda * f(3)\right)\right)*\begin{pmatrix}\left(f(2)*f(2)\right)-\\ f(1)*f(3)\end{pmatrix}+M*f(2)$$

$$\theta'=\mathrm{f}(5)$$

$$\theta''=-\left(\mathrm{Pr}*f(1)*f(5)\right)-Ec*\mathrm{Pr}*f(3)*f(3)-M*\mathrm{Pr}*\mathrm{Ec}*f(2)*f(2)$$

$$\varphi'=\mathrm{f}(7)$$

$$\varphi''=-Sc*f(1)*f(7)-Sc*R*f(6)+\left(Tv*Sc*\begin{pmatrix}-\left(\mathrm{Pr}*f(1)*f(5)\right)\\ -Ec*\mathrm{Pr}*f(3)-\\ M*\mathrm{Pr}*\mathrm{Ec}*f(2)*f(2)\end{pmatrix}\right)$$

The bvp4c solver in MATLAB is employed to obtain numerical solutions for the above system. By analyzing graphical representations of fluctuations, we can investigate the influence of different parameters in the governing differential equations on the flow behavior. The problem involves essential dimensionless parameters like Prandtl number, Schmidt number, Eckert number, magnetic parameter, thermophoretic parameter, and chemical reaction parameter. A comprehensive examination of how various physical factors impact the velocity, concentration, and temperature of the fluid in close vicinity to the surface is obtained from these numerical solutions. The heat transfer parameter *-Θ'(0)* and mass transfer parameter -ϕ'*(0)* are also compared with [31] to evaluate the accuracy of our technique, and they agree very well with it. The association is provided in Table 1.

Table 1. Comparison value of -Θ'(0) and - ϕ'(0) for different Pr & Sc at λ= 0, R=0.0, M= 0, Ec = 0.

f(0)	Pr or Sc	[31] *-Θ'(0)* or -ϕ'*(0)*	Present Value *-Θ'(0)* or -ϕ'*(0)*
0	1	0.4439	0.4473
	10	1.680	1.6819
	100	5.545	5.5432

RESULTS AND DISCUSSION

The solution to the aforementioned problem is

illustrated by several graphs, each of which shows the outcomes for various parameter value sets. These values of the parameters set are taken from the earlier literature [4,5,32–35]. These graphs provide an extensive overview of the outcomes of computations. The relevant parameters including the Prandtl number, Schmidt number, Eckert number, magnetic parameter, thermophoretic parameter, and chemical reaction parameter are considered for the analysis.

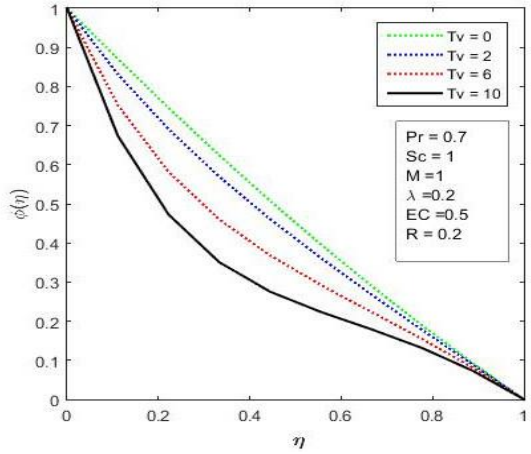

Figure 2. Concentration profile for different values of Tv.

Figure 2 highlights the effect of thermophoresis on the concentration profile. It has been noted that as the thermophoretic parameter increases, the thickness of the concentration at the boundary decreases. As the thermophoretic parameter increases, the thermophoretic force becomes stronger. Consequently, the fluid particles with higher concentration move towards regions of lower temperature, and those with lower concentration move towards regions of higher temperature. This migration of species leads to a reduction in the overall concentration profile. This behavior is clearly explained in Figure 2.

Figure 3 shows that the concentration profile is decreasing for an increasing value of the Schmidt number. When the Schmidt number increases, it implies that molecular diffusivity becomes less effective compared to momentum diffusivity. In other words, momentum transfer dominates over mass transfer. This has a significant impact on the concentration profile within the fluid. Consequently, the concentration gradients in the fluid become less pronounced, leading to a decreasing concentration profile.

Figure 4 shows that the concentration profile is decreasing for an increasing value of the chemical reaction parameter. As the chemical reaction rate increases, it leads to a faster conversion of the reactants into products. In a flow or medium, this results in a depletion of the species concentration as they are consumed more rapidly due to the increased chemical reaction rate. As a consequence, the overall concentration profile decreases along the flow direction.

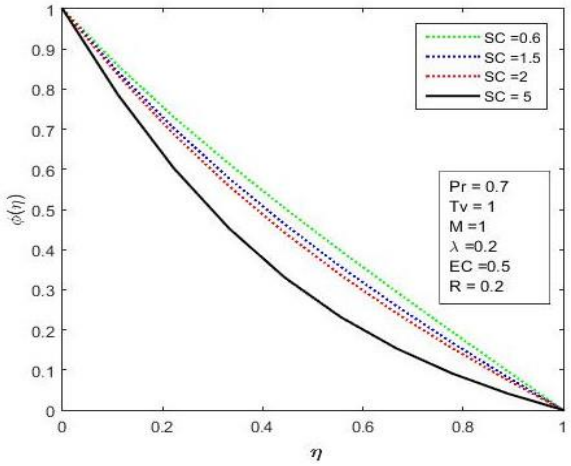

Figure 3. Concentration profile for different values of SC.

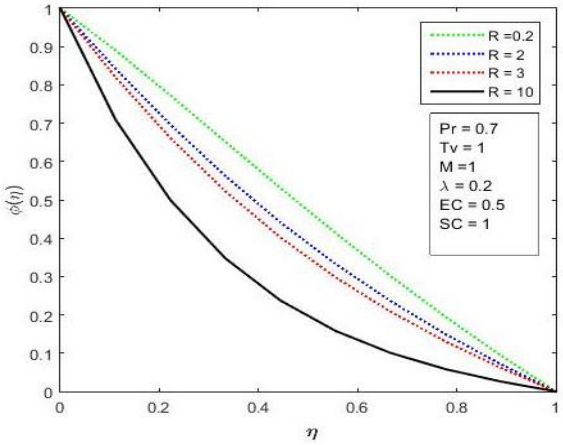

Figure 4. Concentration profile for different values of R.

From Figure 5, it is evident that the temperature profile increases as the Eckert number (Ec) increases. The increase of Eckert number indicates a greater kinetic energy relative to the enthalpy change, which can lead to enhanced convective heat transfer. This behavior is observed in Figure 5.

Figure 6 depicts the variations in temperature profiles for different parameter values Pr. When Pr is relatively low, thermal transmission becomes the dominant mode of heat transfer in the system. Consequently, heat can diffuse more quickly in such cases compared to scenarios where Pr has higher values. As a result, the temperature profile exhibits a steeper decline for smaller Pr values, indicating that heat dissipates more rapidly away from the heating surface. On the other hand, for higher Pr values, the dominance of thermal conduction diminishes, leading to slower heat diffusion and a less steep temperature decline. This behavior is clearly explained in Figure 6. Based on the findings presented in Figure 7, a

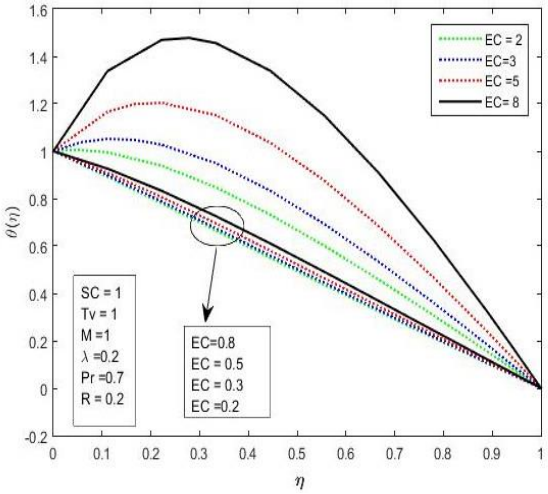

Figure 5. Temperature profile for different values of EC.

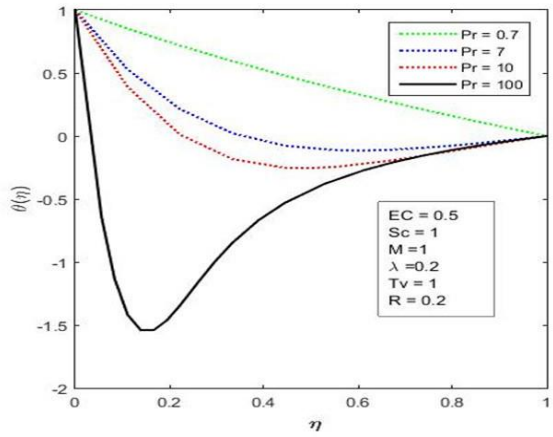

Figure 6. Temperature profile for different values of Pr.

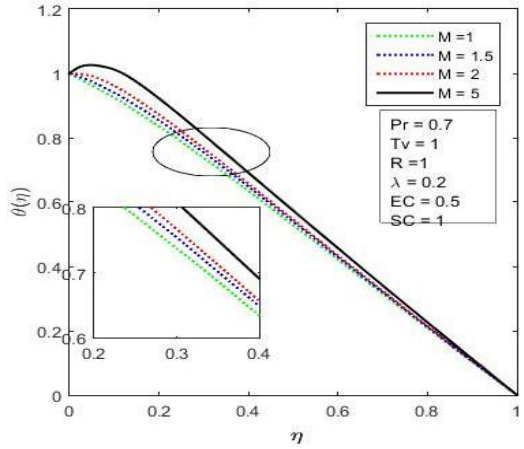

Figure 7. Temperature profile for different values of M.

noteworthy observation is that the temperature of the fluid rises with increasing values of the magnetic parameter (M). When M increases, it imposes a magnetic force on the fluid, which interacts with the fluid's motion and hinders its movement in turn it increases the temperature of the fluid. From Figure 8, it is observed that the velocity profile decreases for increasing Williamson dimensionless parameter.

From Figure 9, it is evident that as the magnetic parameter (M) increases, the fluid velocity progressively decreases. When M increases, it imposes a magnetic force on the fluid, which interacts with the fluid's motion and hinders its movement, thus impacting the velocity profile.

Figure 10 shows the variation in skin friction coefficient for various values of magnetic parameter (M). It is exhibited that the local skin friction coefficient has increased for a higher value of M. Heat transfer tendency of the fluid for different values of magnetic parameters (M) is shown in Figure 11. It is revealed that heat transfer is high for increasing magnetic parameters (M).

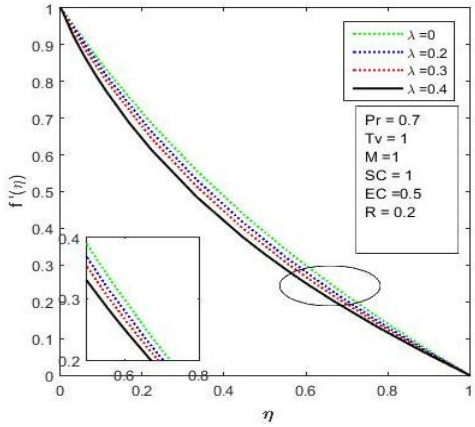

Figure 8. Velocity profile for different values of λ.

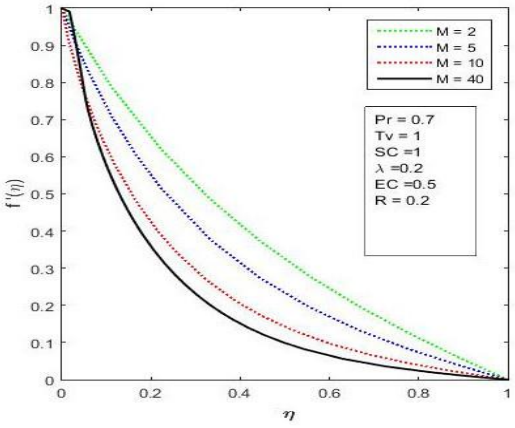

Figure 9. Velocity profile for different values of M.

The mass transfer tendency of the fluid for different values of the chemical reaction parameter (*R*) is shown in Figure 12. It is revealed that mass transfer is high for increasing chemical reaction parameter (*R*).

Future direction

In the literature survey, so far limited research has been made to analyze the problem of hybrid

nanoparticles with Williamson fluid model. Incorporating nanoparticles into Williamson fluid will enhance the traditional heat transfer properties because of their strong thermal conductivity. The idea of using Williamson nanofluid can be researched further in the future to enhance the heat transfer characteristics of the base fluid.

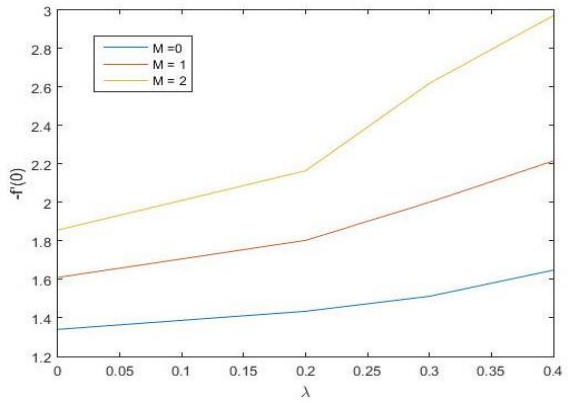

Figure 10. Skin friction coefficient for different value of M.

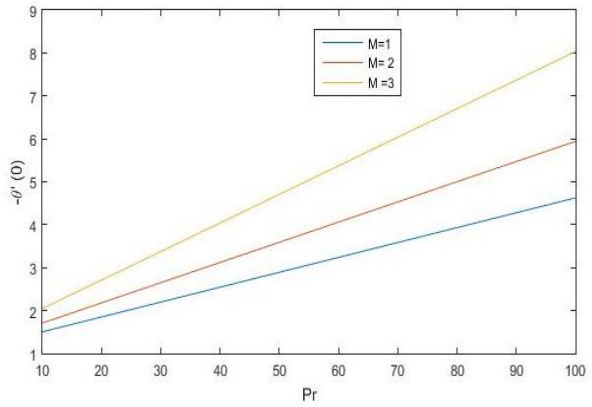

Figure 11. Heat transfer parameter for different values of of M.

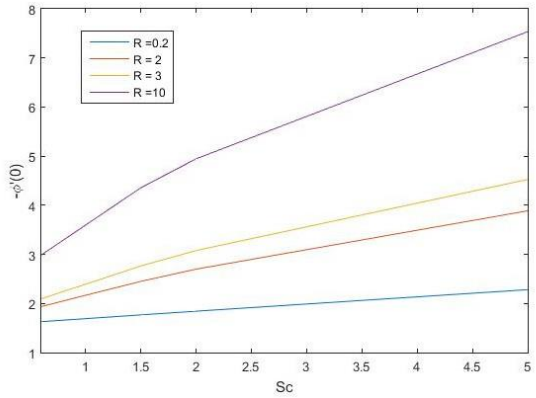

Figure 12. Mass transfer parameter for different values of of R.

CONCLUSION

The study focused on investigating the influences of various dimensionless factors on the temperature, velocity, and fluid concentration near the surface. The findings revealed significant trends in Williamson fluid, which are summarized as:

As the thermophoretic parameter increases, the strength of the thermal diffusion increases, which leads to the migration of species, and in turn, the concentration of the fluid decreases.

As Sc increases, the fluid's concentration near the surface diminishes.

As the chemical reaction factor rises, the fluid's concentration near the surface diminishes.

The fluid temperature rises with rising Eckert numbers suggesting higher Eckert numbers enhance heat transfer near the surface.

A rise in the Prandtl number causes the fluid temperature to rise suggesting that with lower values of Pr, thermal conduction is greater and that heat can diffuse and move away from the heat surface more quickly than at higher values of Pr.

The increase in the magnetic parameter (M) leads to an increase in the fluid temperature distribution and causes a decrease in the velocity profile.

The velocity profile diminishes as the Williamson dimensionless parameter increases.

Nusselt number and skin friction coefficient increase with increasing magnetic parameters, and Sc increases with increasing chemical reaction parameters.

NOMENCLATURE

U_0 stretching parameter
Ec Eckert number
Sc Schmidt number
Cp specific heat at constant pressure
C fluid concentration
T fluid temperature
Pr Prandtl number
B Magnetic field
M magnetic parameter

Greek symbols

η similarity variable
ϕ dimensionless concentration
λ Williamson fluid parameter
μ dynamic viscosity
ν kinematic viscosity
ρ density of the fluid
σ electrical conductivity
Ψ stream function
θ dimensionless temperature
k thermal conductivity

Subscripts

w conditions at the surface
∞ conditions far away from the surface

REFERENCES

[1] R.V. Williamson, Ind. Eng. Chem. Res. 21(1929) 1108–1111. https://doi.org/10.1021/ie50239a035.

[2] B.C. Sakiadis, AIChe J. 7 (1961) 26–28. https://doi.org/10.1002/aic.690070108.

[3] F.K. Tsou, E.M. Sparrow, R.J. Goldstein, Int. J. Heat Mass Transfer 10 (1967) 219–235. https://doi.org/10.1016/0017-9310(67)90100-7.

[4] L.E. Erickson, L.T. Fan., V.G. Fox, Ind. Eng. Chem. 5 (1966) 19–25. https://doi.org/10.1021/i160017a004.

[5] S. Nadeem, S.T. Hussain, C. LeeBraz. J. Chem. Eng. 30(3) (2013) 619–625. https://doi.org/10.1590/S0104-66322013000300019.

[6] T. Hayat, A. Shafiq, A. Alsaedi, Alexandria Eng. J. 55(3) (2016) 2229–2240. https://doi.org/10.1016/j.aej.2016.06.004.

[7] H.M. Shawky, N.T. Eldabe, K.A. Kamel, E.A. Abd-Aziz, Microsyst. Technol. 25(4) (2018) 1155–1169. https://doi.org/10.1007/s00542-018-4081-1.

[8] S. Nadeem, S.T. Hussain, Appl. Nanosci. 4(8) (2014) 1005–1012. https://doi.org/10.1007/s13204-013-0282-1.

[9] S. Nadeem, S.T. Hussain, J. Appl. Fluid Mech. 9 (2) (2016) 729–739. https://doi.org/10.18869/acadpub.jafm.68.225.21487.

[10] T. Kebede, E. Haile, G. Awgichew, T. Waleign, J. Appl. Math. 2020 (2020) 1–13. https://doi.org/10.1155/2020/1890972.

[11] I.C. Liu, Int. Commun. Heat Mass Transfer 32 (8) (2005) 1075–1084. https://doi.org/10.1016/j.icheatmasstransfer.2005.02.003.

[12] M.A.A. Hammad, M. Ferdows, Appl. Math. Mech. 33 (7) (2012) 923–930. https://doi.org/10.1007/s10483-012-1595-7.

[13] F.M. Ali, R. Nazar, N.M. Arifin, I. Pop, Appl. Math. Mech. 32 (4) (2011) 409–418. https://doi.org/10.1007/s10483-011-1426-6.

[14] V. Kumaran, G. Ramanaiah, Acta Mech. 116 (1–4) (1996) 229–233. https://doi.org/10.1007/BF01171433.

[15] M.E. Ali, Int. J. Heat Mass Transfer 16 (1995) 280–290. https://doi.org/10.1016/0142-727X(95)00001-7.

[16] E.M.A. Elbashbeshy, Arch. Mech. 53 (6) (2001) 643–651. https://am.ippt.pan.pl/am/article/viewFile/v53p643/pdf.

[17] E. Sanjayanand, S.K. Khan, Int. J. Therm. Sci. 45 (2006) 819–828. https://doi.org/10.1016/j.ijthermalsci.2005.11.002.

[18] E. Magyari, B. Keller, J. Phys. D: Appl. Phys. 32 (1999) 577–585. http://doi.org/10.1007/s002310000126.

[19] S. Nadeem, S. Zaheer, T. Fang, Numer. Algorithms 57 (2011) 187–205. http://dx.doi.org/10.1007/s11075-010-9423-8.

[20] E.Sanjayanand, S. K. Khan, Intl. J. Therm. Sci. 45, (2006) 819–828. https://doi.org/10.1016/j.ijthermalsci.2005.11.002.

[21] E. Magyari, and B. Keller, J. Physics D: Appl. Physics, 32, (1999) 577–585. http://dx.doi.org/10.1088/0022-3727/32/5/012.

[22] S. Nadeem, S. Zaheer, T. Fang, Numer. Algorithms 57, (2011) 187–205. http://dx.doi.org/10.1007/s11075-010-9423-8.

[23] S. Nadeem, C. Lee, Nanoscale Res. Lett. 7, (2012) 94 https://doi.org/10.1186/1556-276X-7-94.

[24] M.S. Arif, K. Abodayeh, Y. Nawaz, Axioms,12(5), (2023) 460, https://doi.org/10.3390/axioms12050460.

[25] Y. Nawaz, M.S. Arif, K. Abodayeh, Int. J. Numer. Methods Fluids, 94 (7), (2022) 920–940. https://doi.org/10.1002/fld.5078.

[26] P. Loganathan, N.G. Stepha, J. Appl. Fluid Mech, 6(4), (2013) 581–588. 10.36884/JAFM.6.04.21276.

[27] M. Ismail, D.M. Gururaj, Heat Transf. 50(4) (2021), 4019–4038 https://doi.org/10.1002/htj.22062.

[28] M. Ismail, D.M. Gururaj, J. Nanofluids, 12 (3), (2023), 809–818. https://doi.org/10.1166/jon.2023.1962.

[29] M. Ismail, D.M. Gururaj, Numer. Heat Transf. B: Fundam. (2023) 1–27. https://doi.org/10.1080/10407790.2023.2257381.

[30] P. Loganathan, N. Golden Stepha, Asia Pac. J. Chem. Eng. 8(6) (2013), 870–879 https://doi.org/10.1002/apj.1732.

[31] L.E. Erickson, L.T Fan, V.G. Fox, Ind. Eng. Chem. Fundam. 5(1), (1966), 19–25. https://doi.org/10.1021/i160017a004.

[32] V.K. Garg, S. Jayaraj. Int. J. Heat Mass Transfer, 31 (1998) 875–890. https://doi.org/10.1016/0017-9310(88)90144-5.

[33] N.A. Khan, H. Khan, Nonlinear Eng. 3(2), (2014)107–115. https://doi.org/10.1515/nleng-2014-0002.

[34] H. Maaitah, A.N. Olimat, O. Quran, H.M. Duwairi, Int. J. Thermofluids, 19 (2023) 100361. https://doi.org/10.1016/j.ijft.2023.100361.

[35] A.M. Megahed, IJMPC, 31(1), (2020) 2050019. http://doi.org/10.1142/S0129183120500199.

GOLDEN STEPHA NALLATHAMBI[1]

BHARATHI GOWRI SASI KUMAR[2]

GUVVA SWATHY[3]

[1]Department of Mathematics, R.M.K Engineering College, India

[2]Department of Mathematics, Ethiraj College for Women, India

[3]Mathematics Department, S. A. Engineering College, India

NAUČNI RAD

MAGNETOHIDRODINAMIČKI VILIJAMSONOV TOK TEČNOSTI NA PRODUŽENOJ PLOČI SA TERMOFOREZOM I HEMIJSKOM REAKCIJOM

U ovom radu je istraživan stabilan, dvodimenzionalni, nestišljiv tok pseudoplastične Vilijamsonove tečnosti podvrgnute linearno rastegnutom sloju. Studija uključuje efekte magnetnih polja, hemijskih reakcija i termoforeze na ponašanje fluida. Primenom metoda graničnog sloja i sličnosti, glavne jednačine su pojednostavljene za numeričku analizu. Za rešavanje redukovanih jednačina koristi se MATLAB bvp4c rešavač. Dobijeni rezultati su vizuelno predstavljeni i detaljno razmotreni kako bi se sagledale fizičke karakteristike modela. Istraživanje naglašava uticaj magnetnog polja, hemijske reakcije i uticaj taloženja čestica termoforezom na strujno ponašanje Vilijamsonove tečnosti preko produžene ploče. Značajne uloge u određivanju koncentracije tečnosti u blizini graničnog sloja imaju hemijske reakcije i parametri termoforeze. Primećeno je da povećanje parametara hemijskih reakcija i termoforeze dovodi do smanjenja debljine koncentracije tečnosti u blizini graničnog sloja. Primetno je da je povećanje Šmitove vrednosti takođe smanjilo debljinu koncentracije tečnosti blizu graničnog sloja. Magnetohidrodinamički parametar značajno utiče na brzinu tečnosti i temperaturu blizu površine. Primećeno je da povećanje magnetohidrodinamičkog parametra smanjuje brzinu fluida i povećava temperaturu blizu površine. Razmatraće se uticaji koeficijenta trenja, Nuseltovog broja i koeficijenta prenosa mase na Vilijamsonovu tečnost. Dobijeni nalazi se porede sa postojećim istraživanjima, a korelacija je data tabelarno.

Ključne reči: Vilijamsonov fluid, magnetohidrodinamika, hemijska reakcija, termoforeza.

CI&CEQ
Chemical Industry & Chemical Engineering Quarterly

Available online at
Association of the Chemical Engineers of Serbia AChE
www.ache.org.rs/CICEQ

Chem. Ind. Chem. Eng. Q. 30 (4) 335–348 (2024) CI&CEQ

CHITRA DEVI VENKATACHALAM[1]
PREMKUMAR BHUVANESHWARAN[1]
MOTHIL SENGOTTIAN[2]
SATHISH RAAM RAVICHANDRAN[2]

[1]Department of Food Technology, Kongu Engineering College, Perundurai, Tamil Nadu, India.

[2]Department of Chemical Engineering, Kongu Engineering College, Perundurai, Tamil Nadu, India

SCIENTIFIC PAPER

UDC 5/6:620

RELIABILITY-BASED DESIGN OPTIMIZATION OF SCREW SHAFT FOR CONTINUOUS HIGH-PRESSURE HYDROTHERMAL CO-LIQUEFACTION PROCESS

Article Highlights

- Structural analysis was performed on the screw-shaft to withstand high pressure in HTCL reactor
- The uniformly varying pressure was applied to the screw shaft to calculate its structural strength
- Helix angle, depth, pitch, and flight length were the dimensional parameters optimized
- Stress, deformation, shear, and bending stress were crucial responses used for structural analysis
- GFRG, SN ratio, and ANOVA methods were used for optimization and recommended for structural simulations

Abstract

Hydrothermal co-liquefaction (HTCL) is the prominent process for producing bio-products with a higher conversion rate. It is performed at high temperatures and pressure in the presence of water. Earlier, it was mostly conducted in batch reactors, but it has major limitations including operating volume, back mixing, and tedious process for high productivity. With that, the present investigation is performed on designing the screw shaft for the high-pressure HTCL process. The dimensional factors including flight length, pitch, helix angle, and depth were considered to design the optimal screw shaft. Likewise, principal stresses, shear stress, bending stress, bending moment, and total deformation were regarded as inevitable response variables to analyze the internal strength of the shaft. In this regard, the Taguchi approach provides the L_9 (3^4) orthogonal array as an experimental design. Then, the numerical results from the transient structural analysis were analyzed with the assistance of statistical methods such as Grey Relational Grade (GRG), Grey Fuzzy Reasoning Grade, Analysis of Variance (ANOVA), and Taguchi method to find the most influential dimensions for minimizing the response variable. Consequently, the results from both GRG and Taguchi optimization were compared, and selected the most optimum parameters.

Keywords: hydrothermal co-liquefaction, screw shaft, finite element method, stress analysis, Goodman failure criteria, multi and single response optimization technique.

As stated by the Energy Information Administration (EIA), the utilization of liquid fuels was 102.22 million barrels per day at the end of 2022 and also it is expected to increase by 2.4 % in forthcoming years.

These gradual increments in the utilization of conventional fuel and its future demand indirectly suggest the need for alternate fuels like biomass energy, which can be produced via thermochemical conversion processes [1]. The commercialization of these biomass conversion technologies would

Correspondence: C.D. Venkatachalam, Department of Food Technology, Kongu Engineering College, Perundurai, Tamil Nadu - 638060, India.
E-mail: erchitrasuresh@gmail.com
Paper received: 24 November, 2023
Paper revised: 14 February, 2024
Paper accepted: 24 February, 2024

https://doi.org/10.2298/CICEQ231124004V

decrease the emission of greenhouse gases and pollutant particulates, thereby reducing global warming [2]. Among different thermochemical conversion processes, hydrothermal co-liquefaction (HTCL) is the most promising process for the quick conversion of biomass into bio-liquid under both sub-critical and supercritical conditions because of using water as solvent and catalyst. HTCL process focuses on the biological degradation of feedstock at higher temperatures (250 °C to 350 °C) and pressure (20 MPa to 25 MPa) to produce a high amount of bio-crude rather than biosolid and biogas [3,4].

In the last few decades, the HTCL process was performed in single and sequence-type hydrothermal batch reactors for various types of biomass conversion. The capacity of these reactors was in the range of 5 mL to 800 mL, and it also consisted of agitators and electrical band heaters to improve the heat transfer and enhance mixing during the hydrothermal conversion. Some of the major limitations of batch reactors including back mixing and inconsistency of the bioproducts are eliminated in the current HTCL reactor [5–7]. Additionally, a wide range of particle sizes can be used in this reactor compared to batch reactors. In the batch reactor, biomass heating, cooling, discharging, and refilling were time-consuming processes that led to lower energy efficiency. Some researchers have also carried out the same process in a semi-continuous reactor using a high-pressure piston feeder with a heat exchanger in the closed chamber. The major drawback of this process is the use of higher input energy for the high-pressure piston pump of 30 MPa as it also increases the operating cost. [8,9].

To overcome these limitations, Efika *et al.* (2012) and Shengbo *et al.* (2021) performed thermochemical reactions on screw-type reactors for quick transportation and biomass conversion. A two-stage screw kiln reactor (screw diameter = 6 cm and length = 54 cm) was used for the production of syngas from the waste biomass through pyrolysis which is operated at temperatures between 500 °C and 760 °C and it resulted in better biomass mixing and better heat transfer rate than batch reactors [10,11]. Likewise, Hoekman *et al.* (2017) developed a twin-screw extruder (having a 25 mm diameter) operating at high pressure of 25 MPa and temperature of 350 °C. It exhibited a shorter residence time (21–28 sec) compared to the conventional reactor [12]. In addition, an auger-type screw reactor was used for recycling the plastic waste through pyrolysis, it is performed at temperatures between 380 °C and 600 °C with better axial dispersion and uniform flow in thermal conditions over the length with respect to time [13].

From the above studies, it was observed that these continuous-type screw reactors had quick processing rates, higher productivity, and less energy intake. Moreover, the efficiency and chemical properties of the biofuel were also found to be improved in the screw-type continuous reactor with shorter residence time regardless of the thermochemical process [2,10,11,14,15]. Especially, the auger screw was preferred for pyrolysis due to the transition of dry grains and in the case of wet feedstock, the Archimedes screw was preferred for the better transition of particles in the form of slurry [16,17].

Finite Element Method (FEM) is a widely used technique to model and theoretically evaluate the structural integrity of any mechanical component. Likewise, Goodman criteria are preferred while performing the failure analysis under dynamic conditions and it has been used in various designs of components such as the main shaft in gas turbine engines, drive shaft, turbine shaft, and propeller shaft [18,19]. Further, the Grey Relational Grade (GRG) is the most employed optimization technique for multiple responses where the direct responses were converted single response called Grey Relational Grade (GRG), and it is verified with the guidance of Grey Fuzzy Reasoning Grade (GFRG). Recently, it has been performed to achieve machining effectiveness [20], improving the tensile strength of the aluminum alloy pipe [21,22], enhancing the bending and torsional stiffness of the external structure of automobile [23], improving the static and dynamic performance of the drive shaft [18] and beam structure [24].

In the present study, the reactor under consideration consists of an Archimedes screw shaft rotated inside a cylindrical chamber employed with external band heaters, inside which the transition and chemical reaction of the feedstock takes place within the chamber. The shaft was designed to experience both torsional loads (due to shaft rotation) and bending loads (due to reaction pressure) during the continuous HTCL process. The screw shaft is the important component that pushes forward the feedstock towards the length of the reactor and it has to withstand high temperatures of 400 °C and pressure varying from 1 to 25 MPa. To analyze the structural stability of the screw shaft and to study its resistance to stress and deformation at high-pressure FEM is used. In this study, flight length, pitch, depth, and helix angle were considered the vital dimensions to be optimized with respect to principal stresses, bending stress, shear stress, and total deformation. Here, the dimensions for the optimization study were considered by following the standard shaft design procedure. The optimum dimensions of the screw shaft were selected by using the multi-response optimization technique (grey relational grade method), single-response optimization technique (Taguchi's method), and its contribution as

an effective factor is predicted using ANOVA. The method followed for dimensional optimization is given in the flowchart as shown in Fig. 1.

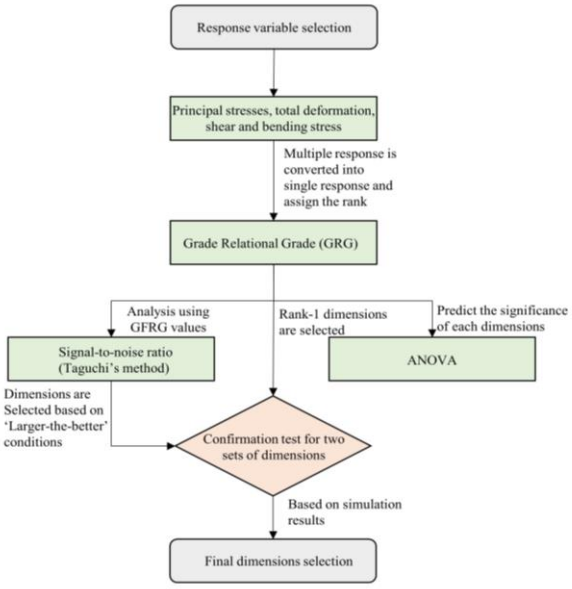

Figure 1. (a) Pressure contour plot; (b) pressure profile for screw shaft enclosed reaction chamber during high-pressure fluid flow.

MATERIALS AND METODS

Materials

During the HTCL process, the water which is used as the solvent becomes more acidic, and thus the screw shaft is more susceptible to corrosion. So, the screw shaft should be made of a material with easy machinability and high resistance to corrosion, wear, and chloride formation. Because of good acidic, corrosion, and chloride resistance, H13, SS304, and SS316 were initially considered to develop the screw shaft. However, SS304 and SS316 were not selected due to their inadequate mechanical properties such as yield and ultimate strength to sustain high stress, whereas H13 is selected for designing the screw shaft. The presence of high Chromium and molybdenum in H13 enhances the resistance to corrosion and chloride formation [25]. Table S1 (Supporting material) compares the mechanical properties like Young's modulus, bulk modulus, shear modulus, and tensile and compressive strength of H13 with SS304 and SS316, and these values were taken for Finite element analysis [26,27].

The screw shaft was modeled by using the Catia V5R21 for which the dimensions were obtained from the Design Expert Software version 8.0 as given in Table S2. The pressure distribution over the length of the screw shaft in each section of the reactor filled with biomass slurry was determined by fluent analysis. Furthermore, the Finite Element Method (FEM) was carried out for the discretization of the screw shaft where the structural analysis is performed to know the stress distribution, deformation, bending stress, and FOS through a transient structural module in Ansys R1.

Metodology

Specification of the screw shaft

Flight length, diameter, pitch, helix angle, and thread depth were considered the important dimensions to be optimized for designing an optimal shaft model. The size of depth is essential to find the cross-sectional area and is responsible for the shear and principal stress of the shaft. Likewise, flight length is the major factor responsible for the bendability of the shaft. At last, helix angle and pitch length were crucial parameters for the flowability of fluid in the shaft. Whence, the shaft diameter (58 mm) was fixed by applying the continuity equation (conservation of mass) given in Eq. (1) for the constant mass flow rate of biomass (1 kg/hr). In general, the L/D ratio ranging from 20 to 30 had chosen for the perfect extrusion of the feed material in the screw shaft and also the pitch was another salient parameter for transporting the biomass which ranges from 0.25 to 0.5 % of the screw diameter. In addition, the helix angle of the square thread provides better flow over the transportation which was calculated by using Eq. (2). The depth used for the square thread is always half of the screw pitch. Moreover, it was quite difficult to select the best value from each dimension to develop the optimized design of the screw shaft. Hence, the Design of Experiments (L_9 - Taguchi's model) was used to select the better combination of the dimensions to model the HTCL screw shaft as given in Table S2. The diameter of the reaction chamber was calculated through the Continuity equation given by:

The mass flow rate through the inlet $\dot{m}_1$ - mass flow rate through the outlet $\dot{m}_2$:

$$\dot{m}_1 = \rho A V \tag{1}$$

The equation for computing the helix angle of the screw shaft:

$$\phi = \tan^{-1}\left(\frac{P}{\pi D}\right) \tag{2}$$

where P - screw pitch, and D - screw diameter.

Finite Element Method (FEM) for the screw shaft

Fig. S1(a,b) illustrates the two-dimensional schematic diagram and 3-D model of the screw shaft used for the finite element analysis. The feed mixture enters zone "A" called as suction zone, and here the

feed material is freely moved along the screw shaft and it reaches the compression zones "B" and "C". The feedstock gets compressed and becomes finer particles during HTCL in this zone. A high-pressure water nozzle is provided to improve the chemical conversion and operating pressure in zone "D". Likewise, zones "E" and "G" represent the second and third compression zones, while "F" and "H" represent the expansion zones respectively. The high-pressure zones (C, D, E) are marked using a red box in Fig. S1 (a). Further, the discretization was made by converting the screw shaft into triangular elements using FEM during structural analysis. The governing Eqs. (3,4) were used for meshing the uniformly rotating shaft considering the gyroscopic effect and resisting moment. Further discretization of the screw shaft was done using the adaptive meshing technique for the size of 2 mm and is given in Fig. S1(c,d). Also, the high smoothing mesh was adapted to get better convergence results, especially on transient conditions [28–30]. For pure torsion acting on the screw shaft, it was assumed that the shaft material is homogeneous and perfectly elastic. It was also assumed that the torsional moment is uniform over the shaft length, the stress does not exceed the limit of proportionality and the deformation is negligible.

The global force equation for screw shaft using FEM is given by Eq. (3):

$$[K]\{u\} = \{F\} \tag{3}$$

where [K]- stiffness matrix, {u} - displacement matrix, and {F} - force matrix.

The derived FEM equation applied for meshing the screw shaft is given by Eq. (4):

$$\begin{Bmatrix} M_{x1} \\ M_{x2} \\ M_{y1} \\ M_{y2} \end{Bmatrix} = \frac{GL}{I} \begin{bmatrix} 1 & -1 & -1 & -1 \\ -1 & 1 & -1 & -1 \\ -1 & -1 & 1 & -1 \\ -1 & -1 & -1 & 1 \end{bmatrix} \begin{Bmatrix} \phi_{x1} \\ \phi_{x2} \\ \phi_{x3} \\ \phi_{x4} \end{Bmatrix} \tag{4}$$

Loading and boundary conditions

The uniformly varying pressure (from 1 MPa to 23 MPa) developed in different zones through the length of the HTCL reactor is given in Fig. S2(a). This pressure variation happens due to the alternate thread portion (left and right thread) in the screw shaft. It was observed that the screw shaft experienced a maximum torque of 125000 Nm while running at 60 rpm and a maximum pressure of 23 MPa. Fig. S2(a) shows the different pressure zones that were found by applying the HTCL operating conditions onto the screw shaft enclosed with the reaction chamber. The pressure analysis was performed using a fluent module pressure profile developed for similar HTCL conditions as shown in Fig. S2(b). It shows a gradual increment in pressure from 1 to 23 MPa till the length of 0.8 m, after which it starts to decrease significantly. High pressure was developed at the mid-section of the screw shaft due to the water injection. Likewise, a slight pressure decrease was observed at the end zones (F, G, H) of the screw shaft due to the choking of feedstock.

During the FEM analysis, the shaft was divided into seven zones based on the different pressure acting on each section of the screw shaft given in Fig. S1(a). In addition, the shaft is free to rotate and pressure (uniformly varying load) is acting in all directions. The analysis was carried out for 7 secs (number of steps) with a time step of 0.5 sec and solved using the work-energy method with governing equation as given in Eq. (4). It was considered that the pressure is acting gradually concerning time in each zone of the screw shaft under transient conditions and the time-dependent pressure was calculated by using the SN curve in FEM analysis shown in Table S3.

Response variable studies to optimize the design

Principal stresses, shear stress, bending moment, bending stress, total deformation, and Factor of Safety (FOS) were the crucial response variables considered for structural analysis. These variables were numerically estimated using the structural analysis in simulation software. Principal stresses were calculated to realize the internal strength of the screw shaft for the given dimensions. It should be less than the ultimate tensile strength (UTS) for any material and its cross-section to resist the external force. Maximum and minimum principal stresses were estimated by using Eq. (5) and it is acting on the corresponding planes, which the angle ranges from 0° to 180° in the finite element method [31,32]. Similarly, bending moment and deformation were considered to evaluate the amount of deflection and change of cross section during the action of external force. The bending moment might be varied along the overall length of the shaft, depending on the distribution of applied load [33]. It is necessary to ensure that the moment developed in the shaft should be within acceptable limits to avoid excessive deflection [34]. The bending moment was calculated by considering the shaft with a simply supported beam with a uniformly varying load which is given in Eq. (6). The Permanent deformation occurs when the stress value exceeds the yield stress and further increment of load leads to fracture due to shear and bending stress [35]. Bending and shear stress were the two major stresses responsible for estimating the fatigue failure or lifetime of the screw shaft. The maximum shear stress acting on the fractured surface of the screw shaft was estimated using Eq. (7).

The Goodman failure criteria given in Fig. 3 show the good relationship between bending and shear stress for calculating the endurance cycle and safe limits of the screw shaft [36].

Maximum and minimum principal stresses were calculated using σ_1 and σ_2 given by Eq. (5):

$$\sigma_{max,min} = \frac{\sigma_1+\sigma_2}{2} \pm \left[\frac{\sigma_1-\sigma_2}{2}\right] X\cos(2\theta) \quad (5)$$

The bending moment of the shaft with a simply supported beam with a uniformly varying load was calculated by using Eq. (6):

$$Bending\ moment, M = \left(\frac{WXL}{2}\right) - \left(\frac{WL^2}{2}\right) \quad (6)$$

The shear stress of any shaft was calculated by using Eq. (7):

$$\tau_{max} = \frac{TD}{2J} \quad (7)$$

Goodman's safety factor for the given dimensions of the screw shaft was estimated using Eq. (8) [36]:

$$\frac{\sigma_{ta}}{s_e} + \frac{\sigma_{tm}}{s_u} = \frac{1}{n} \quad (8)$$

where n - Goodman safe limit.

Total deformation of the screw shaft was calculated by using Eq. (9):

$$\sigma_{total} = \sqrt{X^2+Y^2+Z^2} \quad (9)$$

Procedure for dimensional optimization

The well-established procedure was followed to perform the dimensional optimization based on the flow chart given in Fig. 1. Firstly, the multiple responses were converted into a single response termed GFRG using the fuzzy method. Then, the GFRG result was applied to the signal-to-noise ratio method in Taguchi's technique to carry out single response optimization based on estimated variance. ANOVA was performed to realize the contribution of individual dimensions with respect to the response variable. The two sets of dimensions were predicted from Fuzzy and Taguchi's method. The screw shaft was designed depending on the predicted two sets of dimensions and the best simulation result was taken to the design and fabrication process.

Grade relational grade optimization method

The robustness of the dimensional factors for designing the screw shaft can be improved using a multi-response optimization method termed Grey Relational Grade (GRG). Initially, the normalized value is estimated from the primary results using Eqs. (10,11) based on the requirements of "Larger-the-better" or "Smaller-the-better" conditions. Then, the Grey Relational Coefficient (GRC) was calculated through Eq. (12) and it is an essential term to obtain the GRG values. The final results were verified with the Grey Fuzzy Reasoning Grade (GFRG) and evaluated by following the fuzzy logic. Fuzzification, Rule base, Decision making, and Defuzzification were the four major steps to be followed to bring the value of GFRG. In fuzzification, the Mamdani interface system was applied to relate the input and output parameters. Furthermore, the membership function was prepared using linguistic variables based on the sequential values of both input factors and output response (GRG value), which helps to generate the fuzzy rules. The rank was provided to both GRG and GFRG values depending on the highest value was graded as one and so on [20,37,38]. The normalized values of the original response sequence were obtained by:

$$y_n^* = \frac{y_n(q) - \min y_n(q)}{\max y_n(q) - \min y_n(q)} \quad (10)$$

if Larger-the-better.

$$y_n^* = \frac{\max y_n(q) - y_n(q)}{\max y_n(q) - \min y_n(q)} \quad (11)$$

if Smaller-the-better. Where, y_n^* - normalized value of respective runs, $y_n(q)$ - primary response value of respective run from simulation results, *max* $y_n(q)$ - maximum value of individual response variable, *min* $y_n(q)$ - minimum value of individual response variable, y_d^* - deviation of individual response from normalized value.

The grey relational coefficient (GRC) can be evaluated as follows:

$$\rho(q) = \frac{\Delta\min + \rho\Delta\max}{\Delta y_d^* + \rho\Delta\max} \quad (12)$$

where, $\rho(q)$ - Grey relational coefficient, $y_d^* = 1 - y_n^*$ - deviation from the normalized value, ρ - weightage for coefficient. Generally, ρ =0.5 was taken.

Taguchi's optimization technique

Taguchi's method plays a vital role in optimizing the dimensional parameters with respect to a single response at a minimal number of trials. It also uses the orthogonal array technique to build the design of experiments, which mainly depends on degrees of freedom. Taguchi produces the results based on calculating the mean and deviation of the response

variable. When the deviation is less or equal mean obtained, the response variable will not change concerning dimensional factors. In addition, the signal-to-noise analysis was also considered for building a sustainable model with minimum deviation [21,39,40]. In this regard, three levels with four factors (3^4) models were chosen for designing the efficient screw shaft. For 3^4 models, there were four orthogonal arrays (L_9, L_{12}, L_{16}, and L_{18}) available for constructing the design of experiments.

The GFRG attained from the Fuzzy Interface System (FIS) was implemented in Taguchi's method to find out the optimal values of dimensional factors. Here, the rank was provided to each parameter based on the deviation of the response variable. It was also expressed from the SN ratio graph by measuring the deviation from the target value relative to the noise present in the system. SN ratio is commonly classified into three types namely smaller-the-better, larger-the-better, and nominal-the-better based on the specific objective of the response variable which is given in Eqs. (13–15). Most of the stress values prefer the smaller-the-better type SN ratios to find the optimal dimensional factor [41,42].

When the response variable is recommended to be smaller then:

$$\alpha = -10\log\frac{1}{m}\sum_{a=1}^{m} z_i^2 \tag{13}$$

When the response variable is recommended to be nominal then:

$$\alpha = -10\log\frac{1}{m}\sum_{a=1}^{m}\frac{\mu^2}{\sigma^2} \tag{14}$$

When the response variable is recommended to be larger then:

$$\alpha = -10\log\frac{1}{m}\sum_{a=1}^{m}\frac{1}{z_i^2} \tag{15}$$

Analysis of Variance (ANOVA)

The statistical method (ANOVA) is applied to know the impact of the different factors with respect to the response variable. ANOVA uses the results that were obtained from the GRG optimization. It also defines the null and the alternative hypothesis to find the significance of the different factors by evaluating the means of the response variable. The *P* and *F* values are more important in choosing the suitable hypothesis based on significant values. In case, the *P*-value is less than or equal to 0.05, then the null hypothesis is not applicable for the particular response or else the specific factor is acceptable for the null hypothesis and also it shows a similar mean value at each level. Finally, *R*-squared and adjusted *R*-squared are the salient parameters for explaining the proportion of the variation of the response variable, which ranges from 0 to 1. Null hypothesis (H_o) means a similar response at each level of dimensional factors and alternative hypothesis (H_1) has a different response at each level of dimensional factors [21,40].

RESULTS AND DISCUSSION

Maximum and minimum principal stress affecting the screw shaft

Fig. 2a illustrates the maximum principal stress of the screw shaft, in which run-8 experience the low-stress value of 8.5176 x 10^7 Pa and run-2 exhibits the high stress of 5.9686 x 10^8 Pa was calculated using Eq. (5). Likewise, run-1, 4, 5 and 9 possess the stress values from 3 x 10^8 Pa to 3.7623 x 10^8 Pa and run-3, 6 and 7 resist the external force ranges from 1.05 x 10^8 Pa to 1.51 x 10^8 Pa. These stress values of the screw shaft are under the limit of bulk modulus (160 x 10^9 Pa) of H13. In the case of minimum principal stress given in Fig. 2b, the highest (1.7854 x 10^8 Pa) and lowest (2.2018 x 10^7 Pa) stress value was possessed by run-2 and run-8 respectively. The stress value ranges from 2.7148 x 10^7 Pa to 1.0834 x 10^8 Pa for the remaining sets of Taguchi's runs. By considering the above-mentioned principal stress value, the dimensions used for run-8 were suggested for designing the screw shaft due to their high resistance to external pressure.

Apart from principal stress, the stress ratio is also important for describing the fatigue life of the screw shaft. It is the ratio of the difference between minimum and maximum principal stress to the sum of these two stresses. Fatigue life mainly depends on the temperature, loading, and stress developed in the testing material. In addition, the stress ratio shows an indirect proportionality with the fatigue life [36,43]. In this regard, run-6 and run-2 have the lowest and highest stress ratios of 0.28 and 0.56 respectively. The stress ratio from 0.43 to 0.54 was possessed by the residual runs of the FEM analysis. From the aforementioned data, the dimensions suggested for run-6 and run-8 have higher fatigue life compared to other runs for the given loading conditions shown in Table S3. So, it withstands a large number of cycles under dynamic conditions of the screw shaft. It is also noted that the small L/D ratio delivers the higher fatigue life of the shaft and resists the maximum principal stress.

Total shear force and maximum bending moment acting on the screw shaft

The different dimensions of the screw shaft in

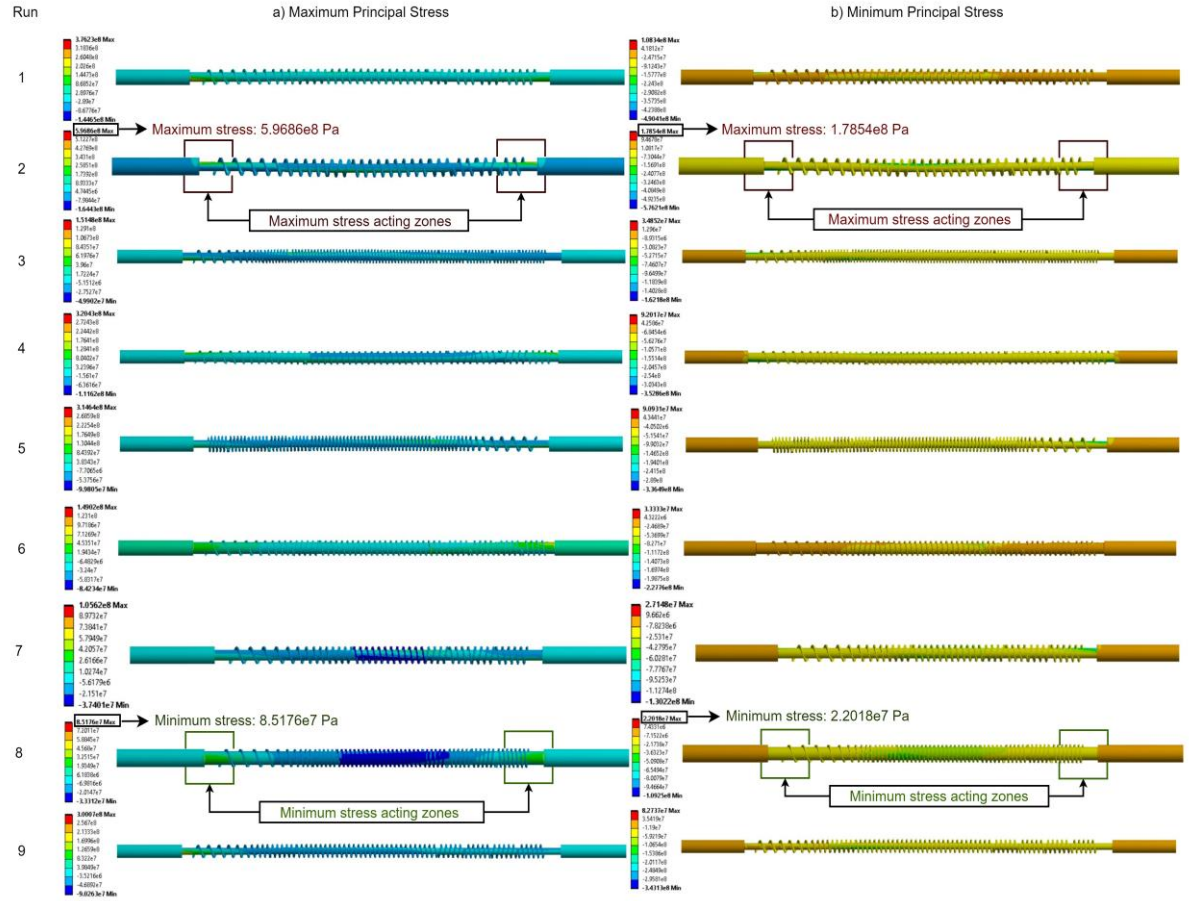

Figure 2. Contour plot for (a) maximum principal stress in Pa; (b) minimum principal stress in Pa under external pressure for Taguchi's design of screw shaft.

each run given in Table S2 were converted into the beam with a corresponding circular cross-section for beam analysis under the finite element method. The cross-section of each beam provides the different area moment of inertia in the Y and Z axes calculated using Eq. (6). Area moment of inertia always shows the indirect proportionality with the bending moment, which implies that the shaft will bend very less for a larger area moment of inertia. Moreover, it depends on the geometrical property of the shaft. The boundary conditions used for the beam analysis are similar to the stress analysis. The beam was segmented into seven sections based on the pressure acting on the shaft given in Fig. S1 (Supplementary material) and Fig.1a.

Shear force at the given section is the rate of change of bending moment with respect to the axial distance given in Eq. (7). It is also the first derivative and shows direct proportionality with the bending moment. In this regard, the bending moment should be minimal for any cross section to withstand the deflection. Additionally, the bending moment mainly depends on the nature and magnitude of the load, type of support, and also dimensional parameters like flight length, diameter, and depth of the shaft [34,44]. Now, the type of load and support are similar for each model of the screw shaft. In this respect, Fig. S3b shows the lowest (9537.2 Nm) and highest (14884 Nm) bending moments of the screw shaft exhibited by run-2 and run-4 respectively. The bending moment lies between 9646.8 Nm and 14771 Nm for the rest of Taguchi's runs. There was a slight difference in bending moment (110 Nm) between run-2 and run-8. As recommended in the principal stress, the dimensions applied for run-2 and run-8 are suitable for designing the screw shaft with minimum bending effects due to having less area moment of inertia compared to the remaining models. Also, these runs have a smaller L/D ratio to resist the bending against the external load.

Influence of maximum bending and shear stress on the screw shaft

Figs. S4a and S4b illustrate the contour plot for bending and shear stress, which were derived by solving the FEM equation under transient conditions. These stresses mainly depend on the geometrical dimensions like radius (distance from the neutral axis), length, and helix angle of the shaft and it should be minimum for any material to withstand the fatigue

failure. In the present study, the minimum values of bending (9.1276 x 10^8 Pa) and shear stress (3.7969 x 10^7 Pa) were experienced in run-8, which also exhibits the maximum fatigue safety factor of n=1.2 estimated using Eq. (8). Moreover, run-8 withstands the stress of 1.2 times higher than the allowable stress of H13. Table S4 shows the maximum endurance limit of 10^7 was observed for run-8, as a result of the intersection of bending and shear stress acting below the modified Goodman line shown in Fig. 3. Meanwhile, run-9 shows the maximum bending stress value of 4.9549 x 10^9 Pa and its corresponding shear stress of 1.2643 x 10^8 Pa but it possesses the minimum safety factor of 0.21 and endurance limit of 10^3, which was inappropriate dimensions for designing the screw shaft. It was noticed that the wide range of bending and shear stress was perceived for the remaining runs from 1.2169 x 10^9 Pa to 4.0939 x 10^9 Pa and 4.6412 x 10^7 Pa to 2.2281 x 10^8 Pa respectively. It also provides an intermediate safety factor from 0.26 to 0.87 and an endurance limit from 10^3 to 10^6 for residual runs, which is also not suitable to design the screw shaft [32,36].

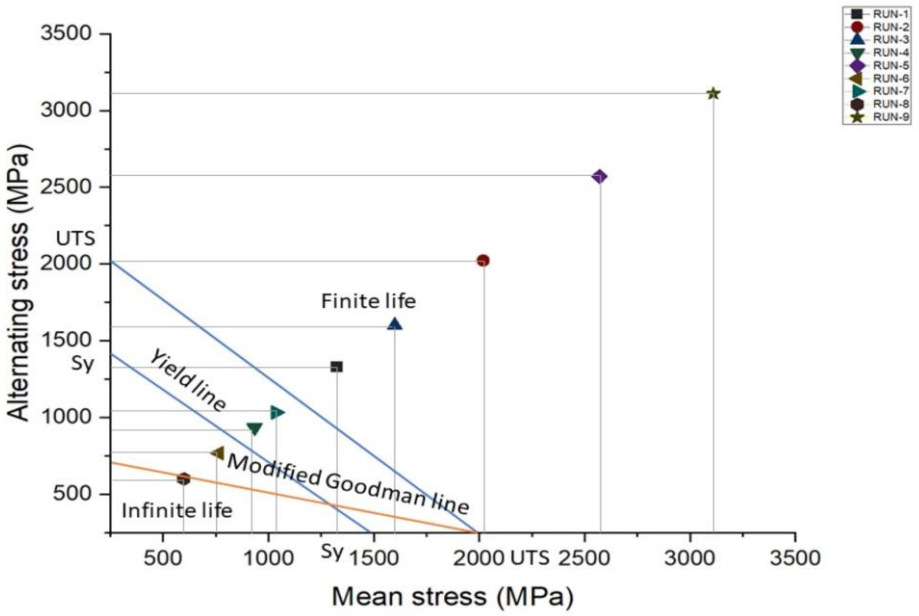

Figure 3. Goodman life diagram for calculating the endurance cycle of the screw shaft.

From the above details, it is noted that the bending and shear stress is gradually increased with decreasing the diameter and increasing the length of the shaft. The safety factor calculated in Table S4 shows a noticeable increase when decreasing the helix angle of the screw. Also, the bendability of the screw is decreased by increasing the helix angle. It is observed that the bending stress decreased as a result of increasing pitch length at the constant diameter of the shaft, which shows that the pitch can indirectly influence the bending and shear stress of the screw shaft. The thread occurs very close for a shorter pitch that can evenly distribute the higher stress over the length of the shaft at a given torque. Hence, run-8 shows a shorter length, larger pitch, diameter, and helix angle which is accepted for designing the safe screw shaft.

Total deformation and its factor of safety experienced by the screw shaft

Fig. S5a,b represents the total deformation and FOS, which was determined for each run of Taguchi's design. In this regard, the maximum deformation of 5.5917 mm was acting on the mid-section of run-2 shown in Fig S5a. Likewise, run-8 shows the minimum deformation of 0.457 mm acting on the mid-section of the screw shaft. In addition, the second and third minimum deformation were experienced by run-6 and 7 which shows the larger diameter and shorter flight length. Run-4, 6, 8, and run-1, 3, and 7 also show that the deformation gives direct proportionality with flight length at a constant diameter. Hence, it is observed that the shaft with a shorter length provides less deformation than the larger flight length.

In Goodman's calculation, the safety factor was calculated using mean bending and shear stress experienced by the shaft. It can endure stress 1.2 times higher than the allowable stress of the material. Now, the principal and shear stress were used for determining the safety factor of the screw shaft. From Fig. S5b, it is observed that the FOS range from 3.94 to 15 was considered a safe design under static and dynamic conditions of the shaft. It shows that the structure can resist the maximum stress of 3.5 to 15

times more than the allowable stress. In specific, the safety factor is comparatively less for runs-1, 2, and 8 due to the minimum helix angle of the screw but these values are not considered inappropriate dimensions for designing the screw shaft. The design with an optimal safety factor suggests the economic structure of the screw shaft for the given hydrothermal process. In the case of FOS, all nine runs are applicable for designing the screw shaft with more reliability and cost-efficient.

Conversion of multiple responses to single response using GRG optimization

The numerical results of each response variable obtained from transient structural simulation are given in Table S5. The multiple responses like principal stress, shear stress, bending stress, bending moment, and total deformation were converted to a single response, called GRG. Initially, the response parameters were converted into normalized values. Then, the computed deviation can be applied to find the GRC values using Eq. (12) for individual runs. Further, Table S6 provides the values of grey relational grade determined by taking the mean of GRC values of respective runs [20]. Finally, the rank was allocated to each run depending on the highest to lowest GRG values given in Table S6. From the GRG analysis, it is observed that run-8 is positioned as rank-1 due to the higher GRG value of 0.992 and run-9 acquired the GRG value of 0.434, positioned as rank-9. It suggested that the dimensions of run-8 are preferred to design the screw shaft.

The Grey Fuzzy Reasoning Grade (GFRG) was predicted to verify the formulated GRG values. In this regard, the Mamdani interface system was applied to relate the input factors like flight length, pitch, helix angle, and depth and also consider the GRG value as output. The linguistic variable was assigned to each level of input parameters as low, medium, and high shown in Fig. S6a. Likewise, it was specified to output parameters as extremely low, very low, low, low medium, medium, high, very high, and extremely high as expressed in Fig. S6b of a certain range from 0.434 to 0.992 as given in Table S7. Then, these linguistic variables were assisted in formulating the nine fuzzy rules based on certain conditions as given in Table S8. Moreover, Fig. S7. illustrates the fuzzy interface system that provides the values of GFRG depending on customized fuzzy rules. It shows the GFRG value of run-8, which is the higher value among other runs. It also provides the intermediate responses to their corresponding inputs, which helps to understand the variation of GFRG value.

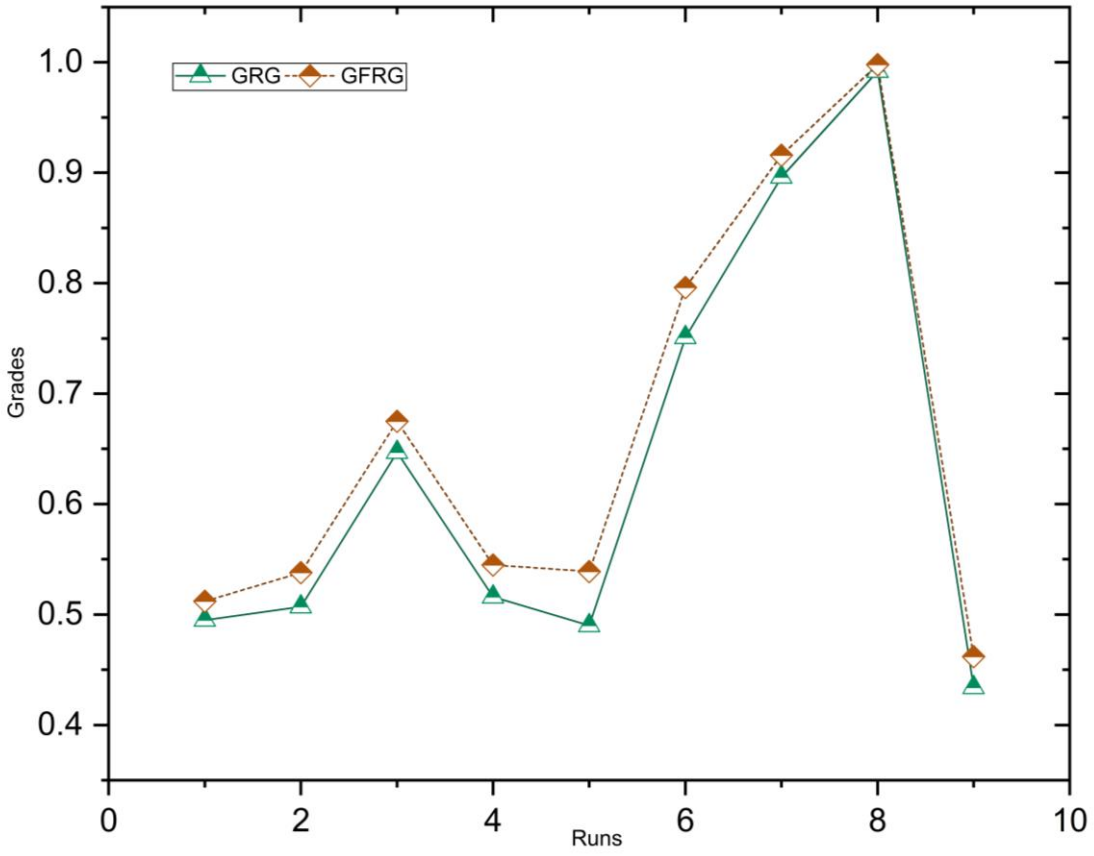

Figure 4. Comparison of grades concerning simulation trials.

The behavior of the response parameters in terms of GRG and GFRG values are given in Table S9 and the graphical representation is shown in Fig. 4. Whence, it is observed that the GFRG is improved up to 6.1 % as compared to GRG, which implies the reduction of fuzziness in the simulation system. Aforementioned in the previous section, run-8 shows the higher GFRG value of 0.998 and is positioned as rank-1 as given in Table S9 and Fig. 4, and is preferred to design the screw shaft.

Signal-to-Noise analysis using GFRG

Signal-to-Noise analysis given in Table S10 provides the ranking method to select the prominent control factors based on the delta value, which is the deviation between the actual and target value of the response variable, GFRG. Higher and lower delta values suggested the extreme and moderate deviation of the response with respect to the control factors. In this regard, the depth of the screw shaft possesses a higher delta value of 3.272 and is positioned as rank-1. Likewise, flight length and pitch show intermediate deviations of 2.52 and 1.25 ranked as 2 and 3 respectively. The Helix angle shows the minimum delta value of 0.76 and is positioned as rank-4, which shows the less significant factor for a corresponding response. These values were compared with the SN ratio graph shown in Fig. 5b, which also suggests the similar behavior of the control factors concerning GFRG. From Fig. 5b, it is observed that flight length and depth showed a higher deviation from the mean than other factors as mentioned in Table S11. Moreover, Fig. 5 also preferred the shorter flight length and depth of 1160 mm and 7.25 mm, nominal pitch, and helix angle of 21.75 mm and 6.8° respectively for reducing the direct responses acting on the screw shaft.

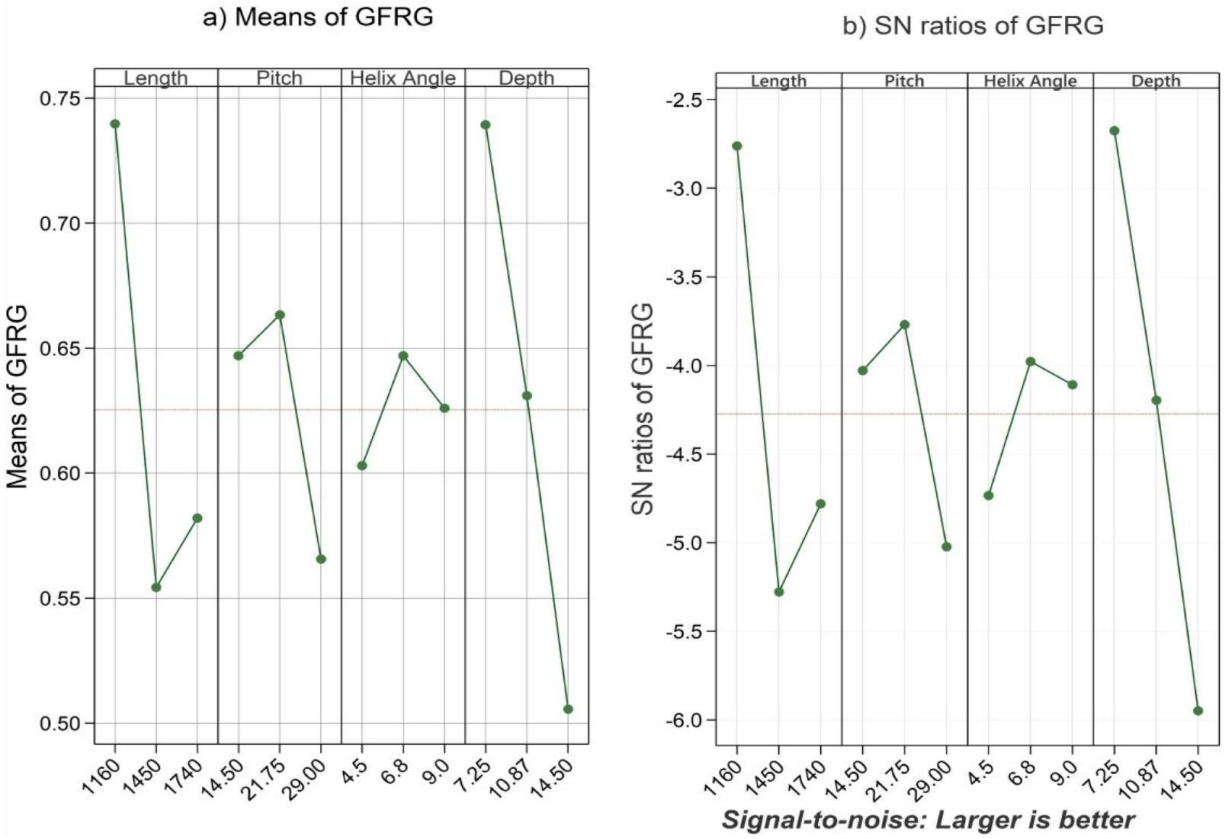

Figure 5. Means and SN ratios of grey fuzzy relational grade.

Single response optimization using GFRG

ANOVA was employed to calculate the contribution of each dimensional factor with respect to a single response referred to as GFRG. It suggests that flight length is the most significant factor with a contribution of 31.52%. Likewise, pitch, helix angle, and depth also convey the noticeable contributions of 27.96%, 22.5%, and 18.02%. The *P*-values calculated in Table S11 were less than 0.05 which rejects the null hypothesis with the acceptance of the alternative hypothesis. It shows potential intent toward the deviation of the GFRG from the mean value. Moreover, Table S11 provides the estimated *R*-squared and adjusted *R*-squared values as 99.34% and 97.36% which also shows the vital deviation in the GFRG with respect to different levels of dimensional factors. Nevertheless, flight length, pitch, helix angle, and depth were crucial factors for controlling direct responses like

principal stress, shear stress, bending stress, bending moment, and total deformation. Eq. (16) proposed the regression equation to find the intermediate GFRG with respect to input factors.

The regression equation for calculating the intermediate GFRG value is given by:

$$GFRG = 0.6700 + 0.1537\ w_1 - 0.0510 w_2 - 0.1027 w_3 + 0.0637 x_1 + 0.0547\ x_2 - 0.1183 x_3 + 0.8231 y_1 + 0.0463\ y_2 - 0.01083\ y_3 + 0.1093\ z_1 + 0.0310\ z_2 - 0.1403 z_3 \quad (16)$$

where, w - flight length, x - pitch, y - helix angle and z - depth.

Confirmation test for the screw shaft

When analyzing the various results obtained from both numerical and statistical methods for the given response variable, it is capable of determining the optimum dimensions for designing the efficient screw shaft. Initially, the two sets of dimensions were selected as 1160 mm, 14.5 mm, 4.5°, 7.25 mm, and 1160 mm, 14.5 mm, 9°, and 7.25 mm based on the results of GFRG and SN analysis. The final transient structural analysis was performed to get the perfect set of values from the above-mentioned dimensions. Fig. 6a,b reveals that similar values of bending stress and bending moment were obtained for both analyses. The values of principal and shear stress possess 9.8% and 37.5% higher internal resistance in SN analysis when compared to GFRG analysis. In the case of total deformation, the value acquired from SN analysis shows 87.5% less deformation compared to GFRG analysis. Even though slight increment in principal and shear stress, this highest value is limited within the ultimate stress of H13. In addition, the total deformation is the most considerable response to design the screw shaft among other responses. Hence, the optimized dimensions obtained from the SN analysis were preferred to design the screw shaft. The optimum values of flight length, pitch, helix angle, and depth were selected as 1160 mm, 21.75 mm, 6.8°, and 7.25 mm respectively.

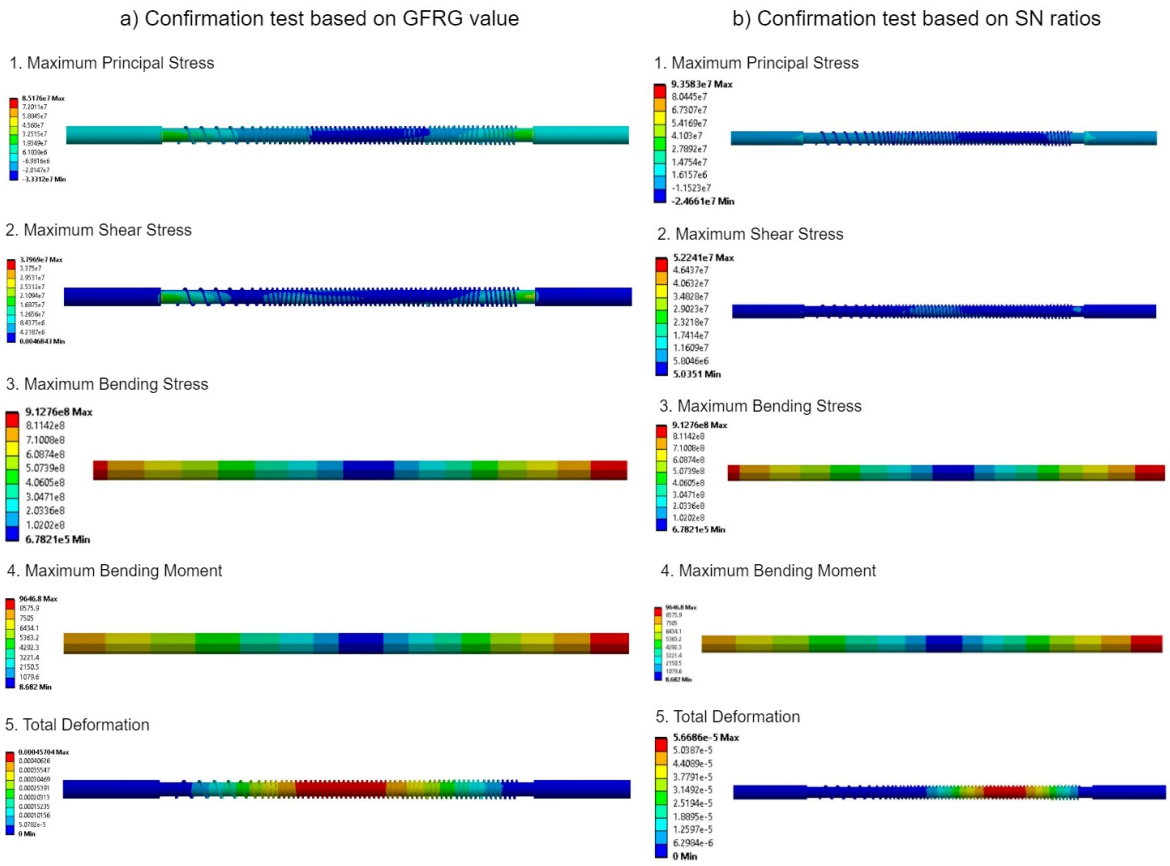

Figure 6. Confirmation structural analysis depends on GFRG and SN analysis.

CONCLUSION

The optimal screw shaft has been designed for the high-pressure HTCL reactor with the help of FEM followed by statistical optimization using GRG, GFRG, ANOVA, and Taguchi's method. Maximum principal stress, maximum shear stress, maximum bending

stress, total bending moment, and deformation were taken as the crucial response variables for dimensional optimization of depth, helix angle, flight, and pitch length. It is observed that the dimensional parameters present in run-8 show the minimum stress and total deformation. In addition, the Goodman method also conveys that run-8 has ensured a higher safety limit and endurance limit of 1.20 and 10^7 cycles respectively. The above-mentioned five response variables were successfully converted into a single response termed GRG during multi-response optimization. The result possesses that run-8 dimensions have the highest GRG and GFRG value of 0.992 and 0.998 respectively, and it is suitable for designing the screw shaft. Conversely, the SN ratio from Taguchi analysis suggests a slightly modified dimension in helix angle compared to run-8. The two sets of dimensions were taken for confirmation test as set-1 consists of flight length=1160 mm, depth=7.25 mm, helix angle=4.5°, pitch length=14.5 mm, and set-2 comprise of flight length=1160 mm, depth=7.25 mm, helix angle=6.8°, and pitch length=21.75 mm depending on the results from GFRG and SN analysis respectively. From the confirmation results, it is recommended that the dimensions obtained from the SN analysis provide very little deformation of 0.0566 mm, which is 87.5 % lower than the deformation formed in the dimensions of the GFRG analysis. From the above details, the optimal dimensions were selected from SN analysis (set-2) as 1160 mm, 14.5 mm, 9°, and 7.25 mm for respective flight length, pitch, helix angle, and depth of the screw shaft.

ACKNOWLEDGMENTS

This research work was supported by the Department of Science and Technology, Ministry of India under the sanction order no. DST/TDT/WMT/Plastic Waste/2021/08(G)&(C). This research article is based on numerical simulations and optimization conducted by the authors. The authors would like to thank all the researchers who contributed to the research work. Throughout this study, the authors acknowledge Kongu Engineering College for their support of the research facility.

REFERENCES

[1] C.D. Venkatachalam, S.R. Ravichandran, M. Sengottian, Environ. Eng. Res. 27(2021), 200555-200571. https://doi.org/10.4491/eer.2020.555.

[2] F. Campuzano, R.C. Brown, J.D. Martínez, Renew. Sust. Energ. Rev. 102(2019), 372-409. https://doi.org/10.1016/j.rser.2018.12.014.

[3] S.S. Toor, L.A. Rosendahl, A. Rudolf, Energy 36 (2011), 2328-2342. https://doi.org/10.1016/j.energy.2011.03.013.

[4] C.D. Venkatachalam, M. Sengottian, S.R. Ravichandran, K. Subramaniyan, P. Kalappan Thangamuthu, Period. Polytech. Chem. Eng. 65 (2020), 105-115. https://doi.org/10.3311/PPch.15187.

[5] M.S. Wahyudiono, M. Goto, Fuel 88 (2009) 1656-1664. https://doi.org/10.1016/j.fuel.2009.02.028.

[6] B. Miljkovic, Period. Polytech. Chem. Eng. 67 (2023) 62-73. https://doi.org/10.3311/PPch.20257.

[7] M.S. Wahyudiono, M. Goto, Chem. Eng. Process 47 (2008) 1609-1619. https://doi.org/10.1016/j.cep.2007.09.001.

[8] I.M. Sintamarean, I.F. Grigoras, C.U. Jensen, S.S. Toor, T.H. Pedersen, L.A. Rosendahl, Biomass Convers. Biorefin. 7 (2017) 425-435. https://doi.org/10.1007/s13399-017-0247-9.

[9] P. Brassard, S. Godbout, V. Raghavan, J.H. Palacios, M. Grenier, D. Zegan, Energies 10 (2017) 288-302. https://doi.org/10.3390/en10030288.

[10] G. Shengbo, Y. Peter Nai Yuh, C. Yoke Wang, X. Changlei, W.M. Wan Adibah, L. Rock Keey, P. Wanxi, Y. Tong-Qi, T. Meisam, A. Mortaza, S.k. Christian, L. Su Shiung, Renew. Sust. Energ. Rev. 135(2021) 110148-110162. https://doi.org/10.1016/j.rser.2020.110148.

[11] C.E. Efika, C. Wu, P.T. Williams, J. Anal. Appl. Pyrolysis 95(2012) 87-94. https://doi.org/10.1016/j.jaap.2012.01.010.

[12] S.K. Hoekman, A. Broch, L. Felix, W.E. Farthing, Energy Convers. Manag. 134(2017) 247-259. https://doi.org/10.1016/j.enconman.2016.12.035.

[13] P. Evangelopoulos, H. Persson, E.K. Kantarelis, W. Yang, Process Saf. Environ. Prot. 143 (2020) 313-321. https://doi.org/10.1016/j.psep.2020.07.006.

[14] S. Ge, P.N.Y. Yek, Y.W. Cheng, C. Xia, W.A.W. Mahari, R.K. Liew, P. Wanxi, Y. Tong-Qi, T. Meisam, A. Mortaza, S.k. Christian, L. Su Shiung, Renew. Sust. Energ. Rev. 135 (2021) 110148-110162. https://doi.org/10.1016/j.rser.2020.110148.

[15] L. Halasz, Period. Polytech. Chem. Eng. 34 (1989) 173-196. https://pp.bme.hu/ch/article/view/2721.

[16] A.Y. Doost, D.L. William, Sustainability 12 (2020) 7352-7385. https://doi.org/10.3390/su12187352.

[17] M. Meise, L. Jäger, A. Wilk, T. Heitmann, S. Scholl, Chem. Ing. Tech. 92 (2020) 1074-1082. https://doi.org/10.1002/cite.202000092.

[18] E.P. Bilalis, M.S. Keramidis, N.G. Tsouvalis, Mar. Struct. 84 (2022) 103194. https://doi.org/10.1016/j.marstruc.2022.103194.

[19] S.P.S. Kumar, R. Rao, B.A. Rajeevalochanam, Procedia Eng. 55 (2013) 499-509. https://doi.org/10.1016/j.proeng.2013.03.287.

[20] C. Moganapriya, R. Rajasekar, P. Sathish Kumar, T. Mohanraj, V.K. Gobinath, J. Saravanakumar, Struct. Multidiscip. Optim. 63 (2020) 1169-1186. https://doi.org/10.1007/s00158-020-02751-9.

[21] S. Ajith Arul Daniel, R. Pugazhenthi, R. Kumar, S. Vijayananth, Def. Technol. 15 (2019) 545-556. https://doi.org/10.1016/j.dt.2019.01.001.

[22] S.M. Senthil, R. Parameshwaran, S. Ragu Nathan, M. Bhuvanesh Kumar, K. Deepandurai, Struct. Multidiscipl. Optim. 62 (2020) 1117-1133. https://doi.org/10.1007/s00158-020-02542-2.

[23] F. Xiong, D. Wang, S. Zhang, K. Cai, S. Wang, F. Lu, Struct. Multidiscipl. Optim. 57 (2017) 441-461. https://doi.org/10.1007/s00158-017-1749-6.

[24] W. Yao, K. Cai, Y. Xu, Optimizing the beam-like structure of a vehicle body using the grey-fuzzy-Taguchi method 53 (2020) 49-70. https://doi.org/10.1080/0305215X.2019.1698033.

[25] M. Saleh, Z. Zaidi, M.H. Ionescu, C. Hurt, K. Short, J.E. Daniels, P. Munroe, L.E. Edwards, D. Bhattacharyya, Int. J. Plast. 86 (2016) 151-169. https://doi.org/10.1016/j.ijplas.2016.08.006.

[26] V.A. Girisha, M.M. Joshi, L.J. Kirthan, A. Bharatish, R. Hegde, Sādhanā 44 (2019) 1-8. https://doi.org/10.1007/s12046-019-1111-3.

[27] H. Kweon, J. Kim, O. Song, D. Oh, Nucl. Eng. Technol. 53 (2021) 647-656. https://doi.org/10.1016/j.net.2020.07.014.

[28] B. Bozorgmehri, V.-V. Hurskainen, M. K. Matikainen, A. Mikkola, J. Sound Vib. 453 (2019) 214-236. https://doi.org/10.1016/j.jsv.2019.03.022.

[29] R. Scheepers, P.S. Heyns, J. Mech. Sci. Technol. 30 (2016) 4063-4074. https://doi.org/10.1007/s12206-016-0819-9.

[30] N.L. Pedersen, J. Strain Anal. Eng. 56 (2020) 195-205. https://doi.org/10.1177/0309324720969530.

[31] O.A. Samuel, I.O. Bankole, O.I. Christianah, O.M.A. Adeyinka, F.K. Joseph, J. Mater. Res. 8 (2019) 105-111. https://doi.org/10.1016/j.jmrt.2017.10.007.

[32] Á. Sass, A. Kummer, Z. Ulbert, A. Egedy, Period. Polytech. Chem. Eng. 65 (2021) 536-549. https://doi.org/10.3311/PPch.17095.

[33] Z. Yongjie No, X. Hongmei No, Appl. Eng. Agric. 35 (2019) 453-460. https://https://doi.org/10.13031/aea.13351.

[34] S. Seifoori, A. Mahdian Parrany, M. Khodayari, Eng. Fail. Anal. 116 (2020) 104752-104768. https://doi.org/10.1016/j.engfailanal.2020.104752.

[35] L. Dao-Kui, L. Xian-Fang, Cr Mecanique 344 (2016) 556-568. https://doi.org/10.1016/j.crme.2016.01.007.

[36] A. Roy, P. Palit, S. Das, G. Mukhyopadyay, Eng. Fail. Anal. 112 (2020) 104511-104526. https://doi.org/10.1016/j.engfailanal.2020.104511.

[37] K. Cai, D. Wang, Struct. Multidiscipl. Optim. 56 (2017) 1539-1553. https://doi.org/10.1007/s00158-017-1728-y.

[38] Q. Sawei, X. Zhigang, H. Hong, Y. Zhong, X. Erli, X. Congchang, L. Luoxing, Struct. Multidiscipl. Optim. 64 (2021) 4129-4145. https://doi.org/10.1007/s00158-021-03035-6.

[39] A. Tanmaya, G. Raghvendra, A. Sudeekcha, S. Vishal, K. Manish, K. Saket, Sustain. Futures 2 (2020) 100039-100050. https://doi.org/10.1016/j.sftr.2020.100039.

[40] X. Deng, S. Wang, H. Youssef, L. Qian, Y. Liu, Struct. Multidiscipl. Optim. 62 (2020) 2833-2847. https://doi.org/10.1007/s00158-020-02640-1.

[41] D. Sunil, R.N. Suresh Kumar, Measurement 169 (2021) 108340-108347. https://doi.org/10.1016/j.measurement.2020.108340.

[42] B. Maël, B. Johan, V. Laura, R.-C. Ainhoa, C. Edwin, Renew. Energy. 172 (2021) 941-954. https://doi.org/10.1016/j.renene.2021.03.076.

[43] M.A. Perras, H. Wannenmacher, M.S. Diederichs, Rock Mech. Rock Eng. 48 (2014) 1647-1671. https://doi.org/10.1007/s00603-014-0656-z.

[44] W. Zhang, J. Yang, C. Li, R. Dai, A. Yang, J. Vib. Control 23 (2016) 1183-1192. https://doi.org/10.1177/1077546315590908.

CHITRA DEVI VENKATACHALAM[1]

PREMKUMAR BHUVANESHWARAN[1]

MOTHIL SENGOTTIAN[2]

SATHISH RAAM RAVICHANDRAN[2]

[1]Department of Food Technology, Kongu Engineering College, Perundurai, Tamil Nadu, India.

[2]Department of Chemical Engineering, Kongu Engineering College, Perundurai, Tamil Nadu, India

NAUČNI RAD

PROJEKTOVANJE ZASNOVANA NA POUZDANOSTI OPTIMIZACIJA PUŽNE OSOVINE ZA KONTINUALNI PROCES HIDROTERMALNE KO-LIKVEFAKCIJE VISOKOG PRITISKA

Hidrotermalna ko-likvefakcija (HTKL) je istaknuti proces za proizvodnju bioproizvoda sa većom brzinom konverzije. Izvodi se na visokim temperaturama i pritisku u prisustvu vode. Ranije se uglavnom sprovodio u šaržnim reaktorima, koji imaju velika ograničenja uključujući radnu zapreminu, povratno mešanje i tegoban proces za visoku produktivnost. S tim u vezi, ovo istraživanje je sprovedeno s ciljem projektovanja pužne osovine za HTKL proces visokog pritiska. Dimenzionalni faktori, uključujući dužinu kretanja, korak, ugao spirale i dubinu, uzeti su u obzir da bi se dizajnirala optimalna pužna osovina. Isto tako, glavni naponi, napon smicanja, napon savijanja, moment savijanja i ukupna deformacija smatrani su neizbežnim odzivnim promenljivima za analizu unutrašnje čvrstoće osovine. U tom smislu, Taguči L9 (34) ortogonalni niz je korišćen kao eksperimentalni plan. Zatim su numerički rezultati analize prelazne strukture analizirani uz pomoć statističkih metoda kako bi se pronašle najuticajnije dimenzije za minimiziranje odzivnih promenljivih. Shodno tome, upoređeni su rezultati različitih metoda i izabrani su najoptimalniji parametri.

Ključne reči: hidrotermalna ko-likvefakcija, pužna osovina, metoda konačnih elemenata, analiza napona, Gudmanovi kriterijumi otkaza, tehnika optimizacije višestrukog i jednog odziva.

CI&CEQ
Chemical Industry & Chemical Engineering Quarterly

Available online at
Association of the Chemical Engineers of Serbia AChE
www.ache.org.rs/CICEQ

Chem. Ind. Chem. Eng. Q. 30 (4) 349–357 (2024) CI&CEQ

ITUMELENG KOHITLHETSE
SUTER KIPLAGAT EVANS
MUSAMBA BANZA
ROBERT MAKOMERE

Department of Chemical and Metallurgical Engineering, Vaal University of Technology, Private Bag X021, South Africa

BLAST FURNACE SLAG FOR SO_2 CAPTURE: OPTIMIZATION AND PREDICTION USING RESPONSE SURFACE METHODOLOGY AND ARTIFICIAL NEURAL NETWORK

Article Highlights

- Blast furnace slag preparation and characterization for SO_2 capture
- BFS optimization through Central Composite Design
- Levenberg-Marquardt algorithm in ANN for predicting the performance of the sorbent
- The combined optimization and prediction approach for optimum performance

Abstract

The main reaction parameters examined were the amount of blast furnace slag, the hydration duration, ammonium acetate concentration, and temperature. The Response surface methodology was employed to quantify their impact on the sorbent's surface area. Using a central composite design, the surface area of the resulting sorbent corresponding to Brunauer-Emmett-Teller (BET) was investigated. The sorbents produced range in surface area from 49.89 to 155.33 m^2/g. Additionally, the effectiveness and response prediction capacities of the Response Surface Methodology (RSM) and Artificial Neural Network (ANN) modeling methodologies were investigated. The models were assessed using various statistical metrics, including (MSE) mean squared error, (ARE) average relative errors, the (SSE) sum of squared errors, (HYBRID) Hybrid fractional error function, (SAE) Sum of the absolute errors, (R^2)coefficient of determination, and Root means square. According to statistical evidence, the ANN approach surpassed the RSM-CCD model approach. The surface area of the sorbent was shown to be significantly influenced by interactions between variables in addition to all the individual variables examined. The sorbent was made from a material with substantial structural porosity based on SEM. The functional groups were identified using FTIR. The XRF determined the elemental composition of BFS-based sorbents.

Keywords: blast furnace slag, optimization, central composite design, artificial neural network, response surface methodology.

SCIENTIFIC PAPER

UDC 669:66:621:519.87

The control of atmospheric pollution brought on by combustion processes like coal has recently been subject to stricter environmental restrictions worldwide.

Correspondence: I. Kohitlhetse, Vaal University of Technology, Departement of Chemical and Metallurgical Engineering, Bag X021, Vanderbijlpark, South Africa.
E-mail: 222386568@edu.vut.ac.za
Paper received: 17 July, 2023
Paper revised: 5 February, 2024
Paper accepted: 4 March, 2024

https://doi.org/10.2298/CICEQ230717006K

The most plentiful and cost-effective energy source is coal, essential for supplying the world's rising need for electricity [1]. Burning coal provides various difficulties even if it is a significant energy source. The discharge of pollutants, particularly sulphur dioxide, into the environment is one of the most critical problems facing enterprises that burn coal. Sulphur in coal combines with air during combustion to create sulphur dioxide (SO_2). Sulphur dioxide is one of the many contaminants in our atmosphere (SO_2) [2]. Burning things containing sulfur releases a harmful gas into the atmosphere. All types of coal and oil include sulphur. Industrial facilities that use fossil fuels to produce energy or extract metal

from ore are the primary sources of SO_2 emissions (smelter). Other anthropogenic sources include locomotives, ships, and other large vehicles or equipment that burn sulphur-rich fuel. Volcanoes are the sole crucial natural source of SO_2. Only roughly one-third of all SO_2 emissions into the atmosphere come from volcanoes. Volcanic SO_2 has little effect in South Africa because no active volcanoes exist [3].

Both direct SO_2 exposure and secondary pollutants created when SO_2 combines with other airborne molecules negatively affect health. A significant secondary contaminant associated with SO_2 is delicate particulate matter. Exposure to SO_2 results in immediate symptoms such as breathing difficulties, respiratory system injury, and a burning sensation in the nose, throat, and lungs. Severe and long-term health effects include early death, heart and lung disease, dementia, and problems with conception [4]. They also have diminished cognitive function. Aside from the harmful effects on human health, every combustion process that releases SO_2 releases large volumes of greenhouse gases into the environment. SO2 sources thus have a disadvantageous immediate consequence on the region's health and a negative long-term impact on human well-being globally due to greenhouse gas emissions, which drive global warming.

Several SO_2 emission control techniques based on emission prevention or flue gas capture turned out to be investigated, and some came to be implemented in sulphur dioxide-discharging industries. Since sulphur dioxide emissions are proportional to the amount of sulphur in fuel and the total used in combustion, reducing sulphur content can result in significant reductions. Using ultra-low sulphur flue is the most environmentally friendly way to reduce sulphur dioxide emissions; however, obtaining cleaner flue comes at a high refining cost [4]. Installing a sulphur restoration unit that generates profit-making sulphur in the form of sulphuric acid is an option if the gas flow consists of a high concentration of sulphur and the restoration unit can withstand the corrosive environment associated with acid sulphur [5]. In industries that use coal as a fuel source, sulphur in pyrite (Fe_2S) can be easily removed by physically washing coal with water. However, increased practical costs and fuel-efficient design property changes could offset this. Even though many treatment methods, including WFGD (FGD), biological processes, and technological innovations based on electron beam irradiation, can achieve high sulphur removal efficiency, several problems still need to be solved, including high space requirements and high safety protection requirements [6]. Coronal pulse discharge, on the other hand, is a relatively new and unproven SO_2 removal method, even though it does not require a particle accelerator and offers the highest level of protection. Because of its simplicity and high desulphurization capacity, flue gas desulphurization (FGD) is the most frequently used method to reduce SO_2 emissions [7].

A variety of sorbents that are various chemical compounds and naturally occurring materials can be quickly produced, or waste generated by a variety of processes can be used in the method. Several flue gas desulphurization (FGD) techniques are water- self-sufficient, resulting in lower operating costs and no wastewater production. It is necessary to utilize the proper Flue Gas Desulphurization (FGD) technology to reduce SO2 emissions into the environment [8]. Coal combustion produces coal fly ash, another type of combustion waste, and pollutants like sulphur dioxide (SO2). Researchers have looked into flue gas desulphurization using absorbent synthesis from a combination of calcium hydroxide, calcium oxide, and calcium sulphate to address these difficulties [9]. Numerous studies have shown that, for instance, when coupled with Ca (OH)2 or CaO during the hydration process, coal ash can create an absorbent with a higher SO2 capture capacity than hydrate lime [2,8,10].

Blast Furnace Slag (BFS), a byproduct of the iron and steel industry, has promise as a practical and affordable substitute sorbent for flue gas desulphurization technology. The two main ingredients for removing SO_2 are abundant in BFS: CaO and silica. They produce Calcium Silicate Hydrate Aggregates, which are essential for increasing the surface area of the Sorbent. According to some studies, sorbent made of iron blast furnace slag and hydrated lime (BFS/HL) exhibits higher SO_2 reactivity than hydrated lime alone under the dry or semi-dry FGD method [4]. It is clear from earlier sources that the production of high surface area calcium silicate hydrates during the sorbent preparation or slurring process is caused by an enhancement in the sorbent's reactivity patterns, using calcium, or the capacity to capture SO_2 [4].

When a dependent output variable is impacted by several independent input factors rather than one factor at a time, the response surface methodology is a statistical method for optimizing the process [11]. The output variable's name is the response. RSM assesses all process factors concurrently while predicting an outcome as an improved systematic approach to experimentation. The central composite design is one of the critical components of RSM. The experiments used a three-level experimental design called the central composite design, which combined the axial and factorial design points. Its key benefit is that it demands multiple experimental runs to determine the

proper conditions for experimentation [12].

A model of computation called an artificial neural network can be used to predict how biological neurons process input. Most neural network models feature hidden layers in addition to input and output layers; the number depends on the inquiry type of investigation [8]. The primary property of a neural network is its ability to carry out internal calculations to derive the desired output from a set of input data. Given enough data, the ANN can evaluate multifactorial, non-linear, linear, and complex procedures by training the multiple input-output networks technique [13,14]. Because it reliably and effectively depicts the non-linear interactions between the variables and responses of various processes, ANN may be used in intricate systems [15].

In the current study, the surface area was assessed by BET analysis by investigating the effect of BFS amount, the ammonium acetate amount, hydration time, and hydration temperature. With the fewest experiments, the RSM approach enables the study of the individual variables and their combined impacts in the experimental range. This study's main objective is to evaluate the surface area of BFS for SO_2 capture using RSM and ANNs, estimate their effectiveness, and compare ANN and RSM techniques. The experimental data was then compared to the outcomes of the two models.

MATERIALS AND METODS

Raw materials

The Blast furnace slag was collected from a local company around Vanderbijlpark, South Africa. The ammonium acetate (>98%) and the calcium oxide (>97%) were all purchased from Merck, and the brine sludge was collected from a local chloral alkali industry.

Sorbent preparation of the sorbent

A known quantity (250 g) of brine sludge was heated for 4 hours, and 900 °C was set as the temperature in a furnace with muffles for maximal calcination. 200 mL of distilled water was heated to 65 °C, and 10 g of CaO was added while vigorously agitated. A certain amount (0–1 g) of ammonium acetate as the hydration agent and blast furnace slag (0–5 g) were added to the slurry at the same time. The hydration process was then accelerated by heating the blast furnace slag slurry for a set amount of time (1–10 hours) at a certain hydration temperature (30–90 °C). The resulting slurry underwent filtration for 2 hours at 210 °C during drying. The powdered sorbents were pelletized, smashed, and crushed to less than 75 μm to produce the required nanoparticle size.

Characterization of the sorbent

The functional compounds contained in the sorbent were examined using Fourier transform infrared spectroscopy (PerkinElmer UATR). Scanning electron microscopy (Philips XL30FEG) was employed to assess the shape of the surface. X-ray fluorescence (Philips expert 0993) was used for qualitative as well as quantitative techniques. The materials' BET surface area and pore volume were measured using an N2 sorption-desorption apparatus and ASAP 2020 Micromeritics.

Analysis using artificial neural networks and the response surface approach

Centrale composite design in Response surface methodology

Recent years have seen a rise in interest in response surface methodology (RSM), a set of mathematical and statistical methods for assessing the effects of numerous independent variables. RSM assesses the relationships between the response(s) and the independent variables, in addition to the effects of individual variables on the processes, whether operating alone or in conjunction [11]. This approach provides many benefits, including being less costly, requiring fewer experiments, exploring how different factors interact to affect response, predicting a response, assessing method suitability, and consuming less time [16]. This strategy employs low-order polynomial equations in a predefined area of the independent variables to attempt to find the optimal values for the independent variables for the most positive results. The sorbents' BET surface area was investigated using the CCD. This design helps assess how the sorbent preparation variables affect the sorbent's particular surface area. The variables for sorbent preparation explored are hydration time, BFS amount, hydrating agent (ammonium acetate) amount, and hydration temperature. The RSM analysis consists of 21 experimental data sets, with six central points.

According to Eq. (1), the response was calculated using an empirical second-order polynomial equation.

$$z = X0 + XaA + XbB + XcC + XdD + XaaA^2 + XbbB^2 + XccC^2 + XddD^2 + XabAB + XacAC + XadAD + XbcBC + XbdBD + XcdCD \quad (1)$$

where Z is the predicted outcome; X_0 denotes the model constant; Xa, Xb, Xc, and d denote linear coefficients; Xab, Xac, Xad, Xbd, and Xcd denote cross-product coefficients, and Xaa, Xbb, Xcc, and Xdd denote quadratic coefficients. A, B, C, and D denote independent variables.

The experimental design, analysis of variance, regression analysis, and optimization of process parameters in the desulphurization process were carried out using Design-Expert 13. ANOVA p-value and the regression coefficient (R^2) were used to assess the model's acceptability.

The steps in the optimization process are as follows: choosing the process variables and responses; choosing the experimental design; conducting experiments to gather data; fitting the model equation to the experimental data; performing an analysis of variance (ANOVA); and finally, determining the optimal conditions [17].

Artificial neural network (Levenberg-Marquardt)

Three-layer system: one neuron on the output layer, one hidden layer with six different modes, four neurons on the input layer, and measurements of hydration temperature, BFS, and ammonium acetate (4-6-1). The most common network, known as a back-propagation (BP-ANN) network, trains an approach for modeling data from experiments using a first-order gradient descent technique. It works well to cut down on errors with each repeat. Out of various back-propagation (BP) methods, we chose the Marquardt-Levenberg learning strategy. In the simulation and prediction of the sorbent production using ANN, the log-sigmoid function of transfer (log sig) in the layer that was hidden with four neurons in the first layer and a linear transfer function in the output node were both used. Modular artificial neural networks were developed using the Neural Networks (NN) toolbox and the mathematical application MATLAB 2022a. The ANN model's configuration processes involve the following steps: collecting data, training and test set selection, conversion of data into ANN inputs, identifying, training, and testing network structures, if necessary, repeating the processes several times to get the best model, and implementation of the best ANN model [13].

Error analysis functions

The Root mean square error (RMSE), Mean square errors (MSE), Average relative errors (ARE), Hybrid fractional error function (HYBRID), Sum of squares of errors (SSE), and Sum of absolute errors (SAE) Statistical evaluation tests were used to prove that the models were satisfactory [16]. The non-linear methods presented in Eqs. (2–7) were used to compare data from experiments with model-predicted data.

$$RMSE = \sqrt{\frac{1}{N}\sum_{i=1}^{n}\left(\frac{\left(Z_{(e)}-Z_{(p)}\right)^2}{Z_{(e)}}\right)} \quad (2)$$

$$SSE = \sum_{i=1}^{n}\left(Z_{(e)}-q_{(p)}\right)^2 \quad (3)$$

$$SAE = \sum_{i=1}^{n}\left[\left(Z_{(e)}-Z_{(p)}\right)\right] \quad (4)$$

$$HYBRID = \frac{1}{N-M}\sum_{i=1}^{n}\left(\frac{\left(Z_{(e)}-Z_{(p)}\right)^2}{q_{e(e)}}\right)x100 \quad (5)$$

$$ARE = \frac{100}{M}\sum_{i=1}^{n}\left(\left[\frac{\left(Z_{(e)}-Z_{(p)}\right)^i}{Z_{(e)}}\right]\right) \quad (6)$$

$$MSE = \frac{1}{N}\sum_{i=1}^{n}\left(Z_{(e)}-Z_{(p)}\right)^2 \quad (7)$$

where N is the total number of measurements, M is the maximum amount of model parameters, and $Z(p)$ and $Z(e)$ are the expected and measured values, expressed as m^2/g, respectively.

RESULTS AND DISCUSSION

The morphological analysis

Figure 1a depicts the morphological appearance of the blast furnace using SEM. An irregularly shaped structure of various sizes with a smooth surface was readily seen in the sample. The increased magnification shows the high structural porosity of the particle. Figure 1b shows SEM micrographs of sorbents after treatment. Before sulphation, the sorbent's overall pore structure and irregularly shaped particle arrangement are seen in the image. The sorbent has open spaces, implying that sulphation reactions can occur [8].

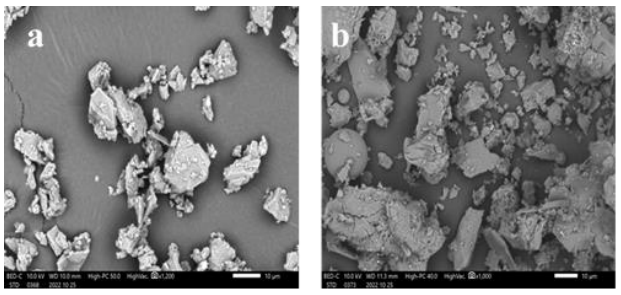

Figure 1. SEM of (a) the blast furnace and (b) after treatment.

Fourier-transform infrared spectroscopy Analysis

Figure 2 shows the antisymmetric vibration of the Ca-O and Si-O-Si bonds due to the strong, intense peak between 570 and 1100 cm^{-1} in the raw blast furnace slag. Because of the presence of calcium

hydroxide, the hydroxyl group is thought to be stretching vibrational bonds around 3500 cm^{-1}, which is related to the weak absorption band. In all the figures, the absorption peak associated with the C-O vibrations in the carbonate structure can be seen at 1600 cm-1 and roughly 700 cm^{-1}. The Ca-O vibration bond is attributed to the significant absorption band at 587 cm^{-1}. Silica and calcium oxide, which are essential in expanding the surface area of the sorbents, are among the components that make up the functional group present [4].

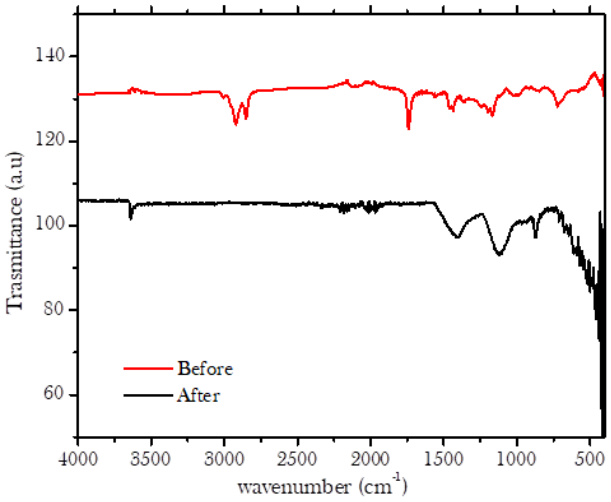

Figure 2. FTIR of the blast furnace slag.

X-Ray Fluorescence analysis

Table 1 below provides the chemical breakdown of BFS before and after treatment as determined by XRF analysis. The total element found in blast furnace slag makes up most of the complex heterogeneous substance known as BFS. After treatment, some elements are absent in the sorbent due to the sulphation and calcination process reaction.

Table 1. The elemental composition of the sorbent.

		Before treatment		After treatment	
Element	Line	Mass %	Atom %	Mass %	Atom %
C	K	7.78	24.63	23.32	39.59
O	K	5.09	11.99	33.23	42.19
Mg	K	0.52	0.8	1.11	0.92
Si	K	1.72	2.32		
S	K	14.36	16.91		
Ca	K	4.11	3.88	34.13	17.3
Mn	K	47.42	32.58		
Fe	K	8.85	5.95		
Au	M	11.69	2.24	9.5	0.98

Response surface plots

A CCD was used to assess the impact of four experimental factors on the area region of an absorbing material made from blast furnace slag. The resulting sorbent's surface area corresponding to Brunauer-Emmett-Teller (BET) was investigated. The sorbents produced range in surface area from 49.89 to 155.33 m^2/g. The surface area of the sorbent is a function of hydration temperature and ammonium acetate content. Figure 3a illustrates the variations in absorbing material surface dimensions as a function of the ammonium acetate concentration (B) and hydration temperature (D). The sorbent surface area significantly increases when large volumes of ammonium acetate are employed. The production of Very significant hydroxyl complexes having a wide area of contact is facilitated by hydrating agents, which may be the cause for this. Although high temperatures raise the sorbent's surface area, when the reaction time is lengthened, the sorbent's surface area also grows over time [18]. The pozzolanic reaction has been reported to create calcium silicate-hydrated compounds at higher temperatures and longer hydration times [19]. Figure 3b shows how the sorbent surface area changes; it expands when the ammonium acetate level is significant. This demonstrates unequivocally that the moisturizing agent ammonium acetate enhances the hydration level of a hydroxide aggregate with a large surface area. The surface area of the sorbent also increases with the addition of more blast furnace slag. The phenomenon is explained by the fact that when more bagasse is used, calcium oxide and more silica are combined, producing more calcium silicate [20].

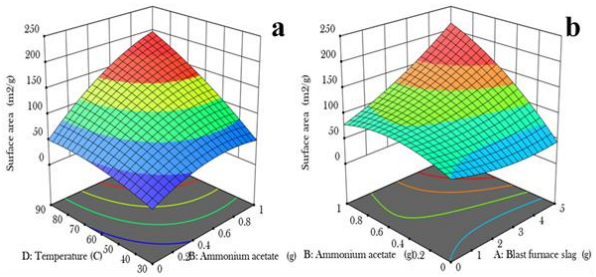

Figure 3. The interaction between (a) temperature and ammonium acetate and (b) blast furnace slag and ammonium acetate on the surface area.

Eq. (8) is produced by the final model displayed below after Fisher's Test is used to exclude the irrelevant terms.

$$Surface\ area = +110.42 + 27.69A + 44.89B - 7.98C + 45.13D + 40.48AB - 3.43AC + 28.96AD + 0.4900BC + 28.91BD - 10.29CD + 12.21A^2 - 20.57B^2 + 15.11C^2 - 11.31D^2 \quad (8)$$

By contrasting the factor coefficients, the coded equation can be used to determine the relative importance of the elements. A positive sign in front of the phrases indicates a synergistic influence, whereas an antagonistic influence is shown by a negative sign [11]. The results of these statistical tests indicate that the regression model equations properly show the link

between the important experimental parameters and the surface area of the sorbent. It is evident through regression analysis that the coefficient for hydration temperature (D) is the largest of all the variables. Therefore, we can conclude that this variable significantly impacts the surface area of sorbents made from blast furnace slag.

The analysis of variance (ANOVA) was used to confirm that the model was adequate by testing for variance-based variations in means between two or more category groups; an ANOVA test is a sort of statistical test used to assess if there is a statistically significant difference variable. Table 3 displays this at a 95% confidence level. The third-order algebraic equation was put to the test. A regularly distributed continuous dependent variable and two or more categorical independent variables (factors) make up a two-way ANOVA (analysis of variance). The model is suggested to be significant by the model's *F*-value of 13.56. An *F*-value this big might happen owing to noise only 0.21% of the time [21].

When the *P*-value is less than 0.0500, model terms are regarded to be significant. A, B, C, D, AB, AD, BD, CD, and B2 are crucial model terms. If the value exceeds 0.1000, model terms are not significant. If your model includes many unnecessary terms (apart from those required to maintain hierarchy), removing them may improve the performance. The lack of fit *F*-value of 45.31 suggests that the lack of fit is considerable. Noise can result in a substantial Lack of Fit F-value only 0.18% of the time. A significant lack of fit in the model is undesirable since we want it to fit. Temperature (D) possessed a major impact on surface area (C) relative to ammonium acetate content (A). In contrast to variables A and B, the quadratic terms D greatly impacted the surface of the absorbent area. The C variable has very minimal influence on the surface region of the sorbent. The absorbing material surface region is unaffected by the cubic expression. The interaction between components B and C does not significantly affect the surface area.

While the other stayed constant, the impact of one factor was assessed and plotted versus surface area. Compared to the other three criteria, hydration substantially affected surface area more. Ammonium acetate concentration came next, and then the impact of time and hydration on blast furnace slag. The surface area rises with temperature and ammonium acetate concentrations. Raising hydration length and hydration time has little effect on surface area [8]. Table 2 also exhibits the impact. A high *F*-value for the hydration temperature indicates that it likely significantly impacts the surface area.

Table 2. ANOVA.

Source	Sum of Squares	df	Mean Square	*F*-value	*p*-value	
Model	15353.31	14	1096.67	13.56	0.0021	significant
A-Blast furnace slag	1532.92	1	1532.92	18.95	0.0048	
B-Ammonium acetate	4029.33	1	4029.33	49.81	0.0004	
C-Time	636.36	1	636.36	7.87	0.0310	
D-Temperature	4073.79	1	4073.79	50.36	0.0004	
AB	2621.42	1	2621.42	32.41	0.0013	
AC	94.12	1	94.12	1.16	0.3222	
AD	1341.89	1	1341.89	16.59	0.0066	
BC	1.92	1	1.92	0.0237	0.8826	
BD	1337.26	1	1337.26	16.53	0.0066	
CD	847.07	1	847.07	10.47	0.0178	
A^2	380.84	1	380.84	4.71	0.0731	
B^2	1079.75	1	1079.75	13.35	0.0107	
C^2	582.46	1	582.46	7.20	0.0364	
D^2	326.49	1	326.49	4.04	0.0913	
Residual	485.35	6	80.89			
Lack of Fit	464.83	2	232.41	45.31	0.0018	significant

R^2 = 0.952; R^2 Predicted = 0.925; R^2 Adjusted = 0. 954.

Artificial Neural network

The backpropagation method of Levenberg-Marquardt was used to train the MLP network (4:6:1). However, it generally takes more Space, so this approach is quicker. This happens when the validation samples' mean square error increases, indicating that generalization is no longer improving. The best number of neurons in the hidden layer, the best number of validation and training data, and the best number of testing samples were all determined using this technique [13]. Of the 21 samples employed in the ANN modeling, 70% (15 samples), 15% (3 samples), and 15% (3 samples) were used for training, testing, and training validation, respectively. The network's interactions with training, testing, and validation data are depicted in Figure 4. Correlation coefficients for training, testing, validation, and total data were determined to be 0.999, 0.994, 0.964, and 0.992, respectively. The straight line also demonstrates a linear relationship. The experimental (goal) and forecasted (output) results are related. The results suggest high agreement between the actual data and

the data predicted by the model. Therefore, the coefficient of total correlation reveals the excellent prediction capacity of the developed ANN model, making it suitable for correctly predicting data [22].

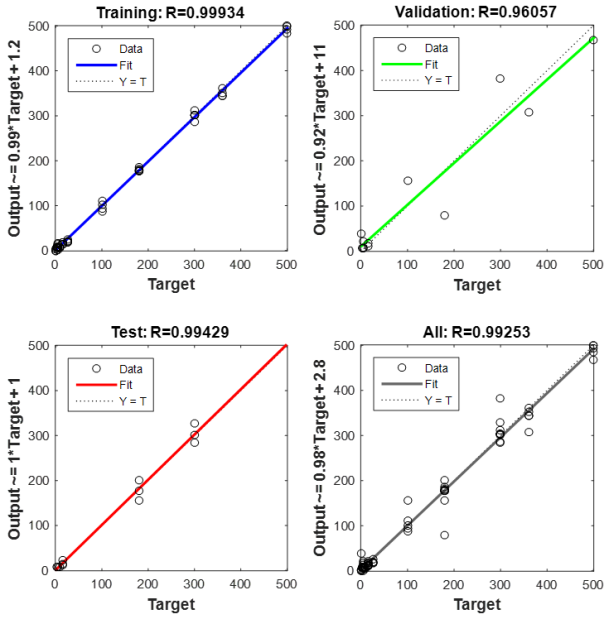

Figure 4. Neural network regression analysis.

Predicted and actual data RSM and ANN

The actual (experimental) and anticipated values for the surface area are compared and statistically analyzed in Table 3. According to the results, both models can adequately predict the surface area. The RMSE, MSE, ARE, HYBRID, SSE, SAE, and R^2 values for the RSM model were all found to be 0.065, 0.049, 0.024, 0.314, 0.018, 0.198 and 0.952, respectively, whereas the ANN model was found to be 0.009, 0.020, 0.012, 0.188, 0.06, 0.110 and 0.992. Both models provide relevant statistical data, according to statistics, indicating that they may be used in this procedure [15]. The accuracy of the RSM and ANN techniques in displaying actual and expected results is seen in Table 3. The linear fit also shows both models' remarkable capabilities. Although both models can predict the surface, the ANN model displayed better RMSE, MSE, ARE, HYBRID, SSE, SAE, and R^2 values.

Both models could accurately predict the sorbent's surface area, the Response surface method, and the Artificial neural network. The artificial neural network (ANN) was implemented in Table 4 to maximize the sorbent's surface area [15].

Table 3. Comparison of artificial neural networks (ANN) and Response surface method (RSM).

Run	Blast furnace slag (g)	Ammonium acetate (g)	Hydration period (hrs)	Hydration temperature (°C)	Surface area(m^2/g) RSM	ANN
1	5	1	8	30	112.71	113.22
2	5	1	2	30	116.62	116.98
3	5	0	8	90	68.6	70.25
4	0	1	2	90	142.18	145.24
5	5	0	2	90	115.64	115.96
6	0	0	8	30	89.18	90.01
7	0	1	8	90	110.74	112.25
8	0	0	2	30	81.34	80.97
9	0	0.5	5	60	99.96	100.00
10	5	0.5	5	60	155.33	156.32
11	2.5	0	5	60	49.96	50.98
12	2.5	1	5	60	139.75	140.21
13	2.5	0.5	2	60	133.18	135.29
14	2.5	0.5	8	60	127.69	130.39
15	2.5	0.5	5	30	58.99	60.28
16	2.5	0.5	5	90	149.25	150.22
17	2.5	0.5	5	60	104,46	105.85
18	2.5	0.5	5	60	101.48	100.40
19	2.5	0.5	5	60	105.17	105.98
20	2.5	0.5	5	60	107.60	108.95
21	2.5	0.5	5	60	103.34	105.37
				RMSE	0.065	0.009
				MSE	0.049	0.020
				ARE	0.024	0.012
				HYBRID	0.314	0.188
				SSE	0.018	0.006
				SAE	0.198	0.110
				R^2	0.952	0.992

Table 4. The optimum predicted conditions.

Variables	Values
Reaction time	5 h
Reaction temperature	60°C
Ammoniumacetate	0.5 g
BFS	5 g
Surface area	150.00 m^2/g

CONCLUSION

This study demonstrated that it is possible to prepare sorbent for DFGD. SEM micrographs indicated high porosity and open spaces, which show that there is room for sulphation reaction. Silica and calcium oxide were identified in the functional group that was observed on the FTIR. The results show that when blast furnace slag is employed as a pozzolan substance, a pozzolanic reaction occurs that results in aggregation of hydrated calcium silicates, expanding the area of the sorbent's surface. RSM analysis revealed that the sorbent preparation variables significantly affect the final sorbent surface area. Higher blast furnace slag and ammonium acetate content increased surface area; a moderate rise was seen at high temperatures and during lengthy hydration time. A quadratic model was developed to link the independent variables and the surface area. The RMSE, MSE, ARE, HYBRID, SSE, SAE, and R^2 values for the RSM model were all found to be 0.065, 0.049, 0.024, 0.314, 0.018, 0.198 and 0.952, respectively, whereas the ANN model generated 0.009, 0.020, 0.012, 0.188, 0.06, 0.110 and 0.992. This can be due to the small number of datasets available for application. Working with a lot of different data sets may be more effective for the ANN model.

ACKNOWLEDGMENTS

The author would like to acknowledge the Department of Chemical and Metallurgical Engineering at Vaal University of Technology for providing continuous operational resources.

ABBREVIATION

ANN	Artificial neural network
BFS	Blast furnace slag
RMSE	Root means square errors
ARE	Average relative errors
MSE	Mean square errors
CCD	Central composite design
BP	Back-propagation
FGD	Flue gas desulphurization
DFGD	Dry flue gas desulphurization
WFGD	Wet flue gas desulphurization
LM	Levenberg-Marquardt model
ML	Multilayer perceptron
HL	Hydrated lime
MPSD	Derivative of Marquardt's percent standard deviation
RMSE	Root means square errors
BP	Back-propagation
LM	Levenberg-Marquardt model

REFERENCES

[1] B.J. Shokri, F. Shafaei, F.D. Ardejani, S. Entezam, Soil Sediment Contam. 32 (2023) 23–40. https://doi.org/10.1080/15320383.2022.2090895.

[2] L. Lerotholi, R.C. Everson, L. Koech, H.W.J.P. Neomagus, H.L. Rutto, D. Branken, B. B. Hattingh, P. Sukdeo, Clean Technol. Environ. Policy 24 (2022) 2011–2060. https://doi.org/10.1007/s10098-022-02308-y.

[3] C. Zheng, K. Li, C. Zhang, D. Deng, Sep. Sci. Technol. 56 (2021) 2499–2506. https://doi.org/10.1080/01496395.2020.1833218.

[4] R.S. Makomere, H.L. Rutto, L. Koech, Arabian J. Sci. Eng. 48 (2022) 8871–8885. https://doi.org/10.1007/s13369-022-07491-0.

[5] A. López-Olvera, S. Pioquinto-García, J. Antonio Zárate, G. Diaz, E. Martínez-Ahumada, J.L. Obeso, V. Martis, D.R. Williams, H.A. Lara-García, C. Leyva, C.V. Soares, G. Maurin, I.A. Ibarra, N.E. Dávila-Guzmán, Fuel 322 (2022) 124213. https://doi.org/10.1016/j.fuel.2022.124213.

[6] X. Li, T. Huhe, T. Zeng, X. Ling, Z. Wang, H. Huang, Y. Chen, Heliyon 8 (2022) 11463. https://doi.org/10.1016/j.heliyon.2022.e11463.

[7] G. Long, C. Yang, X. Yang, T. Zhao, M. Xu, J. Mol. Liq. 302 (2020) 112538. https://doi.org/10.1016/j.molliq.2020.112538.

[8] R. Makomere, H. Rutto, L. Koech, H. Rutto, L. Koech, J. Environ. Sci. Health, Part A 58 (2023) 191–203. https://doi.org/10.1080/10934529.2023.2174334.

[9] D. Gazioglu Ruzgar, S. Altun Kurtoglu, M.F. Fellah, J. Nat. Fibers 19 (2022) 1366–1375. https://doi.org/10.1080/15440478.2020.1764459.

[10] Y. Yu, R. Zhao, J. Chen, H. Yao, Chem. Eng. J. 431 (2022) 134267. https://doi.org/10.1016/j.cej.2021.134267.

[11] M. Banza, H. Rutto, Int. Nano Lett. 12 (2022) 257–272. https://doi.org/10.1007/s40089-022-00369-x.

[12] S. Chellapan, D. Datta, S. Kumar, H. Uslu, Chem. Data Collect. 37 (2022) 100806. https://doi.org/10.1016/j.cdc.2021.100806.

[13] M. Banza, H. Rutto, T. Seodigeng, Soil Sediment Contam. Int. J. 0 (2023) 1–21. https://doi.org/10.1080/15320383.2023.2178384.

[14] C. Mgbemena, S. O. Onyegu, Qeios (2023) 32388. https://doi.org/10.32388/GEGPL7.

[15] A.A. Ayoola, F.K. Hymore, C.A. Omonhinmin, O.C. Olawole, O.S.I. Fayomi, D. Babatunde, O. Fagbiele, Chem. Data Collect. 22 (2019) 100238. https://doi.org/10.1016/j.cdc.2019.100238.

[16] J. Kabuba, M. Banza, Results Eng. 8 (2020) 100189. https://doi.org/10.1016/j.rineng.2020.100189.

[17] M. Banza, H. Rutto, Can. J. Chem. Eng. 101 (2023) 896–908. https://doi.org/10.1002/cjce.24384.

[18] Z. Zhao, K. Patchigolla, Y. Wu, J. Oakey, E.J. Anthony, H. Chen, Fuel Process. Technol. 221 (2021) 106938. https://doi.org/10.1016/j.fuproc.2021.106938.

[19] J.X. Liu, J. Li, W.Q. Tao, Z. Li, Fluid Phase Equilib. 536 (2021) 112963. https://doi.org/10.1016/j.fluid.2021.112963.

[20] J. Lim, J. Kim, Fuel 327 (2022)124986. https://doi.org/10.1016/j.fuel.2022.124986.

[21] J.R. Hanumanthu, G. Ravindiran, R. Subramanian, P. Saravanan, J. Indian Chem. Soc. 98 (2021)100086. https://doi.org/10.1016/j.jics.2021.100086.

[22] D.S.P. Franco, F.A. Duarte, N.P.G. Salau, G.L. Dotto, Chem. Eng. Commun. 206 (2019) 1452–1462. https://doi.org/10.1080/00986445.2019.1566129.

ITUMELENG KOHITLHETSE
SUTER KIPLAGAT EVANS
MUSAMBA BANZA
ROBERT MAKOMERE

Department of Chemical and Metallurgical Engineering, Vaal University of Technology, Private Bag X021, South Africa

NAUČNI RAD

ŠLJAKA VISOKE PEĆI ZA HVATANJE SO_2: OPTIMIZACIJA I PREDVIĐANJE POMOĆU METODOLOGIJE POVRŠINE ODZIVA I VEŠTAČKE NEURONSKE MREŽE

Glavni istraživani reakcioni parametri bili su količina šljake visoke peći, trajanje hidratacije, koncentracija amonijum-acetata i temperatura. Metodologija površine odziva (MPO) u kombinaciji sa centralnim kompozitnim planom je korišćena za kvantifikovanje njihovog uticaj na površinu sorbenta po Brunauer-Emet-Teleru (BET). Površina dobijenhi sorbenata se kreću od 49,89 do 155,33 m^2/g. Pored toga, istražena su efikasnost i kapaciteti predviđanja odgovora metodologija MPO i veštačke neuronske mreže (VNM). Modeli su procenjeni korišćenjem različitih statističkih metrika, uključujući srednju kvadratnu grešku, prosečnu relativnu grešku, (SSE) zbir kvadratnih grešaka, hibridnu funkciju frakcione greške, zbir apsolutnih grešaka, koeficijent determinacije, a koren srednje kvadratne vrednosti. Prema statističkim dokazima, VNM model je nadmašio pristup MPO modela. Pokazalo se da na površinu sorbenta značajno utiču interakcije između faktora pored svih pojedinačnih faktora. Prema SEM-u, sorbent je napravljen od materijala sa značajnom strukturnom poroznošću. Funkcionalne grupe su identifikovane korišćenjem FTIR. Rentgenskm analizom je određen elementarni sastav sorbenata.

Ključne reči: šljaka visoke peći, optimizacija, centralni kompozitni plan, veštačka neuronska mreža, metodologija površine odziva.

CI&CEQ
Chemical Industry & Chemical Engineering Quarterly

Available online at
Association of the Chemical Engineers of Serbia AChE
www.ache.org.rs/CICEQ

Chem. Ind. Chem. Eng. Q. 30 (4) 359–365 (2024) CI&CEQ

MUHAMMAD THORIQ AL FATH[1]
GHENDIS EKAWATI AYU[1]
GINA CYNTHIA RAPHITA HASIBUAN[2]
NISAUL FADILAH DALIMUNTHE[1]
VIKRAM ALEXANDER[1]

[1]Department of Chemical Engineering, Faculty of Engineering, Universitas Sumatera Utara, Padang Bulan, Medan, Indonesia

[2]Department of Civil Engineering, Faculty of Engineering, Universitas Sumatera Utara, Padang Bulan, Medan, Indonesia

SCIENTIFIC PAPER

UDC 606:66.098:678.07

THE EFFECT OF GLYCEROL AND SAGO STARCH ADDITION ON THE CHARACTERISTICS OF BIOPLASTICS BASED ON ORANGE PEEL PECTIN

Article Highlights

- The high pectin content in orange peel boasts 42.5% pectin, suitable for bioplastics synthesis
- Examining orange peel pectin with glycerol and sago starch for improved bioplastics
- Tensile strength (4.22 MPa) and elongation (24%) in pectin:starch (75:25%) and glycerol (40%)

Abstract

Sustainable food packaging materials have significant interest in addressing environmental issues by making renewable substitutes such as bioplastics based on pectin. Orange peel has a relatively high pectin content of 42.5%, which can be synthesized into bioplastics. Pectin-based bioplastics tend to have limitations in terms of mechanical and physical strength due to the hygroscopic nature of pectin. This study aims to determine the effect of adding glycerol and sago starch on the characteristics of orange peel pectin-based bioplastics. The casting method was used in the bioplastic formulation using the variation of the pectin:starch ratio (75:25, 65:35, 55:45; and 50:50%) and glycerol composition (10, 20, 30, and 40%). Based on the results, the pectin obtained was categorized as low methoxyl pectin and ester pectin. The characterizations of bioplastics achieved the maximum value of the tensile strength of bioplastics was 4.22 MPa, obtained by adding pectin:starch (50:50%) and 10% glycerol. The maximum value of the elongation properties at the break of bioplastics is 24%, obtained by adding the composition of pectin:starch (75:25%) and 40% glycerol. The more additions of the pectin:starch and glycerol composition result in a higher water vapor evaporation rate. Hence, utilizing orange peel pectin-based bioplastics offers a sustainable solution by exploring repurposing waste to create bioplastics for food packaging, thereby contributing to environmental preservation.

Keywords: bioplastics, pectin, starch, orange peel.

Plastics are widely used in the packaging industry, especially in food packaging, so it must come from environmentally friendly biodegradable materials.

Bioplastics are a renewable source of great interest to researchers because provide a solution to the limitations of petroleum-based polymer resources and can reduce environmental pollution [1,2]. In 2021, the global production capacity of bioplastics reached approximately 2.42 million tons, with nearly 48 percent (1.15 million tons) of the volume destined for the packaging market - the largest market segment within the bioplastics industry [3]. Bioplastics can be defined as plastics that are bio-based and biodegradable so that microorganisms can naturally decompose them [4]. Bioplastics are usually derived from natural materials

Correspondence: M.T. Al Fath, Department of Chemical Engineering, Faculty of Engineering, Universitas Sumatera Utara, Padang Bulan, Medan, 20155, Indonesia.
E-mail: thoriq@usu.ac.id
Paper received: 14 December, 2023
Paper revised: 29 February, 2024
Paper accepted: 6 March, 2024

https://doi.org/10.2298/CICEQ231214007A

such as polysaccharides (carbohydrates), polypeptides, and lipids [5].

Pectin is a natural biopolymer compound with a high molecular weight (ranging from 50 to 150 thousand), primarily found in plants. Galacturonic acid molecules linked with α-(1-4)-glycoside bonds to form polygalacturonic acid are the constituent components of pectin [6,7]. One source of pectin can be reused as raw material for producing edible films that can be used as food packaging with biodegradable and environmentally friendly capabilities, namely waste derived from fruit peels. Pectin is one of the carbohydrates that can be isolated from orange peel, considering that the productivity of orange plants, especially in Sumatera Utara, Indonesia, is relatively high, around 448,476 tons in 2022 [8]. The pectin content in orange peels is also quite large at around 42.5%, so orange peels have the potential to be reused as a source of pectin in the manufacture of bioplastics [9,10]. Pectin and essential oil are the main contents of citrus peel, especially the albedo part. Pectin in orange peel can be isolated using a solid-liquid extraction process. Pectin can make bioplastics more robust, better, and stable because it has a high gel-forming ability. However, too many hydrocolloids and pectin have hydrophilic properties, so the resulting bioplastics will tear easily [11].

Pectin-based bioplastics with starch can improve pectin-based bioplastics' physical and mechanical characteristics. Starch is a glucose polymer consisting of amylopectin and amylose. Starch can be produced by the extraction process of materials containing high carbohydrates, such as corn, sweet potato, cassava, sago, and taro [12]. Starch is a carbohydrate composed of two components, amylose and amylopectin. Linear polymers with α-(1→4) glucose units in starch are called amylose. Plants with a reasonably high starch content, namely sago (*Metroxylon* sp), are 82.94%. Based on information from the Indonesian Ministry of Agriculture in 2021, sago production is estimated to reach 381,065 tons [13]. Using sago starch as a raw material for bioplastics has several advantages, such as an abundant supply of raw materials that can be biodegradable. Bioplastics made from starch also still have some disadvantages, such as being able to absorb water excessively and being rigid [14].

Bioplastics from natural polymers like pectin and starch are generally brittle and rigid. Glycerol is one example of a plasticizer that can be added to produce flexible and mechanical solid properties [15]. Glycerol as a plasticizer is often chosen because it has a high boiling point of 290 °C. This results in no glycerol evaporating during processing, which is more beneficial. In addition, glycerol can reduce intermolecular and intramolecular bonds found in starch and pectin. Adding glycerol concentration will increase the flexibility of starch, pectin, and gelatin-based biocomposites [16]. Glycerol is widely used in the manufacture of bioplastics, as done by Yuniarti *et al.* [17] researched the manufacture and characterization of bioplastics made from sago starch (*Metroxylon* sp) with acetic acid and glycerol, which concluded that the physical and mechanical properties of bioplastics can increase with the addition of glycerol and acetic acid. Darni *et al.* [18] also researched the effect of plasticizers on the properties of pectin-based edible films, showing better mechanical properties and water vapor permeability in glycerol compared to sorbitol.

Based on this explanation, this study aims to make bioplastics on the effect of adding glycerol and sago starch on the characteristics of orange peel pectin-based bioplastics produced. In the growing field of chemical engineering, exploring sustainable alternatives to plastics is a must. This research also contributes by utilizing growing eco-friendly materials, addressing the issue of environmental problems, and encouraging a more sustainable future.

MATERIALS AND METODS

The materials used such as orange peel for pectin and sago starch, were obtained from supermarkets around Medan, Sumatera Utara, Indonesia. Food-grade glycerol was used. Hydrochloric acid (HCl), ethanol (C_2H_5OH), and aquadest were used as pectin isolation materials, as sodium chloride (NaCl), sodium hydroxide (NaOH), and phenolphthalein indicators. The equipment used in this study were analytical balance, three-neck flask, beaker glass, filter paper, measuring cup, bioplastics mold, hot plate, magnetic stirrer, and 100 mesh sieve.

Procedure for pectin isolation from orange peel

Weighed 6 g of orange peel powder and poured it into a three-neck flask, then added 200 ml of 0.02 N HCl solution at 70 °C for 60 minutes. Filtered and added 96% ethanol to the filtrate with a volume ratio of 1:1 while stirring to form a precipitate.Separated the precipitate using filter paper. Filter the precipitate and wash it using ethanol continuously. The precipitate was dried to a constant weight and sieved using a 100-mesh sieve.

Bioplastics preparation procedure

Weighed 3 g of pectin/starch in the ratio of 75:25; 65:35; 55:45; 50:50%, poured into a beaker glass, and added 75 ml of distilled water. Then, heat the solution

to 70 °C using a hot plate. Glycerol was added with 10, 20, 30, and 40% variations and then stirred until homogeneous. After mixing evenly, the solution was cooled before molding. The solution was poured into the mold and then dried for 48 hours at room temperature. Then, the bioplastics was removed from the mold.

Pectin Analysis

Equivalent Weight

An amount of 0.5 g of pectin was moistened with 5 ml of ethanol and then dissolved in 100 ml of distilled water supplemented with 1 g of NaCl. Titrated slowly using 0.1 N NaOH with phenolphthalein indicator until it turns pink color and the volume of NaOH used is noted [19]. The equivalent weight of pectin can be calculated by Eq. (1).

$$Equivalent\ \ weight\left(mg\right)=\frac{samle\ \ weight\left(mg\right)}{ml\ \ NaOH\times N\ \ NaOH}\times 100\% \tag{1}$$

Methoxyl content

A total of 25 ml of 0.25 N NaOH was added to the neutral solution from the determination of equivalent weight, then stirred and allowed to stand for 30 minutes under closed conditions at room temperature. A total of 25 ml of 0.25 N HCl was added and titrated with 0.1 N NaOH with phenolphthalein indicator until it turned pink color, and the volume of NaOH used was noted [20]. Pectin methoxyl content can be calculated with Eq. (2).

$$Methoxyl\ \ content\left(\%\right)=\frac{ml\ \ NaOH\times 31\times N\ \ NaOH\times 100}{sample\ \ weight\left(mg\right)} \tag{2}$$

The value 31 is the molecular weight of methoxyl which is CH_3O.

Galacturonate content

The volume of NaOH obtained from the determination of equivalent weight and methoxyl content is used to calculate galacturonic content with the following Eq. (3) [20].

$$Galacturonate\ \ levels=\frac{176\times 0.1z\times 100}{sample\ \ weight\left(mg\right)}+\frac{176\times 0.1y\times 100}{sample\ \ weight\left(mg\right)} \tag{3}$$

where, *z*-volume of NaOH based on equivalent weight; *y*-volume of NaOH based on methoxyl content; the value 176 is the molecular weight of galacturonate.

Degree of esterification

The methoxyl content and galacturonic content that have been obtained are used to calculate the degree of esterification of pectin using Eq. (4) as follows [20].

$$Degree\ \ of\ \ esterification=\frac{176\times\%methoxyl}{31\times\%galacturonate} \tag{4}$$

The value 31 represents the molecular weight of methoxyl; the value 176 represents the molecular weight of galacturonate.

Characteristics and physical properties of bioplastics

The physical strength of bioplastics can be determined based on the tensile strength and elongation at break values of the resulting starch/pectin-based bioplastics. The ASTM 882 standard with the provisions of the Universal Testing Machine (UTM) model was used to test the tensile strength and elongation at break of pectin-based bioplastics at the Laboratorium Polimer, Department of Chemical Engineering, Universitas Sumatera Utara, Medan, Indonesia. Eqs. (5) and (6) calculate the tensile strength and elongation at break, respectively:

$$\sigma=\frac{F_{\max}}{A_0} \tag{5}$$

where σ is the tensile strength (N/m^2), F_{max} is the tensile force applied to the cross-section of the specimen (N), and A_o is the initial cross-sectional area of the specimen before force load (m^2).

$$elongation\left(\%\right)=\frac{\Delta l}{l_0}\times 100\% \tag{6}$$

where Δl is the change in length (cm) and l_0 is the initial length (cm).

Analysis Scanning Electron Microscope (SEM)

The morphological of biocomposite was observed by SEM EVO MA 10 ZEISS at magnification ranging from 1000x to 5000x in Laboratorium Penelitian dan Pengujian Terpadu, Universitas Gadjah Mada, Yogyakarta, Indonesia.

Water vapor transmission rate

The film was placed on the mouth of a porcelain dish with a diameter of 7 cm and a depth of 2 cm filled with 10 g of silica gel. The edges of the film and the porcelain cup were glued with glue. Put the porcelain cup into a container containing 40% NaCl (b/v). Calculated the film changes every 1 hour until reaching the 7th hour by Eq. (7) [21].

$$Water-vapor\ \ transmission\ \ rate=\frac{\Delta x}{A} \tag{7}$$

where Δx - linear slope (g/h); A - film area (m^2).

RESULTS AND DISCUSSION

Orange peel pectin analysis

Pectin was characterized from orange peel to see the equivalent weight, methoxyl content, galacturonic content, and degree of esterification produced. These values can be seen in Table 1. The yield value and equivalent weight of pectin from orange peel were 25.38% and 510.52 mg, respectively. These results can be compared with other raw materials such as Dragon Fruit (*Hylocereus polyrhizus*) peel has a pectin content of 12% and yields 11% [22] while Grapefruit (*Citrus Maxima*) peel has a pectin content of 40% and yields 27.3% pectin [23]. Considering the use of this fruit peel material as waste is still small so it needs to be encouraged. The content of unesterified free galacturonic acid in the pectin molecular chain is the equivalent weight. Free galacturonic acid that is free of methyl ester (unesterified) is called pectic acid. The equivalent weight results obtained in this study did not meet the standards of the International Pectin Procedures Association (IPPA) (2003), which ranged from 600–800 mg [24]. This is influenced by pectin content, plant type, and extraction method, which can affect the equivalent weight of pectin [19].

Table 1. Characterization results of orange peel pectin.

Characterization	Values	IPPA Standard
Yield (%)	25.38	-
Equivalent Weight (mg)	510.52	600–800
Methoxyl (%)	5.20	>7.12 (pectin with high methoxyl) <7.12 (pectin with low methoxyl)
Galacturonic acid (%)	64.06	60
Degree of esterification (%)	46.09	>50% (high ester pectin) <50% (low-ester pectin)

Methoxyl content is the number of esterified methyl groups in orange peel pectin that can affect gel formation ability. Pectin with methoxyl content >7% is called high methoxyl pectin, while pectin with methoxyl content <7% is called low methoxyl pectin. In this study, pectin was obtained with a methoxyl percentage of 5.20%, so the pectin produced was categorized as low methoxyl pectin [25].

Galacturonic content is an important parameter affecting the pectin gel's structure. Table 1 shows that the galacturonic content obtained has met the IPPA (2003) standard of 64.06% [24]. Galacturonic levels that have met the standards of IPPA (2003) can be concluded to have broken the chain of pectin components against other components, such as hemicellulose contained in orange peel [19]. The degree of esterification is a parameter that states the percentage of esterified carboxyl groups. Pectin with a degree of esterification > 50% is called high methoxyl pectin, while pectin with a degree of esterification < 50% is called low methoxyl pectin. The study obtained pectin with a degree of esterification of 46.09%, so the pectin obtained in this study is included in the category of low-ester pectin [15,25].

Effect of glycerol and sago starch addition on tensile strength value of orange peel pectin-based bioplastics

Fig. 1 shows the effect of glycerol and sago starch addition on the tensile strength value of orange peel pectin-based bioplastics.

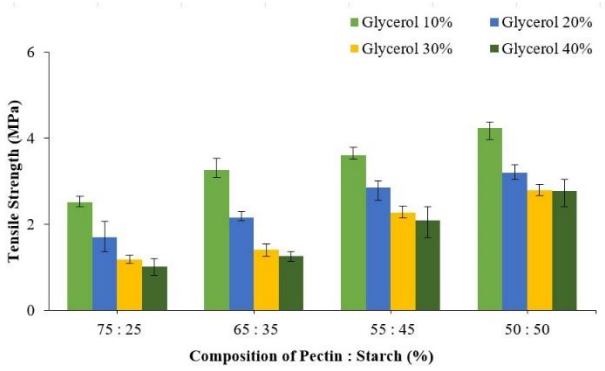

Figure 1. Effect of glycerol and sago starch addition on tensile strength value of orange peel pectin-based bioplastics.

Fig. 1 shows that the maximum tensile strength of bioplastics is 4.22 MPa, which is obtained in addition to pectin:starch composition (50:50%) and 10% glycerol. The minimum value of bioplastics tensile strength is 1.01 MPa in addition to pectin:starch composition (75:25) and 40% glycerol. According to Japanese Industrial Standard 1707:1975, the minimum value for tensile strength for bioplastics is 0.39 MPa [26]. The maximum tensile strength value of bioplastics indicates that the composition of starch has a significant role in the tensile strength value of bioplastics compared to pectin. This is because sago starch is known to have main components in the form of amylose and amylopectin, which will affect the mechanical properties of bioplastics. The more the composition of pectin increases, the tensile strength value of bioplastics will decrease. This is because pectin

comprises galacturonic acid molecules that bind to α-(1-4)-glycoside bonds to form polygalacturonic acid. Polygalacturonic acid is an amorphous region with lower stiffness than crystalline regions, such as amylopectin found in starch.

Fig. 1 also shows that the maximum tensile strength value continues to decrease until the addition of 40% glycerol. At the addition of 10% glycerol in the composition of pectin:starch (50:50%), the highest tensile strength value is due to glycerol reducing intermolecular interactions between pectin and starch [27]. This is also supported by the scanning electron microscopy (SEM) analysis results, shown in Fig. 2a, which shows that bioplastics have a more stable surface.

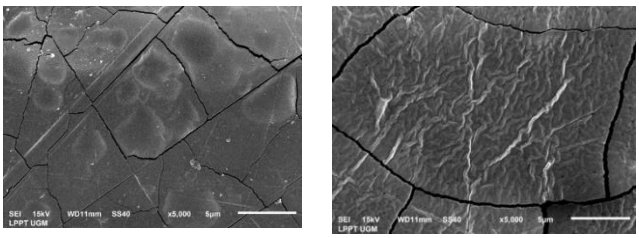

a b

Figure 2. SEM results of pectin:starch (50:50%) composition bioplastics in the addition of (a) 10% glycerol and (b) 40% glycerol.

Fig. 2 shows the scanning electron microscopy (SEM) analysis results of pectin:starch (50:50%) composition bioplastics in the addition of 10% glycerol and 40% glycerol. Bioplastics surfaces must be produced homogeneous and gap-free to maintain the characteristics [28]. However, adding 20%, 30%, and 40% glycerol decreased the tensile strength. This is because the glycerol added is too high, so glycerol disrupts not only intermolecular interactions between pectin and starch molecules but also disrupts intramolecular bonds in starch and pectin, thereby reducing the tensile strength value of the resulting bioplastics as can be seen in Fig. 2b where the resulting surface is less stable and indicated to form a plasticsol film caused by excess glycerol.

Effect of glycerol and sago starch addition on elongation at break value of orange peel pectin-based bioplastics

The effect of glycerol and sago starch addition on the elongation at the break value of orange peel pectin-based bioplastics can be seen in Fig. 3

Fig. 3 shows that the maximum value of elongation properties at the break of bioplastics is 24%, which is obtained by adding pectin:starch composition (75:25%) and 40% glycerol. This is due to the high composition of pectin, which will increase the amorphous area, thereby increasing the bioplastics' flexibility. The Japanese Industrial Standard 1707:1975 for elongation at break value is between 10%–50%[26]. The minimum elongation value at the break of bioplastics is 6.39% in the addition of pectin:starch composition (50:50%) and 10% glycerol. This is due to the difference in polarity between starch, pectin, and glycerol, resulting in a decrease in the elongation at the break value of the bioplastics produced [29]. Hassani *et al.* obtained similar results when observing the decrease in elongation at the break of the nanocomposite bioplastics film of potato starch and gum arabic with the addition of boron oxide nanoparticles and Anise hyssop (*Agastache foeniculum*) essential oil [30].

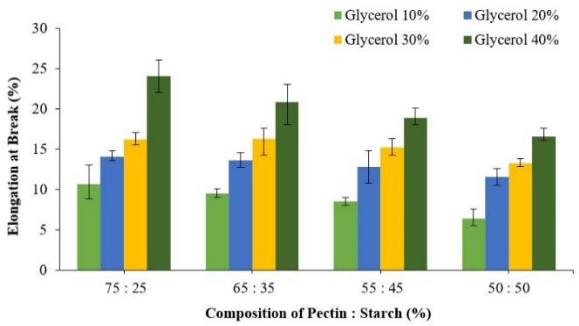

Figure 3. Effect of glycerol and sago starch addition on elongation at break value of orange peel pectin based bioplastics.

Effect of glycerol and sago starch addition on water vapor transmission rate of orange peel pectin-based bioplastics

The effect of the addition of glycerol and sago starch on the water vapor transmission rate of orange peel pectin-based bioplastics is shown in Fig. 4.

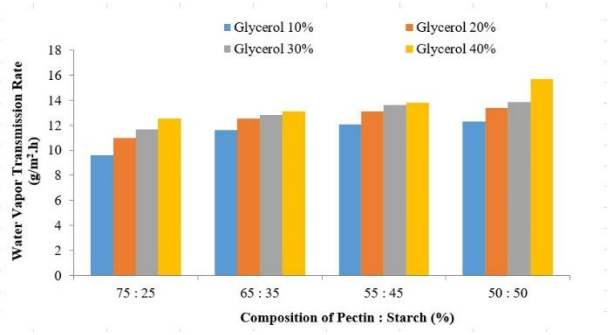

Figure 4. Effect of glycerol and sago starch addition on water vapor transmission rate of orange peel pectin-based bioplastics.

The maximum water vapor evaporation rate is 15.67 g/m^2.h when adding pectin:starch (50:50%) and 40% glycerol. The use of pectin contributes to forming a linked structure in bioplastics that can limit air exchange [31]. Fig. 4 also shows that the more the pectin: starch and glycerol composition is added, the

higher the water vapor evaporation rate. This is due to glycerol, which acts as a plasticizer with water-absorbing properties, so the transfer of water vapor from the environment to the surface of bioplastics becomes faster. In addition, glycerol has a small molecule, so it will more easily enter the amorphous network in pectin and starch so that there are more opportunities for water to be absorbed and water transfer in the film [27,32]. Bioplastics protects the product against ambiance risk variations according to the packaging settings [33].

CONCLUSION

Bioplastics based on pectin from orange peel formulated with sago starch and glycerol have been created in this study. Based on the results, the pectin obtained from orange peel were yielding of 25.38% or equivalent weight of 510.52 mg, categorized as low methoxyl pectin (5.20%) and low ester pectin (46.09%). The addition of glycerol and sago starch in formulating orange peel pectin-based bioplastics showed significant changes in the mechanical and physical properties of the bioplastics produced. The maximum tensile strength of bioplastics is 4.22 MPa, obtained by adding pectin:starch composition (50:50%) and 10% glycerol. The maximum value of elongation at the break of bioplastics is 24%, obtained by adding pectin:starch composition (75:25%) and 40% glycerol. The formulation given follows the Japanese Industrial Standard 1707:1975. Scanning electron microscopy confirms the supported analysis of the surface of the bioplastics to the interaction between the variation formulated. The more the addition of pectin:starch and glycerol composition, the higher the water vapor evaporation rate. The utilization of orange peel as pectin also provides an excellent alternative to orange peel waste solutions. The future research direction is to apply food packaging to prevent oxidation by observing changes in food color and texture.

REFERENCES

[1] L.G. Hong, N.Y. Yuhana, E.Z.E. Zawawi, AIMS Mater. Sci. 8 (2021) 166–184. https://dx.doi.org/10.3934/matersci.2021012.

[2] M. Simonic, F. Zemljic, Chem. Ind. Chem. Eng. Q. 27 (2021) 79–84. https://dx.doi.org/10.2298/ciceq191024026s.

[3] Anonim, Applications for Bioplastics, Berlin, 2022. https://www.european-bioplastics.org/market/applications-sectors/.

[4] I. Karimi Sani, M. Masoudpour-Behabadi, M. Alizadeh Sani, H. Motalebinejad, A.S.M. Juma, A. Asdagh, H. Eghbaljoo, S.M. Khodaei, J.W. Rhim, F. Mohammadi, Food Chem. 405 (2023) 134964. https://dx.doi.org/10.1016/j.foodchem.2022.134964.

[5] M.T. Al Fath, G.E. Ayu, M. Lubis, G.C.R. Hasibuan, N.F. Dalimunthe, RASAYAN J. Chem. 16 (2023) 1630–1636. https://dx.doi.org/10.31788/rjc.2023.1638464.

[6] A.F. Fracasso, C.A. Perussello, D. Carpiné, C.L. de O. Petkowicz, C.W.I. Haminiuk, Int. J. Biol. Macromol. 109 (2018) 784–792. https://dx.doi.org/10.1016/j.ijbiomac.2017.11.060.

[7] I.K. Sani, L. Aminoleslami, S.S. Mirtalebi, M.A. Sani, E. Mansouri, H. Eghbaljoo, A.T. Jalil, R.D. Thanoon, S.M. Khodaei, F. Mohammadi, B. Kazemzadeh, Food Package. Shelf Life 37 (2023) 101087. https://dx.doi.org/10.1016/j.fpsl.2023.101087.

[8] Anonim, Produksi Buah-Buahan Di Sumatera Utara, Jakarta, 2022. https://sumut.bps.go.id/statictable/2022/03/08/2578/produksi-buah-buahan-menurut-kabupaten-kota-dan-jenis-tanaman-di-provinsi-sumatera-utara-2020-dan-2021.html.

[9] V. Bátori, M. Jabbari, D. Åkesson, P.R. Lennartsson, M.J. Taherzadeh, A. Zamani, Int. J. Polym. Sci. 2017 (2017) 9732329. https://dx.doi.org/10.1155/2017/9732329.

[10] M.T. Al Fath, H. Nasution, H. Harahap, G.E. Ayu, AIP Conf. Proc. 2175 (2019) 020012. https://doi.org/10.1063/1.5134576.

[11] M. Chaichi, M. Hashemi, F. Badii, A. Mohammadi, Carbohydr. Polym. 157 (2017) 167–175. https://dx.doi.org/10.1016/j.carbpol.2016.09.062.

[12] M.G. Kupervaser, M.V. Traffano-Schiffo, M.L. Dellamea, S.K. Flores, C.A. Sosa, Food Hydrocoll. Heal. 4 (2023) 100138. https://dx.doi.org/10.1016/j.fhfh.2023.100138.

[13] Direktorat Jenderal Perkebunan, Statistical of National Leading Estate Crops Commodity 2019–2021, Jakarta, 2021. https://ditjenbun.pertanian.go.id/template/uploads/2021/04/BUKU-STATISTIK-PERKEBUNAN-2019-2021-OK.pdf.

[14] J. Prachayawarakorn, W. Pattanasin, Songklanakarin J. Sci. Technol. 38 (2016) 129–136. https://www.thaiscience.info/Journals/Article/SONG/10981886.pdf.

[15] Rosida, Sudaryati, A.M. Yahya, J. Phys. Conf. Ser. 953 (2018) 012248. https://dx.doi.org/10.1088/1742-6596/953/1/012248.

[16] M.A. Bertuzzi, E.F. Castro Vidaurre, M. Armada, J.C. Gottifredi, J. Food Eng. 80 (2007) 972–978. https://dx.doi.org/10.1016/j.jfoodeng.2006.07.016.

[17] L.I. Yuniarti, G.S. Hutomo, A. Rahim, Agrotekbis 2 (2014) 38–46. https://media.neliti.com/media/publications/246268-none-70e1bb8e.pdf.

[18] Y. Darni, H. Utami, R. Septiana, R.A. Fitriana, J. Bahan Alam Terbarukan 6 (2017) 158–167. https://dx.doi.org/10.15294/jbat.v6i2.9707.

[19] Z. Octarya, D. Afni, R. Jurusan, P. Kimia, F. Tarbiyah, K. Uin, S. Riau, J. Agroteknologi 4(2) (2014) 27–31. https://ejournal.uin-suska.ac.id/index.php/agroteknologi/article/view/1134.

[20] P.C. Sharma, A. Gupta, P. Kaushal, Indian J. Nat. Prod. Resour. 5 (2014) 184–189.

https://dx.doi.org/http://op.niscpr.res.in/index.php/IJNPR/article/view/2182.

[21] H. Nasution, H. Harahap, M.T. Al Fath, Y. Afandy, in: IOP Conf. Ser. Mater. Sci. Eng., Institute of Physics Publishing, 2018. https://dx.doi.org/10.1088/1757-899X/309/1/012033.

[22] R.V. Listyarini, P.R. Susilawati, E.N. Nukung, M.A.T. Yua, J. Kim. Sains Dan Apl. 23 (2020) 203–208. https://dx.doi.org/10.14710/jksa.23.6.203-208.

[23] L. Maghfiroh, K.F. Hanum, E. Sedyadi, I. Nugraha, F.A. Nurlaili, Proceeding Int. Conf. Sci. Eng. 2 (2019) 201–205. https://dx.doi.org/10.14421/icse.v2.86.

[24] S. Ranggana, Manual Analysis of Fruit and Vegetable Products, Tata McGraw-Hill, 1977. https://books.google.co.id/books/about/Manual_of_Analysis_of_Fruit_and_Vegetabl.html?id=i3ZGNQAACAAJ&redir_esc=y.

[25] G.W. Pradana, A.M. Jacoeb, S. Ruddy, J. Pengolah. Has. Perikan. Indones. 20 (2017) 609–619. https://pdfs.semanticscholar.org/7cd0/119895e87ddd250b2516445f0270b5771fb0.pdf.

[26] M.A. Budiman, Uju, K. Tarman, IOP Conf. Ser. Earth Environ. Sci. 967 (2022). https://dx.doi.org/10.1088/1755-1315/967/1/012012.

[27] J.S. Yaradoddi, N.R. Banapurmath, S. V. Ganachari, M.E.M. Soudagar, A.M. Sajjan, S. Kamat, M.A. Mujtaba, A.S. Shettar, A.E. Anqi, M.R. Safaei, A. Elfasakhany, M.I.H. Siddiqui, M.A. Ali, J. Mater. Res. Technol. 17 (2021) 3186–3197. https://dx.doi.org/10.1016/j.jmrt.2021.09.016.

[28] I.K. Sani, M. Alizadeh, Food Packag. Shelf Life 33 (2022) 100912. https://dx.doi.org/10.1016/j.fpsl.2022.100912.

[29] M. Fazeli, R.A. Simão, Macromol. Symp. 380 (2018) 1–8. https://dx.doi.org/10.1002/masy.201800110.

[30] D. Hassani, I.K. Sani, S. Pirsa, J. Polym. Environ. 32 (2024) 1972-1983. https://dx.doi.org/10.1007/s10924-023-03114-3.

[31] Z. Farajinejad, I.K. Sani, M. Alizadeh, S. Amiri, J. Polym. Environ. (2023). https://dx.doi.org/10.1007/s10924-023-03159-4.

[32] A. Syarifuddin, Yunianta, J. Pangan Dan Agroindustri 3 (2015) 1538–1547. https://jpa.ub.ac.id/index.php/jpa/article/view/278.

[33] H. Eghbaljoo, M. Alizadeh Sani, I.K. Sani, S.M. Maragheh, D.K. Sain, Z.H. Jawhar, S. Pirsa, A. Kadi, R. Dadkhodayi, F. Zhang, S.M. Jafari, Crit. Rev. Food Sci. Nutr. (2023) 1–17. https://dx.doi.org/10.1080/10408398.2023.2280769.

MUHAMMAD THORIQ AL FATH[1]

GHENDIS EKAWATI AYU[1]

GINA CYNTHIA RAPHITA HASIBUAN[2]

NISAUL FADILAH DALIMUNTHE[1]

VIKRAM ALEXANDER[1]

[1]Department of Chemical Engineering, Faculty of Engineering, Universitas Sumatera Utara, Padang Bulan, Medan, Indonesia

[2]Department of Civil Engineering, Faculty of Engineering, Universitas Sumatera Utara, Padang Bulan, Medan, Indonesia

NAUČNI RAD

UTICAJ DODATKA GLICEROLA I SAGO SKROBA NA KARAKTERISTIKE BIOPLASTIKE NA BAZI PEKTINA OD KORE POMORANDŽE

Održivi materijali za pakovanje hrane imaju značajan interes u rešavanju ekoloških problema stvaranjem obnovljivih zamena, kao što je bioplastika na bazi pektina. Kora pomorandže ima relativno visok sadržaj pektina od 42,5%, koji se može sintetizovati u bioplastiku. Bioplastika na bazi pektina ima ograničenja u pogledu mehaničke i fizičke čvrstoće zbog higroskopne prirode pektina. Ova studija ima za cilj da utvrdi efekat dodavanja glicerola i skroba sagoa na karakteristike bioplastike na bazi pektina od kore pomorandže. Metoda livenja je korišćena u formulaciji bioplastike korišćenjem varijacije odnosa pektin:skrob (75:25, 65:35, 55:45 i 50:50%) i sastava glicerola (10, 20, 30 i 40%). Na osnovu rezultata, dobijeni pektin je kategorisan kao pektin sa niskim sadržajem metoksila i estara pektina. Karakterizacijama bioplastike postignuta je maksimalna vrednost zatezne čvrstoće od 4,22 MPa za bioplastiku dobijenu korišćenjem odnosa pektin:skrob od 50:50% i 10% glicerola. Maksimalna vrednost svojstava elongacije pri lomljenju bioplastike od 24% dobijena je korišćenjem odnosa pektin:skrob 75:25% i 40% glicerola. Više dodataka sastava pektin: skrob i glicerol dovodi do veće brzine isparavanja vodene pare. Stoga, korišćenje bioplastike na bazi pektina od kore pomorandže nudi održivo rešenje istraživanjem otpada za dobijanje bioplastike za pakovanje hrane, čime se doprinosi očuvanju životne sredine.

Ključne reči: bioplastika, pektin, skrob, kora pomorandže.

Journal of the
Association of Chemical Engineers of
Serbia, Belgrade, Serbia

Chemical Industry & Chemical Engineering Quarterly

CI&CEQ Vol. 30 Contents: Issues 1–4 YEAR 2024

No. 1

Sema Akyalcin, Levent Akyalcin, Morten Bjørgen, **Catalytic performance of desilicated HZSM-12 for benzylation reaction of benzene with benzyl alcohol** 1

Lalgudi Srinivas Bhadrinarayanan, Chinthalacheruvu Anand Babu, **A resins-neutralization coupled route for the treatment of stainless-steel pickling effluent: A research study** 11

Puji Wahyuningsih, Muslimah Muslimah, Yusnawati Yusnawati, **Local salt purification in aceh timur regency using alkaline (KOH and NAOH) activated bentonite**..... 25

Cemre Avşar, Suna Ertunç, **Fluoride removal from phosphogypsum: A study on a pre-industrial scale and its mathematical analysis** 35

Bensaber Bensebia, Fatma-Zohra Chaouche, Ouahida Bensebia, Soumia Kouadri Moustefaï, **Bed expansion in turbulent bed contactor: experiments and prediction** 47

Asli Dönmez, Çetin Kadakal, **Hot-air drying and degradation kinetics of bioactive compounds of gilaburu (*Viburnum opulus* L.) fruit**..... 59

Rondang Tambun, Anggara Dwita Burmana, Bode Haryanto, Vikram Alexander, **The effect of vacuum process on biodiesel production from palm kernel fatty acid distillate** 73

Loganathan Gokulanathan, Jegan Annamalai, **Experimental investigation of micro-ECM on MONEL 400 alloy using particles mixed electrolyte** 81

No. 2

Vinila Mundakkal Lakshmanan, Aparna Kallingal, Sreepriya Sreekumar, **Internal model control of cumene process using analytical rules and evolutionary computation** 89

Beatriz Menossi Ribeiro, Leandro Da Rin De Sandre Junior, Giancarlo De Souza Dias, Michelle Da Cunha Abreu Xavier, Alex Fernando De Almeida, Elda Sabino Da Silva, Alfredo Eduardo Maiorano, Rafael Firmani Perna, Sergio Andres Villalba Morales, **Cross-linked whole cells for the sucrose transfructosylation reaction in a continuous reactor**..... 99

Vanessa Dal-Bó , Heitor Otacílio Nogueira Altino, José Teixeira Freire, **System development for monitoring the production process of freeze-dried samples: a simple and low-cost approach** 111

Kadhum Audaa Jehhef, Musaab Kadem Rasheed, Mohamed Abed Al Abas Siba, **Numerical simulation of the oscillating thin plate impact on nanofluids flow in channel**..... 123

Đorđije Doder, Damir Đaković, Borivoj Stepanov, Nikola Milivojević, **Optimization of energy consumption during immersion frying of peanuts**..... 135

Aysu Kayalioğlu, **Eco-friendly coatings composed of lignosulfonate-modified biopolymer and vegetable waxes for nitrogenous fertilizers** 143

Jasim I. Humadi, Muayad A. Shihab, Ghazwan S. Ahmed, Mustafa A. Ahmed, Zeyad A. Abdullah, Shankar Sehgal, **Process modeling and kinetic estimation for desulfurization of diesel fuel using nano - ZnO/Al_2O_3**..... 151

Ricardo Arbach Fernandes De Oliveira, Julio Henrique Zanata, Gabriela Cantarelli Lopes, **Numerical study of turbulence on drag coefficient determination for particle agglomerates** . 161

No. 3

Ananthakumar Sudalaimani, Barathiraja Rajendran, Thiyagaraj Jothi, Ashokkumar Mohankumar, **Effects of exhaust gas recirculation on diesel engine using hybrid biodiesel**..... 179

Heitor Otacílio Nogueira Altino, Giovani Aud Lourenço, Carlos Henrique Ataíde, Claudio Roberto Duarte, **The influence of moisture content on drilled cuttings' properties of bed packing and flowability** 193

Ananthakumar Sudalaimani, Barathiraja Rajendran, Thiyagaraj Jothi, Mathanbabu Mariappan, **Combustion, emission, and performance characteristics of hybrid biofuel at different compression ratios**..... 207

Rengasamy Rajaraman, Rajamanickam Muthucumaraswamy, **Impact of chemical reaction, viscous dissipation, and thermal radiation on MHD flow past an oscillating plate .** 223

Thitiporn Suttikul, Sirimas Manthung, Sasikarn Nuchdang, Dussadee Rattanaphra, Thongchai Photsathian, **One-step conversion of ethane to ethylene oxide in AC parallel plate dielectric barrier discharge**..... 231

Radmila Milenkovska, Nikola Geskovski, Petre Makreski, Anita Grozdanov, Emil Popovski, Gjorgji Petrushevski, Maja Simonoska Crcarevska, Kristina Mladenovska, **Functionalized carbon nanostructures as temozolomide carriers: Physicochemical and biopharmaceutical characterization** 243

Periasamy Manikandan Srinivasan, Pradeep Kumar Chinnusamy, Raghul Thangamani, Suriya Palaniraj, Pranesh Ravichandran, Surya Karuppasamy, Yokeshwaran Sanmugam, **Heat transfer performance of an Al_2O_3-water-methanol nanofluid in a plate heat exchanger** 257

Imene Ghezal, Ali Moussa, Imed Ben Marzoug, Ahmida El-Achari, Christine Campagne, Faouzi Sakli, **Development of a multi-layered, waterproof, breathable fabric for full-weather apparel** 265

No. 4

Anita Smailagić, Sonja Veljović, Steva Lević, Tatjana Šolević Knudsen, Viktor Nedović, Vladimir Pavlović, Maja Natić, **Chemical characterization of different wood fragments and their volatile composition in model spirit solutions** 275

Stefan Vukmanović, Jasmina Vitas, Snežana Kravić, Zorica Stojanović, Ana Đurović, Biljana Cvetković, Radomir Malbaša, **Influence of main production variables on nutritional characteristics of winery effluent kombucha** 285

Kumutha Ramalingam, Ilaiyavel Sivakumaran, Mathanbabu Mariappan, Barathiraja Rajendran, **Effect of salt bath nitriding on tribological properties of AISI52100 steel coatings using response surface methodology** 295

Saman Khawaja, Muhammad Rashid Usman, Rabya Aslam, **Conceptualization and process simulation of a CO_2 based methanol production plant** 309

Golden Stepha Nallathambi, Bharathi Gowri Sasi Kumar, Guvva Swathy, **The magnetohydrodynamic Williamson fluid flow on an extending sheet with thermophoresis and chemical reaction** 325

Chitra Devi Venkatachalam, Premkumar Bhuvaneshwaran, Mothil Sengottian, Sathish Raam Ravichandran, **Reliability-based design optimization of screw shaft for continuous high-pressure hydrothermal co-liquefaction process** 335

Itumeleng Kohitlhetse, Suter Kiplagat Evans, Musamba Banza, Robert Makomere, **Blast furnace slag for SO_2 capture: Optimization and prediction using response surface methodology and artificial neural network** 349

Muhammad Thoriq Al Fath, Ghendis Ekawati Ayu, Gina Cynthia Raphita Hasibuan, Nisaul Fadilah Dalimunthe, Vikram Alexander, **The effect of glycerol and sago starch addition on the characteristics of bioplastics based on orange peel pectin** 359

Contents: Vol. 30, Issues 1–4, 2024 367

Author Index, Vol. 30, 2024 369

Journal of the
Association of Chemical Engineers,
Belgrade, Serbia

Chemical Industry & Chemical Engineering Quarterly

CI&CEQ Vol. 30 Author Index YEAR 2024

A

Ahmida El-Achari (3) 265
Alex Fernando De Almeida (2) 99
Alfredo Eduardo Maiorano (2) 99
Ali Moussa (3) 265
Ana Đurović (4) 285
Ananthakumar Sudalaimani (3) 179; (3) 207
Anggara Dwita Burmana (1) 73
Anita Grozdanov (3) 243
Anita Smailagić (4) 275
Aparna Kallingal (2) 89
Ashokkumar Mohankumar (3) 179
Asli Dönmez (1) 59
Aysu Kayalioğlu (2) 143

B

Barathiraja Rajendran (3) 179; (3) 207; (4) 295
Beatriz Menossi Ribeiro (2) 99
Bensaber Bensebia (1) 47
Bharathi Gowri Sasi Kumar (4) 325
Biljana Cvetković (4) 285
Bode Haryanto (1) 73
Borivoj Stepanov (2) 135

C

Carlos Henrique Ataíde (3) 193
Cemre Avşar (1) 35
Çetin Kadakal (1) 59
Chinthalacheruvu Anand Babu (1) 11
Chitra Devi Venkatachalam (4) 335
Christine Campagne (3) 265
Claudio Roberto Duarte (3) 193

D

Damir Đaković (2) 135
Dussadee Rattanaphra (3) 231

Đ

Đorđije Doder (2) 135

E

Elda Sabino Da Silva (2) 99
Emil Popovski (3) 243

F

Faouzi Sakli (3) 265
Fatma-Zohra Chaouche (1) 47

G

Gabriela Cantarelli Lopes (2) 161
Ghazwan S. Ahmed (2) 151
Ghendis Ekawati Ayu (4) 359
Giancarlo De Souza Dias (2) 99
Gina Cynthia Raphita Hasibuan (4) 359
Giovani Aud Lourenço (3) 193
Gjorgji Petrushevski (3) 243
Golden Stepha Nallathambi (4) 325
Guvva Swathy (4) 325

H

Heitor Otacílio Nogueira Altino (2) 111; (3) 193

I

Ilaiyavel Sivakumaran (4) 295
Imed Ben Marzoug (3) 265
Imene Ghezal (3) 265
Itumeleng Kohitlhetse (4) 349

J

Jasim I. Humadi (2) 151
Jasmina Vitas (4) 285
Jegan Annamalai (1) 81
José Teixeira Freire (2) 111
Julio Henrique Zanata (2) 161

K

Kadhum Audaa Jehhef (2) 123
Kristina Mladenovska (3) 243
Kumutha Ramalingam (4) 295

L

Lalgudi Srinivas Bhadrinarayanan (1) 11
Leandro Da Rin De Sandre Junior (2) 99
Levent Akyalcin (1) 1
Loganathan Gokulanathan (1) 81

M

Maja Natić (4) 275
Maja Simonoska Crcarevska (3) 243
Mathanbabu Mariappan (3) 207; (4) 295
Michelle Da Cunha Abreu Xavier (2) 99
Mohamed Abed Al Abas Siba (2) 123
Morten Bjørgen (1) 1
Mothil Sengottian (4) 335
Muayad A. Shihab (2) 151
Muhammad Rashid Usman (4) 309
Muhammad Thoriq Al Fath (4) 359
Musaab Kadem Rasheed (2) 123
Musamba Banza (4) 349
Muslimah Muslimah (1) 25
Mustafa A. Ahmed (2) 151

N

Nikola Geskovski (3) 243
Nikola Milivojević (2) 135
Nisaul Fadilah Dalimunthe (4) 359

O

Ouahida Bensebia (1) 47

P

Periasamy Manikandan Srinivasan (3) 257
Petre Makreski (3) 243
Pradeep Kumar Chinnusamy (3) 257
Pranesh Ravichandran (3) 257
Premkumar Bhuvaneshwaran (4) 335
Puji Wahyuningsih (1) 25

R

Rabya Aslam (4) 309
Radmila Milenkovska (3) 243
Radomir Malbaša (4) 285
Rafael Firmani Perna (2) 99
Raghul Thangamani (3) 257
Rajamanickam Muthucumaraswamy (3) 223
Rengasamy Rajaraman (3) 223
Ricardo Arbach Fernandes De Oliveira (2) 161
Robert Makomere (4) 349
Rondang Tambun (1) 73

S

Saman Khawaja (4) 309
Sasikarn Nuchdang (3) 231
Sathish Raam Ravichandran (4) 335
Sema Akyalcin (1) 1
Sergio Andres Villalba Morales (2) 99
Shankar Sehgal (2) 151
Sirimas Manthung (3) 231
Snežana Kravić (4) 285
Sonja Veljović (4) 275
Soumia Kouadri Moustefaï (1) 47
Sreepriya Sreekumar (2) 89
Stefan Vukmanović (4) 285
Steva Lević (4) 275
Suna Ertunç (1) 35
Suriya Palaniraj (3) 257
Surya Karuppasamy (3) 257
Suter Kiplagat Evans (4) 349

T

Tatjana Šolević Knudsen (4) 275
Thitiporn Suttikul (3) 231
Thiyagaraj Jothi (3) 179; (3) 207
Thongchai Photsathian (3) 231

V

Vanessa Dal-Bó (2) 111
Vikram Alexander (1) 73; (4) 359
Viktor Nedović (4) 275
Vinila Mundakkal Lakshmanan (2) 89
Vladimir Pavlović (4) 275

Y

Yokeshwaran Sanmugam (3) 257
Yusnawati Yusnawati (1) 25

Z

Zeyad A. Abdullah (2) 151
Zorica Stojanović (4) 285